James Cook University

Doctoral Thesis

# Enery Harvesting for Marine Based Sensors

*Author:*
Josh Davidson

*A thesis submitted in fulfilment of the requirements for the degree of Doctor of Philosophy*

*in the*

School of Engineering and Physical Sciences

January 2016

# Declaration of Authorship

I, Josh Davidson, declare that this thesis titled, 'Enery Harvesting
for Marine Based Sensors' and the work presented in it are my own. I confirm that:

- This work was done wholly or mainly while in candidature for a research degree at this University.
- Where any part of this thesis has previously been submitted for a degree or any other qualification at this University or any other institution, this has been clearly stated.
- Where I have consulted the published work of others, this is always clearly attributed.
- Where I have quoted from the work of others, the source is always given. With the exception of such quotations, this thesis is entirely my own work.
- I have acknowledged all main sources of help.
- Where the thesis is based on work done by myself jointly with others, I have made clear exactly what was done by others and what I have contributed myself.

Signed: _____

Date: _____

# *Abstract*

This work examines powering marine based sensors (MBSs) by harvesting energy from their local environment. MBSs intrinsically operate in remote locations, traditionally requiring expensive maintenance expeditions for battery replacement and data download. Nowadays, modern wireless communication allows real-time data access, but adds a significant energy drain, necessitating frequent battery replacement. Harvesting renewable energy to recharge the MBSs battery, introduces the possibility of autonomous MBS operation, reducing maintenance costs and increasing their applicability. The thesis seeks to answer if an unobtrusive energy harvesting device can be incorporated into the MBS deployment to generate 1 Watt of average power.

Two candidate renewable energy resources are identified for investigation, ocean waves and the thermal gradient across the air/water interface. Wave energy conversion has drawn considerable research in recent years, due to the large consistent energy flux of ocean waves compared to other conventional energy sources such as solar or wind, but focussing on large scale systems permanently deployed at sites targeted for their favourable wave climates. Although a small amount of research exists on using wave energy for distributed power generation, the device sizes and power outputs of these systems are still one to two orders of magnitude larger than that targeted in this thesis. The present work aims for an unobtrusive device that is easily deployable/retrievable with a mass less than 50kg and which can function at any deployment location regardless of the local wave climate. Additionally, this research differs from previous work, by also seeking to minimise the wave induced pitch motion of the MBS buoy, which negatively affects the data transmission of the MBS due to tilting and misalignment of the RF antenna. Thermal energy harvesting has previously been investigated for terrestrial based sensors, utilising the temperature difference between the soil and ambient air. In this thesis, the temperature difference between the water and ambient air is utilised, to present the first investigation of this thermal energy harvesting concept in the marine environment.

A prototype wave energy converter (WEC) was proposed, consisting of a heaving cylindrical buoy with an internal permanent magnet linear generator. A mathematical model of the prototype WEC is derived by coupling a hydrodynamic model for the motion of the buoy with a vibration energy harvester model for the generator. The wave energy resource is assessed, using established mathematical descriptions of ocean wave spectra and by analysing measured wave data from the coast of Queensland, resulting in characteristic wave spectra that are input to the mathematical model of the WEC. The parameters of the WEC system are optimised, to maximise the power output while minimising the pitch motion. A prototype thermal energy harvesting device is proposed,

consisting of a thermoelectric device sandwiched between airside and waterside heat exchangers. A mathematical model is derived to assess the power output of the thermal energy harvester using different environmental datasets as input. A physical prototype is built and a number of experiments performed to assess its performance.

The results indicate that the prototype WEC should target the high frequency tail of ocean wave spectra, diverging from traditional philosophy of larger scale WECs which target the peak frequency of the input wave spectrum. The analysis showed that the prototype WEC was unable to provide the required power output whilst remaining below 100kg and obeying a 40 degrees pitch angle constraint to ensure robust data transmission. However, a proposed modification to the WECs cylindrical geometry, to improve its hydrodynamic coupling to the input waves, was shown to enable the WEC to provide the required 1W output power whilst obeying the pitch constraints and having a mass below 50kg. The thermal energy harvester results reveal that the thermal gradient across the air/water interface alone is not a suitable energy resource, requiring a device with a cross-sectional area in excess of $100\text{m}^2$ to power a MBS. However, including a solar thermal energy collector to increase the airside temperature, greatly improves the performance and enables a thermal energy harvester with a cross-sectional area on the order of $1\text{m}^2$ to provide 1W of output power.

The findings in this thesis suggest that a well hydrodynamically designed buoy can provide two major benefits for a MBS deployment: enabling efficient wave energy absorption by the MBS buoy, and minimising the wave induced pitch motion which negatively affects the data transmission.

# *Acknowledgements*

First and foremost, I would like to thank my supervisor Prof. Peter Ridd, without whom none of this would have been possible. Thanks for the education, the guidance, the support and the mentorship. I would also like to thank the Energy Harvesting Team at CSIRO, especially my supervisor there, Dr Sam Behrens, as well as Chris Knight, thanks for the guidance and the opportunities. Finally, I would like to thank my family and friends for all your support. Cheers.

# Contents

# List of Figures

# List of Tables

# Chapter 1

# Introduction

Following Moore's Law, the size and power consumption of electronics have reduced dramatically, enabling new possibilities in the field of wireless sensor networks (WSNs). It is envisioned that such networks will revolutionise environmental monitoring and data acquisition with applications limited only by the user's imagination. The ability to sample data with greater spatial resolution, due to decreased size and cost of the individual nodes, and then to have that data available in real-time, as the networks communicate results through radio frequency (RF) transmissions, gives significant benefit to users and decision makers reliant on the information being monitored. However one aspect of the sensor nodes which is currently lagging, and hindering the widespread deployment of these WSNs, is a reliable power supply. This thesis investigates novel methods to power sensor nodes deployed in marine environments.

## 1.1 Sensors

A sensor node is an instrument which can measure and record physical parameters. This process is performed electronically, consuming electrical energy provided by a power supply component. A typical node also contains a processing microcontroller, memory chip, one or more sensors and a transceiver. Modern wireless communication technology has enabled groups of sensor nodes to relay information between each other, forming a WSN. At the turn of the century, *Business Week* proclaimed networked microsensors as one of the 21 most important technologies for the 21st century [1]. The current state and evolution of networked sensors is reviewed by Chong and Kumar [2] where they indicate the future potential for WSNs with the following statement "Cheap, smart devices with multiple onboard sensors, networked through wireless links and the Internet

and deployed in large numbers, provide unprecendented opportunities for instrumenting and controlling homes, cities and the environment."

Over the past decade the potential of sensor nodes have significantly increased as their components' capabilities follow Moore's Law. However the power supply component remains an exception to this exponential increase in capability, because sensor nodes are traditionally battery powered. While the density of transistors on a chip doubles every 18 months, the energy density of batteries has only doubled every 5-20 years, depending on the particular chemistry [3]. As sensor networks increase in number and size, replacement of depleted batteries becomes time consuming and wasteful. Alternatively, increasing the size of battery to last the lifetime of a sensor would not be very attractive or practical either, resulting in huge batteries that dominate the overall size of the node.

There is a clear need to explore novel alternatives for powering WSNs, because relying on existing battery technology hinders their widespread deployment. By harvesting energy from their local environment, WSNs can achieve much greater run-times, years not months, with potentially lower cost and weight. This is particularly true for WSNs deployed in the marine environment, as discussed in the next section.

## 1.2 Marine based sensors

Seventy percent of the Earth's surface is covered by water. As such, there are many applications for monitoring environmental data in and around water. Marine biologists, oceanographers, climatologists, environmental scientists, water quality managers and many other users, currently monitor various parameters in aquatic environments, to aide their understanding and decision making. WSNs are ideal to facilitate this process.

Curtin et al [4] proposed the concept of autonomous oceanographic sampling networks in the 1990's, because "...assessing the reality of numerical model fields with ever increasing resolution, testing dynamical balances involving high-order derivatives, and exploring the limits of predictability required measurement of temporal and spatial gradients in the ocean far exceeding the current practical capabilities." The need for high grade data acquisition in the marine environment through WSN monitoring, has been identified by many other researchers since then, who are all working towards making this vision a reality.

Rajasegarar et al [5] reported on the challenges of sensor network implementation in the Great Barrier Reef (GBR) marine environment. The GBR consists of over 3,200 individual reefs, spanning over 280,000 $km^2$. The strategic collection of data at appropriate scales is critical for effective environmental monitoring and analysis of the GBR, with the

scales of fluctuations in this system ranging from kilometre oceanic mixing to millimetre inter-skeletal currents. Although existing data logging systems could provide valuable information, the high acquisition costs and inability to retrieve data in real time, lead the marine research communities to examine emerging technologies, such as WSNs, for real time acquisition of the data. In their paper, Rajasegarar et al [5] identified power requirements as the top technical challenge, along with the fouling and corrosion of equipment used under water, and the general problems of maintaining equipment in a remote and hostile environment.

A number of other researchers have reported on case studies of WSN deployments in marine environment. For example: Cella et al [6] trialled a sensor network, consisting of ten nodes, to retrieve temperature and illuminance data from the sea bed. The work reported by Cella et al is a part of the SEMAT (Smart Environmental Monitoring and Analysis Technologies) project, which is developing advanced remote WSNs, designed to collect data in marine environment locations for research into environmental issues such as climate change, water quality and ecosystem health (see also [7, 8]). Another project focused on the development of WSN for environmental surveillance of the sea, is the OceanSense project [9]. The OceanSense project was originally motivated from a field study in China's second largest coal transportation harbour [10], which was suffering from a severe problem of silt deposition along its sea route. To monitor the water depth required the hiring of three vessels, equipped with sonar, to cruise the shallow sea area around the harbour, costing the harbour millions of dollars per year. By deploying a WSN to monitor the sea depth in this area, they could reduce the monitoring expense by 95% [9].

Bondarenko et al [11] constructed and deployed four wireless nodes, each connected to seven temperature sensors, for monitoring cold water upwelling. Voigt et al [12] also designed and implemented a small scale marine sensor network to collect temperature data. Many more examples can be found in the review by Albaladejo et al [13], which identifies and details a dozen different case studies on WSNs for oceanographic monitoring. More recently Xu et al [14] published another review, with the intent of being an update and extension to Albaladejo et al's [13] review, whereby over twenty published case studies were reviewed. In addition to these cases of deployed marine based WSN, others have been proposed for special applications, for example; Barbosa et al [15] proposed a drifting WSN for monitoring oil spills, and Lloret et al [16] proposed an underwater WSN for fish farms to monitor the amount of uneaten food and fecal waste by the fish.

### 1.2.1 Data transmission

One of the key components of an autonomous WSN, is the data transmission system. Data transmission allows users to access the measured data in real time. Figure 1.1 illustrates the general structure of a marine based WSN. The sensor nodes have surface buoys, which relay the data, via RF transmission to a sink node. The sink node then performs the long range data transmission to the base station.

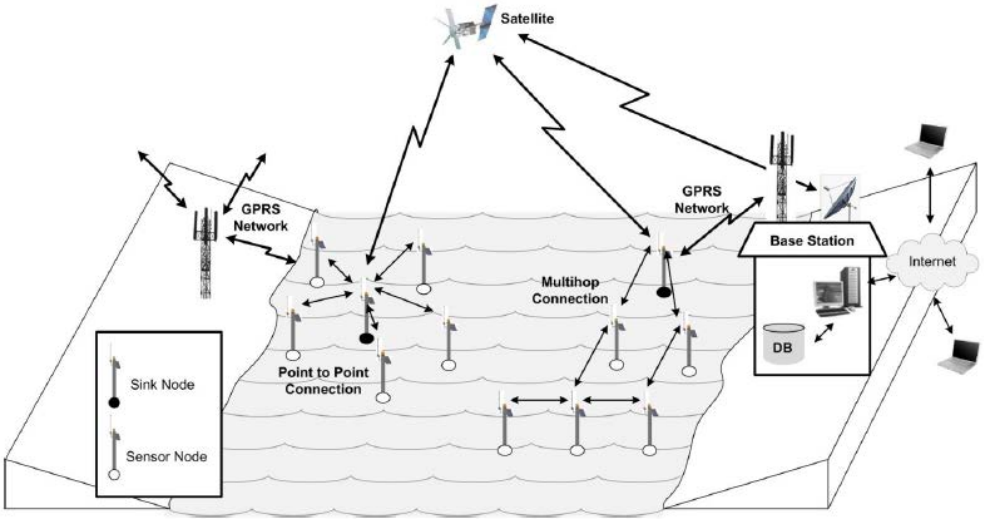


FIGURE 1.1: General structure of a marine based wireless sensor network [13]

Sensors below the surface, can be distributed through the water column or on the sea floor, as depicted in Figure 1.2. The sensors can either be directly connected to the surface buoy with wires/cables, or via underwater wireless communication (such as acoustic modems [17]). Underwater WSN's have been proposed by a number of researchers [6, 18–22], whereby a gateway node at the surface communicates to a cluster of underwater sensor nodes using acoustics, but communicates with other clusters, or base stations, using radio waves. Indeed, Cella et al [6] concluded that underwater wireless communication is the key factor in improving the practicality and versatility of sensor networks for marine environment monitoring. However, this will place a large burden on the power supply component, because the power consumption of underwater acoustic communications is about 100 times greater than that for RF communication [23].

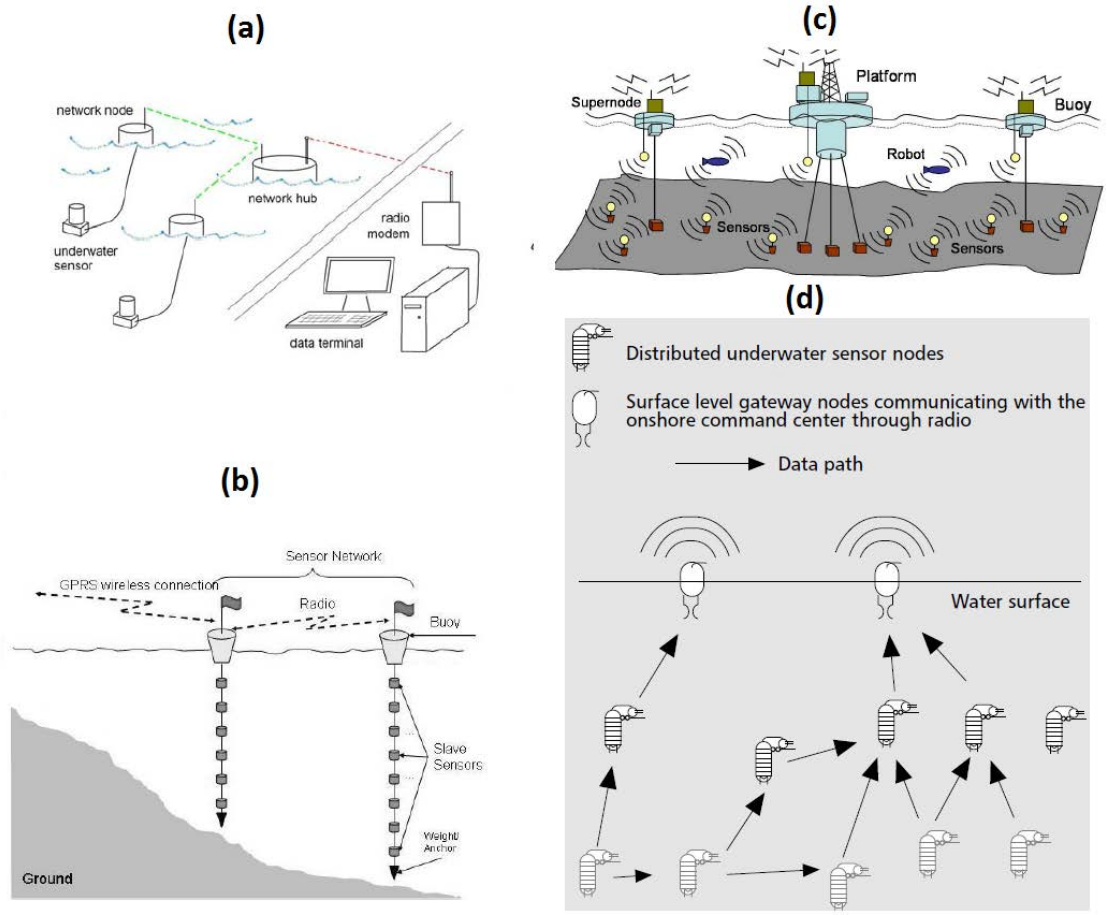


FIGURE 1.2: Communication with underwater sensors: wired (a) [6] and (b) [12] or acoustic (c) [19] and (d) [20]

## 1.3 Energy harvesting for marine based sensors

Marine based sensors (MBSs) intrinsically operate in remote environments. Ideally, the maintenance required for these sensor nodes should be minimal. Maintenance expeditions are time consuming and costly, requiring the hiring of sea vessels, qualified personnel to operate these vessels, and in some cases divers. Historically, maintenance expeditions would entail physically visiting the individual sensor nodes to retrieve the data, inspect that the nodes are operating correctly, and to replace the batteries. Nowadays, modern data transmission allows real time access to the data, eliminating the need for physical data retrieval. Additionally, the node can sending monitoring information of its own state to eliminate the for physical inspection. Unfortunately however, the data transmission comes at the expense of a large demand on the power supply, which increases the need for physical battery replacement. Using energy harvesting to recharge the batteries, would eliminate the need for periodic maintenance expeditions to replenish the energy store, allowing MBSs to run autonomously.

In fact, the lack of energy harvesting for MBSs has caused trade-offs between energy conservation and the system's functional requirements [24]. Voigt et al [12] describes energy harvesting as a must in the 'Remaining challenges' section of their paper. Likewise, in their review of MBS networks, Xu et al [14] identify energy harvesting as one of the four main topics in 'Research challenges and opportunities'. Many other authors have noted the need for energy harvesting systems to extend the lifetime of their MBS application [6, 22, 25, 26].

The academic community are not alone in identifying the need for equipping MBSs with energy harvesting devices. The US Navy issued a Small Business Innovative Research solicitation [27], for energy harvesting devices which could be fitted to their 'sonobuoy' MBSs. A sonobuoy is an acoustic device primarily used for detection of objects moving in the water. Data is relayed from the device back to a station via a radio communications module, housed in an inflatable surface float. A sonobuoy has an operational life limited by its batteries of only 8 hours. Other than their extensive use in scientific research, for example monitoring sea mammals, they also are used by the US Navy for detection of submarines.

## 1.4 Thesis overview and contribution

The main objective of this thesis is to investigate an energy harvesting solution for powering MBSs. Candidate solutions are sought by reviewing the literature related to the general topic of energy harvesting for WSNs and by assessing the energy resources available in the marine environment. Two renewable energy resources are selected for further investigation in this thesis, namely: ocean waves and the thermal gradient across the air/water interface.

Ocean waves provide the largest and most reliable resource and are selected as the core focus of the thesis. Additionally, it is reported in the literature that the wave induced pitching motion of the MBS buoy negatively effects the wireless communication, by causing the antenna to be misaligned, which increases the required power budget for data transmission. Therefore, while investigating a MBS buoy to harvest wave energy, the wave induced pitch motion can simultaneously be investigated and ideally minimised, to provide a stable platform for data transmission by the antenna, allowing the power supply problem to be attacked on two fronts, by increasing the energy supply and reducing the energy demand.

Thermal energy harvesting across the air / water interface is identified as a novel energy resource in this thesis, previously unexplored for powering small scale electrical equipment in the marine environment. A similar resource was uncovered in the literature review, the thermal gradient across the air / soil interface, which was reported to have reasonable potential for terrestrial based sensor nodes. Therefore, the potential of this resource, applied to the marine environment, will be explored in this thesis.

### 1.4.1 Outline of thesis

In Chapter 2, a literature review is presented on the general topic of energy options for WSNs, detailing the different energy storage and harvesting methods available to power sensor nodes distributed throughout the environment. A large body of work exists in the field of energy harvesting for WSNs, which share many similarities with the present topic of energy harvesting for MBSs. Indeed, energy harvesting for MBSs is a specific application of energy harvesting for WSNs, therefore the present thesis begins by looking to the lessons learnt in the more general field.

Chapter 3 then concentrates on the specific topic of powering a MBS. The literature relating to MBS deployments is assessed to determine the power required by an MBS from an energy harvesting device. From this literature, the detrimental effect of wave induced pitch motion on the data transmission is revealed and its drain on the power supply identified. The energy resources available in the marine environment are evaluated, whereby ocean waves and the thermal gradient existing at the air / water interface of the ocean are selected for further investigation in this thesis.

In Chapter 4, concepts relating to ocean waves are outlined and the field of wave energy conversion is reviewed. The disparity between traditional large scale wave energy conversion and the present topic of wave energy harvesting for MBSs is distinguished. The design requirements for a wave energy converter (WEC) for powering MBSs are detailed, and a prototype WEC, the CIPMLG WEC, is proposed to fulfil these design requirements.

Chapter 5 derives a mathematical model to assess the performance of the proposed CIPMLG WEC, and then Chapter 6 uses this model to give a preliminary analysis of the CIPMLG WEC. Chapter 7 investigates the ocean wave resource, to determine the input wave spectra to be used for evaluating the CIPMLG WEC's performance. Chapter 8 presents the results of the CIPMLG WEC's performance, as assessed by the numerical model, and details a number of practical aspects to be considered when evaluating the numerical results. A refinement of the CIPMLG WEC's geometry is then also proposed

and assessed in Chapter 8, before conclusions on the viability of utilising wave energy for powering MBSs are presented.

In Chapter 9 the novel concept of harvesting thermal energy across the air / water interface is introduced and a mathematical model of this process developed and used in conjunction with environmental datasets to assess the potential of this resource. A physical thermal energy harvester prototype is constructed and used to test various system aspects and prove the overall concept.

Conclusions are drawn and presented in Chapter 10, along with details of future work.

### 1.4.2 Contribution of thesis

The main contributions of this thesis are that it:

- Collates a literature review on energy options for WSNs and MBSs.
- Identifies that a well hydrodynamically designed buoy can improve the power supply on two fronts; by harvesting energy from the incident waves to recharge the battery, and by minimising the wave induced pitch motion to reduce the power demand of the wireless communication.
- Proposes a WEC which has the potential to satisfy the constraints of a small and easily deployable device, and analyses this proposed WEC giving conclusions on its applicability.
- Derives a mathematical model of the proposed WEC and develops a methodology for analysing its performance and selecting optimal design parameter values for this type of system.
- Identifies that focussing on the high frequency tail of ocean wave spectra is advantageous for small scale wave energy conversion.
- Identifies a novel energy resource previously unexplored for small scale energy harvesting: thermal energy harvesting across the air/water interface. Performs a preliminary analysis to estimate the potential of the resource for powering MBSs, a series of experiments to further evaluate the concept and then gives conclusions on its applicability.

# Chapter 2

# Energy options for wireless sensor nodes

This chapter is based on literature reviews co-published by the author [28, 29], presenting energy options for wireless sensor nodes. At the commencement of the present thesis, energy harvesting for wireless sensors was an active and growing research field, though almost exclusively for terrestrial based applications. A good volume of literature existed, with many publications reporting the research into this field and sharing knowledge gained, and a number of reviews on this topic were available [30–33]. Due to the similarities between land based and marine based sensors, the purpose of this review for the present thesis, was to learn from the large body of work in this general field of energy options for wireless sensors, and then to apply it to the specific application of marine based sensors.

Providing power for WSNs can be split into two main technology categories: energy storage and energy harvesting. This chapter reviews the state-of-the art technology in each of these fields, outlining different powering options for sensor nodes. These include energy storage utilizing batteries, capacitors, fuel cells, heat engines and betavoltaic systems and energy harvesting methodologies including photovoltaics, temperature gradients, fluid flow, pressure variations and motion harvesting.

## 2.1 Energy storage

Energy storage is the basis of current power sources, whereby the sensor node is powered from energy stored at the node e.g. batteries. The energy is stored in various forms ranging from electrical charge to hydrocarbon based fuels. By itself, energy storage

cannot deliver energy indefinitely, as at some stage the stored energy will be depleted and need replenishing. The metric used in the comparison between these devices is their average energy density, Joules per unit volume. Different energy storage techniques are outlined below.

### 2.1.1 Batteries

Batteries are the most common power source currently utilized. They store energy chemically, releasing it as electricity via an internal chemical reaction which transfers electrons from its anode to cathode. Offering good energy density, they are available commercially in a range of sizes. Their output power is supplied at the correct voltage levels for modern electronics and consists of DC current which eliminates the need for intermediate power conditioning electronics. However, its power output is limited by a number of factors including: the relative potentials of the anode and cathode materials, and the surface area of the electrodes.

There are two main categories of batteries, primary and secondary. Primary batteries are not easily recharged using electricity, while secondary batteries can reverse their internal chemical reaction through a recharging process. This process involves energy being delivered back into the battery and stored in the form of chemical bonds. When using primary batteries the lifetime of the sensor node is restricted by the fixed amount of energy initially stored in the battery. The capacity of energy stored in a battery depends on its energy density and volume. Unfortunately improvements in battery energy density seem to be reaching a plateau. This coupled with the fact that it is desirable to minimise the volume of any sensor node component means batteries are forcing a large trade-off between the node's lifetime and its volume.

Secondary batteries provide the option of extending the sensor node's lifetime, relative to that of a primary battery, through their ability to be recharged. However, this means they need to run in conjunction with another device capable of supplying power. This arrangement is usually desirable as quite often the device supplying the power does so intermittently. The battery stores these bursts of energy, providing the electronics with a stable constant energy interface. A robust system will require electronics to control the charging and discharging of the battery in a way that maximises its life as incorrect charging profiles diminish the battery's usable life.

There is a wide variety of secondary batteries whose characteristics, like primary batteries, are determined by their internal chemistries. Conventional chemistries such as Nickel-Zinc (NiZn), Nickel Metal Hydride (NiMH) and Nickel-Cadmium (NiCd), offer

high energy densities and good discharge rates, but with the disadvantages of short cycle life and adverse "memory" effects. Lithium-ion batteries overcome these drawbacks, with a higher energy density and discharge rate, higher cell voltage, longer cycle life and elimination of "memory" effects [34]. However their major disadvantage is the particular care required when recharging to avoid overheating and permanent damage. Figure 2.1 shows the relative strengths of the different battery chemistries in terms of their energy and power densities.

Some battery chemistries have problems with shelf life. Standard alkaline batteries have shelf lives of around seven years; while newer lithium based systems (both primary and secondary) have even longer lives. Other secondary (rechargeable) chemistries like Nickel Metal Hydride (NiMH) lose 1-2% of their capacity per day of storage.

Two promising new fields of research in battery technology are micro-batteries and flexible batteries. Micro-batteries seek not only to reduce the size of the actual battery but also to improve integration with the electronics they are powering. The goal of micro-batteries is therefore to produce a battery on a chip. A major challenge is overcoming small power outputs due to surface area limitations of micro-batteries, however work into three-dimensional surfaces seem promising [35]. The second field involves a new breed of lightweight flexible batteries [36] which can be moulded to any shape. Hence they can serve a double purpose of acting as structural material, reducing the total volume of the sensor node.

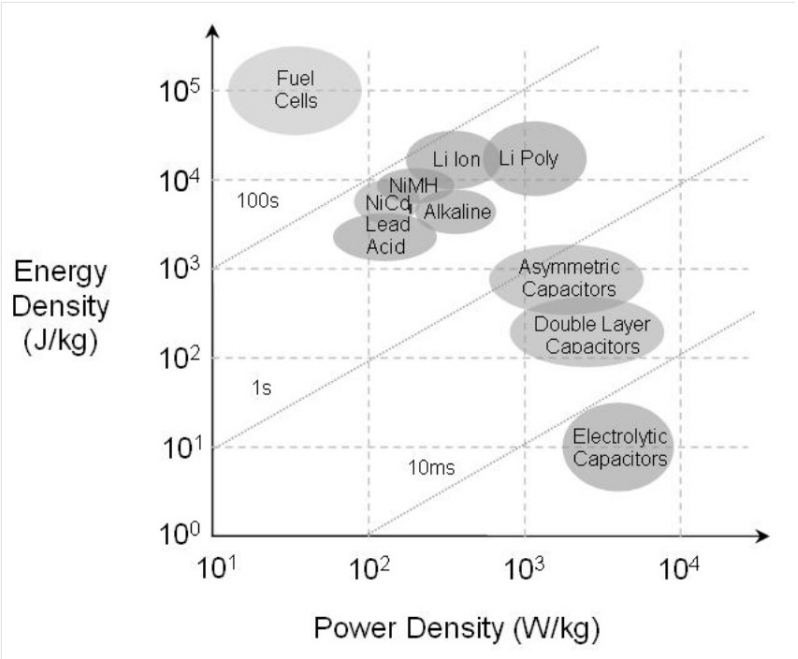


FIGURE 2.1: Ragone chart for various energy storage technologies [29]

### 2.1.2 Capacitors

Capacitors store energy in the electric field between a pair of oppositely charged conductors. They have significantly higher *power density* than batteries, as they are able to charge and discharge over much shorter periods of time. However, their *energy density* is two to three orders of magnitude lower. This makes capacitors ideal for providing short bursts of high power with low duty cycles allowing the capacitor to recharge before the next burst of power is needed. Therefore a combination of capacitor and battery could solve the power requirement across a normal nodal duty cycle. A battery can be used to provide the low power requirements on sleep and receive mode, while a capacitor can provide the high power required for RF transmission on short duty cycles.

The focus of continued research strives to increase capacitor's energy density, with a new breed of supercapacitors. Figure 2.2 shows a charged supercapacitor. The critical difference between a supercapacitor and a standard capacitor is in the surface area supplied by the electrode and the thinness of the double layer formed at the electrode-electrolyte interface. In a standard capacitor the area is simply the surface area of a nominally flat plate. However, the use of porous materials, such as carbon, effectively increases the surface area of each electrode enormously. This allows capacitors with values of the order of 2000 Farads in packages approximating standard battery sizes.

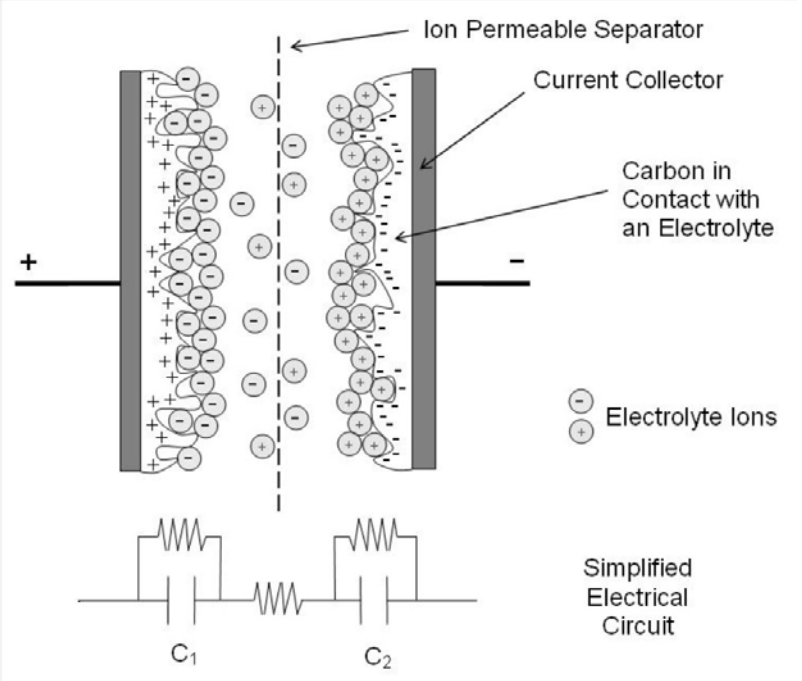


FIGURE 2.2: Representation of a charged electrochemical double layer capacitor [37]

The simplified circuit shown in Figure 2.2 hints at a further improvement: Capacitors in series add such that the total capacitance of a cell is given by;

$$\frac{1}{C_{cell}} = \frac{1}{C_1} + \frac{1}{C_2}. \tag{2.1}$$

For a supercapacitor both $C_1$ and $C_2$ are large, leading to a $C_{cell}$ approximately half the size of $C_1$ or $C_2$. This has lead to the development of so called asymmetric capacitors. An asymmetric supercapacitor typically consists of a battery type electrode (usually a faradaic or intercalating metal oxide) and an electrochemical capacitor type electrode (high surface area carbon). In such an arrangement, the carbon electrode has a much greater capacity than the battery electrode. Thus $C_{cell}$ approaches the capacitance of the carbon electrode alone, resulting in a much larger energy storage capability of a comparable symmetric carbon based supercapacitor. This has lead to development of cells with capacitance values in excess of 8,000 Farads [37].

The increase in capacitance values has led to energy storage capabilities approaching that of some battery chemistries, such as lead-acid storage cells, and power storage capabilities an order of magnitude greater. Critically, the efficiency of capacitors exceeds 90% while batteries have typical values of 60-70%. Some supercapacitors are capable of more than 500,000 charge cycles before noticeable deterioration (compared with about 1,000 for rechargeable batteries) [38]. This factor, along with short charging times and high power densities, make supercapacitors attractive as secondary power sources in place of rechargeable batteries in some wireless sensor network applications [30].

### 2.1.3 Micro fuel cells

Like batteries, fuel cells convert stored chemical energy into electricity. Generally, liquid fuels have much higher energy density than battery chemistries. In the fuel cell, such as the one shown in Figure 2.3, a catalyst promotes the separation of the electrons from the protons of hydrogen atoms drawn from the fuel. The electrons are then available for use by an external circuit, while the protons diffuse through an electrolyte to recombine with the electrons and oxygen on the other side producing water molecules [30]. This technology was pioneered for the NASA space program and has been used on large scales for decades but recent work has focused on reducing their size to replace consumer batteries [39].

As with batteries, the major performance restriction of micro-scale fuels cells results from the small electrode surface area. An opportunity may exist to combine the work of Hart *et al* [35] involving three dimensional surfaces in battery electrodes, with the noted shortcomings of fuel cell electrodes. Another hindrance is the plumbing for the

fuel reservoir which at micro-scales is seen as a harder task than micro-fabricating the electrodes. The main issue here is due to flow considerations and ensuring that the fuel flows throughout the cell particularly to the finer tubing at the extremities.

Matsushita Battery has developed a direct methanol fuel cell (DMFC) incorporated with a lithium ion battery. This system is approximately 400 $cm^3$, with peak output of 20 W and an average of 13 W [40]. This corresponds to a average power density of 0.03 $W/cm^3$. Angstrom Power has completed a six month test program using a hydrogen fuel cell. The fuel is supplied as hydrogen absorbed in a metal hydride. The volume of the fuel storage is around 6 $cm^3$, and the fuel cell itself can be made in many forms. The two presently available are a cylindrical, 1 W unit with a volume of 10 $cm^3$, and a rectangular 0.38 W unit with a volume of 2.5 $cm^3$ [41]. The average power densities for these, including the fuel storage, are 0.06 $W/cm^3$ and 0.04 $W/cm^3$, respectively.

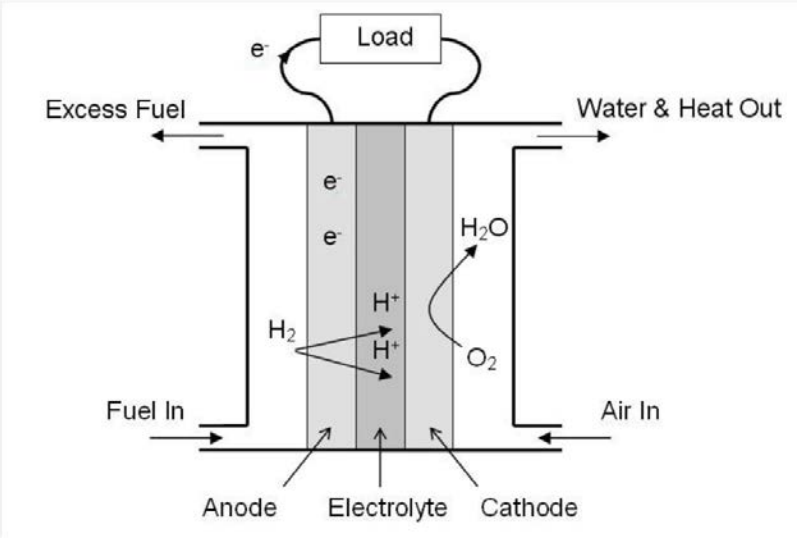


FIGURE 2.3: Example of a polymer electrolyte membrane (PEM) fuel cell. [29]

### 2.1.4 Radioactive power sources

The use of radioactive materials as a power source is attractive due to their extremely high average energy densities, approximately 105 $kJ/cm^3$ [42]. Like many other power sources, it has been used in the large scale for decades but has not yet fully transferred down to a scale useful for sensor nodes. The main technical reason for this is the lack of a high conversion efficiency mechanism at the micro-scale.

Early research into small scale radioactive energy conversion focussed on thermal heating using the kinetic energy of emitted particles. The heat could be converted into electricity using thermoelectric or thermionic techniques which require high temperatures (300 - 900 K) for efficient operation. This scheme works well for operations requiring power in

the watt to kilowatt range but doesn't scale down for micro-power applications since with reducing size, the surface-to-volume ratio increases, leading to high heat leakage to the surroundings, i.e. thermal heat management at the micro-scale is a tough engineering challenge [43].

To date the most promising work for applications in powering wireless sensor nodes is by Lal *et al.* [43] where they have used a radioactive isotope to actuate a conductive cantilever. As shown in Figure 2.4 the emitted electrons collect on the cantilever which causes an electrostatic attraction forcing the cantilever to bend towards the source. When contact is made the charge differential is dissipated and the cantilever oscillates about its equilibrium position. A piezoelectric plate will convert the mechanical energy of the oscillation into electrical energy. They have demonstrated a power conversion efficiency of 2-3% using this radioactive-to-mechanical-to electrical conversion cycle with power outputs in the tens of microwatts, which could power low-power electronics or trickle charge a battery or capacitor.

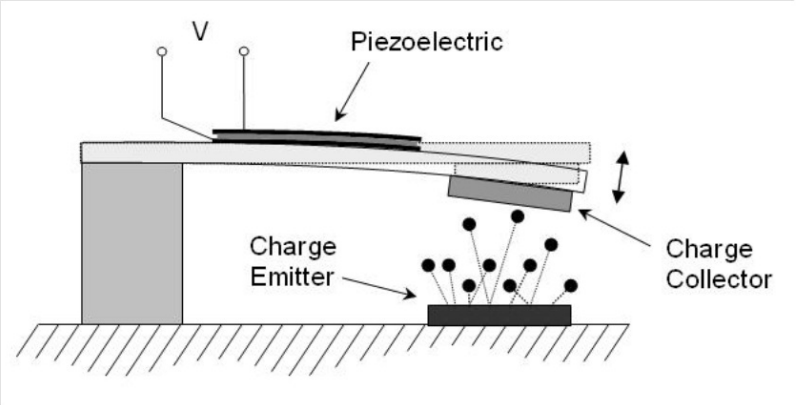


FIGURE 2.4: Radioisotope energy harvester. [29]

## 2.2 Energy harvesting

By harvesting energy from their local environment, sensor networks can overcome their power source problem achieving much greater run-times, years not months, with potentially lower cost and weight. There are numerous alternative energy harvesting options depending on the location and environment of the sensor node's deployment. The metric used for comparison of energy harvesting devices differs from that used for energy storage as they don't have a fixed amount of energy intrinsic to their volume. Therefore, energy harvesting devices are rated on their average power density, watts per unit volume.

In general, energy harvesting will not directly power a sensor. This may be because the levels of power are too low, or it may be as a result of the power being in the wrong form. Typically, sensors and nodes require a voltage in the range 2 - 10 V and peak direct current of approximately 100 mA. Some energy harvesting techniques generate much higher voltages, produce AC power, or simply do not have sufficient power to run the node directly. The result of this is that electronics are required to condition the power for the device and, critically, secondary energy storage in the form of capacitors or rechargeable batteries will be required.

Many of the power options involve taking a technology which has been proven on large scale applications and scaling it down to dimensions suitable for the sensor node. This approach often runs into technical difficulties due to different effects which come into play at smaller scales. Some of these effects include thermal effects as a device's ratio of surface area to volume changes, viscosity issues involving fluid flow at smaller scale and problems related to increasing volume taken up by battery connectors, packaging and other essential hardware. However, through the persistent work of researchers, many technologies have overcome these obstacles and are nearing fruition.

### 2.2.1 Solar photovoltaic

Figure 2.5 displays the average daily levels of solar radiation energy falling on a horizontal surface across Australia. It shows that a majority of populated areas receive 15 - 18 $MJ/m^2$ , which is approximately 0.4 - 0.5 $Wh/cm^2$ of energy per day. In power terms, there is approximately 0.1 $W/cm^2$ at the midday peak. This offers a huge potential for wireless sensor node energy scavenging as a solar collector at 12 - 15% efficiency with the area of 25 $cm^2$ would produce over 300 mW peak of solar power. This would be more than enough to run most wireless sensor node applications.

There are a number of factors which reduce the power realisable from the high values quoted above. The first and most obvious is that the Sun is only in the sky for half the day, thus the cells will yield no power at night. Therefore some form of secondary storage, such as batteries, will be required to store excess energy during the day for use during the night. Other factors, such as cloud cover and shadowing, block the Sun's rays and drastically reduce the level of incident radiation. In extreme cases the sensor node may be deployed in a location which has no direct sunshine upon it. For example inside an office building the available power levels incident on a solar cell are three orders of magnitude less than outside, directly under the Sun. Commercial solar conversion efficiencies range from a low of approximately 8%, to state-of-art values of

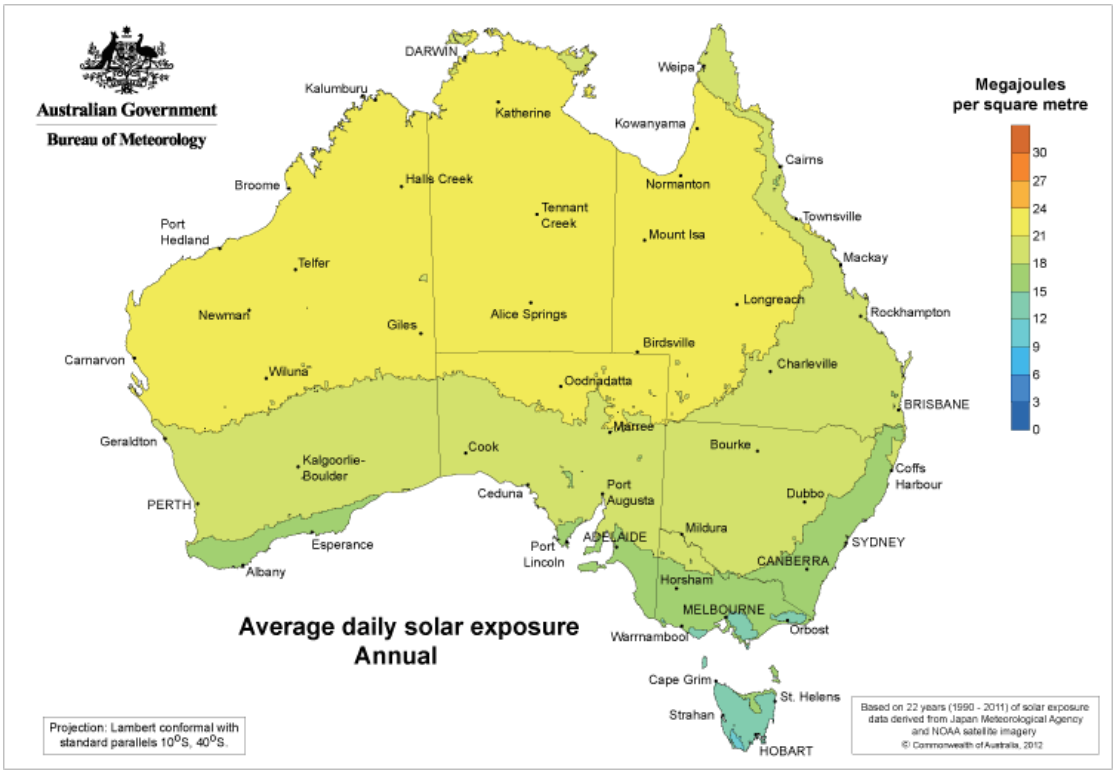


FIGURE 2.5: Average daily solar exposure [44]

20%, with some experimental technologies reaching as high as 40% [45] for multiple-junction research cells, however such cells may cost well over 100 times more than a commercially available cell.

The power incident on the collector drops with the cosine of the angle of incidence of the sun's rays i.e. 100% available when the rays are perpendicular to the surface, 87% when they are 30 degrees from perpendicular and none when the light is parallel and thus not directly striking the surface. Large scale solar collectors use solar tracking devices to ensure the cells are always facing towards the sun. An analysis performed by Thomas *et al.* [33] into the effect of solar tracking on a collector's performance used four different strategies. The first was a standard horizontal flat collector, the next had the collector at a fixed tilt on some optimum angle for the given location, the next had one axis tracking and the last had two axis tracking. Results from the average monthly energies harvested from the four collectors showed that the horizontal flat collector yielded the least energy, the fixed tilt collected 17% more energy, the one axis tracking 50% more and the two axis 54% more energy than the horizontal flat collector. This analysis shows that, as expected, the tracking yields better energy scavenging performance but at the expense of added weight, complexity and cost of the tracking control equipment, so analysis needs to be done to determine the value of adding tracking to a small scale collector used for sensor network applications.

The most basic solar converter is a solar cell, which is made of p-n type semi-conductor materials. The p-n materials are positioned such that it forms a p-n diode junction close to the top surface of the solar cell, as shown in Figure 2.6. When the solar cell is exposed to photon radiation, an electric voltage potential is developed between the p- and n-type materials. A single solar cell has an open circuit voltage of about 0.6 V but can easily be placed in series with other cells to get almost any desired voltage and in parallel with other cells to increase the current.

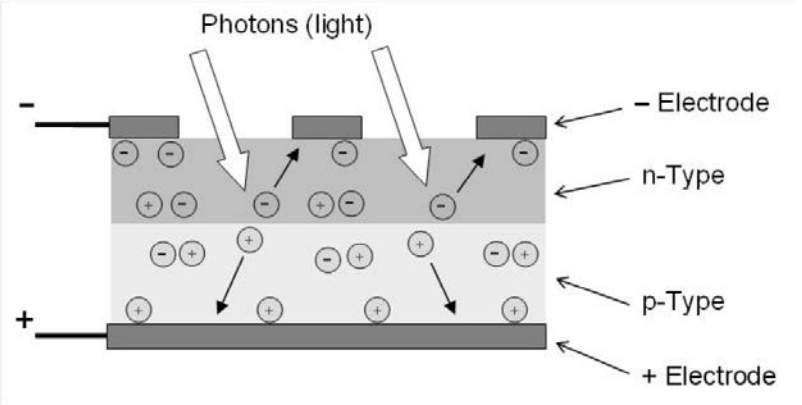


FIGURE 2.6: Photovoltaic cell [29].

"Flexible" solar cells are a new technology which may play a role in sensor node applications. This technology has demonstrated efficiencies in the 10-11% range and can be easily integrated as a multifunctional "power skin" in order to provide some mechanical load-carrying capacity, which allows for a reduction in structural mass [34].

Solar cell power is a good resource where direct sunlight is available. However, where there is a deficient solar resource, the node may harvest insufficient energy to store excess and only operate during daylight hours. Subsequently, during shorter winter days the node may fail to operate continuously even in daylight as the level of solar energy drops further [46]. Figures 2.7, 2.8 and 2.9 show variations in data reliability for a solar powered sensor node, based on full sunlight, partial sunlight and low sunlight respectively. Where direct sunlight is available 2.7 the solar current peaks between 200 and 400 mA (for the system detailed in [46]). In decreased solar resource areas 2.8 this peak occurs between 50 and 100 mA and at very low levels 2.9 the peak falls to between at 10 and 20 mA. This is insufficient to keep the battery fully charged and significant data loss occurs.

A number of groups have explored utilising solar power for sensor nodes and have reached the point of offering plug-and-play solar energy harvesting modules. One such system, Heliomote [47], enables energy harvesting, storage and power management, while delivering information on solar and battery-state through a basic one wire interface to the

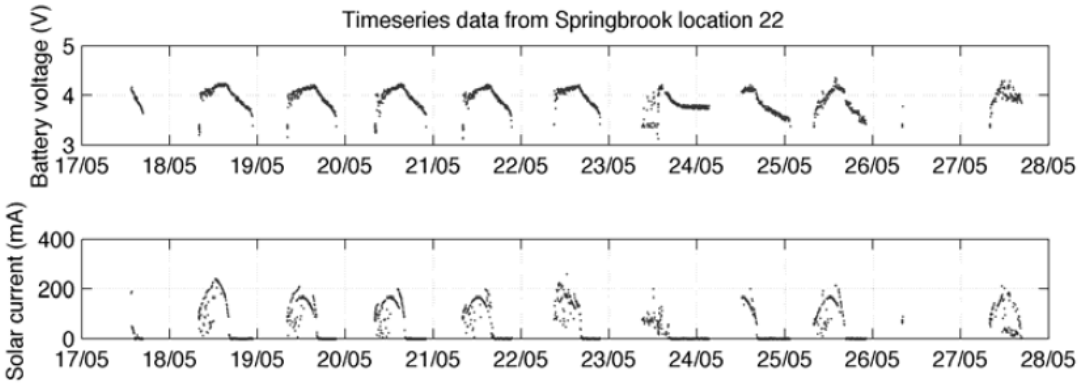


FIGURE 2.7: Solar current and battery voltage in full sunlight [46].

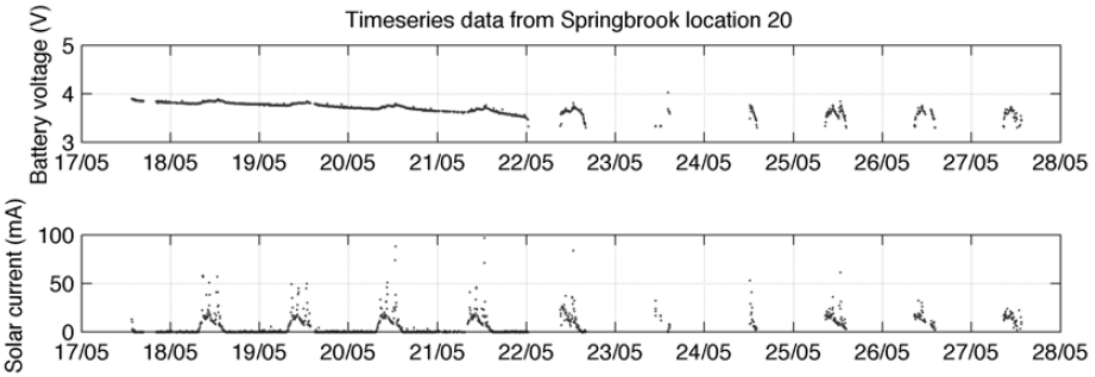


FIGURE 2.8: Solar current and battery voltage in partial sunlight [46].

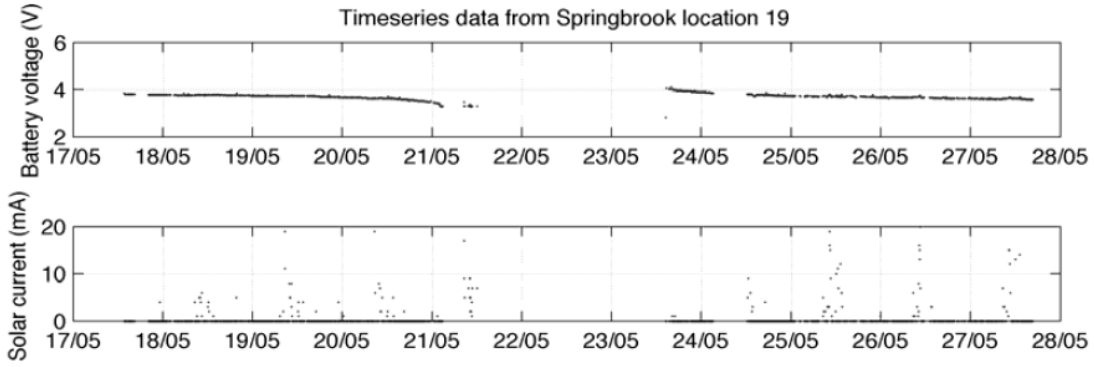


FIGURE 2.9: Solar current and battery voltage in low sunlight [46].

node. There are a number of different systems with different design objectives, a summary of which is given in a report by Enviromote [48], which is a system whose objective is to increase the available energy storing capability. These systems incorporate smart electronics to optimise the efficiency of the solar harvester and the battery charging circuit simultaneously.

### 2.2.2 Thermal energy

A temperature difference existing between two locations will result in a flow of heat energy from the hot location to the cold location in an attempt to develop thermal equilibrium. This heat flow can be exploited to harness useful energy. The process is governed by the laws of thermodynamics therefore its efficiency, the ratio of the useful work extracted out, $W$, to the input heat, $Q$, is constrained by the fundamental Carnot limit. The Carnot efficiency limit applies to all heat engines and generators and can be expressed in terms of the hot, $T_H$, and cold, $T_C$, temperature values [49];

$$\eta = \frac{W}{Q} = \frac{T_H - T_C}{T_C}. \tag{2.2}$$

This results in very low efficiency values for small to modest temperature differences. As an example, the efficiency of harnessing energy from a heat source 5K above room temperature (298K) can never exceed 1.7%. Even if that heat source was increased to the boiling point of water, 75K above room temperature, the maximum efficiency would only be 25%. The Carnot limit is the maximum theoretically achievable efficiency; real world conversion devices as yet do not achieve efficiencies as high as this.

The low efficiencies of this process necessitate a large amount of heat be transferred through a device for it to harvest useful amounts of work. Heat transfer occurs via conduction, convection and/or radiation. Roundy *et al.* [30] derives an analysis to demonstrate the power levels achievable from thermal gradients by assuming heat conduction through a silicon material. At small scales and temperature differentials, convection and radiation would be negligible compared with conduction. The rate of heat, $\dot{Q}$, conducted through a material subjected to a temperature difference, $\Delta T$, is;

$$\dot{Q} = \frac{kA\Delta T}{\Delta x}, \tag{2.3}$$

where $k$ is the thermal conductivity of the material, $A$ is its cross sectional area and $\Delta x$ its thickness.

There are many types of engines designed to extract useful work from sources of heat, examples of which range from thermally powered wrist watches to the engine in your

car to nuclear power plants. These engines can be broadly classified into two categories; mechanical and solid state. For the application of harvesting low amounts of power for wireless sensor nodes, from small ambient temperature gradients, solid state devices have the best potential. This is due to their lack of moving parts which facilitates robustness and low maintenance requirements. Life cycle testing of thermoelectric devices has shown their capability for over 100,000 hours of continuous operation [50]. They are compact and light, noiseless in operation, are highly reliable and eliminate power losses in extra conversion steps needed for mechanical engines. The following section gives an overview of the different solid state thermal energy harvesting techniques currently available.

#### 2.2.2.1 Solid state thermal energy harvesting techniques

Thermoelectricity is by far the dominate solid state conversion technique so a more in depth description will be given for it than the other techniques. It involves the direct conversion of heat into electricity and was discovered by Thomas John Seebeck in 1821 when he observed the flow of electrical current through two different types of metal joined in a loop while their ends were held at different temperatures. This phenomenon is now known as the Seebeck effect; that a thermoelectric EMF will be produced across a circuit consisting of two differing metals or semiconductors in the presence of a temperature difference. Modern thermoelectric devices use n- and p-type bismuth telluride semiconductors. Their operation can be seen in Figure 2.10. The two semiconductors are connected electrically in series and thermally in parallel, with one end exposed to a heat source and the other to a cooler sink, in a configuration known as a thermocouple. The temperature difference causes conduction of heat through the two materials. The charge carriers in the n-type material have a negative charge producing a current from the cold to hot side whereas the carriers in the p-type material have a positive charge producing a current from the hot to cold side, with the total result of a current flowing anti-clockwise around the circuit shown.

The voltage produced across a thermoelectric device is proportional to the temperature difference across it and to the difference between the Seebeck coefficients, $S_1(T)$ and $S_2(T)$, of the two materials. The n- and p-type semiconductors have a negative and positive Seebeck coefficient respectively. These Seebeck coefficients are functions of temperature, therefore the value of the voltage across a thermocouple exposed to a temperature difference, $T_H - T_C$, can be found from the following equation;

$$V = \int_{T_C}^{T_H} (S_1(T) - S_2(T))dT. \tag{2.4}$$

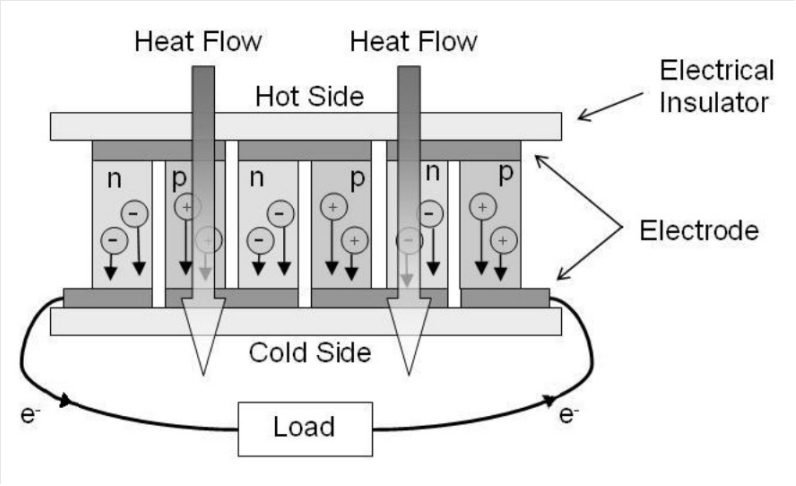


FIGURE 2.10: Thermoelectric module [29].

This voltage is generally quite small so many thermocouples are usually connected in series to form a thermopile in order to achieve useable voltages.

The efficiencies of thermoelectric generators have remained low and unchanged for the past 50 years. The reason for this is that in order to exploit a temperature gradient the thermoelectric device must be a good electrical conductor to allow the flow of charge but be a thermal insulator to maintain the temperature difference. This is contrary to most conventional materials as good electrical conductors are also good thermal conductors therefore a large portion of energy is transferred across the device as heat and not as electrical energy. The dimensionless thermoelectric figure of merit, $ZT$, is a measure of this ability and is roughly proportional to the devices efficiency [51]. $ZT$ is given by Equation 2.5, where $\sigma$ is the electrical conductivity, $\lambda$ is the thermal conductivity and $S$ is the Seebeck coefficient. It has remained around the value of 1 for more than 50 years however modern research into thermoelectric materials is improving this by a factor of over 2 [52].

$$ZT = \frac{\sigma S^2}{\lambda}\{\frac{T_H - T_C}{2}\}. \tag{2.5}$$

Improving this ZT value is crucial for the widespread implementation of thermoelectric converters because typical commercial converters currently operate at efficiencies of less than 6% [50].

Ferrari et al. [53] investigated using a thermoelectric generator to power a wireless sensor node. The paper presents the characterization of three different commercial thermoelectric modules designed for heating/cooling applications. Their analysis included the effects of electrical load resistance, thermal conductivities of the thermoelectric and heat exchanger modules and different temperature gradients. They found that thermoelectric devices could be used for their application of powering a wireless sensor node

consuming 32 mW, when the temperature difference exceeded 30 K.

Another range of solid state heat engines which have been around for decades are those based on thermionic conversion. A simplified description of a thermionic converter is a system where electrons are ejected via thermionic emission from a hot electrode over a potential barrier to a cooler electrode. The barrier that the electrons must overcome is known as the work function of the material and is essentially the heat of vaporization of the electrons from the surface. Due to this, the thermionic conversion works best with large temperatures. Although thermionic conversion has better efficiencies than thermoelectric devices, its reliance on high temperatures would make it unsuitable for most wireless sensor applications. A method similar to thermionic is thermotunnelling, which narrows the potential barrier using properties of quantum physics known as quantum tunnelling. This technology seems plausible to use for small temperature gradients for lower power applications [54].

#### 2.2.2.2 Heat sources

Figure 2.5 displayed the large potential solar energy resource available in regions such as Australia. Rather than use the conventional conversion method of photovoltaics, a growing field is exploring converting solar energy indirectly through thermal energy harvesting. For large scale operation, arrays of mirrors are used to reflect and concentrate the Sun's power to a single point where the temperature rises to hundreds of degrees Celsius. On a smaller scale, suitable for wireless sensor nodes, a black surface facing the Sun can absorb the incoming radiation heating up relative to its shaded underside. A thermoelectric or other thermal energy harvester can then be sandwiched between the two sides to generate power from the difference in temperature of the top and bottom faces.

Yu et al. [55] investigated the use of a hybrid power system for wireless sensors which incorporated solar and thermoelectric conversion. Solar cells heat up when in operation, so to harness this waste heat they attached thermoelectric harvesters underneath the cells with a heat sink underneath the thermoelectric harvesters to the atmosphere, as can be seen in Figure 2.11. In their experiments, for a solar irradiance of 744 W/m$^2$ and ambient temperature of 34 °C, they found that the rear of the solar cells reached 61 °C. In other research by Wang [56], temperatures measured at the rear of solar cells reached over 70 °C in stronger summer light. The advantages of harvesting this relatively large 30-40 K temperature difference are twofold. Firstly and most obviously the thermoelectric devices are harvesting and providing extra power to the sensor node. The second benefit is that it increases the efficiency of the solar cell above its efficiency

without the thermoelectric device there. This is due to the fact that a solar cell's efficiency drops with increasing temperature by about 0.4% per degree. By including the thermoelectric device to harness heat energy from the cell its temperature drops and efficiency increases. In their experiment Yu et al. [55] found that the rear of the cells equipped with thermoelectric harvesters were 13 K colder than those without and measured a 5.2% increase in their efficiency.

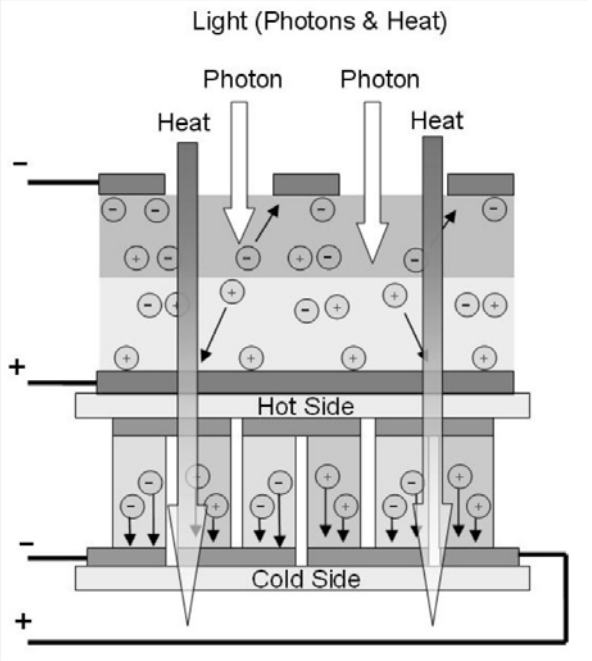


FIGURE 2.11: Hybrid Solar PV/thermoelectric harvester [29].

Another potential source of heat energy is the soil to air boundary. Air temperature will rise during the day in response to the Sun's radiation and then cool during the night. These temperature changes will be transferred to the ground although phase shifted and attenuated with depth. Therefore a temperature difference exists between the air and the ground which is generally positive during the day and negative at night. Figure 2.12 illustrates this concept where air side heat exchanger thermalises with the ambient air, likewise the heat exchanger in the soil thermalises with the ground at a desired depth. The heat pipe then transfers this heat to/from the thermoelectric device allowing the temperature difference from across tens of centimetres of soil to be applied directly across the much thinner thermoelectric device.

Stevens [57] showed that the magnitude of the available temperature difference attenuates with depth and that there is also a depth dependent phase shift between the air and soil temperatures as they fluctuate throughout the day and night. As a consequence there is an optimal depth for the ground side heat exchangers for maximum temperature difference and therefore power harvesting. Placing the heat exchangers at this optimum

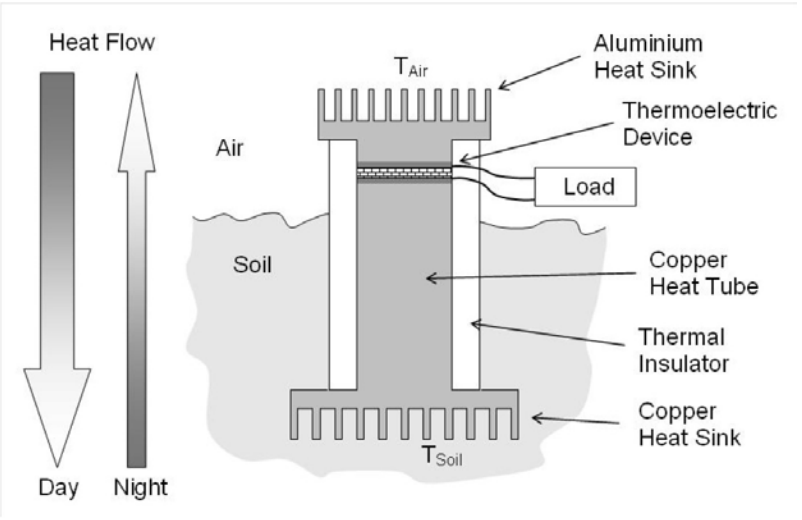


FIGURE 2.12: Simplified diagram of temperature harvesting device [29].

depth resulted in a 7% increase in the temperature difference compared to if the heat exchangers were placed at an infinite depth.

Lawrence and Snyder [58] investigated the effects of the thermal conductance of heat sinks. In his experimental set up he did not actually measure the power harvested but indirectly predicted an average value of about 50 $\mu$W. This low power value lead him to claim that the results do not appear promising and that according to their temperature data most of the temperature drop in the system was across the heat pipe, up to 4.5 K out of the 10 K total across the air and soil.

Meydbray *et al.*[59] experimented on the effects of the thermoelectric generator module surface area when exploiting the soil to ambient air temperature difference. Three different modules, with surface areas of 9, 33 and 131 $cm^2$ were investigated for 110 hours of operation, and were found to produce 23, 71 and 575 $\mu$W of average power respectively over this time, indicating a strong dependence on surface area. The data from this experiment also showed a large decrease in power output during times of cloud cover. These results mirror the sub-milliwatt power values obtained from Lawrence's experiments.

Other potential areas of thermal difference suitable for thermoelectric devices include industrial machinery, mammalian bodies and civil structures. For the application of wireless sensor nodes deployed around industrial machines, piping or vents, there is an abundant source of otherwise wasted thermal energy available. This source is very site specific but for sensors developed to monitor such equipment it is logical to power them from the rich energy source in its environment. An example of this is the automobile industries use of sensors in the engine to provide control units with information, with the sensors being powered by the waste heat from the engine. Bodensohn *et al.* [60] report

thermoelectric generators supplying autonomous sensor systems with up to 7 mW of power utilizing this heat source. Meydbray *et al.* [59] the order of 5 mW/m$^2$.

The human body self regulates its temperature at a constant 37 °C. Harnessing this against the ambient air temperature offers a source for thermal harvesting for sensor nodes applied on the human body. Many companies producing body worn products have already developed devices which utilise the small temperature difference between our body heat and the ambient temperature, generating power on the order of microwatts demonstrating that similar techniques can be applied to sensor nodes [61] [62]. An example of this is Seiko's Thermic watch which uses the small thermal gradient between the wearer's arm and the ambient air to generate microwatts of power to run the movement of its mechanical clock [63].

### 2.2.3 Mechanical

The final collection of energy harvesting technologies falls under the umbrella of mechanical energy harvesting. Mechanical energy harvesting involves converting the ambient kinetic energy in the device's environment into electric energy.

#### 2.2.3.1 Fluid flow

The flow of any fluid (gas or liquid) can be converted to electricity with a variety of techniques. At the macro scale, the use of wind turbines is becoming more common. However, at the miniaturised scale for powering sensor networks, novel approaches are required due to viscosity effects. For example, a number of systems for use in both water and air have been proposed based around the fluid causing a piezoelectric fin or 'eel' to oscillate due to vortex shedding [64].

The potential power from a moving fluid is given by;

$$P = \frac{\rho A v^3}{2}, \tag{2.6}$$

where $\rho$ is the density of the fluid, which for air is $1.2 \times 10^{-6}$ kg/cm$^3$, and for water is $10^{-3}$ kg/cm$^3$, $A$ is the cross-sectional area the fluid is flowing through, and $v$ is the velocity of the fluid.

Betz's Law, analogous to Carnot efficiency for heat engines, is a measure of the maximum efficiency of a wind turbine and is approximately 59%. Large scale wind turbines operate at maximum efficiencies of about 39%. Efficiency is dependent on wind velocity and average efficiencies are usually around 20% [30]. Wind power maps are often quoted at

altitudes of 80 meters, which is a typical hub height of a large wind turbine. Sensor networks would typically be deployed closer to the ground which introduces boundary layer effects, therefore the energy available from air flow will be much less than that available at 80 meters. Reliability may also be an issue with so many moving parts exposed to the elements. Weimer et al [65] investigated harvesting energy for sensor nodes using an aenometer, with a cup face area of 54 $cm^2$, they recorded a maximum output power of 651 $\mu W$ at high wind speeds, and at lower, more common wind speeds, power output of 5-80 $\mu W$.

The process of capturing energy from water is similar to that for air movement. The dependency of the maximum power on the density of the fluid means that for any given volume moving at a fixed speed there is approximately three orders of magnitude more power available in water. Of course any fluid moving can be harnessed. For example an oil pipeline may be a source of fluid energy. The problem of fouling is still a problem with liquid based fluids and consideration of the environment is required before deployment of any sensor network.

#### 2.2.3.2 Pressure variations

Exploiting pressure variations is an energy harvesting technique for which little research has been found on the small scale. Roundy *et al.* [30], however, gives a simplistic theoretical analysis of the potential of this resource, assuming 100% conversion efficiency. For a fixed volume $V$ of gas, the change in energy $\Delta E$ due to a change in pressure $\Delta P$ is;

$$\Delta E = V \Delta P \tag{2.7}$$

Although local pressure can change by as much as 30-40 mbar (3-4 kPa) during cyclonic weather events, a more typical daily pressure change is 3 mbar (300 Pa) [66]. With a device volume of 1 $cm^3$ this will provide 300 $mJ/cm^3$. With two pressure cycles in one 24 h period, this will provide 7 $nW/cm^3$. This assumes 100% efficiency and offers no clue as to the mechanism that could be utilised to capture this energy.

#### 2.2.3.3 Vibrations

A field which has gained a lot of attention for its potential in micro-scale power generation is vibration energy harvesting. Its attractiveness compared to that of other energy harvesting generation methods is the availability of vibrations in most environments and

the device's ability to function inside of other structures. For example, a vibration harvester can be implanted in a human body for medical monitoring or be deployed inside a concrete wall during its construction for lifetime structural monitoring.

Vibration harvesting involves the conversion of the kinetic energy inherent in mechanical vibrations into electricity. There are three known mechanisms by which this can be achieved: electromagnetic, electrostatic and piezoelectric conversion. Electromagnetic conversion utilises Faraday's law to induce an electric current in a coil of wire when it is subjected to a changing magnetic flux. By coupling either the coil or a magnet to the vibrations and having the other mounted in an inertial mechanical frame, relative motion is induced between the two. This results in a changing magnetic flux through the coil and thus power generation.

Electrostatic conversion involves designing a system whereby the external vibrations change the distance between two charged capacitive plates held at constant voltage, $V$, or constant charge, $Q$. As the distance, $d$, between the plates changes their capacitance, $C$, also changes and thus the energy, $E$, can be harvested as;

$$E = \frac{QV^2}{2} = \frac{Q^2}{2C}, \tag{2.8}$$

where;

$$C = \frac{\epsilon_0 A}{d}, \tag{2.9}$$

and $\epsilon_0$ is the dielectric constant of free space and $A$ is the area of the plates.

This method has the advantage of being easily integrated into micro-systems with silicon micromachining and being able to increase energy density with applied voltage, however it does require a separate voltage source to "kick-start" it, and due to its complexity does have some practical difficulties [67].

When a mechanical stress is applied to a piezoelectric material, a charge separation is induced across the material. At the moment the most simple and effective way developed to utilise this phenomenon in vibration harvesting is by mounting the piezoelectric material on a cantilever beam with a mass weighted at its end. This beam oscillates when subjected to vibrations, inducing mechanical stress on the piezoelectric material allowing it to harness power by damping out the oscillation. This method is more difficult to integrate into micro-systems than electrostatic conversion but does not endure the same difficulties the previous method has.

These different conversion techniques show promise for vibration harvesting and are the subject of many research efforts around the world. The harvesters developed, range from 1 - 75 $cm^3$, exploit vibrations from 50 Hz to 50 kHz, induce oscillations between

0.5 $\mu$m to over 1 mm, and produce powers that range from tens of $\mu$W to over a mW [61]. An analysis indicated that vibrational micro-generators (order of 1 $cm^3$ in volume) may have power densities of up to 4 $\mu W/cm^3$ peak from typical human motion (5 mm motion at 1 Hz) and that machine induced stimuli (2 mm motion at 2.5 kHz) may have a power density of up to 800 $\mu W/cm^3$ peak [68]. The results shown possible by this analysis surpass existing devices' actual performance by one to three orders of magnitude, suggesting that researchers have plenty of room for improvement in this field.

Most devices designed to harvest this energy utilise the oscillation of a proof mass resonantly tuned to the environment's dominant vibrational frequency. This resonance condition is vital for efficient conversion. As vibrations in different environments come in a wide range of frequencies and amplitudes which are often stochastic in nature, a robust system needs to be able to dynamically tune its parameters to match the varying peak in the input vibration's frequency spectrum.

## 2.3 Summary

The information presented in this chapter is provided as a review of the state-of-the art technology in powering wireless sensor nodes at the commencement of the present thesis. Since then, numerous more reviews on this topic have been published in the literature [69–79], highlighting the importance and the amount of activity in this area.

Many of the technologies presented are based on devices that work at the macro scale. However, when scaled down to nodal sizes, their efficiencies become prohibitively small. Of the systems that exist at the moment, the best source of energy for short term use remains the battery. Fuel cells are quickly growing in capacity and it should be expected that they will equal and surpass battery storage capability. While interesting, the political and practical aspects of betavoltaics would seem to preclude their widespread use in civilian application. Energy harvesting is essential for long term sensor deployments and there exist many ambient sources of energy which could be utilised. The energy harvesting technology chosen for a particular sensor node will depend on the which of these sources are available in the environment which it is deployed.

# Chapter 3

# Powering Marine Based Sensors

This chapter focuses on powering MBSs. First, the energy usage of typical marine sensor deployments is examined, to determine the required power output of an energy harvesting device for this application. The different energy resources in the marine environment are then identified and their potential to provide the required power assessed. Additionally, any literature relating to harvesting these energy resources for marine based sensors is reviewed. Two energy resources, wave and thermal energy, are then distinguished for further investigation in this thesis.

## 3.1 Power requirements

The amount of power required, on average, by a MBS node is examined in this section. The power requirements are seen to vary from case to case, depending on a number of factors, such as:

- The type of sensors,
- The number of sensors,
- The sampling frequency and duty cycles of the sensors, and
- The volume of data to be transmitted and the transmission distance between the MBS node and the receiver.

The values for these different factors are often restrained by the limitations of the power supply. Therefore, by improving the power supply component, the capabilities of MBSs will become less constrained, enabling more options for ocean monitoring deployments.

Different types of sensors use different amounts of power to operate. For example, James Cook Universitys Marine Geophysical Lab develops nephelometers for measuring water turbidity. These instruments are powered by 9 D-Cell batteries, each with a voltage of 1.5V and capacity of 18000mAh. Discussions with the Scientists in this lab revealed that a typical monitoring deployment will drain the battery pack in about five months, which equates to an average power consumption of 20mW. Whereas a different type of device used by this lab is a commercial instrument, the Aquadopp by Nortek, which measures the current profile in the water using acoustic Doppler technology. The datasheet for this instrument on Nortek's website [80] quotes an average power consumption of 0.2-1.5W depending on sampling frequency. Hormann et al [81] used a GPS, pressure and ultrasonic sensor for measuring water depths/heights which, in addition to the microcontroller, used a combined average power of less than 9mW.

Data transmission from the sensor's marine location back to shore requires the highest level of instantaneous power for the node. However, the duration and the frequency of occurance at which the node transmits/receives data is low, thus the average power consumption for this component is much less than the amount it uses in its active state. Depending on the location of the sensor node there are a number of different telemetry options. Radio telemetry is one of the most common data transmission methods, requiring a clear line of sight between the monitoring system and the base station. Ohmex Ltd [82] offer a long-range and short-range digital radio telemetry systems to complement their tide gauge and weather station products. The long range modem has a range of 25km, consuming 0.25W when receiving and 3W when transmitting. The short range modem's range is only 1.5km and consumes 0.12W and 1.2W when receiving and transmitting respectively. For more remote marine locations, data can be transmitted via satellite, for example the Inmarsat (International Marine Satellite) D+ data service provides near global coverage via four geostationary satellites. The Track800D device utilises an Inmarsat D+ global satellite transceiver to report the location of boats and ships, consuming 0.8W when receiving and 10.2W when transmitting [83]. Alippi et al [84] use a MaxStream 2.4-GHz Xstream Radio Modem long range transeiver which uses 0.75W in transmission. The wireless subsystem in Bromage et al [24] uses a MaxStream 9XTEND 1-Watt transceiver. Cella et al [6] required 50mW of transmission power to relay their data 600m on the 2.4GHz band with a vertical high gain dipole antenna.

Little et al [85] developed a wireless video sensor network for autonomous coastal sensing with panoramic cameras capable of a 360 degree field of view. Their nodes consume 2.5W for the camera when sourcing, 500mW when streaming the data and 5mW when asleep. The report on the SEMAT's Mk2 buoy's show a 5.5W peak power and 1W suspended power usage, and for the Mk3 buoy, 6.3W peak and 0.1W suspended power usage values

[8]. The average power for these systems would depend on the duty cycles of their different operating states. For example, Thosteson and Sepri's [25] marine monitoring system, integrates sensors for measurement of water conductivity, water level, temperature, flow magnitude, flow direction, turbidity, wave height, wave period, package location, package orientation, and speed of sound. When programmed to make measurements from each available sensor once every five minutes and to make cellular transmissions hourly, their system requires an average continuous supply of 0.25W. Hwangbo et al [86] report a total daily power requirement, for their system with an underwater accoustic modem, of 19.4 Wh, which is an average consumption of 0.8W. Albaladejo et al's [26] system includes temperature and pressure sensors for the atmosphere and water, a light emitting beacon and data transmission to a base station 700m away, using an average power of 36mW.

An interesting point to note regarding the power usage of the RF data transmission is that, Rajasegarar et al [5] reported a problem with maintaining wireless connectivity between nodes and shorter life time of the network. The main reason for loss of connectivity between nodes was the movement of antennas caused by ocean wave dynamics. The pitching of the buoy causes a tilting of the antenna which results in reduced range of communication and polarisation issues. Once the communication is lost with the other nodes, the node continuously searches to establish communication and by doing so it is exhausting its battery power. This problem was also reported by Cella et al [6], who quoted that a robust energy harvesting is essential if the nodes experience difficult communications, because the number of retrials may drain a significant amount of energy from the battery. Cella et al [6] state that, a too high inclination of the antenna with respect to the vertical direction would have hindered the radio communicaton by increasing reflection and scattering cause by the water surface. Albaladejo et al [26] also reported on this problem of the wave induced motions negatively affecting the communications.

In conclusion, the power requirement by the marine based sensor node will depend on the application; what type of sensors, how many sensors, how often are they making measurements and transmitting the results, and how much power the transmission requires. In general, an average power supply on the order of 1W would be more than sufficient for most marine based sensor applications reviewed.

## 3.2 Energy harvesting for marine based sensors

The review of energy harvesting for sensor nodes in Chapter 2, shows that energy harvesting does not have a one size fits all solution and is very much dependent on the

energy resources available in environment where the sensor is located. For the case of energy harvesting in the marine environment the following energy resources are identified and assessed in this section:

- Solar
- Wind
- Currents
- Microbial Fuel Cells
- Wave
- Thermal Energy

### 3.2.1 Solar

Solar PV has by far been the dominate means of energy harvesting techniques trialled for marine based sensor applications, most likely due to the maturity of the PV technology and its commercial availability. The good potential for solar PV was outlined in Section 2.2.1. This section reviews the published reports of solar energy harvesting for marine sensor deployments and identifies a number of disadvantages for its use in this application.

Alippi et al [84] performed a four day sea trial of a sensor network consisting of ten nodes, one of which was a gateway node. Energy was provided by two 0.5W solar cells for the regular nodes and and eight 0.5W cells for the gateway node. One dipole omnidirectional antenna is present on nodes for communicating to the gateway, which, differently mounts two omnidirectional antennas: one to communicate with the local cluster network and the other for establishing a radio link to the ground control station. A picture of a regular node is shown in Figure 3.1-(b). Alippi et al employed batteries, with an energy capacity larger than the solar-cell daily energy production and daily system energy consumption, in order to store energy and permit the system to supply power even in case of bad weather.

Albaladejo et al [26] performed a two month sea trial for a sensor buoy system using two 2.5W solar panels (shown in Figure 3.1-(c)). They found that the solar energy harvesting system performed very well in sunny conditions, full charging the battery, but that the battery became very drained at night due to the absence of sunlight and the beacon light consumption. An earlier verification trial by Albaladejo et al [87], where the same

system was deployed in a harbour for one month, reported that the harvesting system didn't receive sufficient sunlight to recharge the batteries on some cloudy and rainy days.

Trevathan et al [8] used a 10W solar panel, with a 12 V - 7 Amp hour lead acid battery, in each of their Mk2 buoys, and three 5W solar panels in their Mk3 bouys (shown in Figure 3.1-(a)). They noted that on overcast days, the solar panel was unable to sufficiently charge the battery.

A related investigation by Hormann et al [81], examined using a wireless sensor node for river monitoring, whereby they utilised a solar cell charging two ultracapacitors for the power supply. Their results showed continuous operation of the system for five days. They reported rainy and foggy weather conditions for the first two days, where the capacitor voltage dropped from the maximum value of 5V, down to as low as 2.8V. However when the weather cleared in the final three days the voltages replenished back to 5V.

Solar power has also been targeted as the energy harvesting resource by other researchers [85, 86], but its performance from an actual ocean deployment not yet reported.

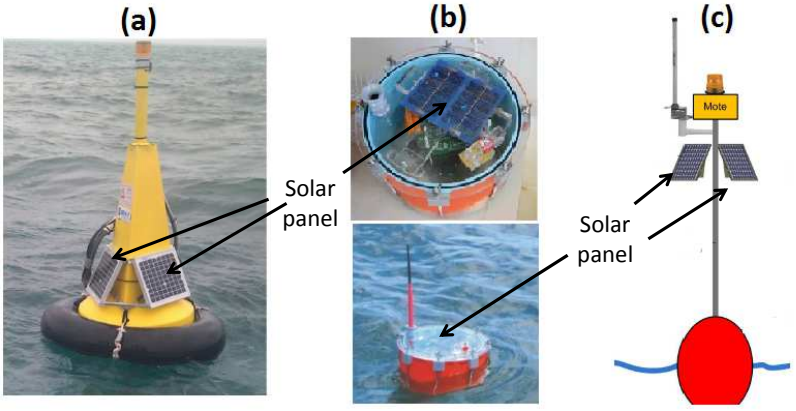


FIGURE 3.1: The set-up of three different deployments using solar panels (a) [8] and (b) [84] and (c) [26]

A disadvantage of solar PV is the limited number of hours that the direct solar radiation is available, due to the night time hours and to possible cloud coverage during the day. This can be prohibitively restrictive for sensor nodes deployed at high latitudes, where the amount of daylight is greatly reduced in winter months. The amount of direct solar radiation on the panel is also reduced if the panel is not directly aligned to face the Sun, which results in the amount of available power being diminished. Torres et al [88] state that the panels require proper orientation to generate enough power for the batteries and therefore are investigating utilising a wind powered auto-positioning system to align the solar panels for optimal energy harvesting. A more passive approach is taken by Albaladejo et al [26], who used two solar panels facing in opposite directions

and inclinated at 45 degrees, shown in Figure 3.1-(c), to increase the chance of incident solar radiation normal to the panel's face. Likewise, Trevathan et al [8] utilised three solar panels facing in different radial directions, as shown in Figure 3.1-(a), so that at least one of the panels may be facing the Sun as it and the buoy both move throughout the day.

Another disadvantage of solar PV is the reduction in system efficiency when the panel surface becomes dusty or covered with water and/or marine salt [84]. For example Ortega et al [89] noted the need for maintenance due to fouling by seabirds. To help reduce this problem, Alippi et al [84] used a maximum power point tracking system to optimally harvests solar energy by adapting the working point of the solar cell to maximise energy transfer from the cells to the batteries when the cell is not directly exposed to the optimal radiation or the solar radiation is low, as it happens when the panel surface is dirty or clouds change the intensity of the solar radiation.

Another drawback for solar is the requirement of substantial fixed or floating structures above the water surface, which increases the risk of vandalism or theft, and may affect the pitching motion of the buoy, which has be reported to negatively affect the data transmission from the antennas.

### 3.2.2 Wind

Figure 3.2 maps the worldwide average wind power levels [90], showing a good potential, on the order of 100's of $W/m^2$ at most locations. This resource has been the target of large scale offshore wind farms for over a decade [91], with offshore wind currently leading the field in commercial offshore renewable energy. However, for the present purpose of energy harvesting for marine based sensors harvesting, wind energy may not be so feasible. Firstly, the average wind power values shown in Figure 3.2 are measured at 80m above the sea level, whereas values close to the surface are much less than this due to the logarithmic boundary layer. Calculating the wind speed 1m above the sea level, using the logarithmic wind profile[92], reveals a reduction by over a third compared to the wind speed at 80m , which relates to a 73% reduction in available power due to the cubic relationship between wind speed and power.

The review in Section 2.2.3.1 revealed that maximum efficiencies for large scale wind turbines are around 39%, with average efficiencies around 20%. These efficiencies are achieved using large stable structures, it is likely that a the dynamic motion of a buoy used for marine based sensors will further reduce the efficiencies of a small scale wind turbine positioned on that buoy. Indeed, maintaining pitch/roll stability for the small floating structure would also be a concern, with a turbine located as high as possible

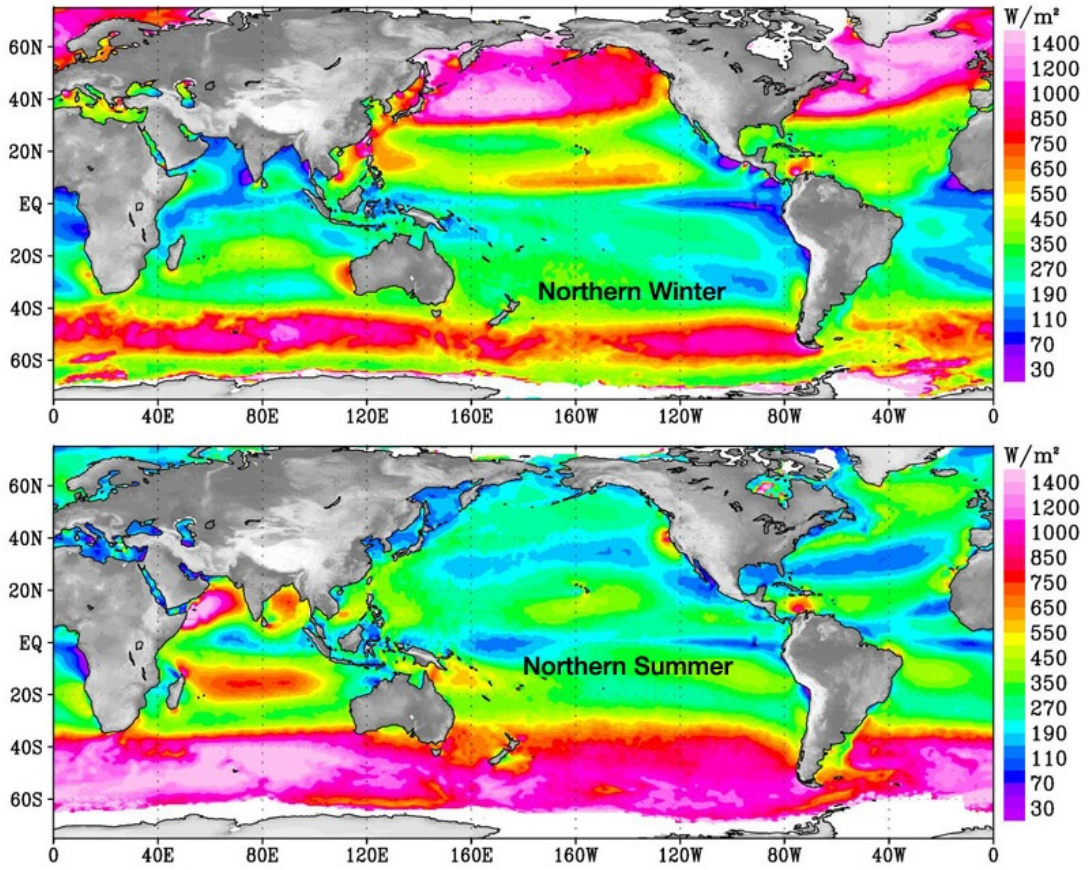


FIGURE 3.2: Worldwide average wind power levels [90].

above the water surface capturing the energy of the wind applying unwanted torques to the buoy.

Concerns over reliability may also be an issue with so many moving parts exposed to the elements. Additionally, the risk of theft or vandalism is increased for the turbine conspicuously located above the water surface.

### 3.2.3 Currents

Different types of currents are present in the ocean, driven by the tides, thermal gradients, salinity gradients, the rotation of the Earth or by the wind. Tidal currents have been the target of large scale tidal energy extraction, due to its extremely high level of predictability. However, in general the energy in marine currents is diffuse and tidal energy extraction limited to locations where it is concentrated via flows through relative constrictions giving rise to strong currents [93]. Figure 3.3 shows the spatial distribution of mean tidal power on the Australian continental shelf, where a number of tidal energy 'hot spots' can be seen.

Trevathan et al [8] proposed using tidal currents as a power source for marine based sensors and compared the use of different types of turbines, though concluded that devices may not be cost effective and are subject to risk in deployment due to bio-fouling and entanglement from drifting alga and sea grass wrack. Maintenance due to marine growth is seen as a problem for tidal turbines [93].

As an alternative to conventional turbine type technologies used at the large scale, Taylor et al [64] developed the energy harvesting 'eel' to convert the mechanical flow energy in rivers and oceans into electrical power via piezoelectric polymers. The eel generator utilises the regular trial of travelling vortices behind a bluff body to strain the piezoelectric elements, with the resulting undulating motion resembling that of a natural eel swimming. The eel has the capacity to generate milli-watts to many watts, depending on the system size and the flow velocity of the local environment. Taylor et al [64] identified future work on the eel to focus on developing and deploying a small, lightweight unit to power remote sensor arrays, with an output power rating of one watt.

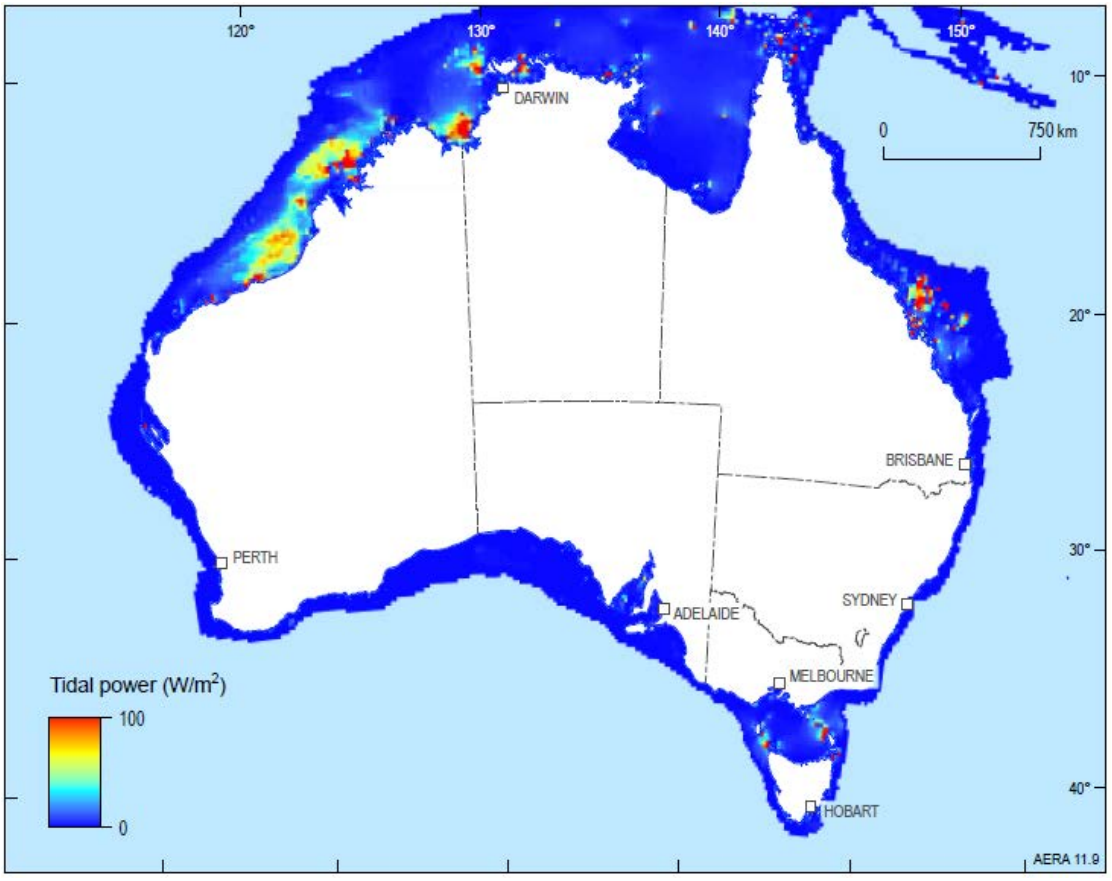


FIGURE 3.3: Spatial distribution of mean tidal power on the Australian continental shelf [102]

### 3.2.4 Microbial Fuel Cells

Microbial fuel cells (MFCs) exploit bacterial metabolic activities to generate electrical energy. The marine environment is rich in microorganisms and nutrients and is therefore ideal for energy harvesting using MFCs. The MFC consists of an anode shallowly embedded in the marine sediment and a cathode in the above seawater, which are connected to each other through an external load, as depicted in Fig 3.4.

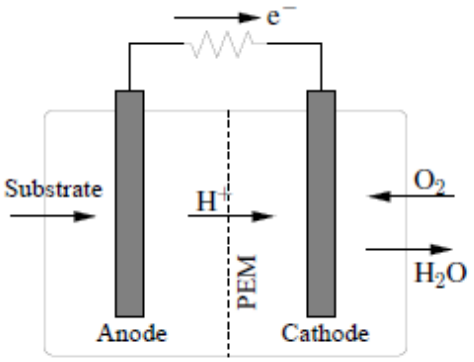


FIGURE 3.4: Schematic of a microbial fuel cell [94].

Aiming at an environmentally friendly and cost effcective power source for marine instruments, Reimers et al [95] developed a benthic microbial fuel cells that convert chemical energy stored in the benthic sediment into electrical current. The objective was to generate a steady energy supply that could be used to power remote oceanographic instruments such as water quality sensors. Scott et al [96] investigated sediment MFC's performance using different cathode and anode materials. The best performance was observed with a peak power density of $60mW/m^3$. Dai et al 2011 [94] presented the design and modeling of a microbial fuel cell as an alternative technique for energy harvesting from the underwater environment. Experimental results showed that the proposed device achieves a maximum power density of $153mW/m^3$. Donovan et al [97] investigated overcoming the limitation of current sediment microbial fuel cells (SMFCs) which to date have only demonstrated power outputs of several to tens of mW continuous power by developing a power managements system that enables a SMFC to operate a remote sensor consuming 2.5W of power by storing energy in capacitors and using the stored energy in short burts. Other studies [98] [99] also demonstrated the feasibility of using sediment MFCs to harvest energy from the underwater environment.

### 3.2.5 Waves

Ocean waves are an attractive renewable energy source. The magnitude and consistency of the power flux provided by waves compares favourably against that of wind and solar.

Wave energy is an indirect form of solar energy with waves being generated from the wind and the wind from the Sun. The energy density increases roughly by an order of magnitude across both conversion steps, from solar to wind and wind to wave [100]. This large energy density is a very significant feature of ocean waves. Figure 3.5 shows estimates of worldwide average wave power levels, from which it can be seen that the resource is generally in excess of $10^4$ Watts per metre of wavefront in the open ocean. For shallow water, frictional effects dissipates the energy from the wave to the sea floor resulting in decreased power levels. Figure 3.6 shows the spatial distribution of the average wave power levels on the Australian Continental Shelf, revealing power levels on the order of kilowatts per meter.

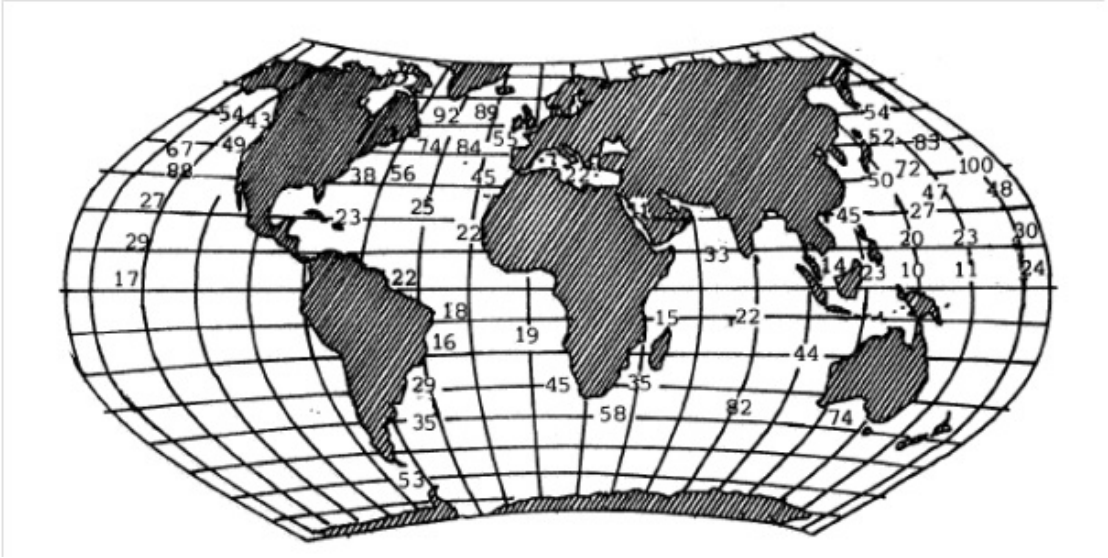


FIGURE 3.5: Estimates of worldwide average wave power levels in kW/m [101].

Not only do waves offer a very high energy flux, they also provide it consistently, with the energy flux of ocean waves attenuating slower than the winds dynamic energy flux. Waves are generated by the wind across the water surface, and then travel with little energy loss, resulting in the wind's variable energy flux being integrated over large areas to produce a wave field with a more constant and reliable energy flux. This is also true when compared to solar energy, which fluctuates due to cloud coverage and is unavailable at night, whereas wave power is consistently available 24 hours a day. In their review of renewable energy from the ocean, Pelc and Fujita [103] state that 'Not only is the wave energy resource vast, but it is more dependable than most renewable energy resources - wave power at a given site is available up to 90 percent of the time, while solar and wind availability tend to be available just 20-30 percent of the time.'

Due to the large energy flux of ocean waves and their relative consistency, wave energy has been identified as the core energy resource to be investigated in this thesis for the purpose of powering MBSs. Therefore, an extended review of the wave resource and

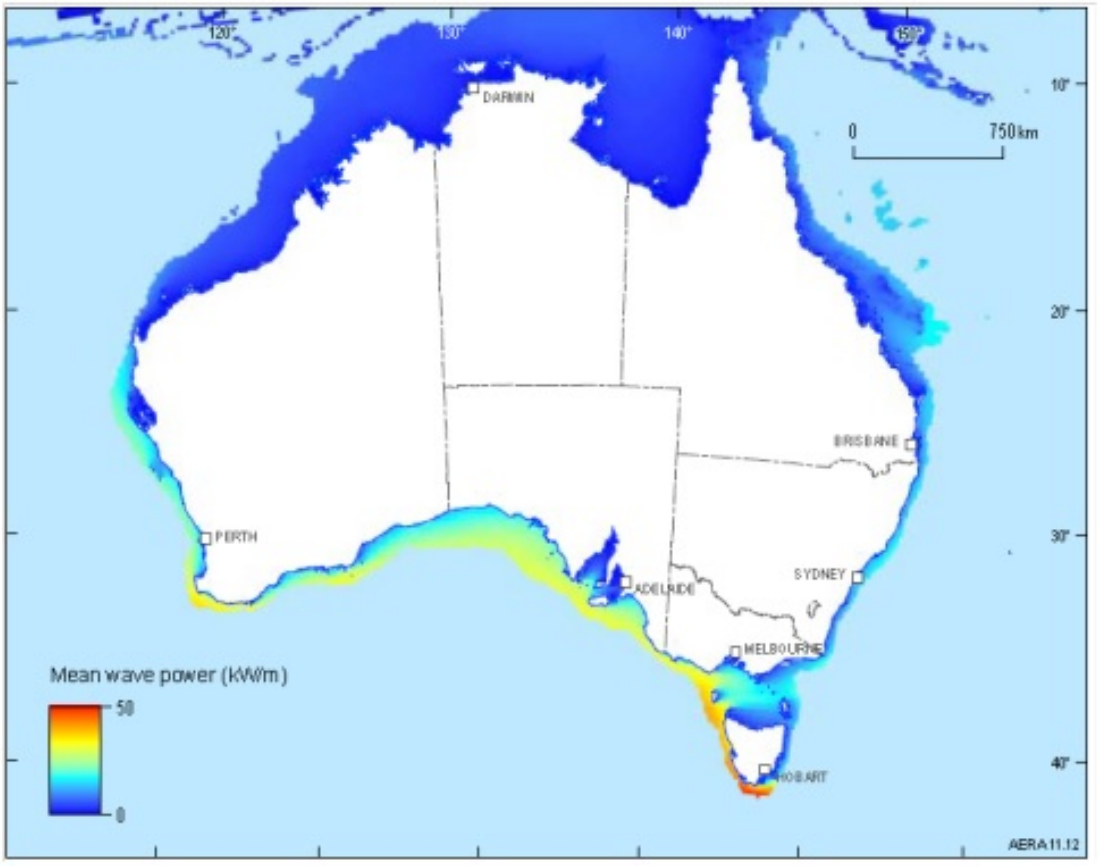


FIGURE 3.6: Spatial distribution of mean wave power on the Australian continental shelf [102]

conversion techniques is given in Chapter 4. Focussing on wave energy to provide power for the MBS, also allows the thesis to simultaneously investigate reducing the increased power drain on the MBS's data transmission due to wave induced dynamics, as identified in Section 3.1.

### 3.2.6 Thermal Energy Harvesting

Thermal energy harvesting across the air-water interface is a newly proposed potential power resource previously unexplored for energy harvesting for MBSs. The ocean will be either a few degrees warmer or colder than the air directly above it; dependant on factors such as the time of day, time of year and global latitude. A thermal energy harvesting device can promote the flow of heat energy across this thermal gradient, a portion of which is converted into usable power for the sensor node.

The possibility of exploiting the thermal gradient across the air/water interface for powering MBSs, was identified by the present author in the progress of compiling the general literature review for energy harvesting for WSNs, as reported in Chapter 2. The

concept is inspired by the work of Stephens [57, 104, 105] for terrestrial sensor nodes, whom investigated utilising the thermal difference between the soil and air to power WSNs (Section 2.2.2.2). By realising that the same thermal phenomena exists in the marine environment and that the potential of this resource had never been examined or quantified, the present author has identified this resource for further investigation in this thesis. Details for this novel energy harvesting technique are reported in Chapter 9, and also in the following publications [106], [107], [108]. This method was also later investigated by Jones et al [109] for powering sea ice instrumentation, during the polar winter when other energy sources are either unavailable or unreliable.

### 3.2.7 Comparison

In this subsection, a basic quantitative comparison is made between the identified energy resources. The energy resources are ranked by their perceived potential for utilisation in energy harvesting for MBSs. Table 3.1 displays the different energy resources, the energy density of the resource, the temporal and spatial availability of the resource, and the ranking given to the resource.

Waves are seen as the most promising energy resource. The energy density provided by waves is an order of magnitude greater than other resources, it is available consistently 24 hours a day and a wave energy device can be located anywhere from the ocean surface to sea bed. Solar is ranked here as the second most promising energy resource. Solar provides a good energy flux, particularly in tropical to mid-latitude locations, however the energy resource is unavailable and nightime and is reduced by cloud coverage. Additionally, the available incoming energy is reduced if the face of the PV panel is not aligned towards in the incident sunlight or if the sunlight is blocked by dirty PV panels.

The requirement of having PV panels located above the ocean surface is a disadvantage for solar, because it requires a substantial fixed structure above the water surface, which increases the MBS size and possibly its pitching motion. The same is true for wind energy, which is ranked next at number 3. Although, wind energy has a good energy density, it is highly variable and reduces with distance towards the ocean surface. Therefore, a wind energy harvester will also require a substantial fixed structure above the water surface to mount the wind turbine with as much elevation from the ocean surface as possible.

Currents are ranked at number 4, due to the lower energy density and the high spatial variability of the resource. MFC's are ranked at number 5 due to the very low energy density and because the resource is only available at on the sea floor. The thermal energy

harvesting was given a score of 'unknown' because there is no quantitative information available for this resource.

| Rank | Resource | Energy density | Availability |
|---|---|---|---|
| 1 | Wave | 500 - 50000 W/m$^2$ | 24 hours per day |
| 2 | Solar | 50-500 W/m$^2$ | Day time only. Reductions due to cloud coverage and misalignment of PV panel with incoming sunlight. |
| 3 | Wind | 100-1000 W/m$^2$ | 24 hours per day. Highly variable. Reductions due to logarithmic friction layer towards the ocean surface. |
| 4 | Currents | 0.1-10 W/m$^2$ | Site dependent. |
| 5 | MFC | 0.1 W/m$^3$ | On the sea floor |
| ? | Thermal | Unknown | Possibly more consistent that solar and wind. |

TABLE 3.1: Comparison of the time domain model's computation time and output power results for various simulation lengths, against the frequency domain model's results.

## 3.3 Summary

The power requirements for marine based sensor networks were reviewed and an average power of 1W was identified as the targeted output for an energy harvesting device. The data transmission was seen to have the largest energy usage, and the pitching motion of the buoy, due to wave induced dynamics, was reported to cause issues for the data transmission, resulting in an increased drain on the power supply.

The energy resources in the marine environment were reviewed and wave energy was identified as providing the largest and most reliable resource. Harvesting wave energy to power the sensor node has therefore been identified for further examination in this thesis. Additionally, by investigating a buoy to absorb wave energy, the buoy's pitch motion due to wave induced loads can also be investigated and ideally minimised, to provide a stable platform for data transmission by the antenna.

Thermal energy harvesting across the air / water interface was identified as a novel resource previously unexplored for powering small scale electrical equipment in the marine environment. A similar resource, the thermal gradient across the air / soil interface, was shown to have reasonable potential for terrestrial based sensor nodes [57, 104, 105], therefore the thesis will follow this line of research applied to the marine environment to explore the potential of this resource for the present application.

Alippi et al [84] were seen to employ batteries, with an energy capacity larger than the solar-cell daily energy production and daily system energy consumption, in order to

store energy and permit the system to supply power even in case of bad weather. They state that, the batteries will therefore undergo partial charging and discharging every day, which can cause a severe reduction of battery nominal energy capacity and, as a consequence, severe limitations to performance (known as the memory effect of chemical batteries). They propose solving this problem by employing two identical battery packs and switching between them, so that while one battery pack powers the system the other is under charge. Once the former is discharged, an embedded circuit allows the battery packs to be inverted. In this way, one battery pack is always in charge while the other is always being discharged and therefore separately performing full discharge and full charge cycles on each battery. Following this idea, of employing two battery packs with an energy capacity larger than the daily system consumption, shall be employed in the present work, and therefore the energy harvesting system does not need to constantly provide 1W of power but rather harvest an average of 1W per day (86400 Joules of energy). Assuming the usage of lithium ion batteries, which were shown in Section 2.1.1 to offer the best performance, would require a minimum total battery weight of about 0.2kg to provide the required 48Wh capacity.

# Chapter 4

# Wave Energy Conversion

This chapter presents a brief review of the ocean wave resource and the field of wave energy conversion. Ideas are identified from this field, to aide in the conception of a micro-scale wave energy converter (WEC) for powering MBSs. The chapter concludes with a description of the proposed WEC design, to be subsequently analysed and developed in later chapters.

## 4.1 Ocean waves

Ocean waves propagate energy across the surface of the ocean through the movement of water particles. The energy is in the form of the kinetic energy of the moving water particles and their potential energy as the water level rises and falls against gravity. The water particles themselves do not propagate with the travelling wave but follow orbital paths, as depicted in Figure 4.1. The motion of the water particles is largest at the surface and decreases exponentially with depth, approaching zero at a depth equal to half a wave length.

### 4.1.1 Regular waves

Figure 4.1 illustrates the simplest type of wave, a regular plane wave, which has a sinusoidal shape in space and time:

$$\eta(x,t) = a\sin(\omega t + kx + \phi), \tag{4.1}$$

where $\eta(x,t)$ is the free surface elevation (FSE), $a$ is the wave amplitude, $\omega$ is the wave frequency, $k$ is the wave number and $\phi$ is the phase angle. The wave amplitude is half

the wave height, $H$, which is the vertical distance between a trough and crest. The wavelength, $\lambda$, is the horizontal distance between two successive crests (or troughs) and it is related to the wave number via, $k = \frac{2\pi}{\lambda}$. The wave period, $T$, is the time for one wave to pass a fixed point and the wave frequency, $f$, is the inverse of the wave period, equalling the number of waves passing a fixed point per second, where $f = \frac{\omega}{2\pi}$.

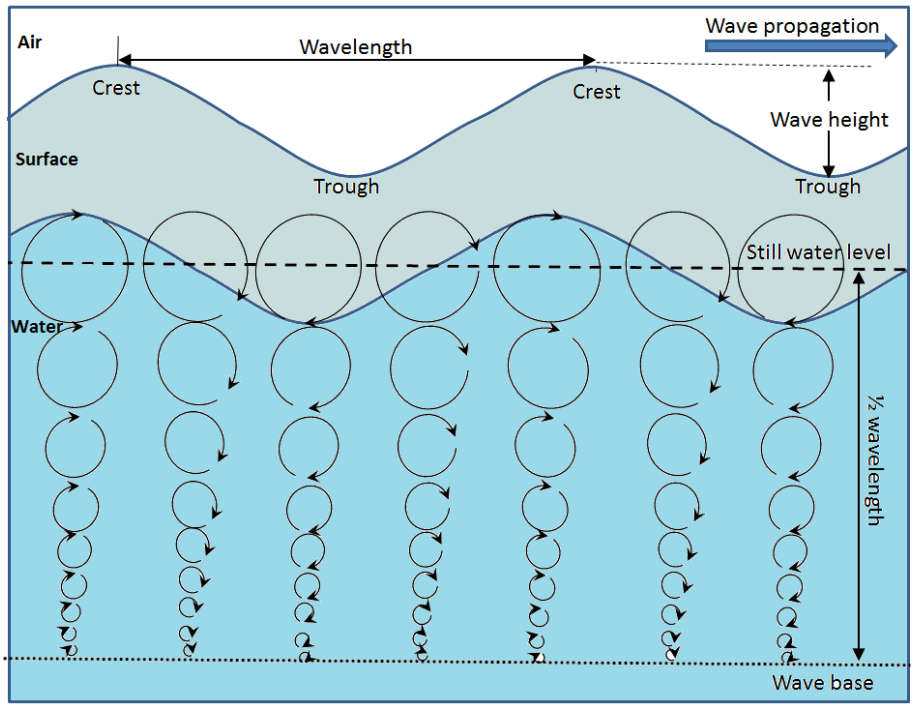


FIGURE 4.1: The orbital motion of fluid particles in a regular wave.

Other important parameters relating to ocean waves are the wave steepness, the wave velocity and the dispersion relation. The wave steepness is the ratio of the wave height to the wavelength, and is physically limited by wave breaking which occurs at a wave steepness of 1/7. The phase velocity, $c_p$, of a wave is the speed at which the crest moves in the direction of travel and therefore equals the wavelength divided by the period:

$$c_p = \frac{\lambda}{T} = \frac{\omega}{k}. \tag{4.2}$$

The wavelength and frequency of ocean waves are related by the dispersion relation:

$$\omega^2 = gk \tanh kh. \tag{4.3}$$

where $g$ is the gravitational constant and $h$ is the water depth. For the case of deep water, the dispersion relation simplifies to $\omega^2 = gk$. Combining the dispersion relation with the phase velocity, Equation 4.2, reveals that the phase velocity is different for different frequency waves or different wavelengths, indicating that ocean waves are dispersive.

The dispersiveness of ocean waves means that longer low frequency waves travel faster than shorter higher frequency waves.

Of course the parameter of most interest to the present work, is the power of the wave. The power per metre of wavefront for a deep water wave ($h > \frac{1}{2}\lambda$) is given by the following relationship [110]:

$$P = \frac{\rho g^2}{32\pi} T H^2. \tag{4.4}$$

### 4.1.2 Irregular waves

Unlike regular sinusoidal waves, real sea waves are irregular, both spatially and temporally. An example of the ocean's FSE measured at a spatial point, $\eta(t)$, is shown in Figure 4.2-(a) [111]. Assuming linear theory and use of the superposition principle, this can be approximated as the sum of many independent regular waves of varying amplitude, $a_n$, frequency, $\omega_n$, and phase, $\phi_n$:

$$\eta(t) = \sum_n a_n \sin(\omega_n t + \phi_n). \tag{4.5}$$

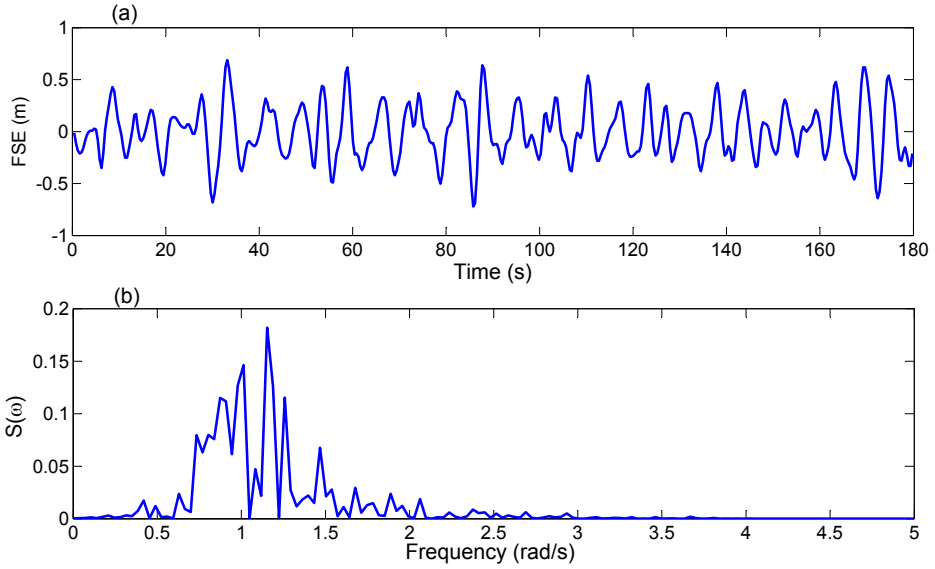


FIGURE 4.2: (a) The free surface elevation (FSE) measured at a spatial point, (b) The power spectrum of the signal in (a).

The average energy per square meter of ocean surface, $E$, is related to the variance of the FSE about its means position, $\overline{\eta^2(t)}$, [112]:

$$E = \rho g \overline{\eta^2(t)}. \tag{4.6}$$

From Equation 4.5, the FSE variance can be represented as:

$$\overline{\eta^2(t)} = \sum_n \frac{1}{2} a_n^2, \tag{4.7}$$

representing a transformation from time to frequency domains and illustrating that the total energy of the irregular wave train is the sum of the energies associated with individual sinusoidal wave components at each frequency. This leads to the concept of the wave spectrum, $S(\omega)$, which quantitatively describes how the different wave frequencies contribute to the wave energy:

$$S(\omega)\Delta\omega = \sum_{\Delta\omega} \frac{1}{2} a_n^2, \tag{4.8}$$

where the sum is taken over the wave components whose frequencies lie between $\omega - \Delta\omega/2$ and $\omega + \Delta\omega/2$. In the limit as $\Delta\omega \to 0$, the total variance can be expressed as:

$$\overline{\eta^2(t)} = \int_0^\infty S(\omega) d\omega. \tag{4.9}$$

Thus from Equation 4.6, the average wave energy per unit surface can be expressed in the frequency domain as:

$$E = \rho g \int_0^\infty S(\omega) d\omega. \tag{4.10}$$

The power transported per metre of crest length length can then be given by:

$$P = \rho g \int_0^\infty c_g(\omega) S(\omega) d\omega, \tag{4.11}$$

where $c_g$ is the wave group velocity,

$$c_g = \frac{g}{2\omega} \left( 1 + \frac{2kh}{\sinh kh} \right) \tanh kh, \tag{4.12}$$

For the case of deep water, the expression for the group velocity simplifies to $c_g = \frac{g}{2\omega}$.

Figure 4.2-(b), plots the power spectrum, $S(\omega)$, of the FSE signal displayed in Figure 4.2-(a). It reveals that the sea surface measured in Figure 4.2-(a) comprises mostly of waves with frequencies between 0.5 and 2 rad/s, with a peak frequency of about 1.2 rad/s. The spikiness of this spectrum is due to the short length of data used to perform the transform (i.e. 3 minutes of data sampled at 2.5Hz), whereas in general it is standard practice to take 30 minutes of data to calculate a spectrum, which classifies the sea state for a given location at a particular time. The sea state is then normally expressed in terms of the peak period/frequency of the wave spectrum and the significant wave height, $H_s$. The significant wave height is the predominant or characteristic height of an irregular wave series and was historically defined as the mean wave height of the highest

third of the waves. In modern practice, the significant wave height is defined in terms of the wave spectrum, as:

$$H_s = 4\sqrt{\int_0^\infty S(\omega)d\omega}. \tag{4.13}$$

### 4.1.3 Wave creation

The process of wave creation from the wind is illustrated in Figure 4.3. Starting with a completely calm sea, when the wind blows over this flat surface it generates turbulence and the pattern of eddies produce pressure difference on the surface, resulting in the creation of micro-ripples. The micro-ripples make the surface rough and give the wind better grip to push the water and create bigger waves. As the wind continues to blow and transfer energy to the waves, the waves will grow from micro-ripples, to ripples, to chop, to wind waves, to a full developed sea. A fully developed sea has the maximum wave size theoretically possible for a wind of a specific strength, duration, and fetch, where the fetch is the distance over which the wind blows.

The term wind sea is used for waves that are actively growing due to forcing from local wind. When the wind dies or the waves propagate out of the wind's zone of influence, the waves will continue to travel while transferring energy to lower frequencies, forming swell. Swell waves can travel thousands of kilometers, with little loss of energy, until the water depth decreases and the wave begins to interact with the sea floor. Swells in deep water will, typically, have wavelengths of 100 - 500m whilst wind seas may range from a few metres to 500m depending on the wind speed [100]. The wave field at a given location can contain a mix of local wind sea and swell which has originated from a distant storm.

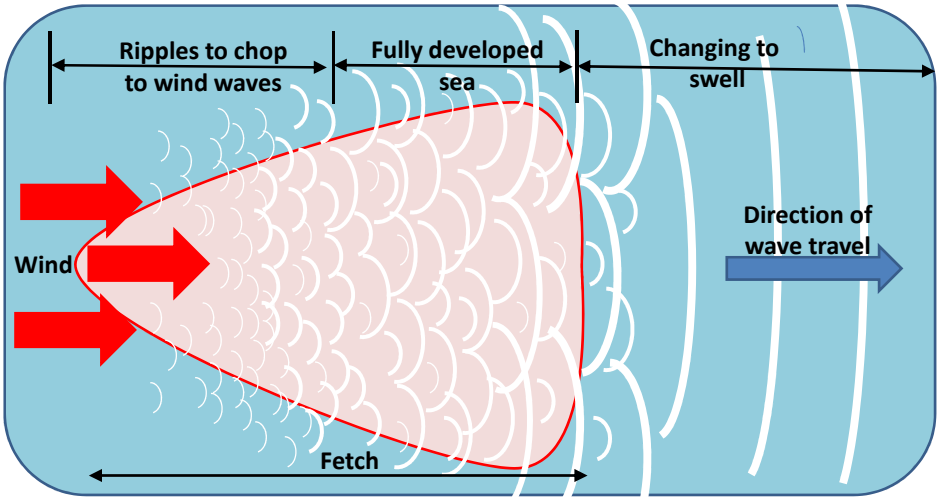


FIGURE 4.3: The creation of waves from the wind.

### 4.1.4 Standard ocean wave spectra

It turns out that the shape of ocean wave spectra can be fairly well described by standard formulae which take as input, parameters such as the wind speed and fetch length. With some theoretical guidance, these formulae were derived empirically from many datasets of measured wave spectra, and have been found to generalise well to most wave conditions, being used successfully in ocean engineering for many decades. The two most widely used spectra are the Pierson-Moskowitz (PM) spectrum and the JONSWAP spectrum [112].

#### 4.1.4.1 The Pierson-Moskowitz spectrum

The PM spectrum [113] assumes a fully developed sea where the winds have been blowing steadily over a long duration and a large fetch. For a given wind speed, $U_{19.5}$, at an altitude 19.5m above the sea surface (the height of anemometers on the weather ships used by Pierson and Moskowitz), the PM spectrum equals:

$$S(\omega) = \frac{\alpha g^2}{\omega^5} e^{-0.74(\frac{g}{U_{19.5}\omega})^4}, \tag{4.14}$$

where $\alpha = 0.0081$.

#### 4.1.4.2 The JONSWAP spectrum

The JONSWAP spectrum was derived from data from the Joint North Sea Wave Observation Project (JONSWAP) [114], and applies for developing seas that are fetch limited and therefore not fully developed. For a given wind speed, $U_{10}$, at an altitude 10m above the sea surface (note that $U_{10} = 0.93U_{19.5}$), and a fetch, $F$, the JONSWAP spectrum equals:

$$S(\omega) = \frac{\alpha g^2 \gamma^r}{\omega^5} e^{-1.25(\frac{\omega_p}{\omega})^4}, \tag{4.15}$$

where $r = e^{-\frac{(\omega-\omega_p)^2}{2\delta^2\omega_p^2}}$.

Wave data collected during the JONSWAP experiment were used to determine the value of the constants in Equation 4.15, [115]:

$$\alpha = 0.076 \left(\frac{U_{10}^2}{Fg}\right)^{0.22},$$
$$\omega_p = 22 \left(\frac{g^2}{U_{10}F}\right)^{1/3},$$

$$\gamma = 3.3,$$
$$\delta = \begin{cases} 0.07 & \omega \leq \omega_p \\ 0.09 & \omega > \omega_p \end{cases}.$$

The JONSWAP spectrum is similar to the PM spectrum, as shown in Figure 4.4, except that the JONSWAP spectrum is more 'peaky', as determined by the $\gamma$ parameter, and it continues to grow with the fetch distance, as determined by the $\alpha$ parameter, while the peak frequency decreases, as determined by the $\omega_p$ parameter.

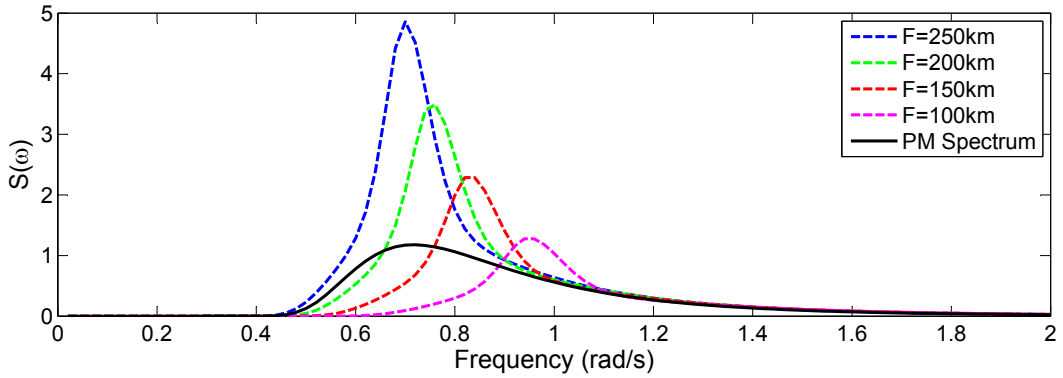


FIGURE 4.4: Comparison of the JONSWAP spectrum for varying fetch distance (dashed lines) against the PM spectrum for a 12m/s wind speed.

## 4.2 Wave energy review

The concept of harnessing the natural power of ocean waves is over 200 years old with the first patent into the area dating back to 1799 (Girard & Son, France). From there development progressed gradually, by 1970 there were 340 patents in Britain on wave-powered devices [116]. The 1970s saw intensive research and development of wave energy owing to fears of impending fuel shortages after the dramatic increase in oil prices. Thus, most research was focused on large scale schemes capable of contributing significantly towards national power grids. By the early 1980s oil prices subsided and focus moved away from wave energy research as cost estimates were significantly greater than those for coal-fired or nuclear power stations [117]. Today with growing concerns over carbon emissions from fossil fuels, research in the wave energy conversion arena is once again gaining momentum, but is relatively immature compared to other renewable technologies. Good reviews on the field of ocean wave energy conversion can be found in the papers by Falnes [100], Falcao [118] and Drew et al [119], and in the books by McCormick [120] and Cruz [121].

### 4.2.1 Principles of capturing energy from waves

Conservation of energy stipulates that the energy transported by a wave should diminish after passing a WEC. The difference in the wave's energy before and after intercepting the WEC should ideally be the amount of electrical energy produced by the WEC. However due to inefficiencies inherent in all systems, there will be energy lost to other sources during the conversion process. For a wave to be diminished, another wave must destructively interfere with it. Thus, during the process of absorbing energy from a wave, a WEC creates its own wave which destructively interferes with the incoming wave, reducing the receding wave on the lee-ward side. Falnes [110] described the crux of this concept as; "for an object to be a good wave absorber it must be a good wave maker".

Using this line of thought it has been shown [122] that axisymmetric objects restrained to move in only one degree of freedom can at best only absorb 50% of the incoming wave energy. It requires motion in two degrees of freedom to completely absorb an incoming wave as is shown in Figure 4.5 [110], where $a$ is the incident wave, $b$ is the wave produced by a body oscillating in heave, $c$ is the wave produced by a body oscillating in the surge or roll, and $d$ is the resultant of all three waves showing the incident wave totally absorbed by the body. However, non-symmetric bodies oscillating in one mode of motion only, can theoretically extract almost all of a waves energy [123].

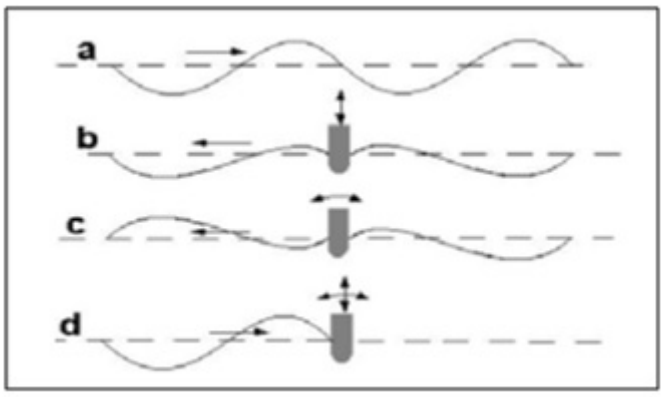


FIGURE 4.5: Wave creation/absorption by an axisymmetric buoy, illustrating that to absorb a wave means to generate a wave. (a) Represents an undisturbed incident wave. (b) Illustrates symmetric wave generation (on otherwsie calm water), by a body oscillating in heave. (c) Illustrate antisymmetric wave generation by a body oscillating in surge. (d) Represents the superposition of the above three waves, illustrating complete absorption of the incident wave energy [110]

The great Greek philosopher Archimedes said "Give me somewhere to stand and I will move the Earth". His point is applicable to WECs, as to convert motion into power you need something to react against. Power is not derived from motion itself, but rather from relative motion between two objects. In his review of WECs, Bracewell [117] identified

that all proposed types of WECs have three things in common; they need a working surface for the waves to act against, there must be something providing a stable frame of reference to react these wave forces against, and the working surface must be capable of being moved by the wave forces relative to this frame of reference. He also notes that, for the devices reviewed, the frame of reference was the largest single element in the final estimated cost of power produced. French [124] identifies four options for the reaction:

1. A large structure with extreme dimensions of the order of a wavelength which is subject to a number of wave forces of different phases that provide reactions for each other,
2. Reacting against the seabed,
3. Reacting against a mass that is part of the WEC, or
4. Reaction from a part of the sea.

### 4.2.2 Wave energy converters

There are well over 1000 patented wave energy conversion techniques[116], with inventors and researchers imagining a myriad of different possibilities to convert the raw energy of the oscillating ocean surface into useful electricity for society's consumption. Therefore a thorough review of all the different technologies is outside the scope of the present work, but instead will direct the interested reader to the following references which provide a review of the different WECs [116, 118–121, 125] and an extensive list of different wave energy concepts can be found on the European Marine Energy Centre's website [126].

WECs can however be broadly grouped into three main categories dependent upon their geometries: terminators, attenuators and point absorbers. Terminators are aligned parallel to the incident wave fronts, being geometrically wide to intercept and stop as much of the incoming wave as possible. Attenuators are aligned perpendicular to the incoming wave and utilise the phase difference along the length of the wave to derive power through relative movement between subsections of the WEC. Point absorbers are by definition of very small extension compared to the wavelength [110] and absorb power analogously to antennas in electromagnetic wave fields. Although relatively small in size a point absorber can absorb energy from part of the wave front equal to the wavelength divided by $2\pi$ [122]. Therefore its absorption width can be greater than its own width, increasing the available power for extraction. This can be understood by considering that as a point absorber oscillates it generates circular waves which radiates outward which can destructively interfere with the incident wave over a large area.

#### 4.2.2.1 Power take-off mechanisms

The power take off (PTO) mechanism converts the mechanical energy from the WEC into electrical energy. Reliable PTO systems are rarely seen with a power conversion efficiency above 60% from absorber motion to grid [127]. The problem faced is that the movement or oscillations of bodies caused by sea waves are very slow, bidirectional and irregular, yet the majority of WECs use conventional high speed rotational electromagnetic generators. These types of generators have been used by other electricity production techniques (e.g. coal fired power stations and hydro electricity) for decades and are thus a well established commercially available technology. However, WECs are not directly compatible with off the shelf rotational electromagnetic generators, but rather require intermediate conversion steps to convert the slow vertical oscillations of the waves into high speed rotation. These conversions are achieved via air and water turbines, gearboxes or hydraulic systems for example, which add extra moving parts to the system increasing its complexity, introducing reliability issues and adding inherent efficiency losses.

To reduce the number of conversion steps, linear generators have been investigated as an alternative to the rotational generator [128–131]. A linear generator allows the vertical motion of the wave to be directly coupled to the moving part of the generator. Linear generators are a direct drive PTO, and can potentially provide a simpler system requiring fewer moving parts, lower maintenance requirements and higher efficiency. In this case, the velocity of the generator is equal to the oscillatory motion of the WEC, being of the order of 0.5-2m/s [132, 133]. These slow velocities require large forces to be achieved in order to produce significant power outputs, resulting in large, heavy, expensive generators [134].

## 4.3 Wave energy harvesting for marine based sensors

This section details the specifics of wave energy harvesting for marine based sensors, by first identifying the differences between this application and that of conventional large scale wave energy conversion in Section 4.3.1. The characteristics of the wave resource available at MBS deployment locations is outlined in Section 4.3.2, which can be significantly different to the those for large scale wave energy conversion. Section 4.3.3 then proposes a WEC device for powering MBSs and details the design requirements of the WEC for the present application. The section then concludes with a review other similar work in this area, highlighting the novelty of the present work and the issues it aims to address.

### 4.3.1 Comparison with conventional large scale wave energy conversion

The following key differences between conventional wave energy conversion and the present application of wave energy harvesting for MBSs have been identified:

- **Scale:** Conventional WECs are designed to output kW-MW of power, whereas MBSs require many orders of magnitude less power than this. A wave energy harvesting device for powering MBSs can therefore be considered a microscale WEC.
- **Location / Wave resource:** Conventional WECs are typically deployed at targeted sites with good wave resources, whereas the deployment sites of microscale WECs for powering MBSs depends entirely on the monitoring objectives of the MBS and as such can be deployed in sheltered sites with little wave resource compared to that sought by conventional WECs.
- **Permanence:** - Conventional WECs are typically deployed with minimum life times of 20 years, whereas MBSs may only be deployed at a certain site for a few months or years, and in some cases may be freely drifting [15] and therefore never permanently in one location.
- **Cost:**
  - Construction costs: Due to the scale difference, conventional WECs are many orders of magnitude more expensive than a microscale WEC. However, the cost of conventional WECs are offset by the income they accrue by selling electricity to the grid, whereas the cost of the microscale WEC device for powering MBSs is only offset by the reduction in maintenance expenses from eliminating the need for regular battery replacement. For the microscale WEC device to remain a viable option for powering MBSs, the material and construction costs need to be low.
  - Installation costs: The installation costs of conventional WECs are one of the most expensive parts of their overall costs [135], for example the hiring of specialist vessels during installation can cost in excess of €50,000 per day. However, due to the permanence of the deployment, the WEC has over 20 years to payback this cost. For MBS applications, the deployment is less permanent and therefore will occur more frequently, highlighting the need for an easily deployable device. Ideally, the device should be small enough for a single person to deploy it from an arbitrary vessel and not require specialist equipment, vessels, divers etc.

Albaladejo et al [26] report 'low cost' and 'ease of deployment' as the number one and two strong points of their MBS buoy design. They claim that with the design and materials used, their sensor buoy can be made for €340, and that only very simple infrastructure is necessary for its deployment in view of its small size and weight (12 kg), so that a leisure craft is sufficient. Thus, for a microscale WEC to be suitable for powering MBSs, it is crucial that it does not significantly increase the cost or deployment complexity.

- **Heave only:** Due to reported troubles with data transmission when the antennas pitch, the microscale WEC should predominately move in the heave mode of motion only.

### 4.3.2 Wave resource at sensor node deployment sites

Unlike conventional WECs, microscale WECs for MBSs do not have the luxury of choosing favourable locations with optimum wave resources, but will be located wherever the MBS is deployed for its monitoring objectives. The goal of a microscale WEC is to provide a robust power supply for the MBS regardless of where it is deployed in the marine environment. This section therefore seeks to outline the diverse sea conditions where a MBS may be deployed, and therefore a microscale WEC would have to operate in.

To investigate the range of different possible wave resources at MBS deployment sites, this thesis considers the coast of Queensland, Australia as a case study. As shown in Figure 3.6, the south-west coasts of Australia have large wave resources, which have drawn the attention of large scale WECs and is in fact is the location of the world's first grid connected WEC array [136]. Whereas, the wave resource along the coast of Queensland is a much smaller, however it is the location of many MBS deployments due to monitoring of the Great Barrier Reef ecosystem and for other purposes such as environmental monitoring of port developments to accommodate the exports from Queensland's extensive mining industry. Queensland's main coastline is 6,973km in length with another 6,374km of island coastline [137], and is subjected to a wide range of wave conditions, extending from tropical latitudes in the north, which are sheltered from the Pacific Ocean by the Great Barrier Reef, to the southern surf beaches with a good wave resource, such as Surfer's Paradise, and even to a west facing coastline in the Gulf of Carpentaria.

Wave data is obtained from the Queensland Government Department of Science, Information Technology and Innovations's Coastal Impact Unit, which maintains a network of wave monitoring sites [111]. Each of the monitoring sites, has a Waverider buoy which

continuously monitors the FSE by using accelerometers to measure the heaving motion of the buoy. The locations of the buoys is detailed in Section 4.3.2.1 and then the data is analysed and discussed in Section 4.3.2.2.

#### 4.3.2.1 Case study buoy locations

The case study considers eight sites, marked on the map in Figure 4.6 and shown in more detail in the zoomed in maps of Figures 4.7 - 4.14. The sites are chosen to span the length of the coast and the types of different possible deployment locations e.g. sheltered, not sheltered, various water depths etc. (The maps in this section are made using Google maps [138]).

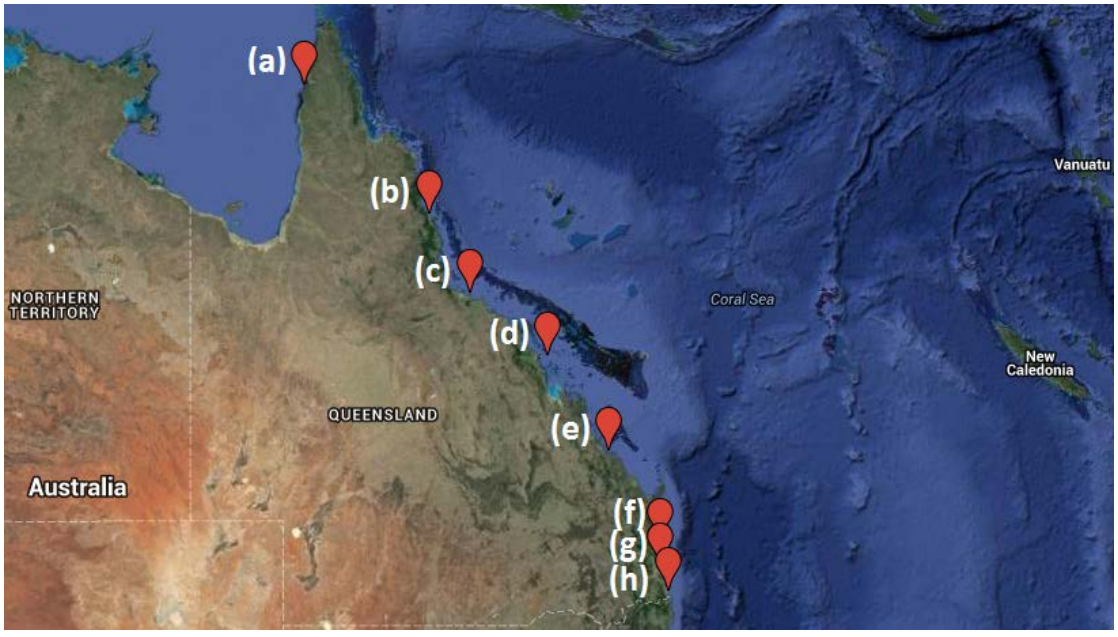


FIGURE 4.6: Locations of the Waverider buoys used for analysis.

Site (a) at Albatross Bay is in 10m water depth, sheltered in the north, east and south by the bay which opens westward to the Gulf of Carpentaria. Sites (b) at Cairns, (c) at Townsville and (d) at Mackay, are in water depths of 12, 17 and 30m respectively, and are all partially sheltered to the east by the reefs and islands in the Great Barrier Reef and to the west by the Queensland coast, additionally Cairns and Townsville are also sheltered to the south by the coast. Site (e) at Gladstone in 16m water depth, is located towards the most southerly part of the Great Barrier Reef and is less densely sheltered to the east than sites (b), (c) and (d), and is unsheltered from the Pacific Ocean swells to the east southeast. Sites (e) at Mooloolaba in 32m water depth and (g) at Gold Coast in 17m water depth, are at unsheltered locations near popular recreational surfing beaches due to the good wave resources at these sites from the Pacific Ocean swells. Site (f) at

Moreton Bay is in 10m water depth and is in the middle of a very well sheltered bay with the Stradbroke Islands to the east.

**(a) Albatross Bay (Water depth 10m)**

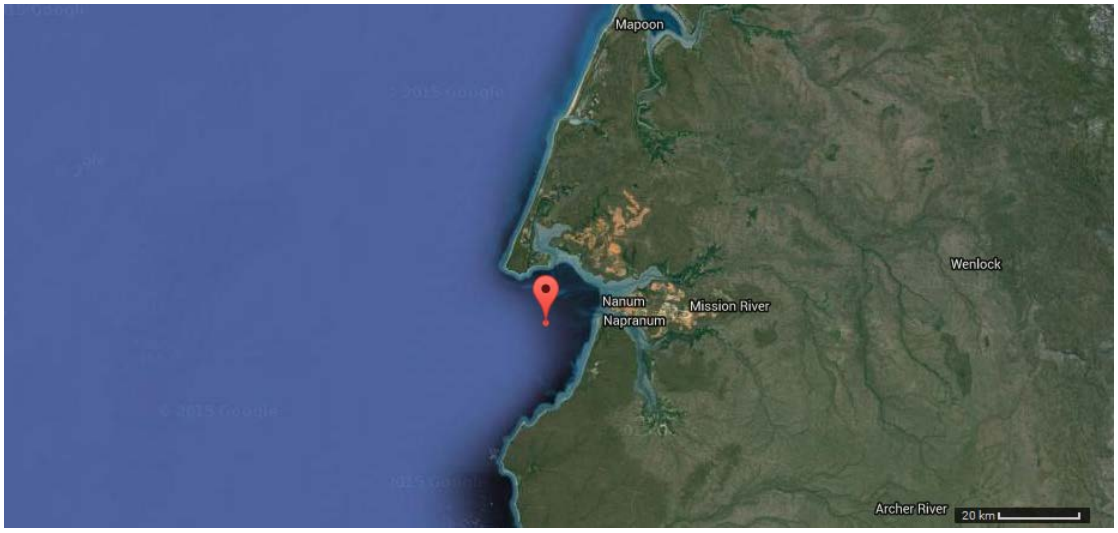


FIGURE 4.7: Location of the Albatross Bay waverider buoy.

**(b) Cairns (Water depth 12m)**

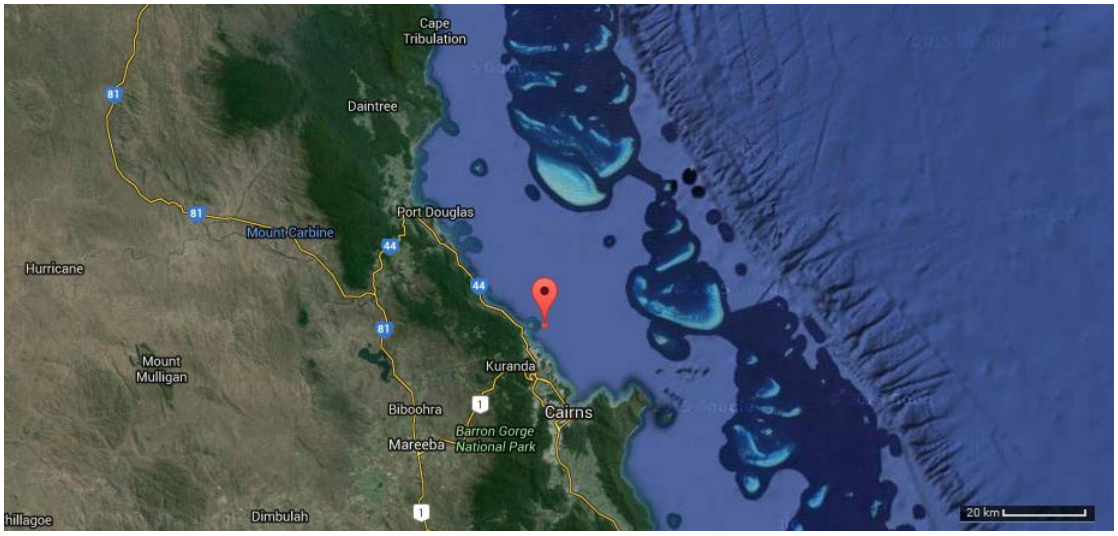


FIGURE 4.8: Location of the Cairns wave rider buoy.

**(c) Townsville (Water depth 17m)**

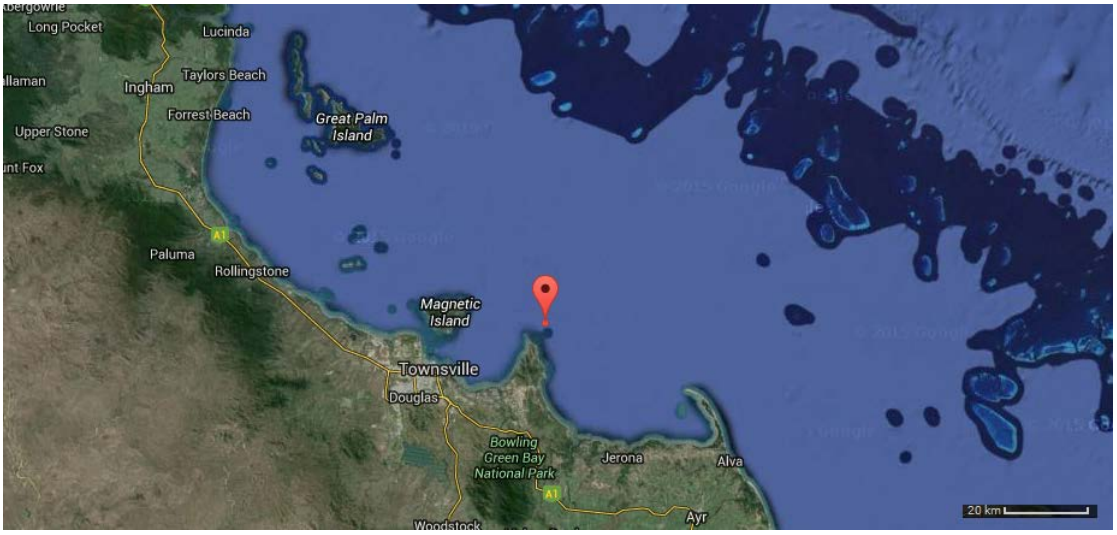


FIGURE 4.9: Location of the Townsville waverider buoy

**(d) Mackay (Water depth 30m)**

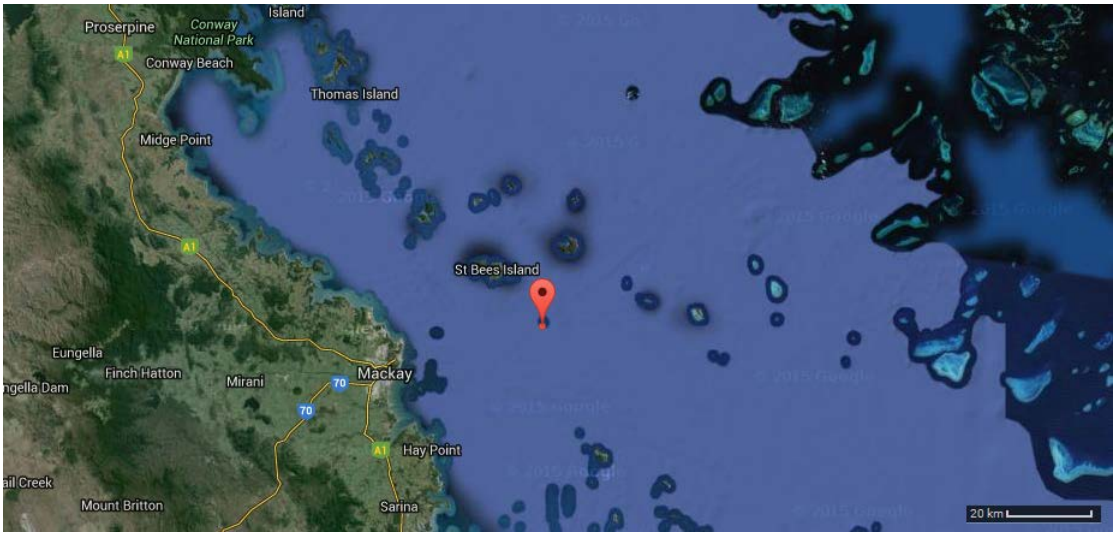


FIGURE 4.10: Location of the Mackay waverider buoy

**(e) Gladstone (Water depth 16m)**

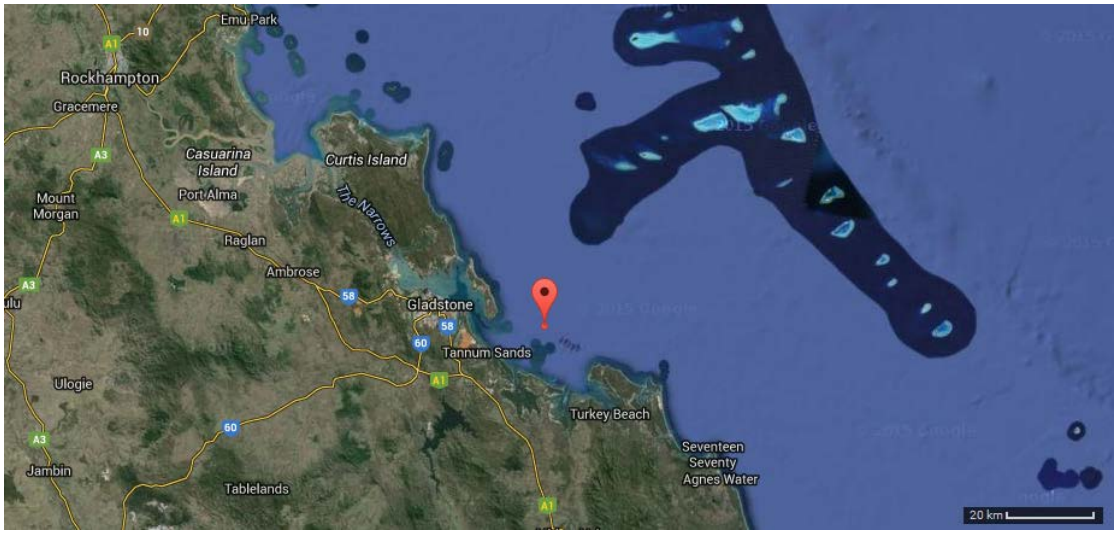


FIGURE 4.11: Location of the Gladstone waverider buoy.

**(f) Mooloolaba (Water depth 32m)**

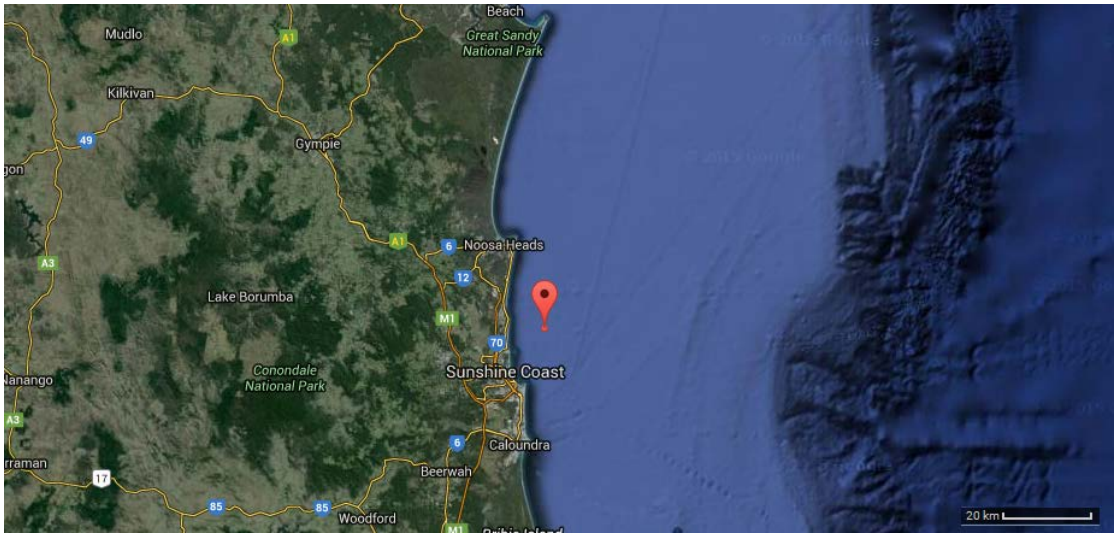


FIGURE 4.12: Location of the Mooloolaba waverider buoy.

**(g) Moreton Bay (Water depth 10m)**

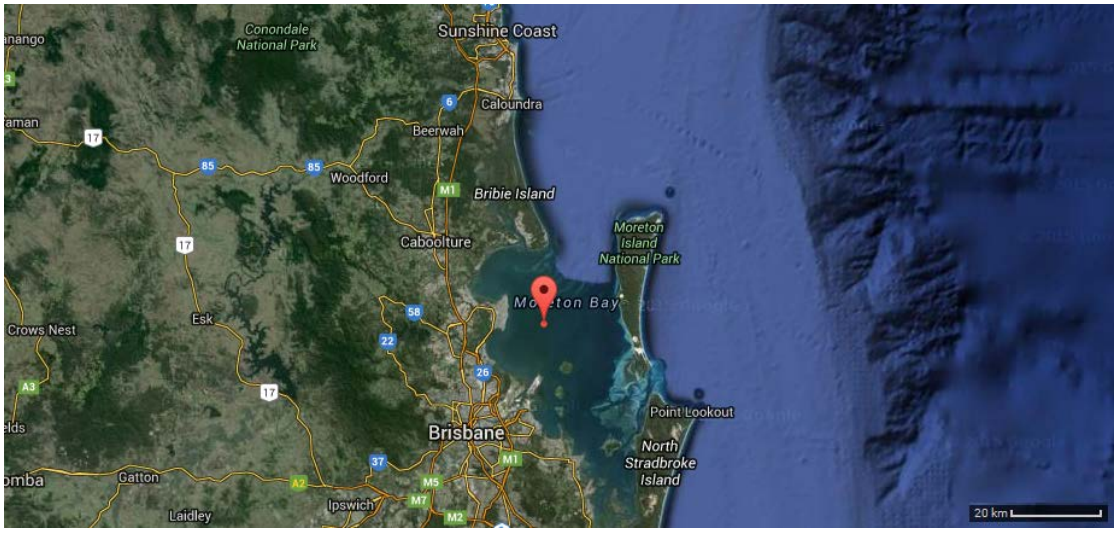


FIGURE 4.13: Location of the Moreton Bay waverider buoy.

**(h) Gold Coast (Water depth 17m)**

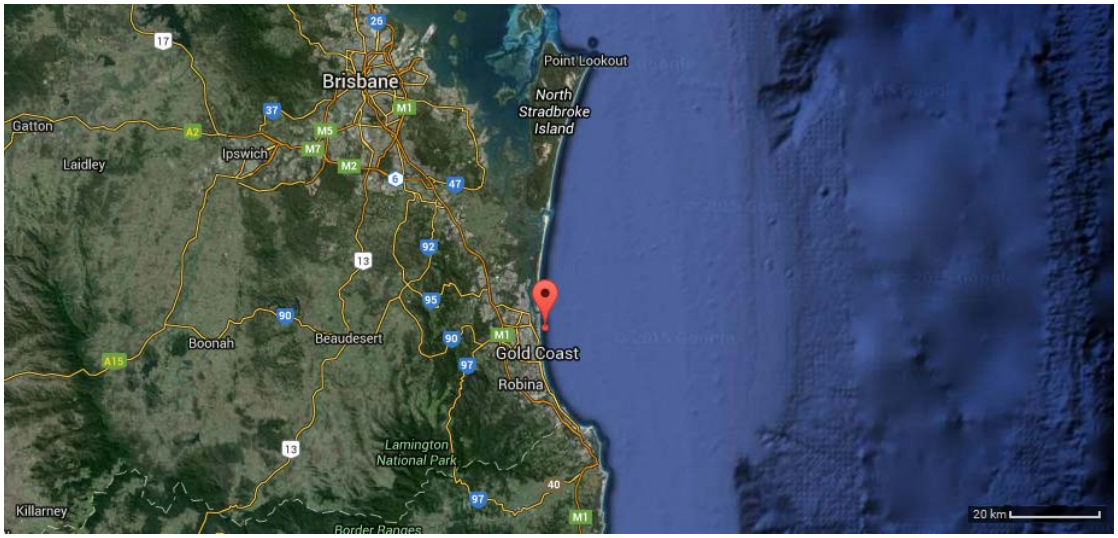


FIGURE 4.14: Location of the Gold Coast waverider buoy.

#### 4.3.2.2 Data analysis

Wave data for the selected sites is freely available on the Queensland Government website [111]. The sea state for each site is recorded every 30 minutes, in the form of the peak period, $T_p$, and the significant wave height, $H_s$, derived from the calculated spectrum of the 30 minute time series of FSE measurements by the Waverider buoy. Figure 4.15 shows a plot of the significant wave height and peak period data from the Townsville site for one year.

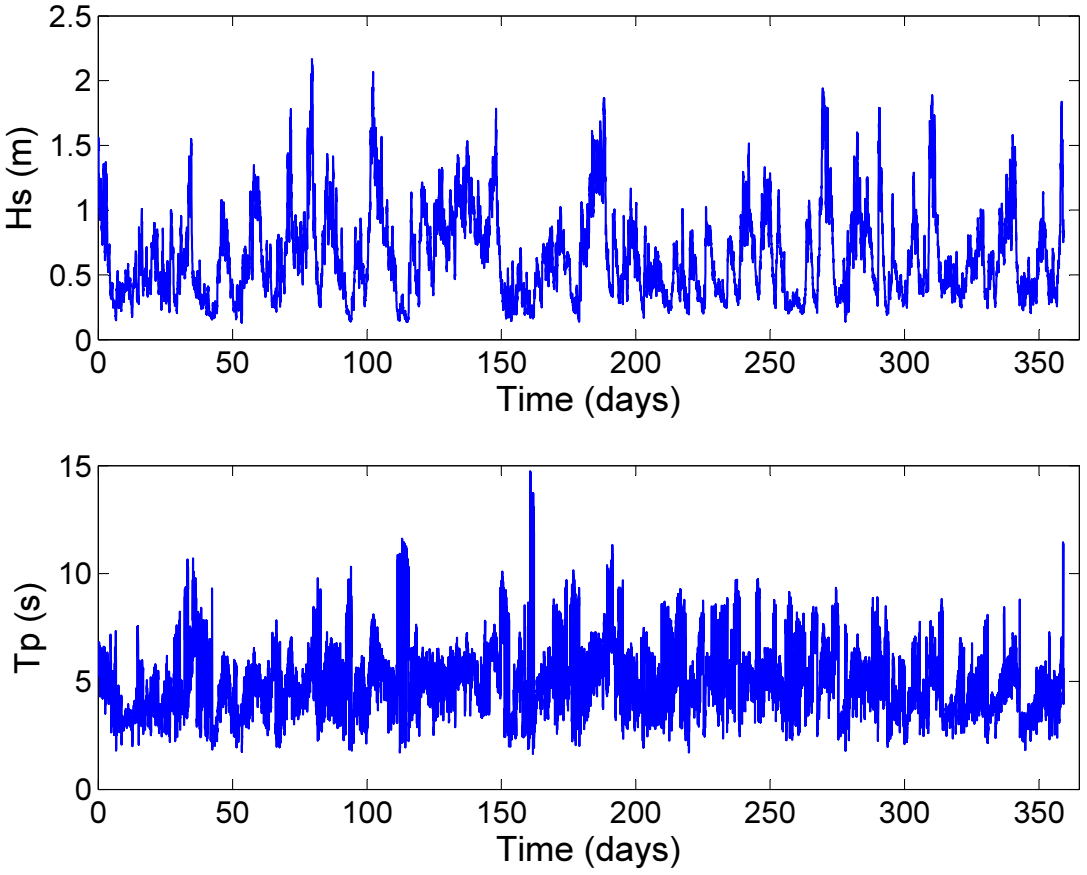


FIGURE 4.15: Significant wave height and peak period recorded at 30 minute intervals at the Townsville buoy in 2012

The analysis of the wave resource at each location is performed by taking three years of data for each site, resulting in 17,520 sea state samples. Each sample contains a $T_p - H_s$ pair, which are used to produce a scatter diagram, as shown in Figure 4.16 for the Townsville location. The samples are then binned into 0.1m signifcant wave height bins and 0.2s peak period bins, and the percentage occurrence for each of these bins is calculated to produce a occurrence matrix, plotted in Figure 4.17 for the Townsville location. Figure 4.18 shows the occurrence matrix for all of the 8 sites along the Queensland coast, which is used to compare the different wave resources.

Figure 4.18 shows the wide variety of sea states that a microscale WEC for powering MBSs may have to operate in. The figure display a large variation between the individual sites, with the unsheltered locations, (f) and (h), containing the largest wave heights and longest wave periods and therefore the most power ( Equations 4.4 and 4.11), whereas the more sheltered sites such as (a) and (g) contain small wave heights and short period waves. As such, sites (a) and (g) would not be considered as candidate location for large scale WECs, however they are indeed the location of MBS deployments, with [6] and [8] reporting on their deployments in Moreton Bay, and JCU's Marine Geophysical Laboratory having made numerous deployments in the Albatross Bay region (the present author himself has been out on the water there on several occasions to perform maintenance, data downloads and battery replacements on nephelometers measuring turbidity in the bay).

Not only is there a large variation in the wave resource between the different sites, but the sea states are seen to vary within the individual locations as well. Figure 4.18 shows a trend of the wave resource becoming more variable the less sheltered the site is. Sites (a) and (g) have the least variation in their resource, with the majority of sea states measured at these sites having peak periods between 2 and 4s and significant wave heights between 0.2 and 1m. The unsheltered sites (f) and (h) on the other hand, have peak periods varying between 4 and 15s and significant wave heights between 0.5 and 2.5m. The other four sites, have a variation between these two extremes.

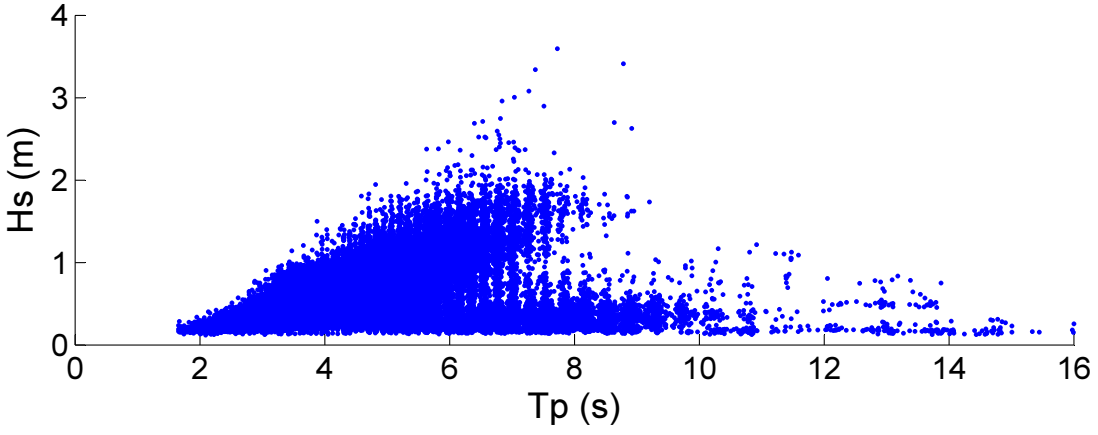


FIGURE 4.16: Scatter plot of all the significant wave height and peak period 30 minute interval measurements at the Townsville buoy for 3 years (Jan 2012- Dec 2014)

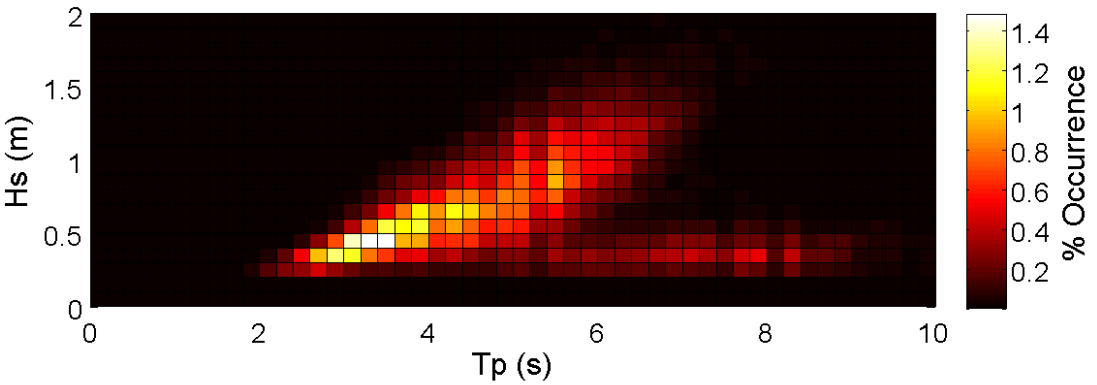


FIGURE 4.17: Percentage occurance of the 30 minute interval significant wave height and peak period measurements at the Townsville buoy for 3 years grouped into 0.1m significant wave height bins and 0.2s peak period bins

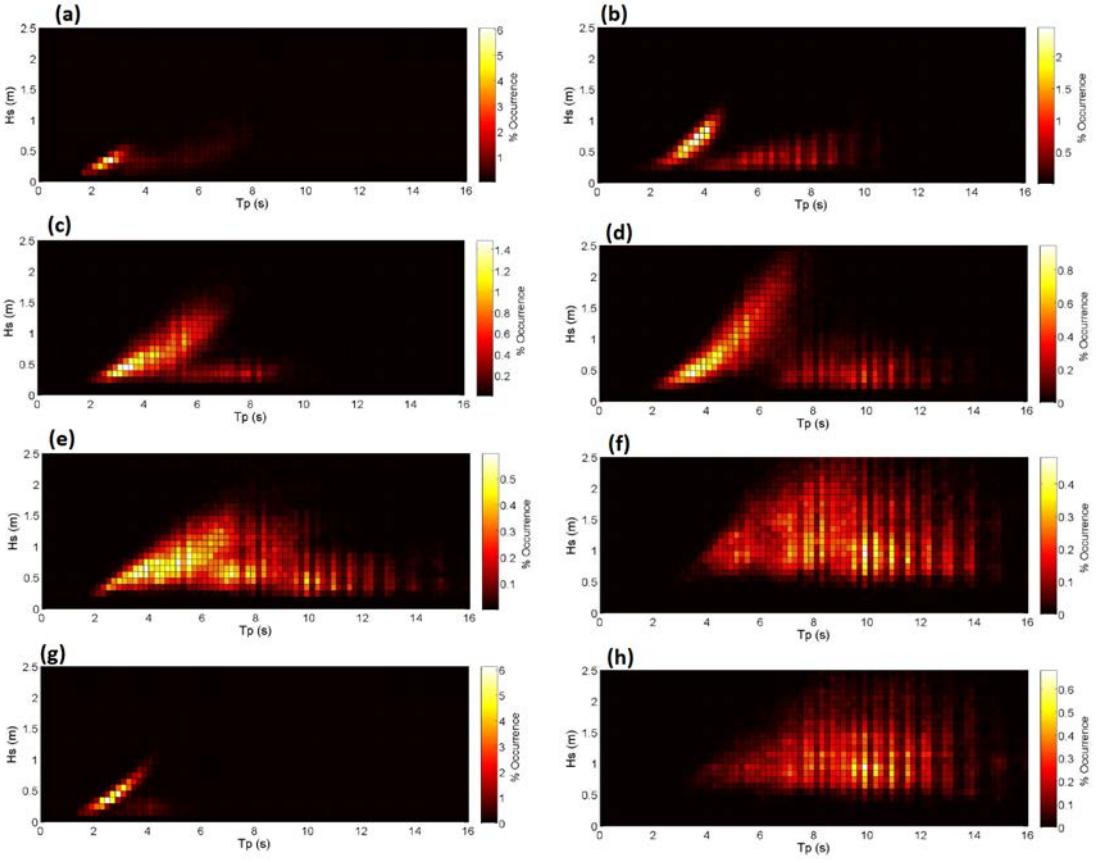


FIGURE 4.18: Percentage occurance of the 30 minute interval significant wave height and peak period measurements for 3 years grouped into 0.1m significant wave height bins and 0.2s peak period bins for the Queensland coast sites. (a) Albatross Bay, (b) Cairns, (c) Townsville, (d) Mackay, (e) Gladstone, (f) Mooloolaba, (g) Moreton Bay (h) Gold Coast

### 4.3.3 Proposed system

With the aim of a small, cheap, easily deployable device, Figure 4.19 illustrates the proposed system for wave energy harvesting for MBSs. The proposed device is a cylindrical inertial permanent magnet linear generator (CIPMLG) WEC. Of the three main WEC categories, a point absorber type WEC was chosen for the present application due to its intrinsically small size, rather than the physically large terminator and attenuator type WECs. An axisymmetric geometry is chosen for the point absorber, to eliminate the requirement of any specialised mooring configuration to align the orientation of the device with the incoming wave direction, allowing easy deployment.

The frame of reference chosen for the CIPMLG WEC to react the wave motion against, is the third option identified by French [124] (outlined in Section 4.2.1), "Reacting against a mass that is part of the WEC." The first option requires a very large structure and is therefore unsuitable for the present application. The second option, requires special mooring configurations to react against the sea bed and therefore increases the complexity of the deployment. Choosing the third option over the fourth option, allows the system to be completely sealed, reacting against an internal mass rather than an external part of the sea. To achieve the reaction against an internal mass, the PTO mechanism is chosen as an inertial permanent magnet linear generator (IPMLG). Selection of this type of system was inspired by the vibration energy harvesters reviewed in Section 2.2.3.3, which are small in size and utilise the oscillation of an internal proof mass against the external vibration sources to harvest power.

The IPMLG comprises of a moving part, the translator, and a stationary part, the stator, where the translator contains permanent magnets and the stator contains coils of wire. The translator's mass acts as a proof mass, providing inertia to react the wave motion against. According to Newtons first law of motion, the proof mass will tend to remain stationary with respect to an inertial reference frame, while the buoy will oscillates in that frame due to interaction with the ocean waves. This creates relative motion between the buoy and the reaction mass which can be utilised to draw power. Coupling the buoy and translator mass together with a spring, and tuning the various parameters of this coupled system, allows the buoy and mass to oscillate with different amplitudes and phases to each other. This results in continuous relative motion between the translator and stator throughout the wave cycles. Therefore during operation the relative motion between the translator and stator leads to a varying magnetic flux through the armature coils resulting in an induced voltage proportional to the rate of flux change (Faraday's law).

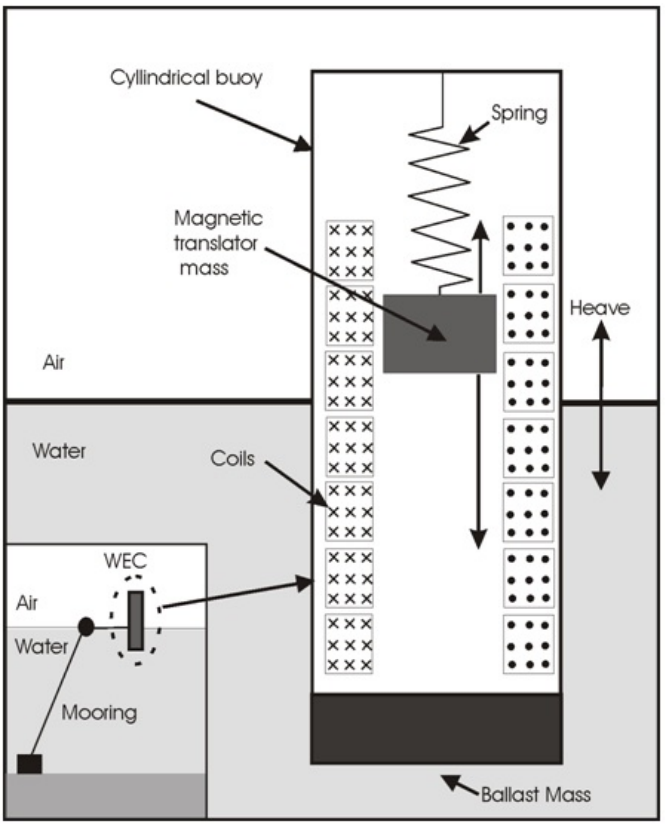


FIGURE 4.19: Schematic of proposed microscale WEC, consisting of a cylindrical buoy, with an internal linear generator, floating vertically on the ocean surface. The linear generator comprises of a magnet, coupled to the buoy via a spring, which oscillates inside copper wire coils. A ballast mass is located on the bottom of the buoy to ensure the cylinder remains vertical. The mooring system keeps the device on station.

The electromagnetic linear generator is employed as the PTO mechanism because the system is simple with few moving parts, no intermediate energy conversion steps, is expected to require little maintenance and have high survivability compared to its rotational counterpart. The challenges related to the large forces required when utilising linear generators in large scale WECs are not relevant at the small scale of the present application of powering MBS's. Permanent magnets are favoured over electrically excited magnetic systems (e.g., induction or switched-reluctance machines) because the magnetic flux density available from a permanent magnet is independent of its size, whereas unfavorable scaling of the currents that are necessary to establish the magnetic fields for electrically excited magnetic systems render them undesirable for miniaturization [139].

The geometry of the point absorber is chosen as a cylinder, with its central axis aligned vertically. To ensure the cylindrical buoy remains vertical in the water, a ballast mass is located on the bottom of the buoy. The axisymmetric geometry of the vertical cylinder eliminates any dependence on the directionality of incoming waves and is chosen over other axisymmetric geometries, such as spheres, because its long vertical geometry is

more accommodating for an internal linear generator. The cylinder shape is also selected for cost purposes, with cheap premade materials like PVC piping envisioned to be ideal for the buoys hull.

#### 4.3.3.1 Design problem

The CIPMLG WEC concept has been proposed as a potential means of powering a MBS from the renewable wave energy resource. The challenge now is to design this concept into a device capable of fulfilling a number of requirements, which forms the design problem. The design problem of the proposed CIPMLG WEC, which will be analysed and evaluated in the subsequent chapters, is summarised in the following bullet points:

- **Power requirment:** Harvest 1W of average power per day.
- **Minimise the size and weight of the device:** Relating to ease of deployment, the microscale WEC should ideally be as small and light as possible. A smaller device is generally a cheaper device, therefore this design requirement also relates to reducing the cost of the device.
- **One size fits all design:** Can a one size fits all microscale WEC be designed for any deployment site, or does an a priori knowledge of the wave climate at the intended site need to be used to tune the device design to that particular site before it is deployed? Section 4.3.2 outlined the wide variety of wave climates the microscale WEC may have to operate in. It is common practice with large scale WECs to optimise the design for the wave climate in which it will be deployed. The extra costs involved in aquisition of wave climate data and bespoke designs for each deployment site, is paid back over the lifetime of the large scale WECs by revenues from increased power production. However, the costs of a microscale WEC for powering MBSs must remain as low as possible, and a one size fits all design would reduces the cost of the device by allowing mass production and reusability. Additionally, unlike large scale WECs where resource assessment and site selection are part of the whole deployment process, previous wave measurements and wave climate data at the MBS sites are generally not available unless it already exists in the public domain. Therefore, the design ideally should allow a single device which is able to perform well at any site and at any time, regardless of the wave climate.
- **Pitch resilience:** The pitch motion of the buoy should be minimised to enable the antenna to be relatively stable for data transmission. This pitch constraint is

further analysed in the next subsection 4.3.3.2. Additionally, the vertical cylinder must remain vertically stable in the water to avoid capsizing.

#### 4.3.3.2 Pitch constraint

The pitch motion must be constrained due to the tilting of the antenna disrupting the data transmission. For MBSs, dipole type antennas are the most commonly used, because they are horizontally non directional, with a 360 degrees beamwidth. However, the dipole antenna is vertically directional, with a half power beamwidth of 78 degrees in the vertical plane [140], meaning that when the buoy is at equilibrium and the antenna is perfectly vertical, the half power beamwidth is about 40 degrees above and below the horizontal plane. If the buoy pitches and the antenna tilts from vertical, then the beamwidth is also tilted by this amount. The present thesis will therefore seek to constrain the pitch motion of the buoy to below 40 degrees, so that other MBS nodes are always within the half power beamwidth of the antenna.

Gyroscopic WECs could provide a possible solution to restrain the pitch motion. For example the ISWEC, [141], uses a the inertia of a gyroscope to react a rotational PTO against, however only along one axis of rotation. The ISWEC is not axisymmetric and must be aligned into the oncoming waves and only harnesses power from pitch motion but not roll. To utilise an ISWEC type system while remaining invariant to the incoming wave direction, would require two such PTO systems aligned orthogonal to each other, increasing the cost and complexity of the system. The gyropscopic WEC requires input power to keep the flywheel spinning, which is located inside of a vacuum chamber to reduce the air resistance on the flywheel. Thus, the proposed CIPMLG WEC is favoured over a gyroscopic WEC in the present work due to its perceived simplicity and cheaper cost, and its pitch motion will be analysed to determine if it can indeed satisfy the pitch constraints.

### 4.3.4 Similar work

A number of small scale type WECs for similar tasks have been proposed and investigated by other researchers and are outlined in this subsection. The research reported in these publications offer results and analysis to compare against the work to be reported in the current thesis. The major difference identified between these published results and what is proposed in the current thesis, is the size, weight and/or choice of reaction frame. The devices reported have masses in excess of 100kg or react against the sea floor, which goes against the proposed philosophy of the CIMPLG WEC; to be small, light and easily deployable. However, the reported system are in general aiming at a power

output an order of magnitude larger than that identified for the present system, which accounts for the discrepancy is device sizes and highlights another difference between the current thesis and the published literature. The second major difference, is the current thesis's goal to produce a pitch resiliant device, due to the identified influence of this motion on the data transimission, which is not considered in reported work elsewhere.

The Electro Standards Laboratories, in collaboration with the Department of Ocean Engineering at the University of Rhode Island, has focussed on the development of small scale point absorber buoys capable of providing power to on-board sensors and instrumentation [142–144]. Their systems target power levels of 1-10W and are a continuation on from [145, 146] which originally sought to develop small scale buoys capable of producing on the order of 1kW of power. Bastien et al [142] present numerical simulations and experimental measurements on ocean energy harvesting systems that utilize anchored linear generators driven by heaving surface buoys. Their results demonstrate the feasibility of using ocean wave energy harvesting buoys and simple linear generators to provide sufficient power for ocean sensor applications (1-10W). They use a linear generator inside of a water tight canister, one end attached to a surface buoy and the other to an anchor on the sea floor or a resistance plate. The resistance plate is shown to be preferable to bottom anchored system, which requires a mechanism to adjust for changing water depth due to tides. they calculate that the system size and weight are reasonable with a 1m diameter buoy and a 2m diameter resistance plate with a weight of 500kg and a power output of 3-4 W. This system was further refined in [143] and also in [144] where flexible solar panels were also included into the system to produce a hybrid wave - solar energy harvesting buoy for sensor applications.

Symonds et al [147] and Engelmann et al [148] investigated a novel WEC for powering distributed remote sensing and communications applications. Their device converts the linear motion into rotary motion, using a winding spool that reacts heaving motion of the a surface buoy against an anchor on the sea floor, capturing energy by a pull cord mechanism. They demonstrated 20-50W consistent power in 2 day sea trials. They claim their rotational spooling PTO mechanism has an advantage over linear generators which are very resonant compared to their more broadbanded system.

The work by Avadhany et al [149] aims at proving power on the range of 50-100W for distributed applications. Their OceanGen$^TM$ device harnesses wave motion via tension cable from the surface a surface buoy, via hydraulic-electric PTO based from their GenShock valve developed for energy recovery from vehicle suspension systems. Their simulations showed an output power on the order of 10-100W across a range a sea states, for a PTO weighing 110kg tethered to a buoy with a mass of over 2300kg.

One author has however investigated a system very similar to the one proposed in this thesis. Cheung and Childress [150] from Teledyne Scientific and Imaging, issued a technical report, for the U.S. Defence Advanced Research Projects Agency, detailing their research to develop a simple and robust wave energy harvesting device that can be used as a renewable energy source for ocean monitoring systems, which is the only published literature on their work. They investigated an inertial linear generator inside of a heaving spar buoy, and while their numerical simulations were limited to regular wave analysis, they performed numerous insightful physical experiments on the system in their laboratory. Most notably, they used a ferrofluid as a lubricant to reduce friction in the generator. The current thesis focusses solely on numerical analysis of the system, as discussed in Chapter 5, therefore some of the results and lessons learned from the experiments performed by Cheung and Childress [150] offer a good compliment to the present numerical analyses.

## 4.4 Summary

This chapter began the investigation of utilising ocean waves for powering MBSs, after they were identified in the previous chapter as the target energy resource to be examined in this thesis. Important properties of ocean waves were discussed, such as the concept of a wave spectrum, the mechanisms of wave creation and the dependence of the created wave fields on the wind speed, duration and fetch, and on the standard wave spectra which result from these wind conditions. The field of large scale wave energy conversion was reviewed and differences between that field and the present application of microscale WECs for powering MBSs, were identified. Characteristics of the wave resource at MBS deployment locations were investigated and were shown to differ to those typically targeted by large scale WECs. A micro-scale WEC device, the CIPMLG WEC, was proposed and design requirements for the device to be analysed in the subsequent chapters were detailed. A review of similar work in the literature, related to small scale wave energy conversion for distributed power generation, was collated. The present work was found to differ from the other research in this area, due to its focus on a smaller sized device which doesn't react against the seafloor and which addresses the problem of wave induced pitching motion on the MBS data transmission.

# Chapter 5

# Numerical modelling of the proposed CIPMLG Wave Energy Converter

## 5.1 Introduction

This chapter presents the numerical model of the CIPMLG WEC proposed in Chapter 4. The numerical model is used to analyse and assess the performance on the CIPMLG WEC in in this dissertation. Through numerical analysis many design configurations can be tested and optimised more easily and cheaply compared to performing the same task experimentally. Indeed, physical experiments are important and will naturally follow as an important step, however at this preliminary stage the present dissertation focuses on numerical analysis to initially gauge the potential of the proposed system before physical prototypes are developed for experimentation and validation of the numerical results.

The importance of early numerical analysis during the initial stages of device design, was recently illuminated by Weber [151], in which he introduced a Technology Performance Level (TPL) metric, to be used in conjunction with the traditional Technology Readiness Level (TRL) metrics, to assess the development of a prototype design. Combining the TPLs with the TRLs could be used to investigate the optimal development trajectory towards an economically competitive WEC. Analysis of these development trajectories strongly suggests optimising and refining the design, through the use of numerical tools, in the very early design stages to increase its performance ability before investing time and money into physical prototype experimentation.

The performance of the WEC is assessed on its ability to satisfy the design problem, outlined in Section 4.3.3.1. The numerical model must therefore be able to calculate the output power of the CIPMLG WEC to assess its ability to produce the required output of 1W average power. Additionally, the design problem also requires that the size of the CIPMLG WEC be compact to allow ease of deployment, therefore the numerical model should be able to calculate the linear generator's stroke length, to ensure it is not excessively large. The stroke length is the maximum distance the translator oscillates from equilibrium inside the stator. Finally, to enable assessment of the CIPMLG WEC's pitch resilience, the numerical model must also be able to calculate the pitch motion of the CIPMLG WEC.

The output power, stroke displacement and pitch motion of the CIPMLG WEC system will be calculated using a dynamical model. The dynamics of the system are modelled following Newton's law of motion. The CIPMLG WEC consists of two bodies, the main WEC/buoy structure and its internal generator's translator mass. In addition to the gravitational force, both bodies are subjected to the generator's PTO forces, which couple the two bodies together. The buoy is subjected to an additional force, the hydrodynamic force from the surrounding fluid.

The hydrodynamic force is calculated using a hydrodynamic model, which is detailed in Section 5.2. The modelling of the PTO system is then described in Section 5.3. The hydrodynamic and PTO models are then coupled together in Section 5.4, and finally the use of the derived model to analyse the CIPMLG WEC is then outlined in Section 5.5.

## 5.2 Hydrodynamic modelling

The fluid-structure interaction between WECs and the ocean is described by a hydrodynamic model. This section gives a background on hydrodynamic modelling for WECs, and then outlines the linear hydrodynamic model to be used in the present work to analyse the CIPMLG WEC.

### 5.2.1 Background

The force on the buoy from the surrounding water, results from integrating the pressure of the water over the buoy's wetted surface. The water pressure is a spatially and temporally varying value, influenced by factors such as the incoming waves and the motion of the buoy in the water, and calculating its value is the subject of fluid dynamics. The

dynamics of fluids are governed by the transfer of mass, momentum and energy, and these three processes are described by the Navier-Stokes equations, a set of partial differential equations derived in the early nineteenth century. In general, these equations have no known analytical solution; however they may be treated numerically to obtain a solution. Traditionally, such levels of computation were unfeasible, necessitating many linearising assumptions, such as small amplitude waves and body motions, in inviscid, irrotational and incompressible fluids to allow a computationally tractable solution, based on the linear theory of the velocity potential and the boundary element method (BEM) [152].

BEMs allow the fluid-structure interaction between WECs and the ocean to be described by a linear hydrodynamic model. In their systematic review of hydrodynamic modelling methods for point absorber WECs, Li and Yu [153] show that these methods evolved from the hydrodynamic modelling of ships and offshore floating structures. An excellent description and comparison of the different hydrodynamic modelling methods for the dynamic response of marine structures is given by Taghipour et al [154]. At the heart of these modelling methods is the Cummins equation, derived in 1962 [155], which is a linear integro-differential equation and is used in the present work (outlined in Section 5.2.2).

Linear hydrodynamic models have formed the basis for design, simulation and control of WECs, and have been well verified and validated over operating conditions for which small amplitude assumptions apply. However, at larger amplitudes a number of nonlinear effects may appear, prompting research in recent years into the development of nonlinear hydrodynamic models. Reviews of these nonlinear hydrodynamic modelling techniques are given by Wolgamot and Fitzgerald [156] and Penalba Retes et al [157]. The present author has been involved in developing nonlinear hydrodynamic models for WECs [158–166], and this work will be detailed in Section 10.1.6. However, for the preliminary design and analysis of the CIPMLG WEC, linear hydrodynamic models will be used to allow frequency domain analysis and timely investigation of the broad parameter space. The high fidelity, computationally costly, nonlinear models can then be used subsequently for a more refined analysis.

### 5.2.2 The linear hydrodynamic model for the CIPMLG WEC

In linear theory, the total force from the fluid on the body can be separated into three hydrodynamic forces [110]: the wave excitation force, $F_e(i\omega)$, the reaction force due to the wave radiation, $F_r(i\omega)$, and the hydrostatic restoring force, $F_s(i\omega)$, which forms the basis of the Cummins equation.

The wave excitation force, is the force exerted on a body which is held fixed in the presence of an incident wave, and is proportional to the wave elevation, i.e.;

$$F_e(i\omega) = H_f(i\omega)\eta(i\omega). \tag{5.1}$$

Here, $H_f(i\omega)$ is the heave excitation force coefficient and $\eta(i\omega)$ is the wave elevation at the origin. The origin is assumed fixed at the vertical axis through the center of the buoy.

The wave radiation force is the reaction force due to the radiated wave created by a body moving in the fluid, and is proportional to the velocity of the body i.e.;

$$F_r(i\omega) = -[N(\omega) + i\omega m_a(\omega)]\dot{Y}(i\omega) = Z_r(i\omega)\dot{Y}(i\omega). \tag{5.2}$$

Here, $\dot{Y}(i\omega)$ is the velocity of the buoy and $Z_r(i\omega)$ is the radiation impedance which comprises of the radiation resistance, $N(\omega)$ and the added mass, $m_a(\omega)$.

The hydrostatic restoring force arises when the body oscillates into and out of the water from its equilibrium position, resulting in a mismatch between the upwards buoyancy force and the downwards force from gravity. The hydrostatic restoring force acts like a spring and can be expressed as;

$$F_h(i\omega) = -KY(i\omega), \tag{5.3}$$

where, the restoring coefficient $K \geq 0$. For the case of a body moving in heave, the linear restoring coefficient is given by:

$$K = \rho g S, \tag{5.4}$$

where $\rho$ is the water density, $g$ is the Earth's gravitational field strength and $S$ is the water plane area of the buoy.

From Newton's 2$^{\text{nd}}$ law, the motion of the buoy in response to the hydrodynamic forces may be expressed as;

$$M\ddot{Y}(i\omega) = F_e(i\omega) + F_r(i\omega) + F_h(i\omega), \tag{5.5}$$

here, $M$ is the mass of the buoy and $\ddot{Y}(i\omega)$ its acceleration. Substituting Equations 5.1 - 5.3 for the hydrodynamic forces, gives:

$$M\ddot{Y}(i\omega) + [N(\omega) + i\omega_a(\omega)]\dot{Y}(i\omega) + KY(i\omega) = H_f(i\omega)\eta(i\omega). \tag{5.6}$$

The motion of the buoy can therefore be expressed as;

$$Y(i\omega) = \frac{H_f(i\omega)\eta(i\omega)}{-\omega^2(M + m_a(\omega)) + i\omega N(\omega) + K}. \tag{5.7}$$

#### 5.2.2.1 Hydrodynamic coefficients

The hydrodynamic coefficients, $H_f(i\omega)$, $N(\omega)$ and $m_a(\omega)$ are represented by complex functions, which depend on the geometry of the buoy. An example of these functions for a cylindrical buoy with radius 0.5m and draught of 1m is plotted in Figure 5.1. In the present work, these functions are computed using hydrodynamic BEM software. In particular the commercial computer software packages WAMIT (Version 6.4) [167] and the open source equivalent, Nemoh [168] are used, which are radiation/diffraction panel programs developed for the linear analysis of the interaction of surface waves with offshore structures. WAMIT was used initially, until the 12 month license expired, and then for the remainder of the work Nemoh was used. The outputs from both codes were compared and found to agree, before the Nemoh outputs were used for analysis. Other comparisons between the two codes, verifying their agreement is reported in the literature [169].

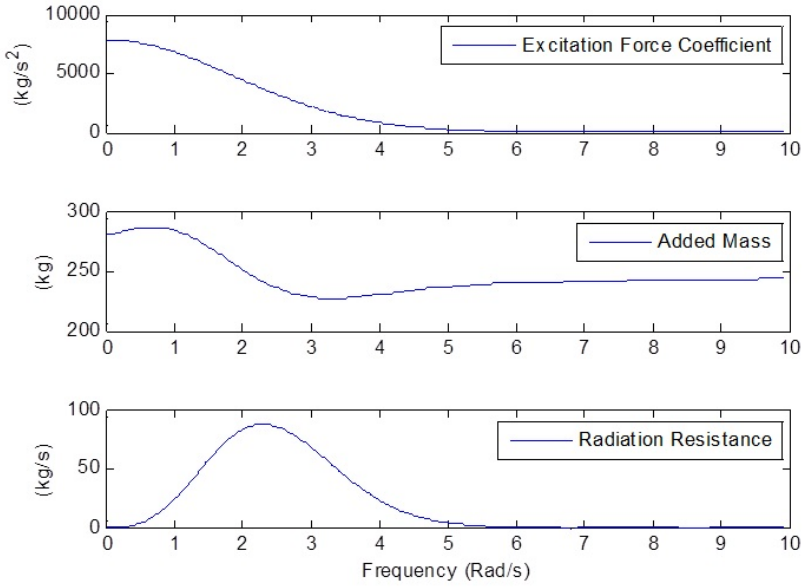


FIGURE 5.1: WAMIT outputs for $|H_f(i\omega)|$, $N(\omega)$ and $m_a(\omega)$ as a function of frequency, for a cylindrical buoy with radius 0.5m and draught 1m.

#### 5.2.2.2 Time Domain

The inverse Fourier transform of Equation 5.6 yields the time domain expression for the motion of the buoy;

$$(M + m_\infty)\ddot{y}(t) + \int_{-\infty}^{\infty} h_r(t-\tau)\dot{y}(\tau)d\tau + Ky(t) = \int_{-\infty}^{\infty} h_f(t-\tau)\eta(\tau)d\tau 0. \tag{5.8}$$

At infinite frequency the added mass, $m_a(\omega)$, tends to a finite constant, $m_\infty$, which is taken outside of the integral in Equation 5.8, to avoid divergence. The impulse response function of the radiation, $h_r(t)$, is the inverse Fourier transform of the reduced radiation impedance, $H_r(i\omega) = N(\omega) + i\omega[m_a(\omega) - m_\omega]$. The radiation impulse response function is causal, meaning the output is not affected by future values of the input, $h_r(t) = 0$ for $t \leq 0$. Physically this is the case because the buoy's velocity is the actual cause of the radiated wave. Therefore the upper-limit in the radiation force convolution integral is $t$. However, for the excitation force this is not the case. As an example consider the effect of the incident wave interacting with the buoy's exterior before it travels past the conveniently chosen reference point at the buoy's central axis. Therefore the upper limit in the excitation force convolution integral remains at positive infinity.

$$(M + m_\infty)\ddot{y}(t) + \int_{-\infty}^{t} h_r(t-\tau)\dot{y}(\tau)d\tau + Ky(t) = \int_{-\infty}^{\infty} h_f(t-\tau)\eta(\tau)d\tau. \tag{5.9}$$

The two convolution integrals cause this description of the system to be difficult to use. To overcome this, Yu and Falnes [170] use the state space method to model the system, allowing the integrals to be approximated by a finite-order system of differential equations with constant coefficients:

$$\dot{\mathbf{s}}(t) = \mathbf{A}\mathbf{s}(t) + \mathbf{B}\mathbf{u}(t), \tag{5.10}$$

$$\mathbf{v}(t) = \mathbf{C}\mathbf{s}(t), \tag{5.11}$$

where $\mathbf{s}(t) = \begin{bmatrix} s_1(t) & s_2(t) & \cdots & s_n(t) \end{bmatrix}^T$ is the state vector; $\mathbf{u}(\mathbf{t})$ is the input, which is either the buoy velocity, $\dot{y}(t)$, or the wave height, $\eta(t)$, depending whether the state space subsystem is approximating the radiation force integral or the excitation force integral; and $\mathbf{v}(t)$ is the output, which is the state space model's approximation to the relevant convolution integral. Yu and Falnes recommend using the companion form realisation

of the state-space model, whereby the matrices **A**, **B** and **C** are of the form:

$$\mathbf{A} = \begin{bmatrix} 0 & 0 & 0 & ... & 0 & -a_1 \\ 1 & 0 & 0 & ... & 0 & -a_2 \\ 0 & 1 & 0 & ... & 0 & -a_3 \\ \vdots & \vdots & \vdots & \ddots & \vdots & \vdots \\ 0 & 0 & 0 & ... & 0 & -a_{n-1} \\ 0 & 0 & 0 & ... & 0 & -a_n \end{bmatrix}, \tag{5.12}$$

$$\mathbf{B} = \begin{bmatrix} b_1 & b_2 & b_3 & ... & b_{n-1} & b_n \end{bmatrix}^T, \tag{5.13}$$

$$\mathbf{C} = \begin{bmatrix} 0 & 0 & 0 & ... & 0 & 1 \end{bmatrix}. \tag{5.14}$$

For this state space model to approximate the relevant convolution integral the following equivalence must hold:

$$h(t) = \mathbf{C}e^{\mathbf{A}t}\mathbf{B}. \tag{5.15}$$

Thus the $2n$ unknowns $(a_1, a_2, \cdots, a_n, b_1, b_2, \cdots, b_n)$ can be computed via the minimisation of the following target function:

$$\sum_{k=1}^{m}(h(t_k) - \mathbf{C}e^{\mathbf{A}t_k}\mathbf{B})^2. \tag{5.16}$$

Figure 5.2 shows the impulse response function for a cylindrical buoy with a 1m diameter and draught, and the fourth order state space model's approximation to this function, demonstrating excellent agreement between the two.

The time domain model, Equation 5.9, can now be represented by the following state equation:

$$\begin{bmatrix} \dot{s}_1(t) \\ \dot{s}_2(t) \\ \dot{s}_3(t) \\ \dot{s}_4(t) \\ \dot{y}(t) \\ \ddot{y}(t) \end{bmatrix} = \begin{bmatrix} 0 & 0 & 0 & -a_1 & 0 & b_1 \\ 1 & 0 & 0 & -a_2 & 0 & b_2 \\ 0 & 1 & 0 & -a_3 & 0 & b_3 \\ 0 & 0 & 1 & -a_4 & 0 & b_4 \\ 0 & 0 & 0 & 0 & 0 & 1 \\ 0 & 0 & 0 & -\frac{1}{\mu} & -\frac{K}{\mu} & 0 \end{bmatrix} \begin{bmatrix} s_1(t) \\ s_2(t) \\ s_3(t) \\ s_4(t) \\ y(t) \\ \dot{y}(t) \end{bmatrix} + \begin{bmatrix} 0 \\ 0 \\ 0 \\ 0 \\ 0 \\ \frac{1}{\mu} \end{bmatrix} f_e(t), \tag{5.17}$$

where $\mu = (M + m_\infty)$.

Here the input to the model is the excitation force,

$$f_e(t) = \int_{-\infty}^{\infty} h_f(t-\tau)\eta(\tau)d\tau, \tag{5.18}$$

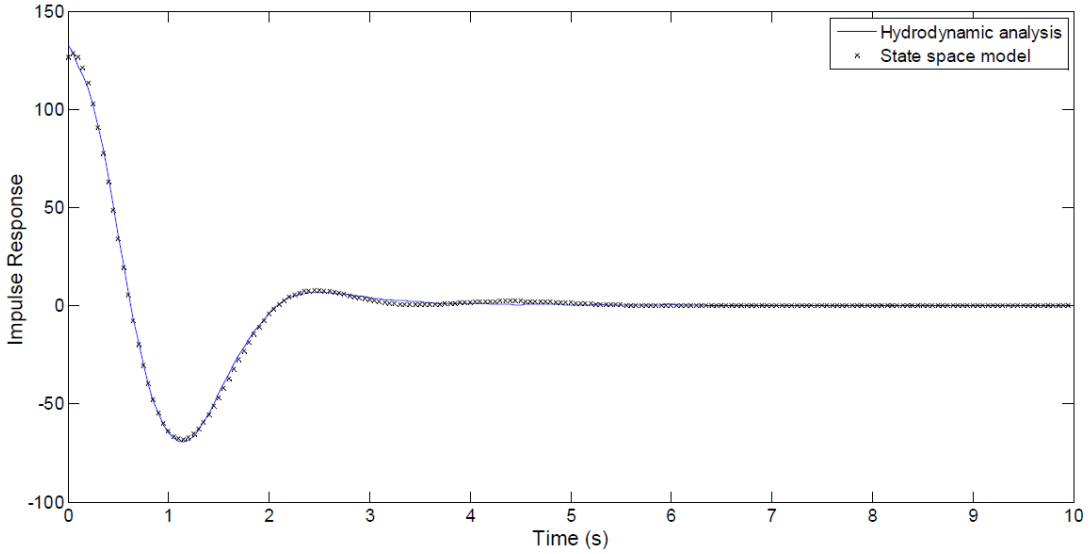


FIGURE 5.2: The radiation impulse response function for a heaving cylindrical buoy (radius 0.5m, draught 1m) as calculated by hydrodynamic analysis and state space modeling

which, like the radiation reaction force, shall also be approximated by a subsystem of differential equations. However this approach is only valid for causal impulse response functions, therefore Yu and Falnes [170] show that if, $h_f(t) = 0$, for $t < -t_c$, where $t_c \geq 0$, then the following 'causalised impulse response function', can be obtained,

$$h_{fc}(t) = h_f(t - t_c). \tag{5.19}$$

A state space model can now be constructed using the same method as for the radiation reaction force, using $h_{fc}(t)$ instead of $h_r(t)$ to obtain the system matrices $\mathbf{A}_{fc}$, $\mathbf{B}_{fc}$ and $\mathbf{C}_{fc}$. A state space model corresponding to the non-casual impulse response function, $h_f(t)$, can now be expressed as;

$$\dot{\mathbf{s}}_{fc}(t) = \mathbf{A}_{fc}\mathbf{s}_{fc}(t) + \mathbf{B}_{fc}\mathbf{u}(t), \tag{5.20}$$

$$f_e(t) = \mathbf{C}_{fc}\mathbf{s}_{fc}(t + t_c), \tag{5.21}$$

where the input, $\mathbf{u}(t)$, is the wave height, $\eta(t)$. Equation 5.21 illustrates the non-causality of the system, with the output at time $t$ being dependent on future values of the input. The excitation force time series output from Equation 5.21 is therefore time shifted by $-t_c$ before being input to Equation 5.17. In their paper Yu and Falnes use a fifth order state space model to approximate the excitation force, hence the same order is applied here. Figure 5.3 shows the excitation force impulse response function and the state space model's approximation to this, where $t_c = 1.6s$.

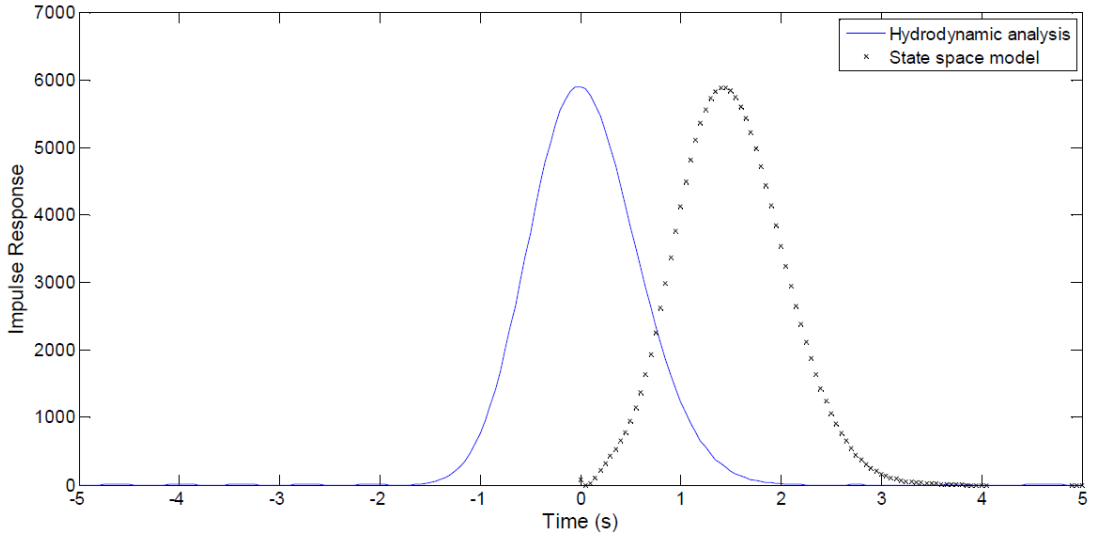


FIGURE 5.3: The excitation impulse response function as obtained from hydrodynamic analysis (solid line) and the state space model's approximation to this using a causalising time shift of $t_c = 1.6s$ (x's)

#### 5.2.2.3 Pitch

The rotation of the buoy about its horizontal axes, are the pitch, $Y_5(i\omega)$, and roll, $Y_4(i\omega)$, modes of motion. For an axisymmetric buoy, the pitch and roll modes are identical, i.e. $Y_4(i\omega) = Y_5(i\omega)$. Therefore, only the pitch mode shall be modelled and analysed here.

The pitch motion is modelled in a similar way to heave, Section 5.2.2, resulting in the following expression for pitch displacement:

$$Y_5(i\omega) = \frac{H_{f5}(i\omega)\eta(i\omega)}{-\omega^2(I + m_{a55}(\omega)) + i\omega N_{55}(\omega) + K_{55}}. \tag{5.22}$$

Equation 5.7 is the pitch equivalent of Equation 5.7, where $I$ is the moment of inertia, $m_{a55}(\omega)$ the pitch added mass, $N_{55}(\omega)$ the pitch radiation resistance, $K_{55}$ the pitch hydrostatic restoring co-efficient and $H_{f5}(i\omega)$ the pitch excitation force co-efficient. The same procedure can be followed as in Section 5.2.2.2 to obtain a state-space description of the pitch motion in the time domain.

#### 5.2.2.4 Coupled heave and pitch

For axisymmetric geometries, the linear coupling between the heave and pitch modes of motion is zero [110]. Therefore in the present analysis for the cylindrical buoy, each mode of motion can be considered independently without any coupling between heave and pitch.

## 5.3 Modelling the inertial permananet magnet linear generator power take-off

In this section, a model for the IPMLG PTO is derived, based on the body of work which exists for similar IPMLG systems. IPMLGs have been used in a variety of applications, such as; vibration energy harvesting for powering remote embedded microsystems and WSNs [171–174], powering body worn sensors from human movement [175], and in WECs [150]. The analysis reported in these sources, model the IPMLG as mass-spring-damper system governed by a second order differential equation [173, 174]. The main idea behind this model is that the conversion of kinetic energy from the oscillating mass to electrical power in the generator, looks like a linear damper to the mass-spring system, which is a fairly accurate model for electro-magnetic generators [173].

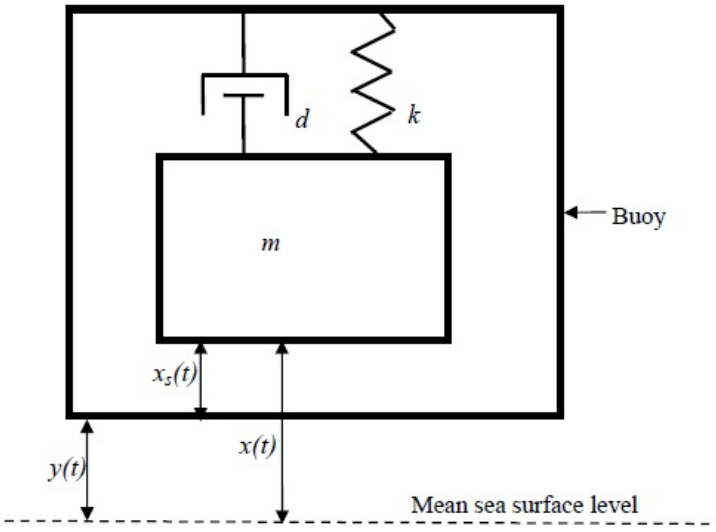


FIGURE 5.4: Schematic of WEC model

The second order differential equation can be derived with consideration of Figure 5.4, which illustrate's the model's representation of the IPMLG. The IPMLG consists of an internal mass, $m$, coupled to an external buoy via a spring, $k$, and a linear damper, $d$. The position of the mass, $x(t)$, and the buoy, $y(t)$ are both measured relative to the mean sea surface level. The relative displacement between the mass and buoy represents the generator's stroke;

$$x_s(t) = x(t) - y(t). \tag{5.23}$$

Likewise the relative velocity between the mass and the buoy represent's the generator's stroke velocity;

$$\dot{x}_s(t) = \dot{x}(t) - \dot{y}(t). \tag{5.24}$$

The mechanics for the mass are derived from Newton's second law of motion;

$$F(t) = m\ddot{x}(t). \tag{5.25}$$

Here two forces act on the mass, namely the spring force (Hooke's law),

$$F_s(t) = -kx_s(t), \tag{5.26}$$

and the damping force,

$$F_d(t) = -d\dot{x}_s(t). \tag{5.27}$$

The dynamics of this system can therefore be represented by the following second order differential equation;

$$m\ddot{x}(t) + d\dot{x}(t) + kx(t) = d\dot{y}(t) + ky(t). \tag{5.28}$$

The damping force can be considered to compose of both the electromagnetic damping from the generator, $d_e$, as well as mechanical damping due to parasitic effects such as friction, $d_m$:

$$d = d_e + d_m. \tag{5.29}$$

The electrical power converted by the generator, is the rate at which the electrical damping force does work, and can therefore be calculated via:

$$P(t) = d_e\dot{x}_s^2(t). \tag{5.30}$$

Equation 5.28 can be represented in the frequency domain as:

$$X(i\omega) = \frac{i\omega d + k}{-m\omega^2 + i\omega d + k}Y(i\omega). \tag{5.31}$$

The generator's stroke, $X_s(i\omega) = X(i\omega) - Y(i\omega)$, can be shown to equal;

$$X_s(i\omega) = \frac{m\omega^2}{(-m\omega^2 + i\omega d + k)}Y(i\omega). \tag{5.32}$$

## 5.4 Full CIPMLG WEC model

Here the hydrodynamic and PTO models are coupled to form one complete model of the WEC system. The motion of a cylindrical buoy due to its hydrodynamic interaction with the surrounding fluid was given by Equation 5.7. For the present case, where the

buoy is acting as a WEC, this description needs to be extended to include the effect that the motion of the internal IPMLG's translator mass has on the buoy's motion.

### 5.4.1 Frequency domain

The generator's translator mass is coupled to the buoy via a spring and damper force. According to Newton's 3$^{\text{rd}}$ Law, the buoy will also experience equal and opposite forces from translator mass due to this coupling. Incorporating the spring force, $F_s(i\omega)$, and damper force, $F_d(i\omega)$, into Equation 5.5 for the motion of the buoy gives:

$$M\ddot{Y}(i\omega) = F_e(i\omega) + Fr(i\omega) + F_h(i\omega) + F_s(i\omega) + F_d(i\omega), \tag{5.33}$$

Substituting the expressions for the relevant forces into this equation gives:

$$M\ddot{Y}(i\omega) = H_f(i\omega)\eta(i\omega) - [N(\omega) + i\omega m_a(\omega)]\dot{Y}(i\omega) - KY(i\omega) - d[\dot{Y}(i\omega) - \dot{X}(i\omega)] - k[Y(i\omega) - X(i\omega)], \tag{5.34}$$

which can be simplified to;

$$Y(i\omega) = \frac{H_f(i\omega)\eta(i\omega) + [i\omega d + k]X(i\omega)}{-\omega^2[M + m_a(\omega)] + i\omega[N(\omega) + d] + K + k}. \tag{5.35}$$

This equation gives the motion response of the buoy in terms of the incident wave height and the position of the generator mass. Substituting in Equation 5.31 for $X(i\omega)$ and performing algebraic rearrangement, gives the motion of the buoy in terms of the input wave height:

$$Y(i\omega) = \frac{H_f(i\omega)\eta(i\omega)}{-\omega^2[M + m_a(\omega)] + i\omega[N(\omega) + d] + K + k - \frac{[i\omega d + k]^2}{-\omega^2 m + i\omega d + k}}. \tag{5.36}$$

The stroke displacement can therefore be shown to equal:

$$X_s(i\omega) = X(i\omega) - Y(i\omega),$$

$$= \frac{\omega^2 m H_f(i\omega)\eta(i\omega)}{\{-\omega^2[M + m_a(\omega)] + i\omega[N(\omega) + d] + K + k - \frac{[i\omega d + k]^2}{-\omega^2 m + i\omega d + k}\}\{-\omega^2 m + i\omega d + k\}}. \tag{5.37}$$

The stroke velocity is given by:

$$\dot{X}_s(i\omega) = i\omega X_s(i\omega),$$

$$= \frac{i\omega^3 m H_f(i\omega)\eta(i\omega)}{\{-\omega^2[M+m_a(\omega)]+i\omega[N(\omega)+d]+K+k-\frac{[i\omega d+k]^2}{-\omega^2 m+i\omega d+k}\}\{-\omega^2 m+i\omega d+k\}}. \tag{5.38}$$

#### 5.4.1.1 Pitch

There is no coupling between the pitch mode of motion and the PTO model. Both the spring and damper forces act along the vertical axis of the buoy, therefore acting through the buoy's centre of mass (CoM) and not applying any torque to the buoy. The CoM is supposed to lie on the buoy's vertical axis under the assumption that the buoy and its mass distribution are axisymmetric (more on the CoM is Section 6.2.2). Thus, the full model for pitch is described by Equation 5.22.

### 5.4.2 Time Domain

Incorporating the spring and damper forces into the time domain model for the motion of the buoy, Equation 5.8, gives;

$$(M+m_\infty)\ddot{y}(t)+\int_{-\infty}^{\infty} h_r(t-\tau)\dot{y}(\tau)d\tau+Ky(t)+d[\dot{y}(t)-\dot{x}(t)]+k[y(t)-x(t)] = f_e(t). \tag{5.39}$$

And

$$m\ddot{x}(t)+d\dot{x}(t)+kx(t) = d\dot{y}(t)+ky(t). \tag{5.40}$$

Here we have two coupled equations governing the motion of the buoy, $y(t)$, and the translator mass, $x(t)$. Thus to analyse the full WEC system these two coupled equations need to be simultaneously solved. This task can be simplified using the state space method.

By introducing $x(t)$ and $\dot{x}(t)$ as additional state variables, to the state space model derived in the previous section, Equations 5.39 and 5.40 can be simultaneously solved. The state vector, $\mathbf{s}_g(t)$, input vector, $\mathbf{u}_g(t)$, state matrix, $\mathbf{A}_g$, and input matrix, $\mathbf{B}_g$, are as follows;

$$\mathbf{s}_g(t) = \begin{bmatrix} s_1(t) & s_2(t) & s_3(t) & s_4(t) & y(t) & \dot{y}(t) & x(t) & \dot{x}(t) \end{bmatrix}^T, \tag{5.41}$$

$$\mathbf{u}_g(t) = f_e(t), \tag{5.42}$$

$$\mathbf{A}_g = \begin{bmatrix} 0 & 0 & 0 & -a_1 & 0 & b_1 & 0 & 0 \\ 1 & 0 & 0 & -a_2 & 0 & b_2 & 0 & 0 \\ 0 & 1 & 0 & -a_3 & 0 & b_3 & 0 & 0 \\ 0 & 0 & 1 & -a_4 & 0 & b_4 & 0 & 0 \\ 0 & 0 & 0 & 0 & 0 & 1 & 0 & 0 \\ 0 & 0 & 0 & -1/\mu & -(\rho g S + k)/\mu & -d/\mu & k/\mu & d/\mu \\ 0 & 0 & 0 & 0 & 0 & 0 & 0 & 1 \\ 0 & 0 & 0 & 0 & k/m & d/m & -k/m & -d/m \end{bmatrix}, \tag{5.43}$$

$$\mathbf{B}_g = \begin{bmatrix} 0 & 0 & 0 & 0 & 0 & 1/\mu & 0 & 0 \end{bmatrix}^T. \tag{5.44}$$

The following output matrix, $\mathbf{C}_g$, will yield an output vector, $\mathbf{v}_g(t)$, consisting of the stroke displacement and velocity;

$$\mathbf{C}_g = \begin{bmatrix} 0 & 0 & 0 & 0 & -1 & 0 & 1 & 0 \\ 0 & 0 & 0 & 0 & 0 & -1 & 0 & 1 \end{bmatrix}, \tag{5.45}$$

$$\mathbf{v}_g(t) = \begin{bmatrix} x_s(t) & \dot{x}_s(t) \end{bmatrix}^T. \tag{5.46}$$

#### 5.4.2.1 Implementation

The model is implemented in Matlab/Simulink, as represented in Figure 5.5. The wave height values are input to the subsystem for calculating the excitation force with the output being returned to Matlab. A routine is then performed to apply the time shift, $t_c$, to the excitation force vector. The time shifted excitation force is then input to the full system state space model which outputs the stroke displacement and velocity of the WECs generator. The state space models are solved using a fixed time step and the ode4 Runge-Kutta solver. The choice of time step is discussed in the next sub-section.

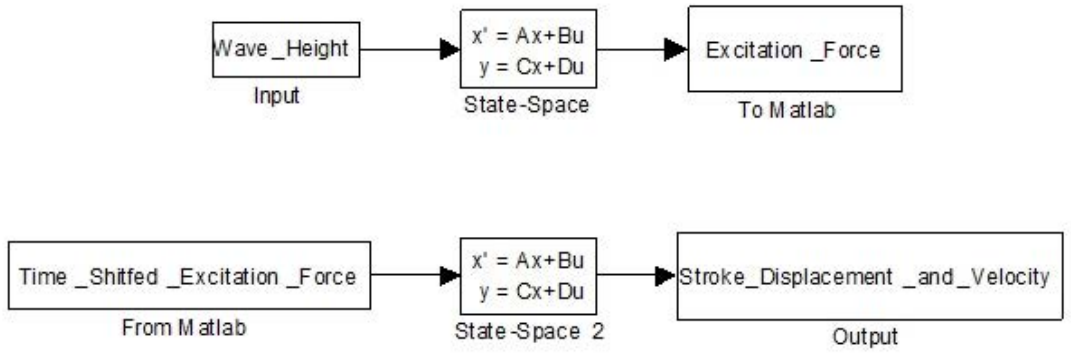


FIGURE 5.5: Representation of model implementation

#### 5.4.2.2 Selecting the time step

A time step must be chosen for the time domain simulations, if the time step is too large then the simulations will be inaccurate, whereas too small of a time step will unnecessarily increase the computation time of the simulation. Here, a parsimonious value for the time step is selected by performing some quick tests on the system. The tests are based on energy balance, whereby the modelled system is given an initial amount of energy, by setting the position and/or the velocity state variables to non-zero value, and no additional energy enters the system because the input wave series is set to zero. The model is then simulated until the system reaches equilibrium and the energy is tracked through the outputs to ensure that it is conserved.

The tests are performed on an arbitrary WEC system whose parameter values are all set equal to 1: diameter of 1m, draught of 1m, generator mass of 1kg, generator damping coefficient of 1Ns/m and spring constant of 1N/m. This leads to the following state space description of the system:

$$\begin{bmatrix} \dot{s_{p1}}(t) \\ \dot{s_{p2}}(t) \\ \dot{s_{p3}}(t) \\ \dot{s_{p4}}(t) \\ \dot{y}(t) \\ \ddot{y}(t) \\ \dot{x}(t) \\ \ddot{x}(t) \end{bmatrix} = \begin{bmatrix} 0 & 0 & 0 & -13,60 & 0 & 0 & 0 & 0 \\ 1 & 0 & 0 & -18.64 & 0 & 480.0 & 0 & 0 \\ 0 & 1 & 0 & -14.66 & 0 & 601.3 & 0 & 0 \\ 0 & 0 & 1 & -4.138 & 0 & 126.7 & 0 & 0 \\ 0 & 0 & 0 & 0 & 0 & 1 & 0 & 0 \\ 0 & 0 & 0 & -0.001 & -7.515 & -0.001 & 0.001 & 0.001 \\ 0 & 0 & 0 & 0 & 0 & 0 & 0 & 1 \\ 0 & 0 & 0 & 0 & 1 & 1 & -1 & -1 \end{bmatrix} \begin{bmatrix} s_{p1}(t) \\ s_{p2}(t) \\ s_{p3}(t) \\ s_{p4}(t) \\ y(t) \\ \dot{y}(t) \\ x(t) \\ \dot{x}(t) \end{bmatrix}. \quad (5.47)$$

**Initial Potential Energy**

In this test, the system will be given an initial amount of energy by displacing the buoy 0.5m from its equilibrium position. This is achieved by setting the initial conditions for the $x(t)$ and $y(t)$ state variables to 0.5. The initial potential energy contained in the system equals the product of the hydrostatic restoring force and the distance over which it works i.e.

$$\text{Energy} = \int_0^{0.5} (\rho g S y) dy = 982.5\text{J}$$

Figure 5.6 displays some results obtained from the state space model. The upper graph shows the position of the buoy starting at 0.5m and then oscillating about its equilibrium position with a decaying amplitude as energy is dissipated from the system. The middle graph shows the oscillation of the generator mass inside the buoy in response to the

buoy's oscillation and the lower graph displays the output power from the generator. Numerically integrating the output power signal gives the total energy absorbed by the generator. The remaining energy must be radiated away by the surface waves created by the buoys oscillation, whose value equals the product of the radiation force with the displacement i.e.,

$$\int_{start}^{finish}(\int_{-\infty}^{t} h_r(t-\tau)\dot{y}(\tau)d\tau).dy = \int_{0}^{200}(\int_{-\infty}^{t} h_r(t-\tau)\dot{y}(\tau)d\tau).\frac{dy}{dt}dt.$$

Note that the *finish* time in the integral of 200s is visually selected as the time when all the energy has been dissipated from the system with the buoy and generator coming to rest. The results of these model simulations and numerical integrations, using varying time increments, are recorded in Table 5.1. Here it can be seen that using a time increment in the model simulations of 0.01 seconds is most economical as it conserved energy with a relative error of 0.0016 with a model run time of 0.2768 seconds.

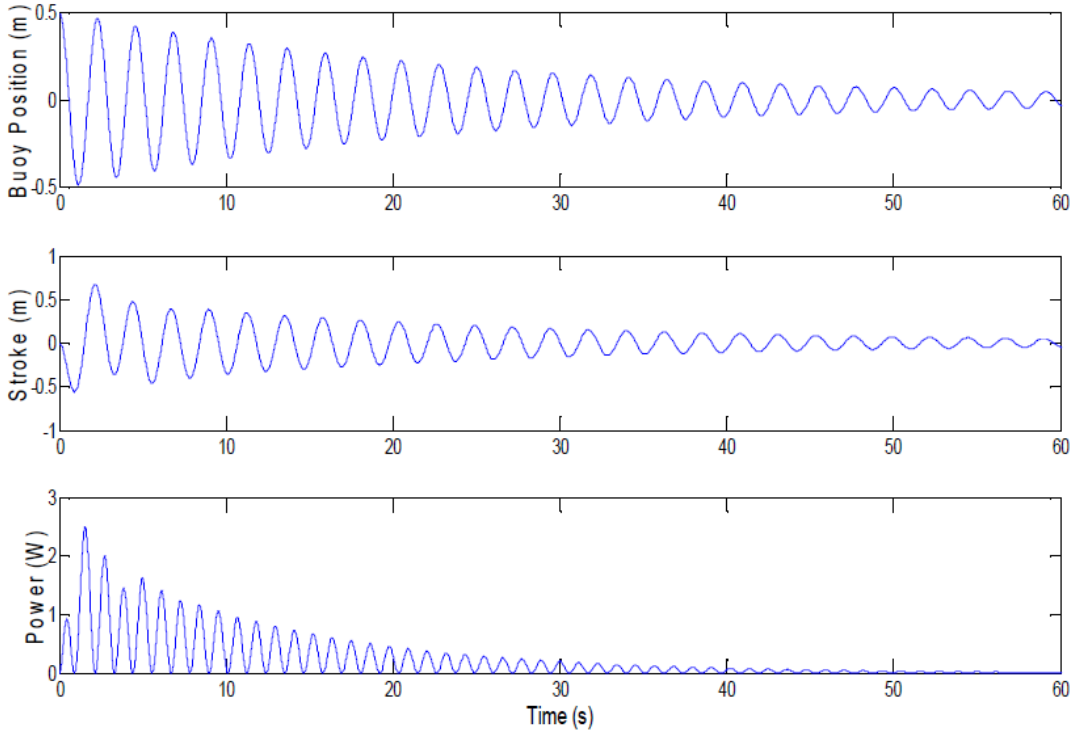


FIGURE 5.6: Model outputs for the Initial Potential Energy test showing the displacement of the buoy (top), the generator stroke (middle) and the generator output power (bottom).

| Simulation time step (s) | 0.1 | 0.01 | 0.001 | 0.0001 |
|---|---|---|---|---|
| Output energy (J) | 923.265 | 980.893 | 980.953 | 980.955 |
| Relative error | 0.0603 | 0.0016 | 0.0016 | 0.0016 |
| Model run time (s) | 0.09319 | 0.2768 | 3.399 | 166.8 |

TABLE 5.1: Output energy calculated from model simulations using varying time increments for a system starting with 982.5J of potential energy

**Initial Kinetic Energy**

This test is similar to the Initial Potential Energy test, in that the system is given an initial amount of energy; the difference in this test being that the energy is in the form of kinetic energy with the buoy given an initial velocity of 1m/s by setting the initial condition of the $\dot{y}(t)$ state variable to 1. This corresponds to an energy value of;

$$\text{K.E.}=\frac{1}{2}mv^2 = \frac{1}{2}(M + m_\infty)\dot{y}^2 = 522.5\text{J}.$$

The results for this test are recorded in Table 5.2. Once again the optimum time step is around 0.01s as this gives a reasonable relative error and model run time.

| Simulation time step (s) | 0.1 | 0.01 | 0.001 | 0.0001 |
|---|---|---|---|---|
| Output energy (J) | 490.483 | 521.628 | 521.658 | 521.658 |
| Relative error | 0.0613 | 0.0017 | 0.0016 | 0.0016 |
| Model run time (s) | 0.09180 | 0.2757 | 3.419 | 166.7 |

TABLE 5.2: Output energy calculated from model simulations using varying time increments for a system starting with 522.5J of kinetic energy

#### 5.4.2.3 Example outputs

Here some example simulation outputs from the time domain model are shown. Figure 5.7-(a) plots an input wave height time series and the resulting calculated motion of the buoy and the translator mass. As can be seen from this figure, the floating buoy follows closely but not exactly the input wave profile, likewise for the translator mass, which is seen to have an amplified motion compared to that of the buoy. The difference between the motion of the buoy and the generator mass is plotted in Figure 5.7-(b), representing the stroke displacement of the generator, $x_s(t)$. The generated power is then plotted in Figure 5.7-(c), showing a spiky output which decreases to zero every time the stroke displacement reaches its turning point. For this reason, the output power produced by the CIMPLG WEC needs to be interfaced with an energy storage device such as a battery, as discussed in Chapters 2 and 3, to provide a stable power output for the MBS.

### 5.4.3 Frequency vs Time Domain

Here results from the time and frequency domain models are compared against each other. The purpose of the comparison is to, firstly to verify that the models have been implemented correctly, secondly to determine how long the time domain simulation needs to be to provide an accurate representation of the average power for a given sea state, and then finally to compare the relative computation times of the two different models. This comparison is achieved via Parseval's theorem which states that the power in either domain equals the power in the other.

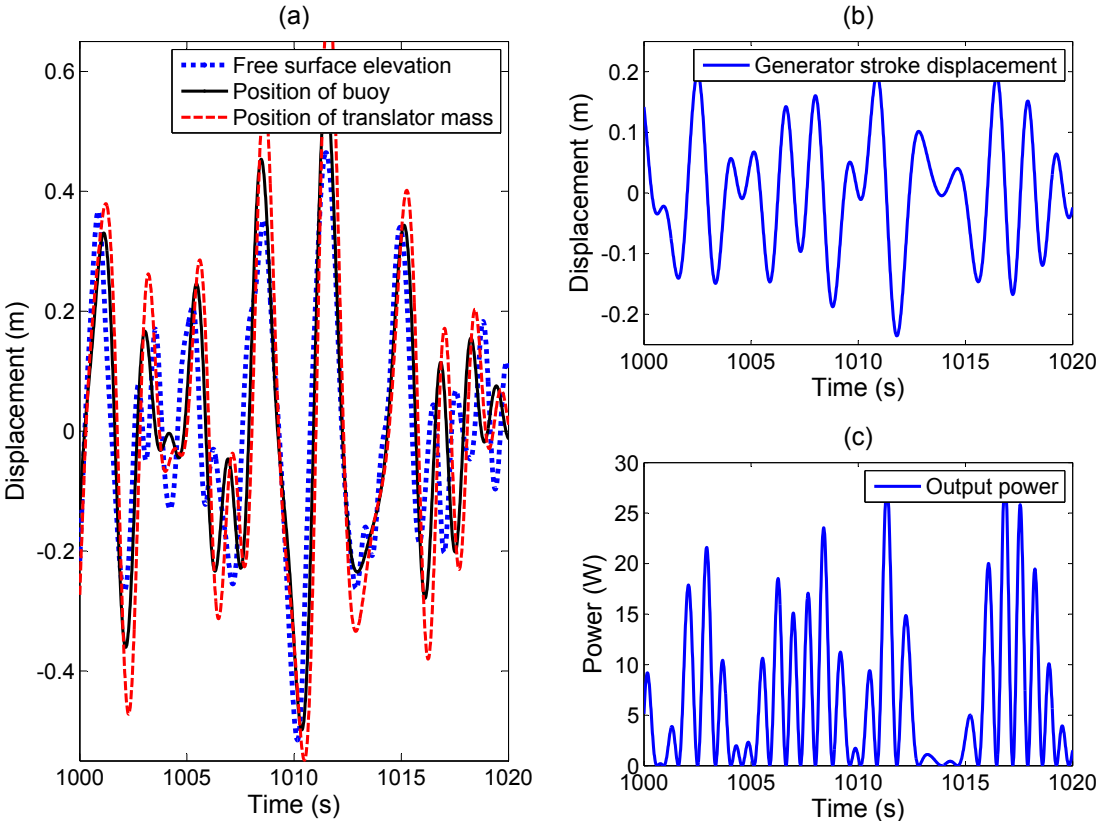


FIGURE 5.7: Example time domain simulation outputs.

Using Fourier analysis the stroke velocity in the time domain can be represented as:

$$\dot{x}_s(t) = \sum_{n=0}^{\infty} a_n sin(\omega_n t + \phi_n). \tag{5.48}$$

If the time and frequency domain models developed here are equivalent then the following should hold:

$$a_n = |\dot{X}_s(i\omega_n)|. \tag{5.49}$$

The average output power in the time domain is:

$$\overline{P(t)} = \frac{d}{T} \int_0^T [\dot{x}_s(t)]^2 dt. \tag{5.50}$$

Using Equation 5.48 and 5.49 it can be shown that Equation 5.50 is equivalent to:

$$\overline{P(t)} = \frac{d}{T} \int_0^T [\dot{x}_s(t)]^2 dt = \frac{d}{2} \sum_{n=0}^{\infty} [\dot{X}_s(i\omega_n)]^2, \tag{5.51}$$

which is an expression of Parseval's theorem.

#### 5.4.3.1 Wave Height Inputs

The input for the frequency domain model is a wave height spectrum derived from a PM spectrum parameterised by the wind speed, Equation 4.14. The PM spectrum is a wave energy spectrum and has dimensions $m^2s$. It can be converted to a wave height spectrum via:

$$Y(\omega_j) = \sqrt{2S(\omega_j)\Delta\omega}. \tag{5.52}$$

The real sea in the time domain is simulated using the same PM Spectrum as used in the frequency domain analysis. The spectrum is discretised into 500 frequencies between 0 and 10 rad/s. If the interval between each frequency is constant then the time series will repeat itself. To avoid this, a method used by Wacher and Neilsen [176] is followed here whereby each frequency is calculated as,

$$\omega_j = \frac{\Delta\omega \cdots rand(1)}{2} + j \cdots \Delta\omega, \tag{5.53}$$

here $\Delta\omega = 0.02, rand(1)$ is a random number between 0 and 1, and $j$=0,...,499. Using a randomly chosen number for each frequency eliminates constant intervals between each frequency. Sinusoidal waves, with amplitudes calculated by Equation 5.52, are then assigned to each of these frequencies and stops the series from repeating itself. The sinusoidal waves are then assigned a random phase and summed together to yield a time series for the irregular sea. Figure 5.8 shows the PM spectrum for an 8 m/s wind speed and its corresponding time series.

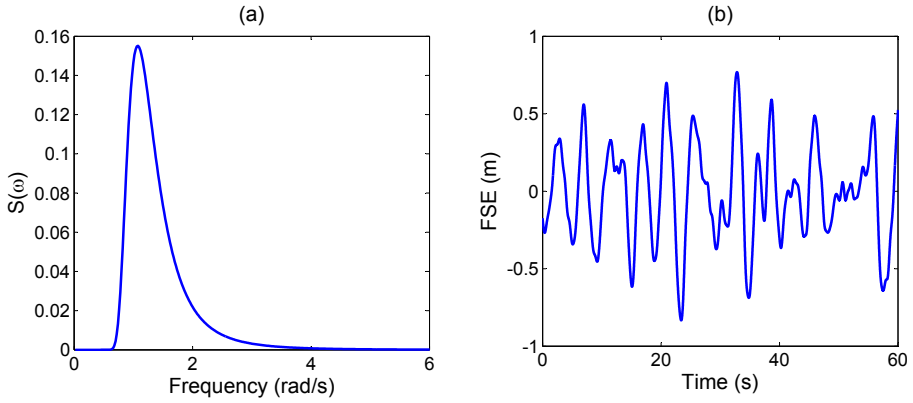


FIGURE 5.8: (a)PM spectrum for 8m/s wind speed and (b) its corresponding simulated time series

#### 5.4.3.2 Simulations and results

Both the time domain and frequency domain models were implemented using the same set of parameters and equivalent wave height inputs (WEC with a 0.2m radius, 0.4m draught, damping value of 10 Ns/m, translator mass of 20kg and spring constant of 185 N/m, and an input sea state of a PM spectrum parameterised by a 6m/s wind speed). The frequency domain model was evaluated for frequencies between 0 and 10 rad/s with a resolution of 0.02 rad/s, requiring 0.012s to compute the average power output value of 37.5W.

The results of the time domain model for various simulation lengths are displayed in Table 5.3. For each simulation length, the time domain model was run five times, and the difference between the calculated output power compared to the frequency domain model result is recorded. The output power calculated from the time domain model is seen to vary between each test, due to the random selection of frequency components and phases for the input wave series, as discussed in Section 5.4.3.1. The output power is seen to converge to the frequency domain result as the simulation length increases, with the difference between the two model's results reducing below 1% for simulation lengths greater than 60 minutes. The relative computation time of the time domain simulation compared to the frequency domain calculation is also quoted in Table 5.3, showing that the time domain model approximately requires 500 - 1000 the computation time to achieve the same average output power accuracy as the frequency domain model.

| **Simulation length (minutes)** | **1** | **2** | **4** | **8** | **16** | **32** | **64** | **128** |
|---|---|---|---|---|---|---|---|---|
| Increased computation time relative to frequency domain model | 21 | 29 | 48 | 86 | 167 | 350 | 792 | 2017 |
| Difference in output power relative to frequency domain model: | | | | | | | | |
| Test 1 (%) | 41 | 42 | 9.2 | 7.7 | 2.7 | 1.7 | 0.95 | 0.20 |
| Test 2 (%) | 44 | 47 | 5.1 | 12 | 2.9 | 1.3 | 0.58 | 0.68 |
| Test 3 (%) | 40 | 42 | 5.7 | 6.2 | 3.1 | 3.2 | 0.52 | 0.35 |
| Test 4 (%) | 36 | 41 | 18 | 0.44 | 3.9 | 1.1 | 0.40 | 0.03 |
| Test 5 (%) | 43 | 31 | 13 | 6.6 | 4.5 | 2.3 | 0.89 | 0.66 |
| Average (%) | 41 | 41 | 10 | 6.6 | 3.4 | 1.9 | 0.67 | 0.38 |

TABLE 5.3: Comparison of the time domain model's computation time and output power results for various simulation lengths, against the frequency domain model's results.

The results in Table 5.3 illustrated the superior speed of calculating the average power in the frequency domain compared to the time domain. Additionally, and perhaps more importantly, is the time and effort required to implement the two different models, with the frequency domain model also being far quicker and easier to implement. Once the hydrodynamic parameters are obtained from the BEM software, they may be used directly

in Equation 5.38 to obtain the stroke velocity, which can then be used in Equation 5.51 to obtain the power. On the other hand, for the time domain model, the hydrodynamic parameters must first be transformed to obtain the impulse response functions, $h_r(t)$ and $h_f(t)$, via an inverse Fourier transform. Next the parameters of both the radiation and excitation force state-space subsystems (Equations 5.10, 5.11, 5.20 and 5.11) must be optimised to satisfy Equation 5.16, representing a non-convex optimisation problem. Once the parameters for the state-space subsystems are calculated, then the time domain model can be simulated, and the average power calculated from Equation 5.51.

## 5.5 Analysis approach

This section details how the numerical model of the CIPMLG WEC, derived in this chapter, shall be used to analyse the CIPMLG WEC's performance and aide in its design. The analysis approach is based on frequency domain analysis, due to the speed of implementation and computation, as discussed in Section 5.4.3.2, and due to the visual insight offered by the graphing the system's transfer functions, to be discussed in this Section.

Section 5.5.1 details the frequency domain calculation of the power and then discusses how comparing the graph of the system's stroke velocity transfer function against the graph of the input wave spectrum, gives a visual aide to the analysis of the system. Section 5.5.2 then details the analysis procedure for the stroke displacement and Section 5.5.3 the pitch motion.

### 5.5.1 Power

Equation 5.51 showed that the average power output of the WEC could be expressed as:

$$\overline{P(t)} = \frac{d}{2}\sum_{n=0}^{\infty}[\dot{X}_s(i\omega_n)]^2. \tag{5.54}$$

The average power output is therefore proportional to the area under the frequency domain curve of the stroke velocity squared.

The stroke velocity can be calculated in the frequency domain, from Equation 5.38, as the product of the input wave spectrum, $\eta(i\omega)$, and a transfer function, $T_{sv}(i\omega)$:

$$\dot{X}_s(i\omega) = T_{sv}(i\omega)\eta(i\omega), \tag{5.55}$$

where, $T_{sv}(i\omega)$ is the stroke velocity transfer function (SVTF);

$$T_{sv}(i\omega) = \frac{i\omega^3 m H_f(i\omega)}{\{-\omega^2[M + m_a(\omega)] + i\omega[N(\omega) + d] + K + k - \frac{[i\omega d+k]^2}{-\omega^2 m+i\omega d+k}\}\{-\omega^2 m + i\omega d + k\}}. \tag{5.56}$$

Equation 5.55 is depicted graphically in Figure 5.9 to show how the frequency domain calculation can offer a visual insight to aide in design. The spectral shape of the transfer function (Figure 5.9-(a)), as determined by the system parameters, should be designed with regard to the shape of the input wave spectrum (Figure 5.9-(b)), to optimise the area under the stroke velocity curve (Figure 5.9-(c)) and therefore the output power, Equation 5.54.

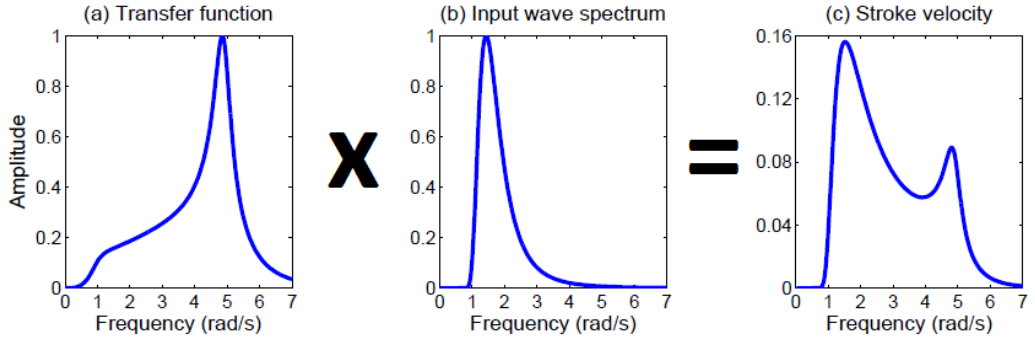


FIGURE 5.9: Depiction of the calculation to obtain the frequency domain stroke velocity.

### 5.5.2 Stroke displacement

The frequency domain model for the stroke displacement, Equation 5.37, can also be expressed in terms of the input wave spectrum and a transfer function:

$$X_s(i\omega) = T_{sd}(i\omega)\eta(i\omega). \tag{5.57}$$

Here, $T_{sd}(i\omega)$ is the stroke displacement transfer function (SDTF):

$$T_{sd}(i\omega) = \frac{\omega^2 m H_f(i\omega)}{\{-\omega^2[M + m_a(\omega)] + i\omega[N(\omega) + d] + K + k - \frac{[i\omega d+k]^2}{-\omega^2 m+i\omega d+k}\}\{-\omega^2 m + i\omega d + k\}}. \tag{5.58}$$

Parsevals theorem can be used to give a measure of the average stroke length via the frequency domain, similar to Equation 5.51 for the average power:

$$\overline{x_s(t)}_{RMS} = \sqrt{\frac{1}{T}\int_0^T x_s^2(t)dt} = \sqrt{\frac{1}{2}\sum_{n=0}^{\infty} X_s^2(i\omega_n)}. \tag{5.59}$$

here, $\overline{x_s(t)}_{RMS}$ is the root mean square (RMS) stroke length.

### 5.5.3 Pitch motion

Similarly, the RMS pitch displacement, $\overline{y_5(t)}_{RMS}$ can be examined in the frequency domain. Minimising the pitch motion of the buoy has been identified as an objective of the thesis, therefore the pitch displacement transfer function (PDTF), should be designed with respect to the input wave spectrum to minimise the area under frequency domain curve of the pitch displacement. From Equation 5.22, the pitch displacement model in the frequency domain is:

$$Y_5(i\omega) = T_{pd}(i\omega)\eta(i\omega), \tag{5.60}$$

where, $T_{pd}(i\omega)$ is the PDTF;

$$T_{pd}(i\omega) = \frac{H_{f5}(i\omega)}{-\omega^2(I + m_{a55}(\omega)) + i\omega N_{55}(\omega) + K_{55}}. \tag{5.61}$$

The RMS pitch displacement, $\overline{y_5(t)}_{RMS}$, can be calculated via:

$$\overline{y_5(t)}_{RMS} = \sqrt{\frac{1}{T}\int_0^T y_5^2(t)dt} = \sqrt{\frac{1}{2}\sum_{n=0}^{\infty} Y_5^2(i\omega_n)}. \tag{5.62}$$

### 5.5.4 Obtaining maximum values from the time domain

The frequency domain analysis only permits the calculation of average values, such as the RMS value. For the stroke displacement and pitch motion, knowledge of the maximum displacement value is also beneficial, but can only be obtained from the time domain. However, implementation and simulation of the time domain models is relatively slow. A faster approach which yields the same results, is to construct a time series directly from the frequency domain curve:

$$x_s(t) = \sum_n X_{sn}\sin(\omega_n t + \phi_n), \tag{5.63}$$

and

$$y_5(t) = \sum_n Y_5\sin(\omega_n t + \phi_n). \tag{5.64}$$

Here $\phi_n$ is a randomly selected phase, which is valid because the phases of the input frequency components are also random. This allows the construction of a time series of length $2\pi/\omega_0$, which then starts repeating itself because the frequency domain components are solved at integer multiples of $\omega_0$. However, a number of different realisations can be easily constructed to increase the length of time domain data if required. From these constructed time series, the maximum vales of the stroke and pitch displacements can be analysed without requiring the effort of constructing the time domain model, and then the computation time of simulating the models.

Calculating the maximum value from this approach was found to agree with calculating the same values by constructing and simulating the time domain models. However the computation time was over 10 times faster, for the $2\pi/0.02$ second length signal. Additionally, this approach could be implemented with a few additional lines of code to the frequency domain model, rather than the tedious procedure, involving nonconvex optimisation, required to implement the time domain models.

## 5.6 Summary

The initial analysis and assessment of the proposed CIPMLG WEC is performed numerically, allowing many design configurations to be tested and optimised more easily and cheaply compared to performing the same task experimentally. The numerical model for the CIPMLG WEC was derived in this chapter, which calculates the following key output parameters; the generated power, stroke displacement and pitch motion. The derived numerical model is linear, based on established linear hydrodynamic and PTO models commonly found in the literature. Linear models are selected for the present initial design analysis because they allow frequency domain analysis and are computationally fast, permitting assessment of many designs in the broad parameter space. Once optimal designs are identified from the linear models, high fidelity nonlinear models can be used for further refinement.

# Chapter 6

# Preliminary Analysis of the CIPMLG Wave Energy Converter

## 6.1 Introduction

In this chapter, the model developed in Chapter 5 will be used to analyse the CIPMLG WEC. The analysis aims to gain insight into how the CIPMLG WEC's different parameters affect its performance. Section 6.2 identifies the parameters which influence the CIPMLG WEC's performance and whose values we have free design choice over.

The analysis approach, detailed in Section 5.5, considers the CIPMLG WEC as a system which transforms a given input to a specific output. Here, the input are the ocean waves, described by the FSE frequency domain amplitude spectrum, and the outputs are the generator's stroke displacement and velocity and the buoy's pitch displacement. The transformation from the input to these different outputs is described the system's relevant transfer function, the SDTF, SVTF and PDTF respectively. This chapter analyses the WEC system by investigating the effect that the various design parameters, identified in Section 6.2, have on the stroke velocity, stroke displacement and pitch displacement transfer functions, in Sections 6.3, 6.4 and 6.5, respectively.

## 6.2 Design parameters

There are a number of design parameters which influence WEC's performance, namely:

- The bouy's geometry

- The buoy's mass distribution
- The mass of the translator
- The spring constant of the generator,
- The damping co-efficient of the generator, and
- The stroke limit of the generator.

Other parameters can be derived from these design parameters, such as the mass of the buoy, $M$, the centre of mass (CoM), the moment of inertia, $I$, the hydrodynamic parameters, $H_f(i\omega)$, $N(\omega)$ and $m_a(\omega)$, the natural frequency of the buoy, $\omega_{nb}$, and the natural frequency of the generator, $\omega_{ng}$.

### 6.2.1 Mass of the buoy

The total mass of the WEC equals the weight of the fluid it displaces at its equilibrium position and is therefore dependent on the buoy's geometry. For a WEC whose geometry is a vertical cylinder, the total mass is linearly proportional to the buoys draught and to the square of its radius:

$$M_{Total} = \rho_w D \pi R^2. \tag{6.1}$$

Figure 6.1 plots the mass of a cylindrical WEC for varying buoy radius and draught. This mass equals the entirety of the WEC system, including the buoy's mass, $M$, and the generators translator mass, $m$:

$$M_{Total} = M + m. \tag{6.2}$$

The buoy's mass will consist of its shell, the sensor node equipment/antenna etc, the generator coils, battery and any ballast mass. The generator's translator mass is therefore constrained by the total WEC mass and the buoy's mass.

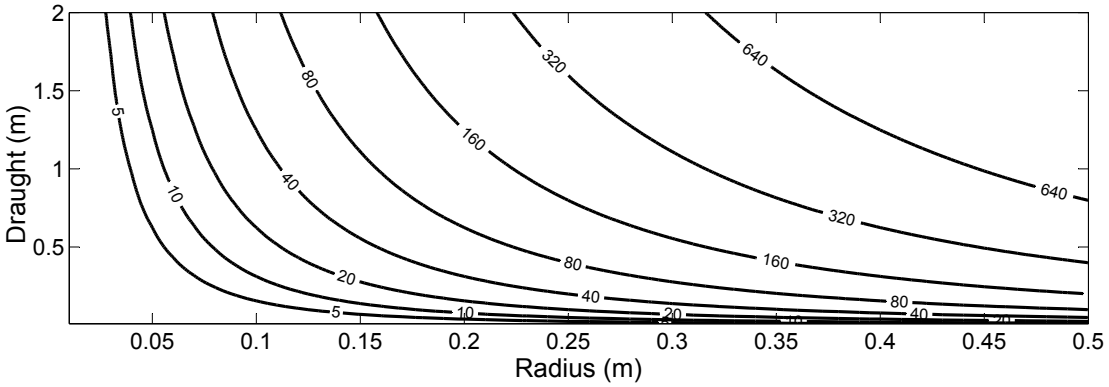


FIGURE 6.1: Mass (kg) of a cylindrical WEC for varying buoy radius and draught.

### 6.2.2 Center of mass

The CoM is determined by the buoy's mass distribution and is a relevant parameter for analysing the WEC's pitch motion. It is not possible to calculate the exact position of the CoM until the complete design of the buoy, including the location of all its components and their masses, is known. However, the converse approach may be taken, whereby the effect of various CoM values can be analysed and a wise location for the CoM chosen from this analysis. The buoy's mass distribution can then be subsequently designed to obtain a favourable CoM value selected from this analysis.

### 6.2.3 Moment of intertia

The moment of inertia (MoI) is a relevant parameter for analysing the WEC's pitch motion and is determined by the distribution of mass around the buoy's CoM. Like the CoM, it is not possible to calculate the exact MoI value until the complete design of the buoy, including the location of all its components and their masses, is known. For a distribution of $N$ masses, $m_i, i = 1, ..., n$, located a distance $r_i$ from the CoM, the MoI is given by:

$$I = \sum_{i=1}^{N} m_i r_i^2. \tag{6.3}$$

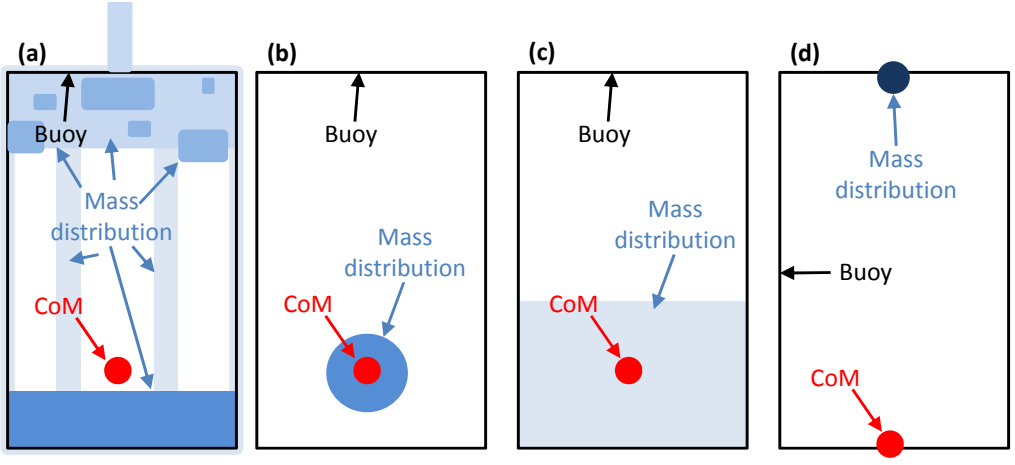


FIGURE 6.2: Schematic of the WEC's mass distribution, represented by the blue areas where the shade of blue gives an indication of the relative mass density. The CoM is represented by the red dot. (a) represents a possible realistic configuration, (b) represents a lower bound where all the mass is located around in the CoM in a dense sphere, (c) represents where the mass is uniformly distributed around the CoM, and (d) represents an extreme upper bound with the unrealistic case where the mass is distributed in a point the length of the draught from the CoM.

Figure 6.2-(a) illustrates what the mass distribution of the CIPMLG WEC might look like, where the different shades of blue represent different mass densities (the darker the blue the more dense the mass). The red dot then represents the CoM. Equipped with this information, the MoI could then be calculated from Equation 6.3. However, this information will not be available for the preliminary analysis in this thesis. Therefore, like the CoM value in Section 6.2.2, the effect of various MoI values will be analysed, to determine the MoI's effect on the WEC's performance and to inform a wise choice for the WEC's mass distribution.

The range of MoI values to be considered in the subsequent analyses in this thesis are estimated from the mass distributions illustrated in Figures 6.2-(b), (c) and (d). Figure 6.2-(b) depicts the lower bound of MoI values to be considered, whereby the entire WEC mass is located in a dense sphere around the CoM (the analysis will assume a steel ball of density 7600kgm$^{-3}$), which represents the smallest possible MoI value for a given WEC mass. Figure 6.2-(d) illustrates the largest MoI values to be considered, whereby the entire WEC mass is located in a point, the length of the buoy's draught away from the CoM. Clearly, the case depicted in Figure 6.2-(d) is not realistic, but definitely sets an upper bound which the the MoI value can not possibly exceed. Figure 6.2-(c) then depicts a more realistic case between the two extremes in Figures 6.2-(b) and (d), whereby the mass is uniformly distributed from the CoM to the buoy's radius and symmetrically above and below the CoM.

### 6.2.4 Hydrodynamic coefficients

The hydrodynamic coefficients depend on the geometry of the buoy's wetted body. This section investigates the effect that the changing the radius and the draught of the vertical cylinder has on these hydrodynamic coefficients.

#### 6.2.4.1 Heave

Figure 6.3 shows the effect that varying the cylinder's radius has on the heave mode's hydrodynamic coefficients, and Figure 6.4 shows the effect of varying the cylinder's draught. These figures were produced using the BEM software outlined in Section 6.2.4 by calculating the hydrodynamic coefficients for numerous buoys of various radii and draughts at frequencies from 0.02-8 rad/s at 0.02 frequency intervals. The excitation force co-efficient is shown in the top graph of these figures, and its value represents the excitation force experienced by the buoy if subjected to a wave with unit amplitude for the given frequency. At low frequencies its value increases with the radius but displays little dependence on the draught. Considering the limiting case of zero frequency, which

corresponds to a constant increase in water level of 1m, the excitation force simply equals the buoyancy force due to the increase in water height, $\rho_w g \pi R^2$. As the frequency increases and the input wave oscillates faster, it begins to impart less force onto the buoy. The deeper the draught the more rapidly the excitation force amplitude decreases with frequency, with the excitation force at high frequencies for buoys with a small draught being much larger than their deeper draught counterparts.

The radiation resistance coefficients are plotted in the middle graph of Figures 6.3 and 6.4, and their values represent the force experienced by the buoy due to the radiated wave it creates when it is oscillating with unit velocity at the given frequency. Here it can be seen that the larger the buoy's radius the greater the force, with the inverse of this being true for the buoy's draught. At the zero and infinite frequency limits the function equals zero with a peak value occurring at a frequency in between. The peak frequency appears to be mostly dependent on the buoy's draught, with little change in the location of the peak occurring for varying radius.

The added mass coefficient is plotted in the bottom graph of Figures 6.3 and 6.4, and its value represents the mass of fluid that the buoy must also move when oscillating in that fluid. Increasing the buoys radius increases the added masss value, whereas increasing the buoys draught is seen to decrease the function's variation with frequency.

The hydrostatic restoring force coefficient for the heave mode, was shown in Equation 5.4 to be proportional to the water plane area of the buoy, and therefore increases with the square of the buoy's radius, whereas the draught has no effect on its value.

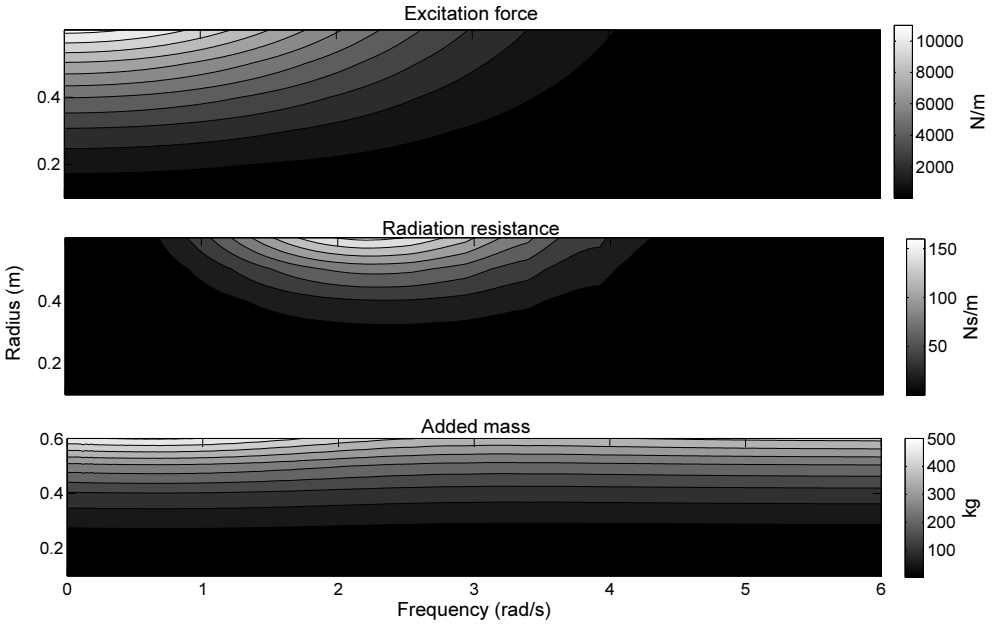


FIGURE 6.3: The heave mode hydrodynamic coefficients as a function of frequency for a cylindrical buoy with 1m draught and varying radius.

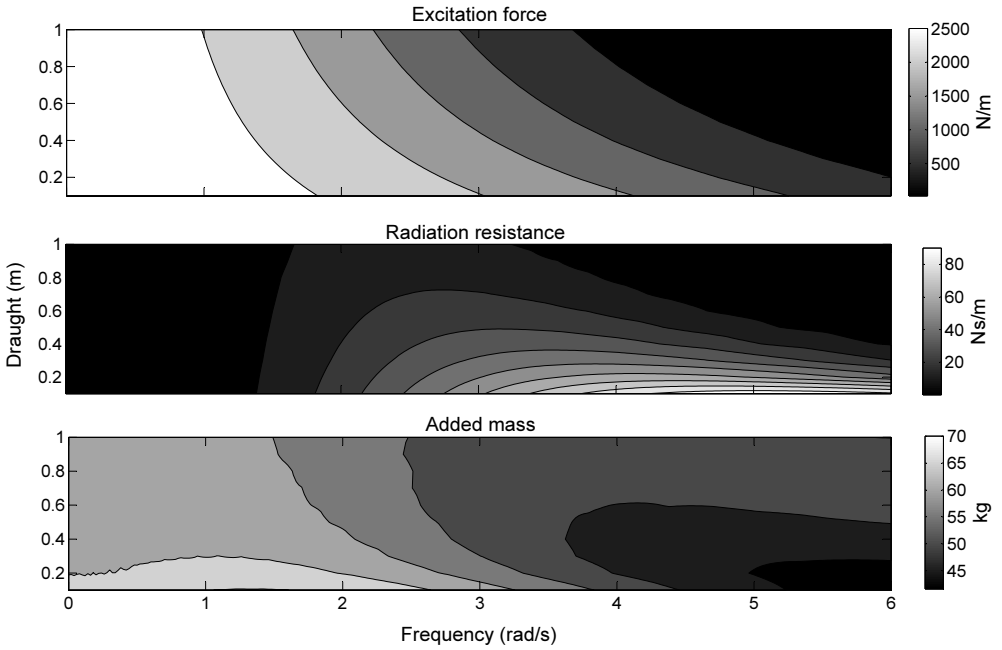


FIGURE 6.4: The heave mode hydrodynamic coefficients as a function of frequency for a cylindrical buoy with 0.3m radius and varying draught.

#### 6.2.4.2 Pitch

The hydrodynamic coefficients for the pitch mode of motion, depend on the position of the buoy's CoM, as well as its radius and draught. The buoy rotates around its CoM, and therefore pitches differently for different CoM locations, outlining the reason why the hydrodynamic coefficients depend on the CoM position.

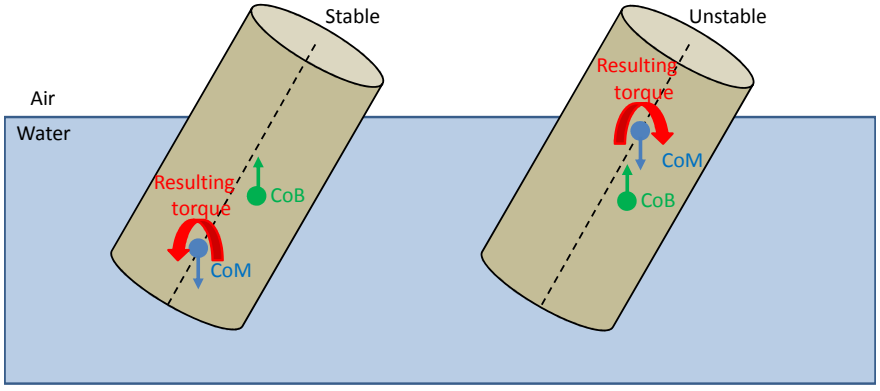


FIGURE 6.5: Illustration of a stable buoy (left) with its centre of buoyancy (CoB) above its centre of mass (CoM) thus experiencing a restoring torque and an unstable buoy (right) whose CoB is below its CoM thus experiencing a torque which acts to further tilt the buoy

The location of the CoM is most important for the hydrostatic restoring torque coefficient, because unlike the heave mode of motion, which always has a positive restoring

force coefficient, the pitch restoring torque can have a negative value, resulting in an unstable system. For the buoy to be stable in the water, it should experience a restoring torque when tilting away from the vertical, as depicted in Figure 6.5. This concept is well known in the design of sea craft and may be theoretically expressed as; a vessel will be vertically stable if its centre of buoyancy (CoB) is above its CoM. When the cylindrical geometries considered are at rest, the CoB is located on their central axis at a depth 50% of the draught. However, when the cylinder pitches, the CoB moves from this position, as depicted in Figure 6.5. Therefore, the CoM can be located at a vertical depth less than 50% and still experience a restoring torque, as shown in Figure 6.6 which plots the pitch restoring force coefficient as a function of the vertical CoM position for three different buoy radii. Figure 6.6 shows that for the buoys with larger radii the restoring force remains positive until the CoM is located at about 45% of the bouy's draught, and that these buoys with a larger radii experience a stronger restoring torque.

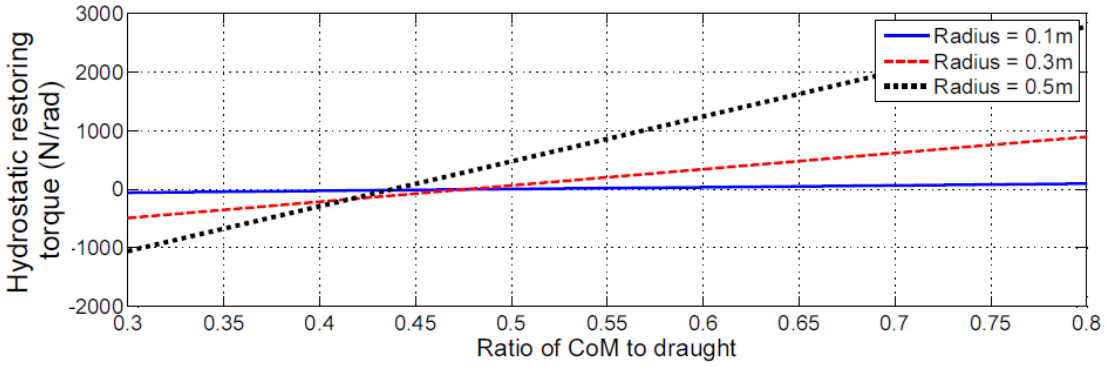


FIGURE 6.6: The hydrostatic restoring force coefficient for a buoy with 1m draught as a function of the center of mass location along its central axis.

The excitation force, radiation resistance and added mass coefficients for the pitch mode of motion are plotted in Figures 6.7 - 6.9, which show the effect of varying radius, draught and CoM, respectively. The excitation force is shown in the top graph of these figures. The excitation force can be seen to equal zero for the case of zero frequency, owing to its axisymmetric geometry, and has a peak at a frequency between zero and infinity. The magnitude of the excitation force is seen to increase with radius, draught and CoM depth.

The radiation resistance is shown in the middle graph of Figures 6.7 - 6.9. The value of the radiation restistance is seen to increase with increasing radius, draught and depth of CoM, and also has a peak at a frequency between zero and infinity. The added mass is shown in the bottom graph and its value also increases with increasing radius, draught and depth of CoM.

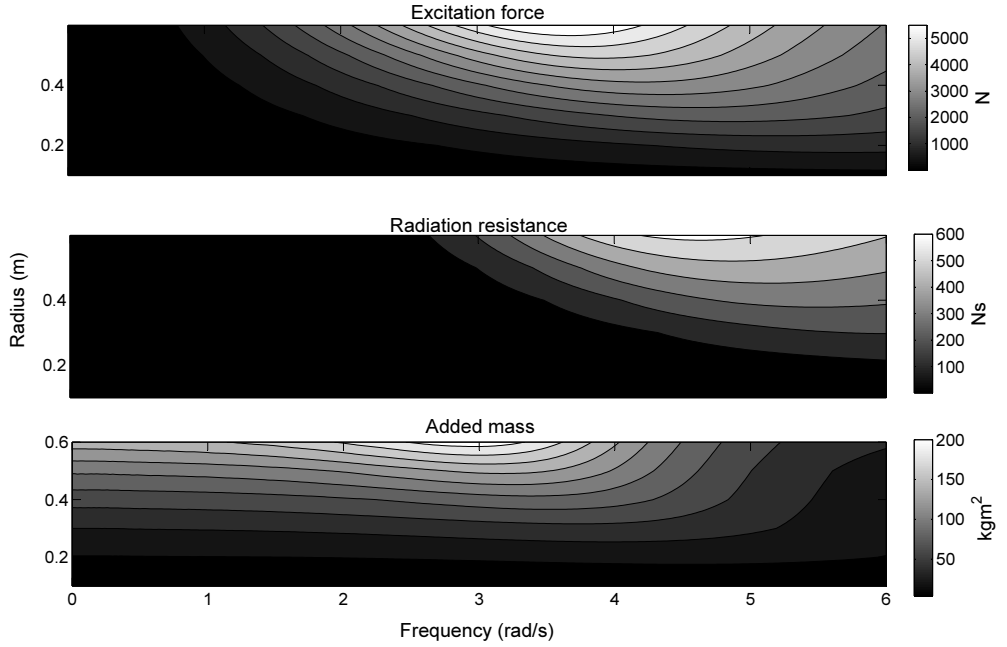


FIGURE 6.7: The pitch mode hydrodynamic coefficients as a function of frequency for a cylindrical buoy with 1m draught and varying radius, with a centre of mass 0.8m below the surface on its central axis.

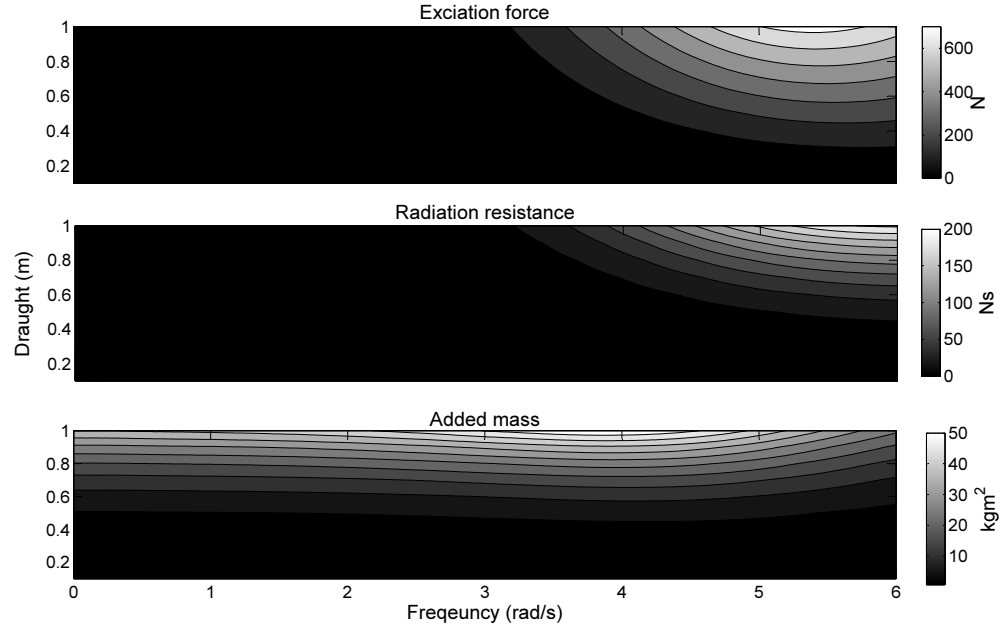


FIGURE 6.8: The pitch mode hydrodynamic coefficients as a function of frequency for a cylindrical buoy with 0.3m radius and varying draught, with a centre of 80% the depth of the draught on its central axis.

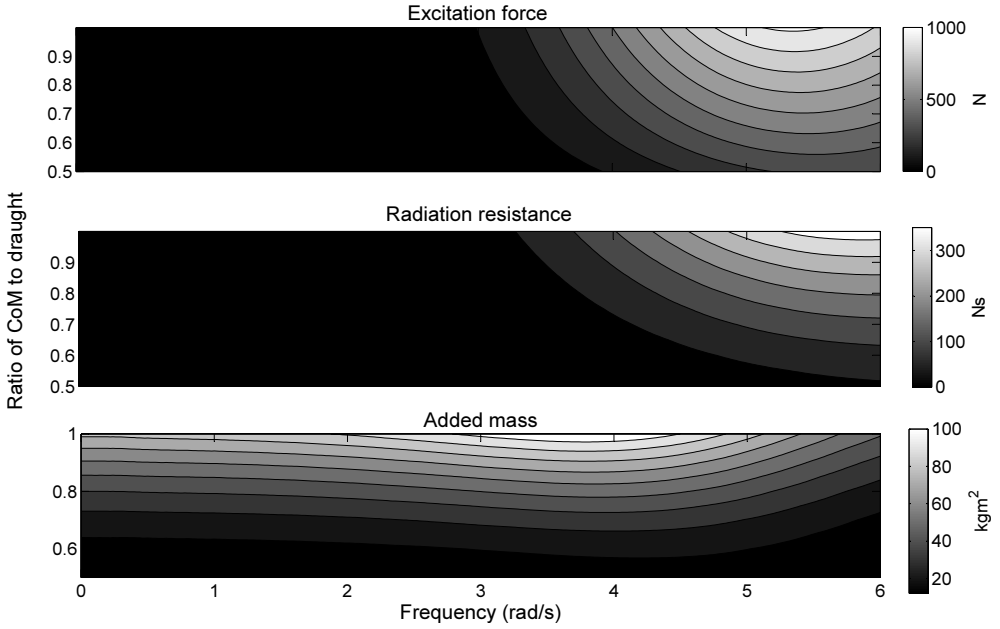


FIGURE 6.9: The pitch mode hydrodynamic coefficients as a function of frequency for a cylindrical buoy with 0.3m radius and 1m draught, with a varying centre of mass location along its central axis.

### 6.2.5 Hydrodynamic natural frequency

The hydrodynamic natural frequency of a floating object corresponds to the input wave frequency which results in the largest motion response from the object. The motion of the cylindrical buoy, without an internal generator ($m = k = d = 0$), in response to an input wave spectrum was given by Equation 5.7:

$$Y(i\omega) = \frac{H_f(i\omega)\eta(i\omega)}{-\omega^2(M+m_a(\omega))+i\omega N(\omega)+K}.$$

The denominator in this expression represents the impedance and is minimised when:

$$\omega = \omega_{nb} = \sqrt{\frac{K}{M + m_a(\omega)}}, \tag{6.4}$$

which is the hydrodynamic natural frequency. The velocity at the natural frequency therefore equals:

$$\begin{aligned} \dot{Y}(i\omega) &= \frac{i\omega H_f(i\omega)\eta(i\omega)}{i\omega N(\omega)}, \\ &= \frac{F_e(i\omega)}{N(\omega)}, \end{aligned}$$

which is the resonance condition, that the velocity is always in phase with the excitation force at this frequency. At all other frequencies than the resonant frequency, the excitation force will act in the opposite direction to the velocity during part of the buoy's

oscillation, therefore reducing its amplitude. Whereas at the resonant frequency the excitation force always acts in the same direction as the buoy's velocity.

Figure 6.10 is a plot of the heave velocity amplitude response as a function of frequency, for a cylinder with a 0.5m radius and three different draught values of 0.5, 1 and 2m. The hydrodynamic natural frequency corresponds to the peak of these response curves, illustrating the large increase in velocity due to input waves at this frequency compared to other wave frequencies. The natural frequency is seen to decrease with increasing draught, due to the mass of the buoy increasing while its restoring force coefficient remains the same (see Equation 6.4). Figure 6.11 then plots the natural frequency (rad/s) as a function of the cylinder's radius and draught, showing that the hydrodynamic natural frequency has little dependence on the radius but decreases in value for increasing draught. Figure 6.11 also shows that smaller buoys have a higher natural frequency and that very large buoys are required for resonance with low frequency input waves.

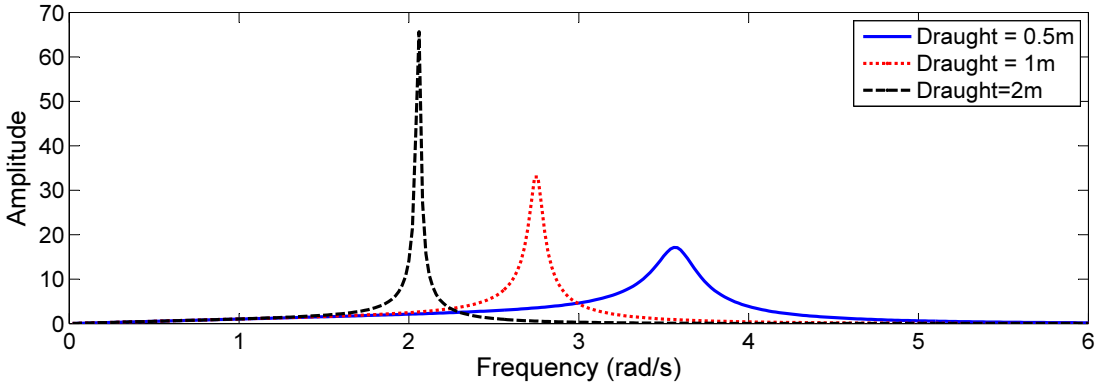


FIGURE 6.10: Heave velocity amplitude response as a function of frequency for a cylinder with 0.5m radius.

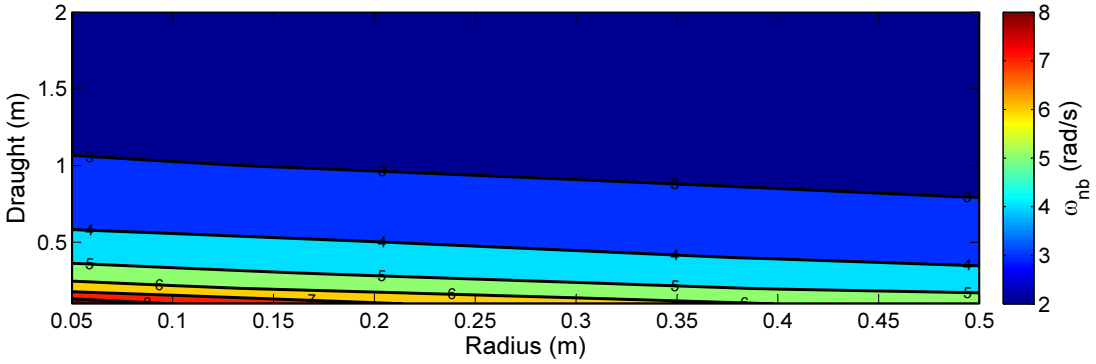


FIGURE 6.11: Hydrodynamic natural frequency of a heaving vertical cylinder as a function of draught and radius.

Similarly, the hydrodynamic natural frequency for the pitch mode of motion is given by:

$$\omega = \omega_{np} = \sqrt{\frac{K_{55}}{I + m_{a55}(\omega)}}. \tag{6.5}$$

### 6.2.6 Generator Natural Frequency

Analogous to the hydrodynamic natural frequency, is the generator natural frequency. Inspection of Equation 5.32, for the motion of the translator mass, shows that the impedance (denominator) is minimised when:

$$\omega = \omega_{ng} = \sqrt{\frac{k}{m}}, \tag{6.6}$$

which is the natural frequency of the generator.

### 6.2.7 Mechanical damping

Mechanical damping represents unwanted dissipation of energy from the system. Therefore in an ideal system the mechanical damping would be zero. The practical design and physical implementation of the CIPMLG WEC should aim to minimise and eliminate any mechanical damping. For example, Cheung and Childress [150], use a ferrofluid lubricant in their IPMLG, which they claim results in a near frictionless generator.

A value for the mechanical damping can not be determined numerically, only measured experimentally after the system is constructed. The present analysis will therefore assume a mechanical damping of zero, i.e. $d = d_e$, and will then evaluate and discuss the consequences of larger mechanical damping values on the system.

## 6.3 The Stroke Velocity Transfer Function

The stroke velocity is a key system output, having a large effect on the power produced by the WEC. Equations 5.54 and 5.55 showed that the output power is proportional to the stroke velocity squared, and that the SVTF determines the system's stroke velocity in response to a given input wave spectrum. This section investigates the effect of the design parameters on the SVTF.

The SVTF is a function of frequency and is not a simple expression, as shown by Equation 5.56. The SVTF is dependent on many parameters and it made particularly complicated by the fact that itself contains functions of frequency, in the form of the

hydrodynamic coefficients, which were shown in Section 6.2.4 to vary with the buoy's radius and draught parameters. Analysing the effect that the design parameters have on the SVTF is a challenge, because changing the value of any of the design parameters influences the effect that the other design parameters have on the SVTF. However, through investigation of the inter-relation between these parameters and the SVTF, Figures 6.13-6.14 have been obtained, to describe these effects.

Figure 6.13 shows multiple plots of the SVTF, with the frequency axis normalised to the buoy's hydrodynamic natural frequency, $\omega_{nb}$, for a cylindrical buoy with radius 0.2m, draught 0.5m and with a translator mass 50% the total mass. The figure contains four graphs, whereby the generator damping is increased by a factor of 10 between each graph, from 1 to 1000 Ns/m, and each graph contains three plots of the SVTF, whereby the generator natural frequency, $\omega_{ng}$, is doubled between each plot, from half to double the buoy natural frequency, $\omega_{nb}$. The plots show that, for a lightly damped generator the SVTF has two peaks, one either side of the buoy natural frequency, and that the lower the value of $\omega_{ng}$ the lower the frequency of the peaks. However, when the value of the damping increases, the SVTF converges to a single dominant peak at $\omega_{nb}$, with the convergence occurring earliest for the systems with the higher $\omega_{ng}$. Figure 6.13 also shows that the magnitude of the SVTF decreases as the generator damping increases.

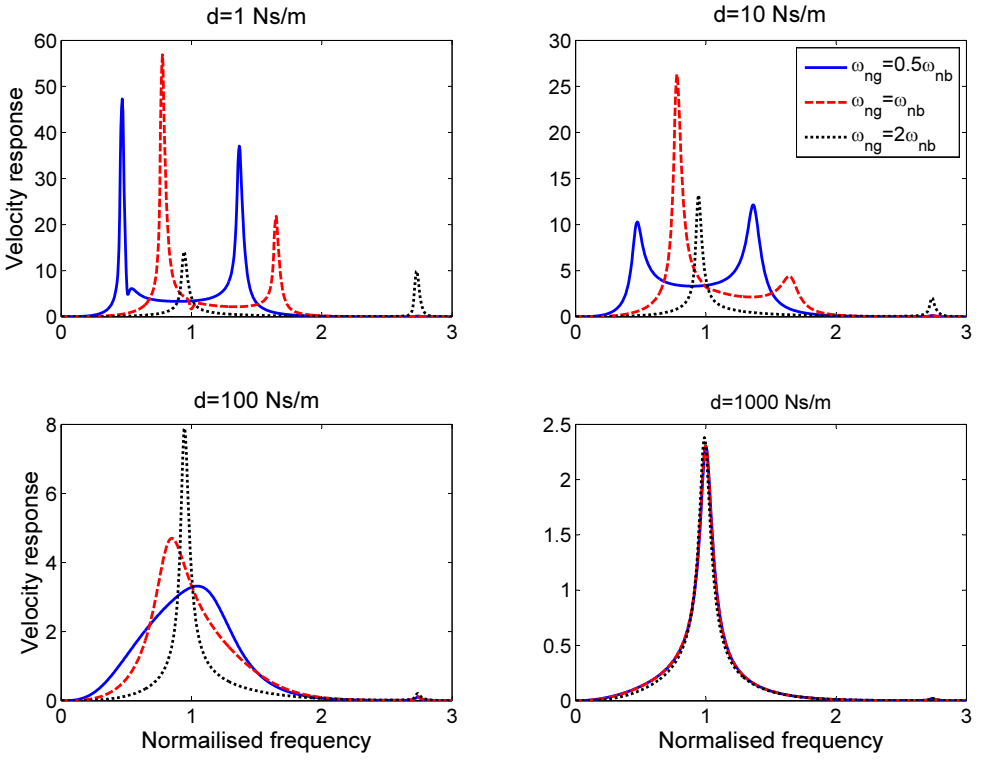


FIGURE 6.12: The stroke velocity transfer function with the frequency normalised to the hydrodynamic natural frequency, for a cylindrical buoy with radius 0.2m and draught 0.5m, with translator mass 50% the total mass and varying generator natural frequency and generator damping.

To investigate the translator mass's effect on the SVTF, and to further investigate the generator damping's effect, Figures 6.13 and 6.14, plot the SVTF for the same buoy as in Figure 6.12, except with the translator mass varying between graphs and the generator damping having a value of 10Ns/m and 100 Ns/m, respectively. From these graphs it can be seen that whether the SVTF has two peaks or the single dominant peak depends on the ratio of the translator mass to the generator damping, whereby large translator masses and small generator damping values lead to a SVTF with a double peak, and small translator masses and large generator damping values lead to a SVTF with a single dominant peak at $\omega_{nb}$.

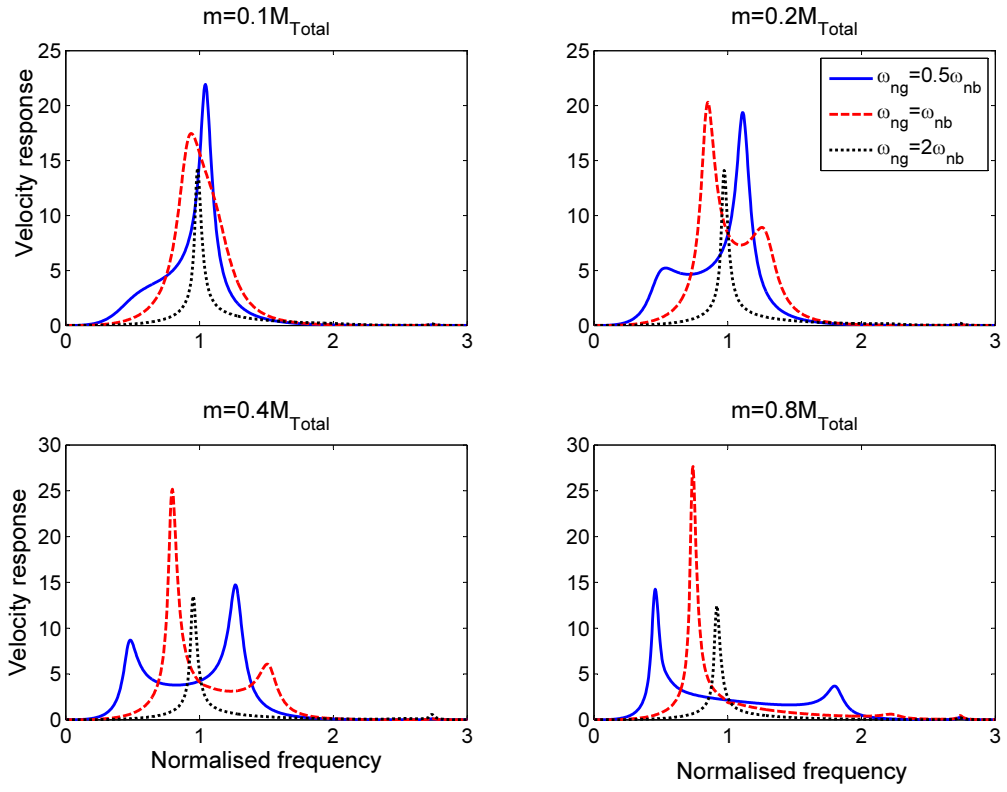


FIGURE 6.13: The stroke velocity transfer function with the frequency normalised to the hydrodynamic natural frequency, for a cylindrical buoy with radius 0.2m and draught 0.5m, with generator damping of 10 Ns/m and varying generator natural frequency and translator mass

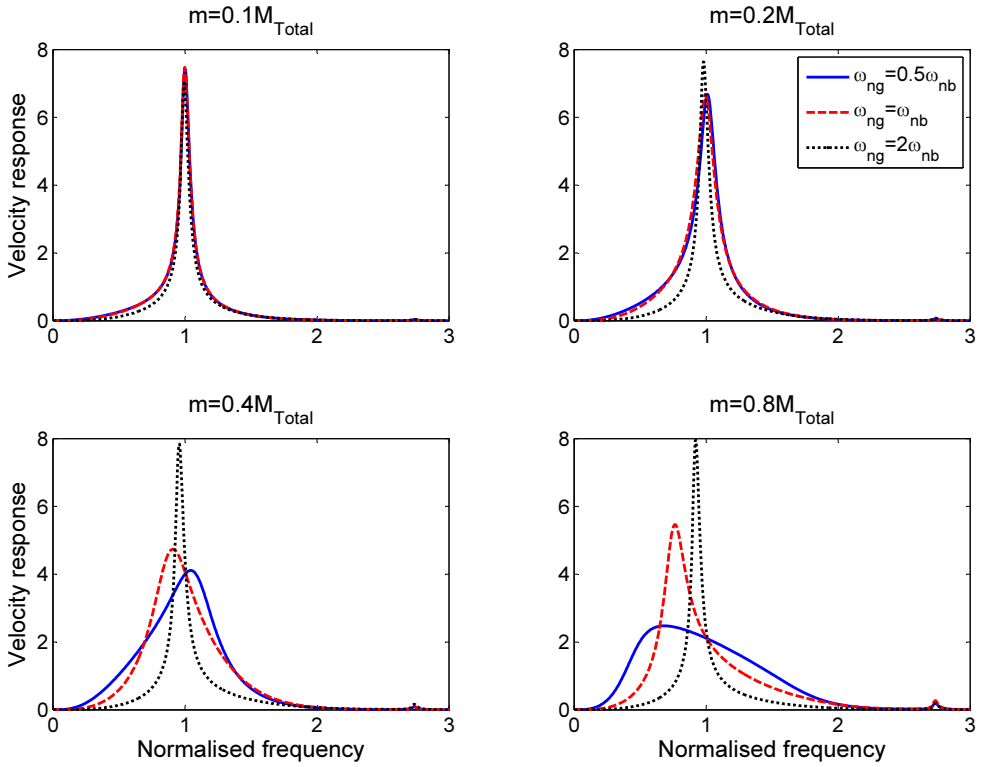


FIGURE 6.14: The stroke velocity transfer function with the frequency normalised to the hydrodynamic natural frequency for a cylindrical buoy with radius 0.2m and draught 0.5m, with generator damping of 100 Ns/m and varying generator natural frequency and translator mass

It is worth noting here that Cheung and Childress [150] noticed the same doubled peaked frequency domain response for lightly damped generators and single peaked response for heavily damped generators on their output power measurements in their experiments. Although no quantitative results were presented, Cheung and Childress illustrated their findings in the diagram shown in Figure 6.15, whereby increasing the resistive load has the effect of reducing the generator damping (as discussed in Appendix A). The numerical analysis performed in this chapter gives an explanation for their findings and offers guidance in designing the location of the spectral peaks in terms of the design parameter values.

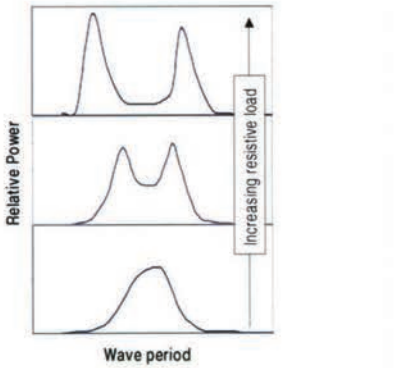


FIGURE 6.15: Illustration of the qualitative differences in spectral response, for power output versus wave period for different loads reported by Cheung and Childress [150].

### 6.3.1 The effect of the SVTF in the time domain

The time domain consequences of the single and double peaked SVTFs, shown in Figures 6.13 - 6.14, are plotted here in Figure 6.16. This figure shows the input FSE time series and the position of the buoy and translator mass calculated by time domain model. The case of the double peaked SVTF is plotted in Figure 6.16 - (a), showing that the buoy and translate mass oscillate at different amplitudes and frequencies. Whereas, for the case of the single peaked SVTF, plotted in Figure 6.16 - (b), both the buoy and the translator mass oscillate in phase with each other at the same frequencies, although with different amplitudes.

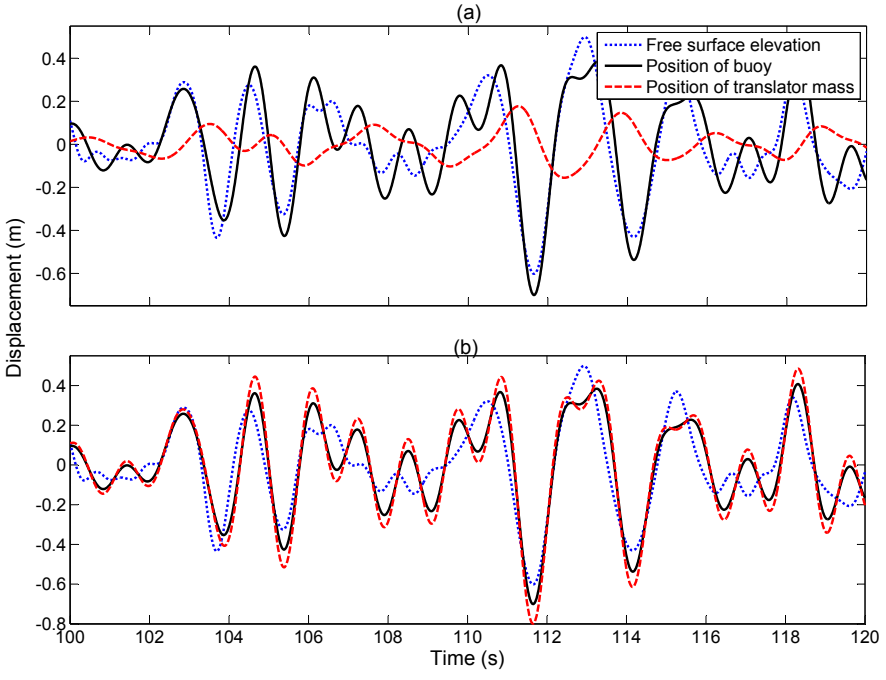


FIGURE 6.16: Time domain example of the FSE input and the calculated buoy and translator mass output, for the case of: (a) $\omega_{ng} < \omega nb$, and (b) $\omega_{ng} > \omega nb$.

## 6.4 The stroke displacement

Analysis of the stroke displacement is important because the length of the stroke must be small enough to fit inside the buoy geometry. Some design parameter configurations which yield high power outputs may also require very large strokes and therefore be infeasible. To analyse the maximum stroke length, the time domain model must be used. However, as shown in Equation 5.59, frequency domain analysis may also be used to calculated the RMS stroke length.

### 6.4.1 The output power's dependence on the stroke length

The stroke velocity and displacement are related via;

$$\dot{X}_s(i\omega) = i\omega X_s(i\omega). \tag{6.7}$$

Therefore the average power can be expressed in terms of the stroke displacement as;

$$\overline{P(t)} = \frac{d}{2}\sum_{n=0}^{\infty}\omega_n^2 {X_s}^2(i\omega_n). \tag{6.8}$$

Comparison of Equations 5.59 and 6.8 reveals that for two systems with equivalent RMS stroke lengths, the system which has the higher average frequency components will generate more power. Intuitively this makes sense; if two generators are oscillating with the same amplitude but different speeds, the faster one will obviously generate more power. This also means that a generator oscillating at a high frequency with a small stroke can produce the same power as one with a much larger stroke but operating at a low frequency.

### 6.4.2 The generator damping's influence on the stroke length

The generator damping parameter is found to have the most significant effect on the stroke length, as illustrated in Figure 6.17. Here both the RMS (a) and the maximum (b) stroke lengths are plotted as a function of the generator damping coefficient for an arbitrary WEC configuration and input wave conditions. Both the RMS and maximum stroke lengths are seen to rapidly decrease as the damping is increased from zero, and then a slow asymptotic decrease for large damping values, with the knee of the curve in both graphs occuring around 50Ns/m for the system considered. The maximum stroke length for this system is three to four times greater than the RMS stroke displacement.

Figure 6.17-(a) plots both the time and frequency domain calculations of the RMS stroke length to verify the equality presented in Equation 5.59.

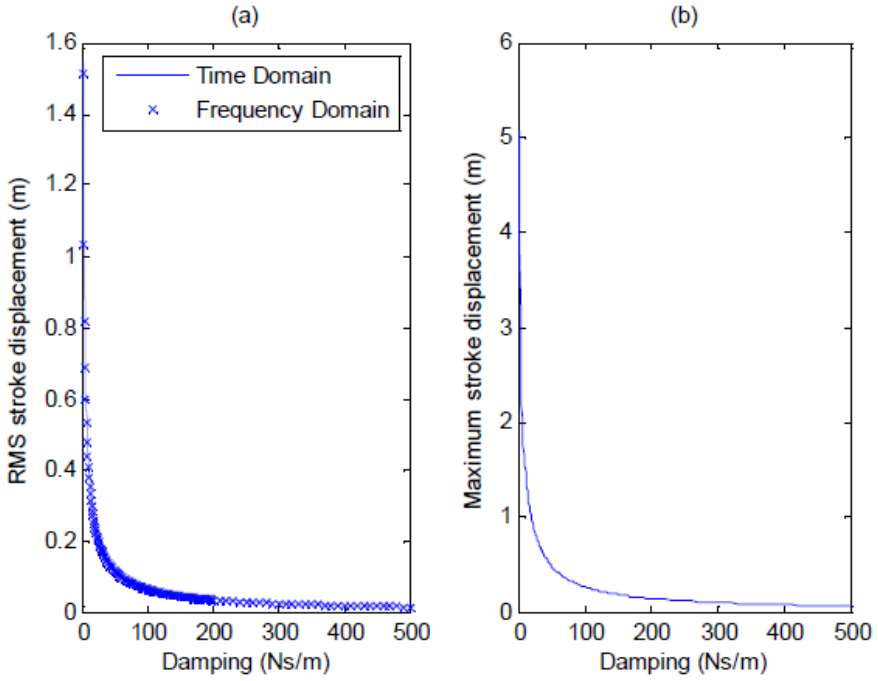


FIGURE 6.17: The stroke length of the linear generator as a function of the generator's damping coefficient for a particular WEC configuration. (a) Is the RMS stroke displacement as calculated in both the time and frequency domains; (b) is the maximum stroke length recorded from a 30 minute time domain simulation.

### 6.4.3 The effect of the maximum allowable stroke length

The stoke limit, $X_{SL}$, is the geometrical constraint of the maximum allowable distance the translator mass can be displaced from equilibrium. The stroke limit is a design parameter, whereby its length must be chosen when designing/constructing the WEC. The stroke limit must be large enough to cater for the expected stroke displacements but small enough to oblige the geometrical constraints of the buoy. The total length of the linear generator, as depicted in Figure 6.18, is at least twice the stroke limit plus the translator length, $T_L$, plus the spring rest length, $S_{RL}$, which must be able to fit inside the buoy's geometry.

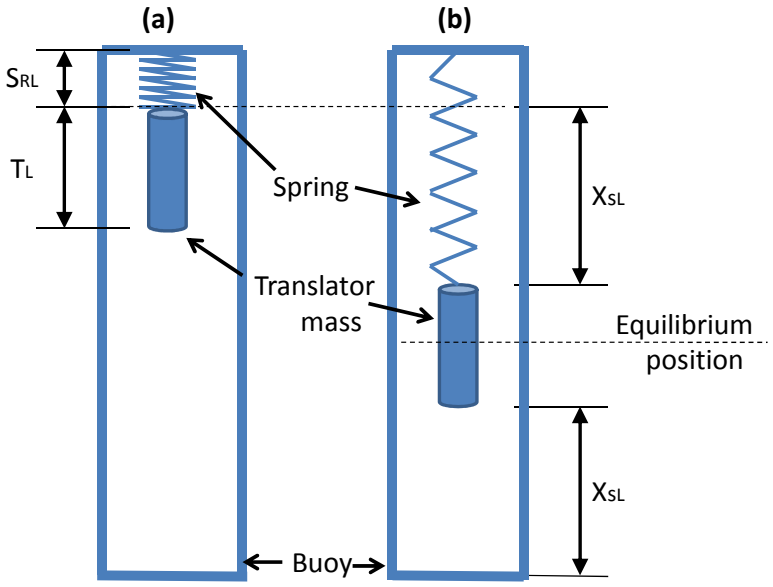


FIGURE 6.18: The limit of the translator stroke and the extension of the spring.

In analysing the stroke limit for the present system, the value of the stroke limit was found to determine the natural frequency of the generator. This important relationship, between the stroke limit and generator natural frequency, can be shown by the following argument. At equilibrium (see Figure 6.18-(b)), the translator mass will hang in the middle of the generator, where the spring is extended by the stroke limit, $X_{sL}$, and the weight of the translator mass will be balanced by the spring force:

$$mg = kX_{sL}. \tag{6.9}$$

Substituting for the spring constant, $k$, from Equation 6.6:

$$mg = m\omega_{ng}^2 X_{sL}, \tag{6.10}$$

and rearranging, it can be seen that the natural frequency is indeed a function of the stroke limit:

$$\omega_{ng} = \sqrt{\frac{g}{X_{sL}}}. \tag{6.11}$$

This is a very significant finding for the application of this type of generator in wave energy conversion, where the peak frequencies of the energy spectrum are typically below 1 rad/s. Figure 6.19 graphs this relationship, showing that a very long stroke limit is required for a generator with a low natural frequency. For example, a generator natural frequency of 2 rad/s, would require a stroke limit of about 2.5m and therefore a total generator length of over 5m. For a generator natural frequency of 1 rad/s the stroke limit would need to be nearly 10m, which is clearly infeasible for the present application

of a small, light, easily deployable device. Therefore in the present work, the generator natural frequency will likely be constrained to frequencies 3 rad/s and above, relating to stroke limits of 1m and less.

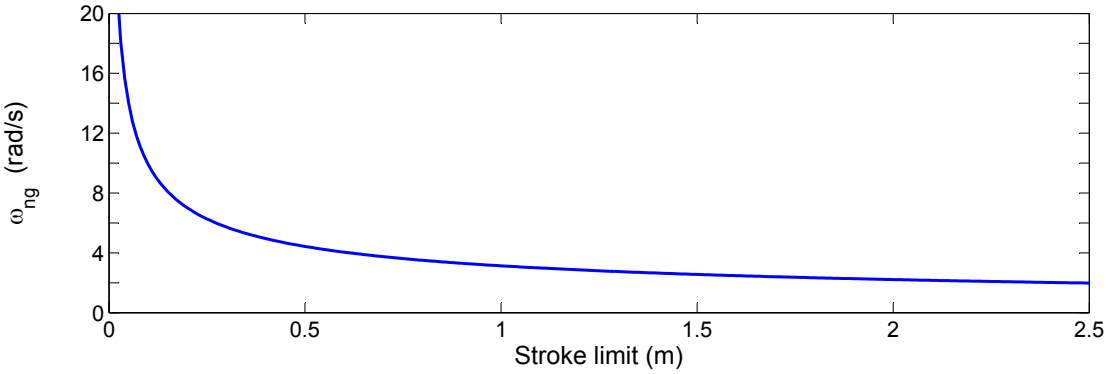


FIGURE 6.19: The natural frequency of the generator as a function of the stroke limit.

## 6.5 Pitch motion

The pitch displacement of the WEC, in response to a given input wave spectrum, is given by the PDTF, Equation 5.61, which is a function of the hydrodynamic parameters and the MoI. The pitch hydrodynamic parameters were discussed in Section 6.2.4 and were shown to depend on the buoy's geometry and CoM. This section examines the PDTF for various buoy radii, draughts and CoM configurations. The MoI is calculated for each case assuming the mass of the buoy is uniformly distributed from the buoy's axis to its radius and vertically symmetric above and below the buoy's CoM (the case displayed in Figure 6.2 - (c)).

Figure 6.20 shows multiple contour plots of the PDTF, where the radius is varying on the $y$-axis and the frequency on the $x$-axis, and the draught is varied between each plot, for a buoy whose CoM is 60% of the draught depth. Increasing the buoy radius, was shown in Figure 6.7 to increase the excitation force coefficient, while also increasing the radiation resistance and added mass coefficients, and was shown in Figure 6.6 to increase the hydrostatic restoring force coefficient. Here in Figure 6.20 the net overall effect of increasing the buoy radius is shown to decrease the PDTF and therefore the pitching motion of the buoy. Increasing the draught of the buoy is shown in Figure 6.20 to reduce the bandwidth of the PDTF and lower its peak frequency.

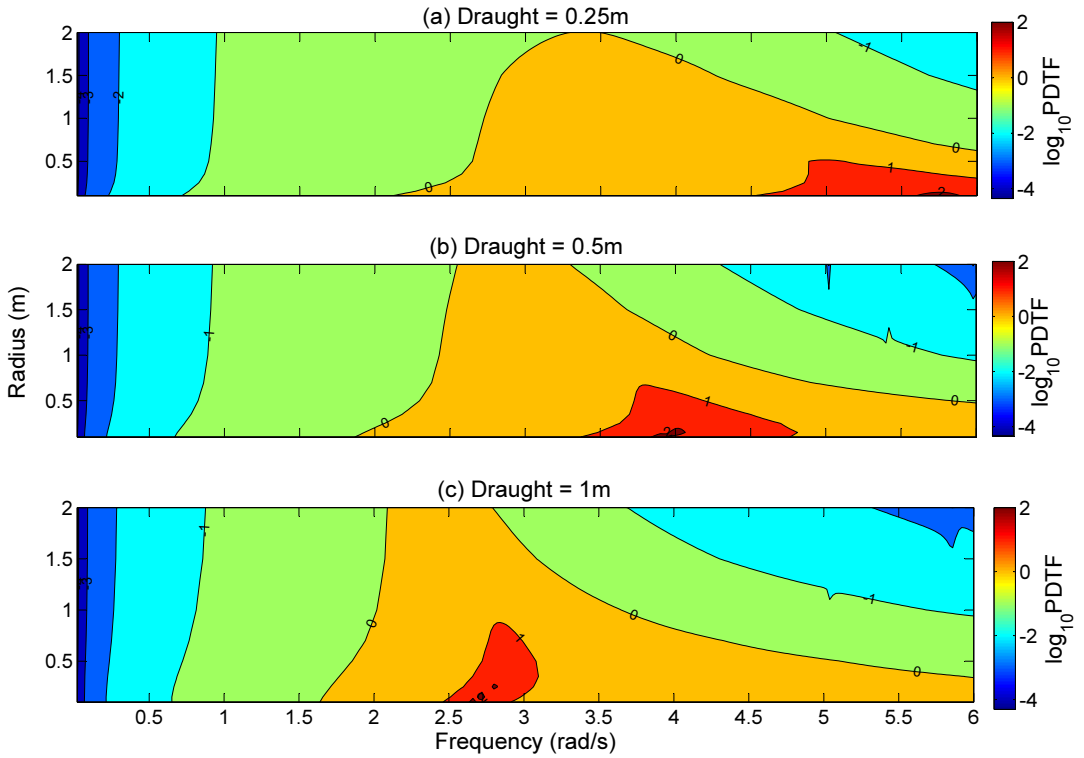


FIGURE 6.20: The pitch displacement transfer function for a buoy with CoM 60% the draught depth for varying radii and draughts.

Figure 6.21 is the same as Figure 6.20, except that the CoM is changed to 90% of the draught depth. Comparing the two figures shows that the maximum amplitude of the PDTF decreases by an order of magnitude due to the decreasing the depth of the CoM. The peak frequency of the PDTF is seen to increase, as the depth of the CoM is decreased.

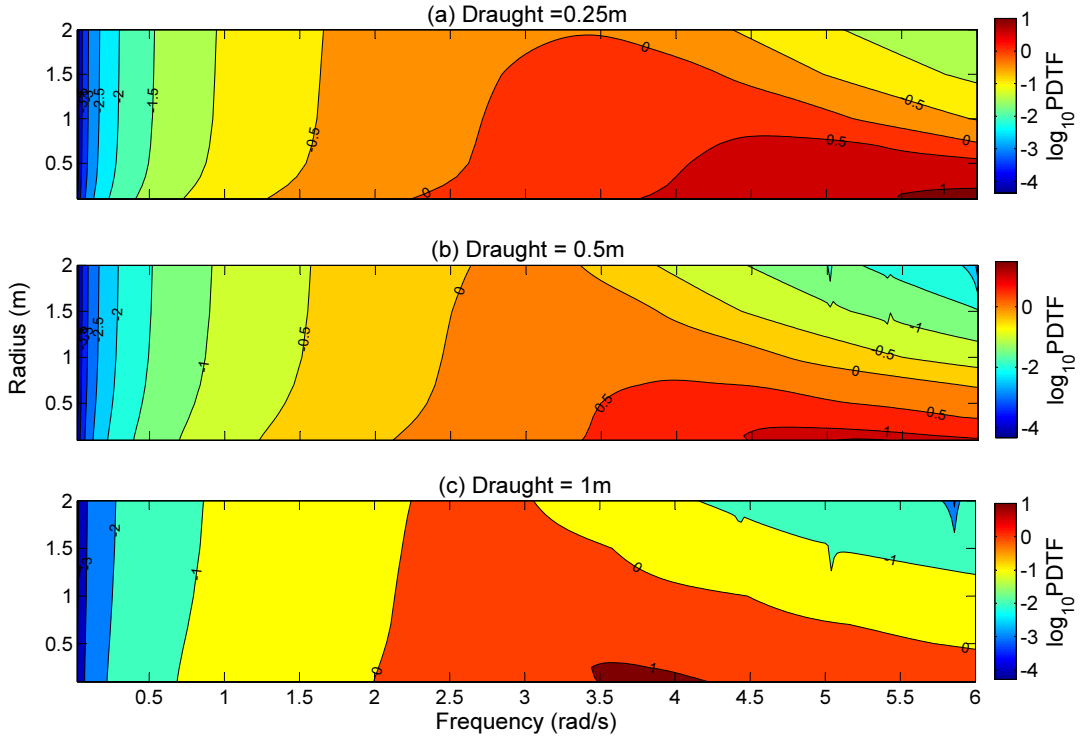


FIGURE 6.21: The pitch displacement transfer function for a buoy with CoM 90% the draught depth for varying radii and draughts.

To show the effect of changing the MoI and CoM, Figure 6.23 plots the PDTF for the case for a buoy with a radius of 0.25m and draught of 0.5m, which has a mass of 100kg. The horizontal position of the buoy's CoM will be assumed to lie on the buoys central axis, and its vertical position is varied across Figures 6.23-(a), (b) and (c), with values of 0.5, 0.7 and 0.95 of the draft depth respectively. The MoI will consider three cases: the first being the smallest possible value (the case shown in Figure 6.2 - (b)) which equals 0.86kgm$^2$, the second is largest possible value (the case shown in Figure 6.2 - (d)) which equals 25kgm$^2$. and the third is a value chosen geometrically half way between the smallest and largest, 4.5kgm$^2$. To illustrate how these MoI values compare against the case shown in Figure 6.2 - (c) with a uniform mass distribution around the CoM, Figure 6.22 plots the MoI as a function of the CoM for this case, showing that the MoI varies from a value of 2.4kgm$^2$ when the CoM is 50% of the draught depth and the mass is uniformly distributed throughout the entire buoy, to a value of 1.6kgm$^2$ when the CoM is 100% of the draught depth and the mass is then distributed on a thin circular disc on the bottom of the buoy.

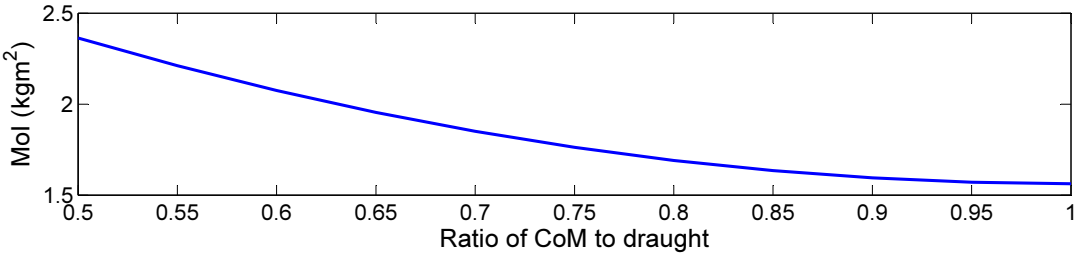


FIGURE 6.22: The MoI as a function of the CoM, where mass of the buoy is uniformly distributed from the buoy's axis to its radius and vertically symmetric above and below the buoy's CoM, for a buoy with 0.25m radius and 0.5m draught.

Figure 6.23 shows that increasing the MoI decreases the frequency of the PDTF peak, which should be expected from Equation 6.5. Decreasing the depth of the CoM is seen to generally increase the frequency of the PDTF peak. At high frequencies the amplitude of the PDTF is seen to decrease with increasing MoI, whereas at low frequencies the amplitude of the PDTF is larger for the bigger MoI values.

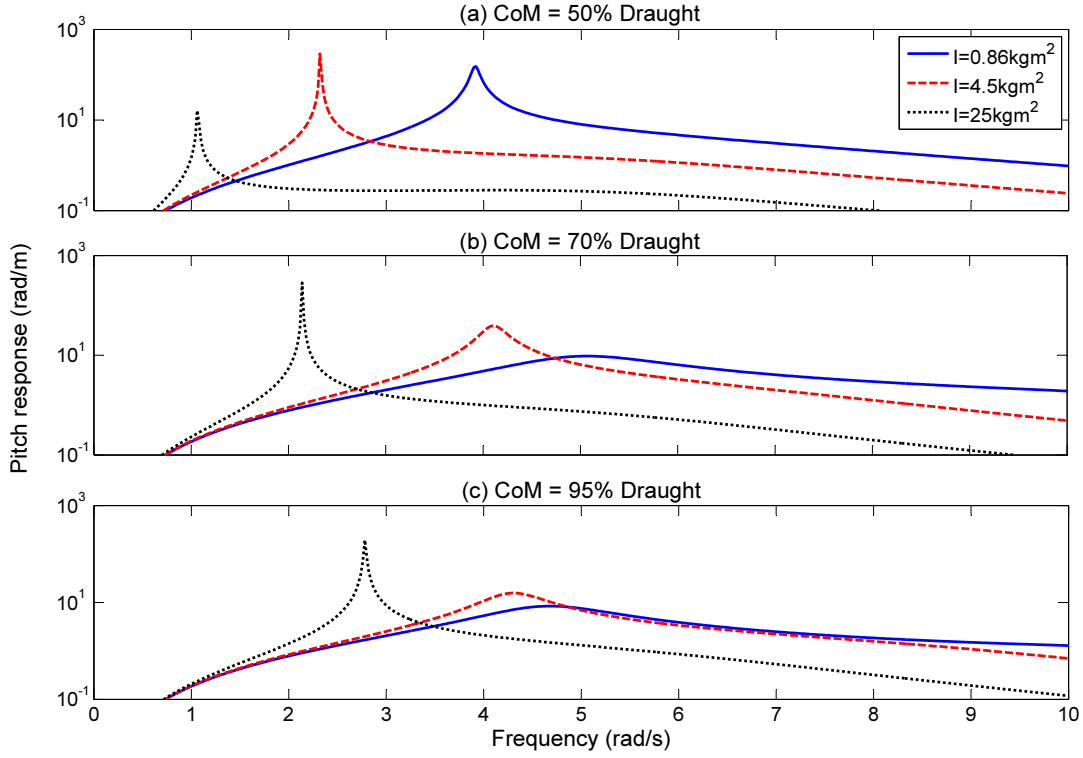


FIGURE 6.23: The PDTF for a buoy with 0.25m radius and 0.5m draught for varying CoM and MoI values.

### 6.5.1 Effect of generator on pitch

The numerical model does not consider a direct coupling between the translator mass and the pitch motion of the buoy, because both the spring and damping forces act

along the central axis of the buoy. However in reality, if the buoy starts to pitch then the translator mass will come in contact with the stator wall, and will then apply a force/torque to the buoy. If the translator mass is below the CoB then this will result in a restoring torque, however, if the translator mass is above the CoB then this may cause the buoy to capsize. The significance of the effect of generator on pitch will therefore depend on the relative mass of the translator mass to the total buoy mass, and the position of the translator stroke with respect to the CoB. Values for the translator mass and stroke location are investigated in the next Chapter, where their possible effect on the pitch motion should be considered.

## 6.6 Summary

A preliminary analysis of the CIMPLG WEC was undertaken by identifying and assessing the various parameters which affect the CIPMLG WEC's performance. The design parameters, whose values must be selected by the designer, were identified to be; the buoy's geometry (cylinder radius and draught), the mass distribution within the buoy, the translator mass, the generator's spring constant, the generator's damping coefficient and the stroke limit of the generator. A number of additional parameters, which are important in the analysis of the WEC's performance, could be derived from these design parameters, namely; the mass of the buoy, the CoM, the MoI, the hydrodynamic parameters, and the natural frequencies of the buoy and the generator. These parameters influence the transfer functions and therefore the WEC's performance.

The SVTF was shown to depend on the buoy's natural frequency, the generator natural frequency, the translator mass value and the generator damping value. A wide variety of spectral shapes for the SVTF were possible depending on the different combination of values for these parameters. However, the finding in Section 6.4.3, that the stroke limit determines the generator natural frequency, effectively constrains the generator natural frequency to relatively high values. This constraint on the generator natural frequency, has the effect of reducing the dimensionality of the SVTF parameters, which causes the SVTF to also be constrained to one particular spectral shape, with a single peak centered on the buoy's natural frequency. This single peaked spectral shape was displayed in Figures 6.12 - 6.14 for the case of, $\omega_{ng} = 2\omega_{nb}$, where the generator's natural frequency was larger than the buoy's natural frequency. Considering that the total length of the generator will be constrained by the depth of the draught, therefore the maximum stroke limit can't exceed half the draught, then comparison of Figures 6.11 and 6.19, shows that the generator's natural frequency will indeed always be larger than the buoy's natural frequency.

The major conclusion to come from this analysis, is that the proposed WEC may only be able to perform well in response to waves with relatively high frequencies. Considering that the proposed WEC needs to be small, light and easily deployable, Figures 6.1 and 6.11, showed that small buoys have high natural frequencies. Additionally, the generator's natural frequency will be higher than the buoy's natural frequency, as was discussed in the previous paragraph. Therefore small buoys will have high natural frequencies coupled to a generator with a higher natural frequency. Although conventional large scale WECs target the low frequency waves in the spectrum, which contain the larger amplitudes and power, it was shown in Section 6.4.1 that a system operating with small amplitude stroke lengths at high frequencies can produce as much power as a larger system at operating at low frequencies (Equation 6.8). Chapter 7 will therefore investigate whether there is sufficient power in the higher frequency part of the input wave spectrum for the present application.

Analysis of the pitch motion was seen to be very complicated, due to its strong dependence on the CoM, which can't be known until the system is fully designed and information is available for the mass density, geometry and location of all the buoy's components. Likewise, the MoI also has a strong effect on the pitch motion and its value can't be known until the distribution of all the component masses is provided. However, the analysis can be used to provide preferable CoM and MoI values, to guide how the distribution of mass throughout the system should be designed. Analysing the effect of the buoy's geometry on the PDTF revealed that buoys with larger radii were generally more stable than their thinner counterparts.

# Chapter 7

# Investigation of the input wave spectrum

## 7.1 Introduction

The performance of the CIMPMLG WEC is driven by the input wave spectrum, therefore the SVTF, SDTF and PDTF should be designed with respect to the frequency content of the input wave spectrum (as was discussed in Section 5.5). However, Section 4.3.2 showed that the ocean wave spectra vary with time and location, which means that a WEC designed to perform well in one particular location may perform poorly at another. Indeed, even at a single location, the performance of a WEC will vary as the wave conditions change over time. This chapter analyses ocean wave spectra to gain an understanding of how a WEC system can best be designed, to meet the required performance criteria outlined in Section 4.3.3.1, while subjected to such variable input wave conditions.

Considering the goal of designing a 'one size fits all' WEC able to perform well at any deployment site, this chapter seeks to identify properties of ocean wave spectra which are consistent at all locations. The high frequency tail of ocean wave spectra is identified as being omnipresent in all ocean wave spectra and is therefore the focus of this chapter. Section 7.2 introduces the high frequency tail, reviewing theoretical descriptions of the high frequency part of ocean wave spectra. The theoretical descriptions are then compared against measured data, and frequency content which is spatially and temporally persistent across the data identified. Section 7.3 then discusses the input wave spectrum to be used for analysing the WEC pitch motion.

## 7.2 The high frequency tail of ocean wave spectra

The review of wave creation in Section 4.1.3 outlined that the generated wave field is dictated by the wind speed, duration and fetch length. This results in a wide range of wave spectra being created a single site due to the changing wind speeds and directions, and also a wide variety between sites, with different locations having differing proximity to leeward shores and therefore varying fetch distances. However, Phillips [177] noted that, "...for low frequencies, the spectrum curves depend quite strongly on the fetch and the meteorological conditions, but their most remarkable property is that for high frequencies, the curves obtained under different conditions very nearly coincide and become apparently independent of the fetch and of the strength of the wind."

This property of the high frequency part of all wave spectra was first identified by Burling [178], who found empirically that the mean values of his observed spectra at high frequency obeyed a relation of this type:

$$S_B(\omega) = 0.7\omega^{-5}. \tag{7.1}$$

Using dimensional analysis Phillips [177] derived the following expression for the high frequency components of the wave spectrum:

$$S(\omega) = \alpha g^2 \omega^{-5}, \tag{7.2}$$

which for an $\alpha$ value of $7.4 \times 10^{-3}$ agrees with Burling's measurements. This is also consistent with the Pierson-Moskowitz and JONSWAP spectrums for high frequencies, where an $\alpha$ value of $8.1 \times 10^{-3}$ is used. Figure 7.1 plots a comparison of the PM spectrum for varying windspeeds against Burling's curve, $S_B(\omega) = 0.7\omega^{-5}$, showing that the convergence of the PM spectrum to Burling's curve at high frequencies.

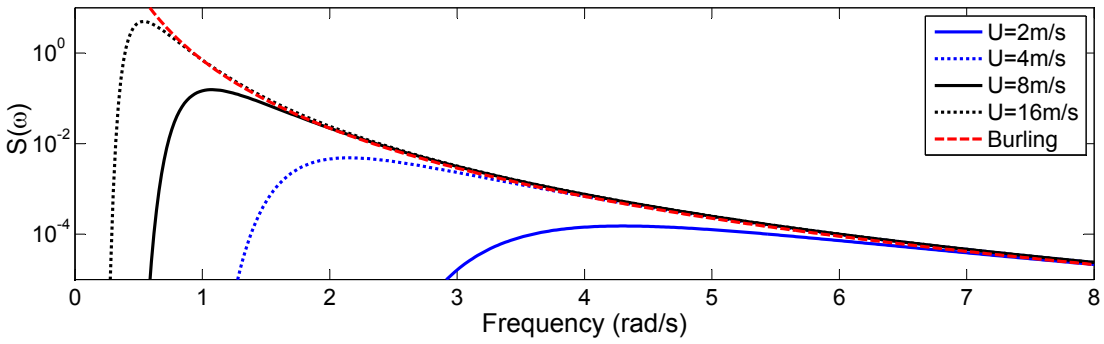


FIGURE 7.1: The PM spectrum for varying windspeed compared against the Burling spectrum.

Although the low frequency part of the spectrum contains larger waves and greater energy, the spectral curve at these frequencies is heavily influenced by the wind conditions and its fetch length. Therefore, this part of spectrum varies from location to location and from day to day. The high frequency part of the spectrum on the other hand, is first part to be created when the wind blows and forms a similar shaped spectrum independent on the fetch and wind speed. This consistency in spectrum shape is a very attractive feature of the high frequency part of the spectrum, allowing the WEC system to be designed for this input condition, with confidence that it will be persistently present irrespective of location or time. Additionally, considering the findings in Chapter 6 that the proposed system is not well suited to low frequency operation, since small devices have high frequency natural responses, means that targeting the high frequency part of the spectrum is a very well suited for the goals of the proposed CIPMLG WEC device.

However, the question beckons of whether there is sufficient energy in this part of the spectrum for the WEC to harvest. Figure 7.2-(a) shows the significant wave height, and Figure 7.2-(b) the power per metre of wavefront, for the Burling high frequency spectrum, as a function of where the low frequency cut-off, $\omega_{cutlow}$, for the spectrum is imposed. That is:

$$S_B(\omega) = \begin{cases} 0.7\omega^{-5} & \omega \geq \omega_{cutlow} \\ 0 & \omega < \omega_{cutlow} \end{cases}. \tag{7.3}$$

From Figure 7.2 it can be seen that for a low frequency cut-off of 2 rad/s, the Burling wave spectrum has a significant wave height is over 0.4m and carriers over 200W of power per metre of wavefront. Due to the $\omega^{-5}$ dependence of the spectrum, these values drop quickly and by a low frequency cut off 3 rad/s the significant wave height is less than 0.2m and the power less than 30W/m, and by 4 rad/s the significant wave height is 0.11m and the power is 7W/m. Therefore, depending on where the low frequency cut-off actually is for the omnipresent high frequency tail of the spectrum, there appears to be a relatively high amount of power transported per metre of wave front for the present application. To determine what value should be considered for the low frequency cut-off, the next section will investigate the case study wave data.

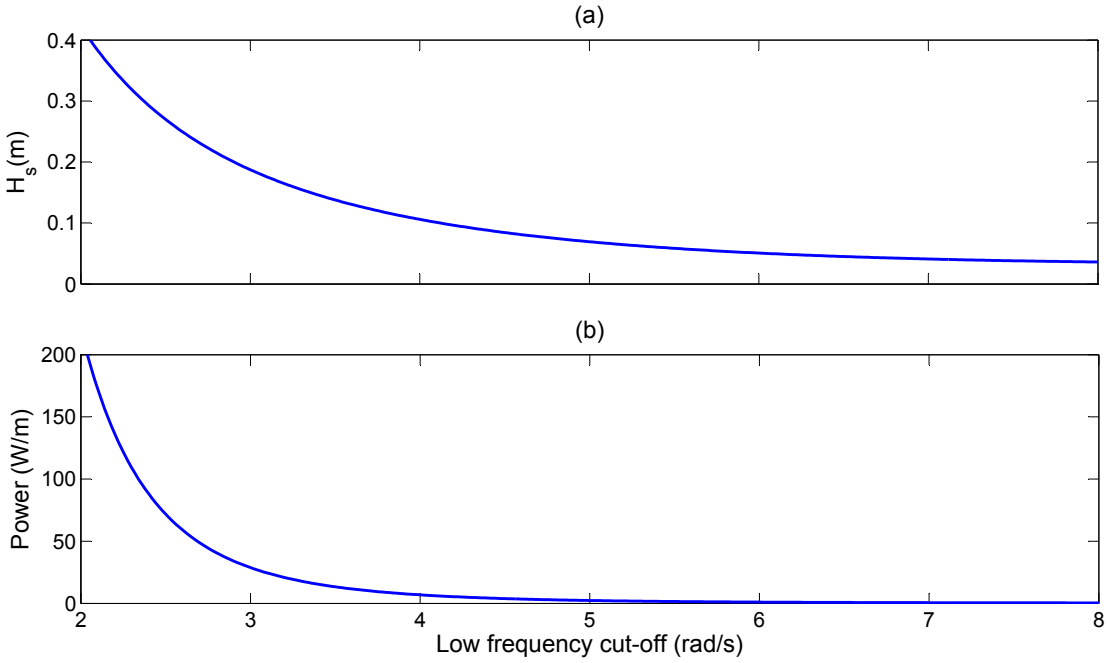


FIGURE 7.2: The significant wave height, (a), and power per metre of wave front, (b), as a function of the low frequency cut-off for the Burling spectrum with a high frequency cut-off of 20 rad/s.

### 7.2.1 Comparing the theoretical high frequency tail of ocean wave spectra with measured wave data

Figure 4.18 showed that the peak period for the all of the sites along the Queensland coast was generally above 2 seconds (3.14 rad/s). Therefore, all of the measured wave data should contain the Burling spectrum curve with a low frequency cutoff at 3.14 rad/s. To verify this hypothesis, the actual time domain data was sought from the Queensland Government's Waverider buoys [111], to investigate the actual spectrum shape of the measured data versus the Burling curve.

An example of the time domain data of the FSE measured by the Waverider buoys is plotted in Figure 7.3-(a). The Waverider buoy samples the FSE every 0.39s for 30 minutes, from which the wave spectrum is calculated and used to characterise the sea state by it peak period and significant wave height, as displayed in Section 4.3.2.2. The time domain data in Figure 7.3-(a) is used to calculate the spectrum in Figure 7.3-(b), from which a significant wave height value of 0.31m and a peak period of 4.45s is calculated. The significant wave height is calculated using Equation 4.13 and the peak period is determined by selecting the frequency with the highest amplitude, which in this case occurred at 1.4 rad/s, which is equivalent to a 4.45s period.

Figure 7.3-(b) shows a bi-modal spectrum, containing a swell and a wind sea, where the peak from the swell is slightly larger than the wind sea's peak. Figure 7.4-(b) shows the calculated spectrum from the same location 6 hours later where the wind sea's peak has grown larger than the swell's. Figure 7.4-(a) shows a zoom in on a 100s portion of the 30 minute FSE time series data used to obtain Figure 7.4-(b). The sea state at this location is now characterised by a significant wave height of 0.38m and peak period of 2.5s. Figures 7.3 and 7.4, illustrate that the wave resource can be multi-modal and that using just the single peak period value does not give a good understanding of the wave spectrum's frequency distribution.

Figures 7.3-(b) and 7.4-(b) also compares the measured wave spectra against the Burling spectrum. The goal of the present analysis was to determine if the hypothesis that Burling spectrum with a low frequency cutoff of 3.14 rad/s is omnipresent in the measured wave data. For the case when the wind sea is high, Figure 7.4-(b), the measured spectrum and the Burling spectrum roughly coincide with each other all the way down to 2.5 rad/s. However, for the case when the wind sea was lower, Figure 7.3-(b), the two spectra coincide down to 4 rad/s and then the measured spectrum drops slightly below the Burling spectrum though still follows it closely down below 3 rad/s. Obviously, no conclusive statements can be made regarding the hypothesis from just two measured sea states at the one location, rather Figures 7.3-(b) and 7.4-(b) are used just to provide a lead in example to the following analysis on a more encompassing data set.

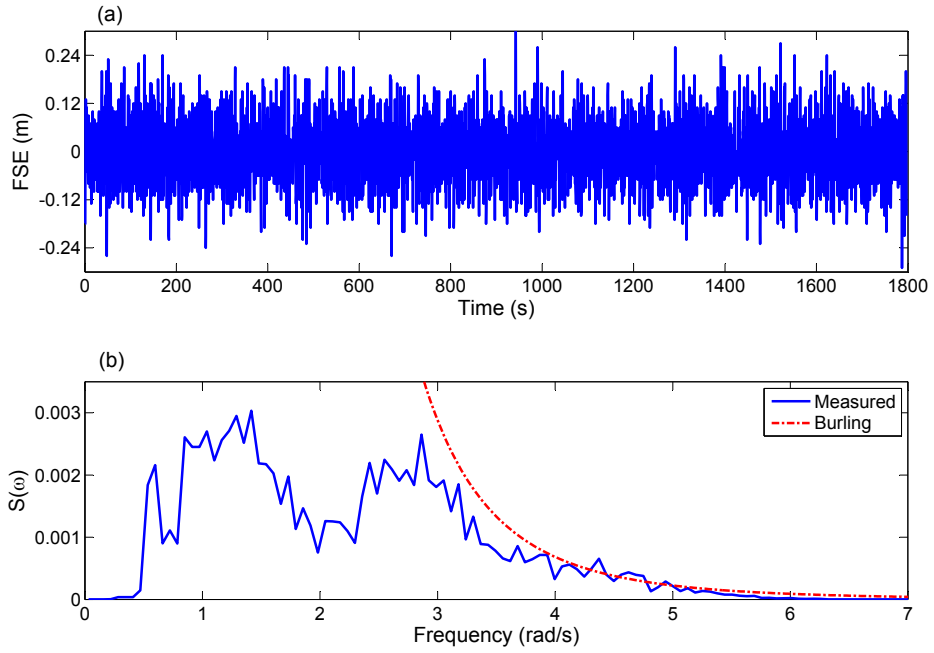


FIGURE 7.3: Cairns 12:00am

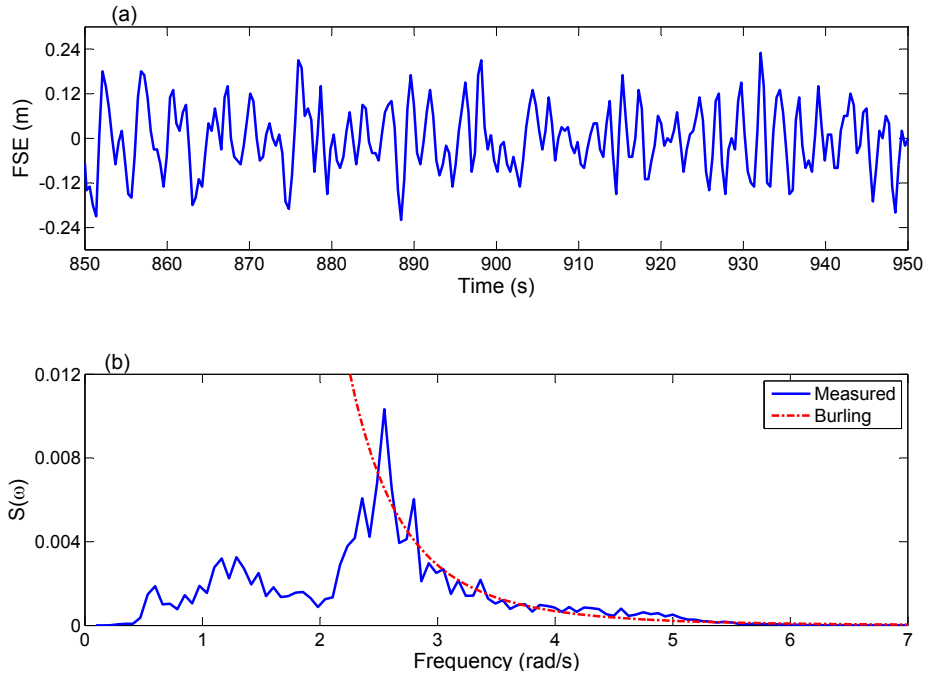


FIGURE 7.4: Cairns 6:00am

Unlike the peak period and significant wave height data which was freely available on the Queensland Government's website, the time series data measured by the Waverider buoys could only be obtained via negotiations with the Queensland Government Department of Science, Infor- mation Technology and Innovationss Coastal Impact Unit's staff. Therefore due to file size limitations and restraints on the Coastal Impact Unit staff's man hours to collect and send the files, only a finite amount of data could be obtained. For example, one weeks worth of data at a single site, sampled at 0.39s, results in over one and half million samples.

To get a representative selection of data from the different locations, it was decided to group the sites into high, medium and low energy sites, and take data from one site in each group. From Figure 4.18, Gold Coast and Mooloolaba were classified as high energy, Gladstone, Mackay, Townsville and Cairns as medium energy, and Moreton Bay and Albatross Bay as low energy sites. An additional constraint on the choice of sites to acquire the data from, was that some of the sites had non-directional Waverider buoys and the others had directional Waverider buoys, with the key difference between the two being that non-directional buoys sample at 0.39s, whereas the directional buoys sample at half this rate, 0.78s. Therefore, to investigate the high frequency tail of the spectrum, only sites with the non-directional buoys and their higher sampling rate were chosen, resulting in the selection of the Moreton Bay, Cairns and Gold Coast sites. One week of continuous data was obtained for each of these sites, during the summer and the winter, resulting in over 2,000 sea state spectra for comparison against the Burling spectrum.

Figures 7.5-(a) to 7.10-(a) examine the measured wave spectrums over a full week of continuous monitoring, in January and July, for the three different locations. Each 30 minute time series file, is transformed into its corresponding spectrum, resulting in 336 sea spectrums, which are then plotted along on the y-axis, with the frequency along the x-axis and the amplitude plotted as a contour (using a $\log_{10}$ scale). The Cairns data show a bimodal swell and wind sea spectra, with consistent swell in the winter and a number of large wind sea events, whereas in the summer week the swell is less consistent but a number of wind sea events with maximum amplitude of $S(\omega) = 10^{-1.5}$ are also present. The Moreton Bay data is wind sea dominated, with maximum amplitude in the winter reaching $S(\omega) = 10^{-1}$, however low amplitude swell signals can be seen every 12 hours in Figures 7.7-(a) and 7.7-(a), possibly due to the swell being diffracted into the bay at high tides with attenuated amplitude. The Gold Coast data is swell dominated, with maximum amplitudes of $S(\omega) = 10^{0}$ for both summer and winter, and no trace of wind seas detectable in the spectral data.

Figures 7.5-(b) to 7.10-(b) then compare the measured spectra against the Burling spectrum, with the dark blue regions indicating when the measured data is more than half of the Burling spectrum, the light blue regions when the measured data is more than the Burling spectrum and the red regions for when the measured data is more than double the Burling spectrum. These Figures show the measured spectra at the Cairns and Moreton Bay sites to be greater than the Burling spectrum for the majority of the time for frequencies between 3 and 5.5 rad/s, however for the Gold Coast site the measured spectra is seldom greater than the Burling spectrum.

It is believed the attenuation of the measured spectra at high frequencies for the Gold Coast site is an artefact of the Waverider buoy. Tucker [112] concluded that the motion of the Waverider bouys reduces the magnitude of the higher spectral harmonics. Therefore the measurements of the spectrum at high frequencies is likely underestimating the actual content at those frequencies, especially for the cases which contain large amplitude spectral content at low frequencies. The other possibility for the low amplitude of the measured wave spectra at high frequencies for the Gold Coast site, is that there truly was no energy in the waves at these freqeuncies. This would correspond to the case of pure swell with zero local wind present, as the presence of any wind in the area would have created a local wind sea superposed onto the swell. It therefore seems very unlikely that for a full continuous week, on two separate occasions, there was zero wind at that location.

Another questionable result of the high frequency measurements, occurs just after 6 rad/s for all of the measured spectra where the amplitude suddenly drops by over an order of magnitude and flattens out. The data is sampled at 0.39s, therefore due to

the Nyquist theorem it contains information up to 8.05 rad/s. The large and sudden attenuation of the wave amplitude at 6 rad/s is possibly due to the hydrodynamic properties of the waverider buoy filtering out waves above this frequency or to numerical preprocessing of the data.

In general, the effect of the Waverider buoys underestimating the high frequency wave components is negligible for most ocean engineering applications, where the effects of the largest waves in the spectrum are of most interest. Unfortunately however, for the present case of evaluating the potential of wave energy conversion at high frequencies, the underestimation of the wave heights at these frequencies makes the data measured by the Waverider bouys unsuitable. To further evaluate the high frequency wave resource along the QLD coast, the wave spectra will be hindcast from measured wind data, which shall be used as a proxy to in-situ wave height measurements from Waverider bouys, due to the the limited accuracy of the Waverider buoys at high frequencies.

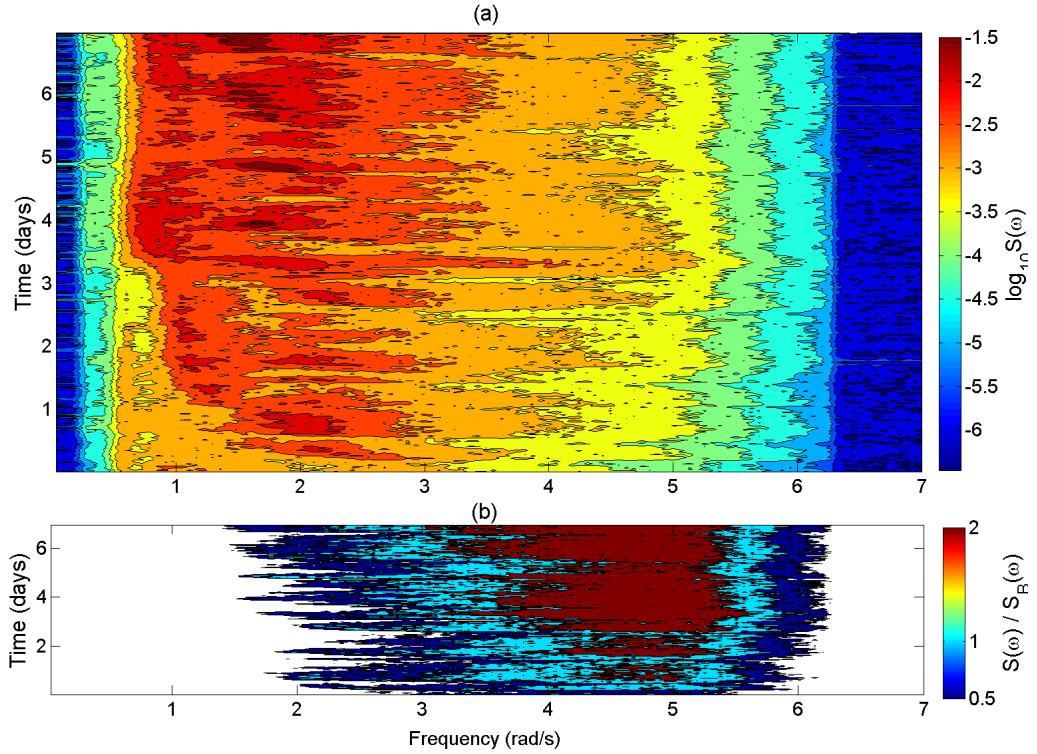


FIGURE 7.5: Cairns Januray (a) The measured wave spectrum every 30 mins for one week (b) The ratio of the measured wave spectrum to the Burling spectrum.

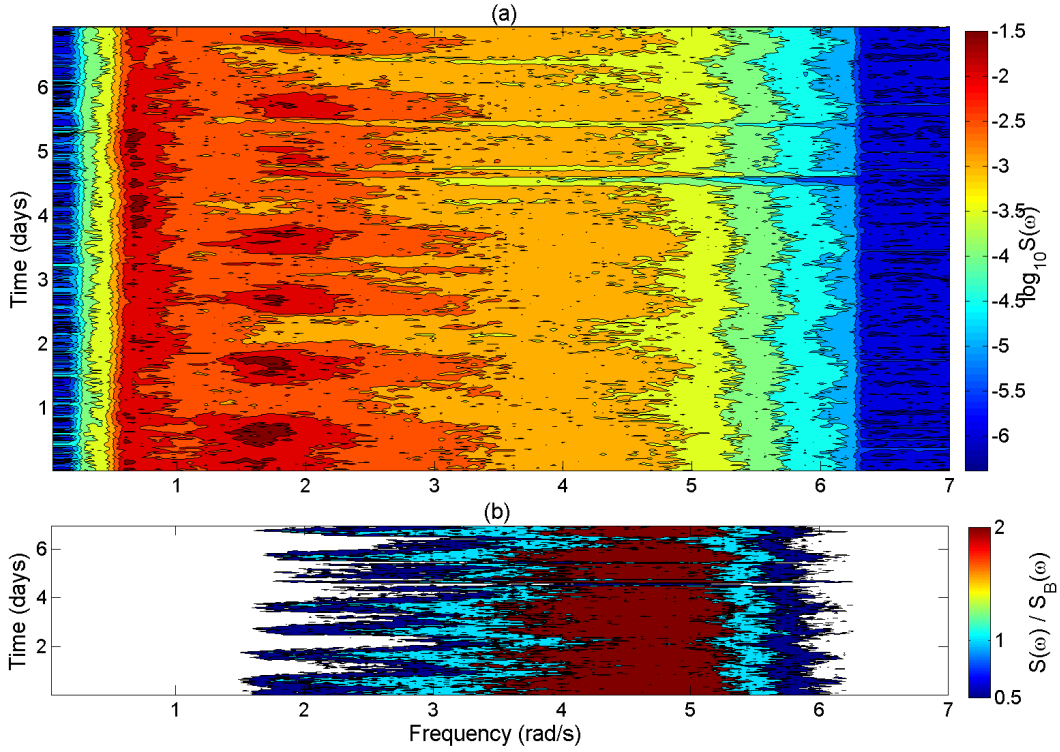


FIGURE 7.6: Cairns July (a) The measured wave spectrum every 30 mins for one week (b) The ratio of the measured wave spectrum to the Burling spectrum.

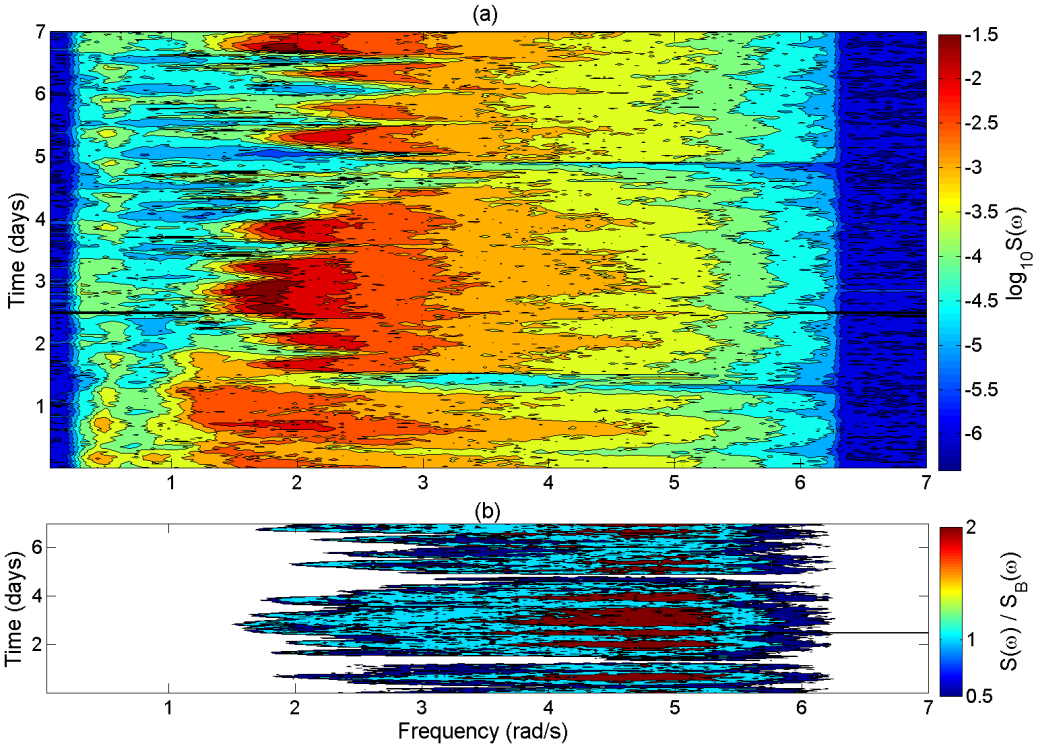


FIGURE 7.7: Moreton Bay January (a) The measured wave spectrum every 30 mins for one week (b) The ratio of the measured wave spectrum to the Burling spectrum.

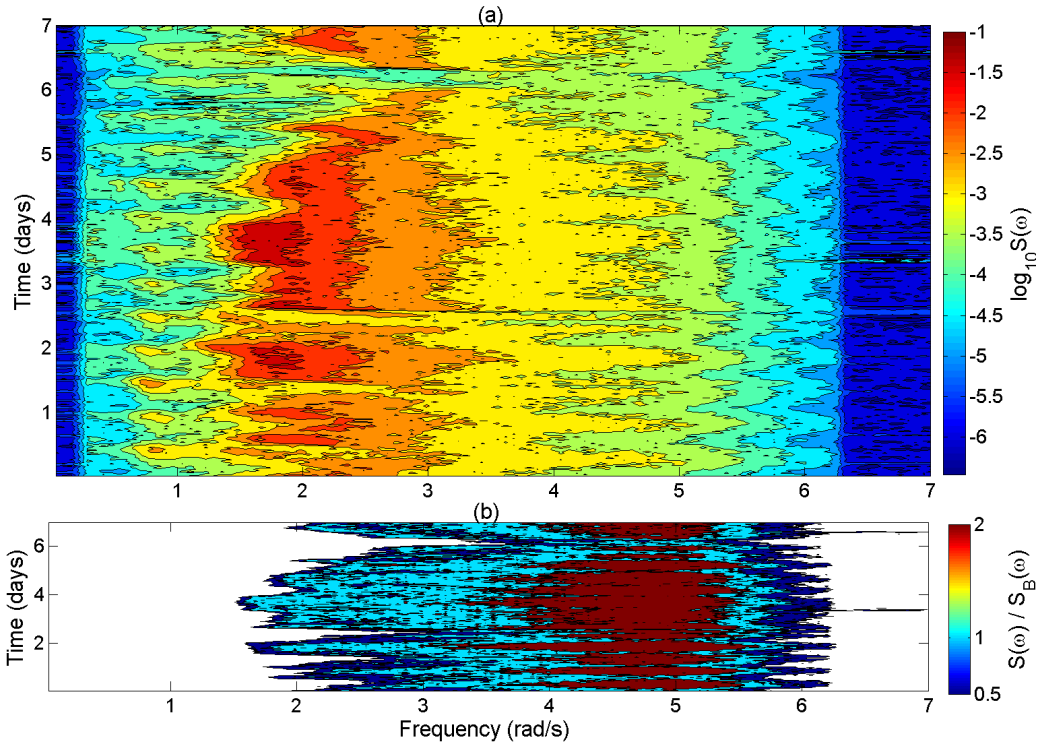


FIGURE 7.8: Moreton Bay July (a) The measured wave spectrum every 30 mins for one week (b) The ratio of the measured wave spectrum to the Burling spectrum.

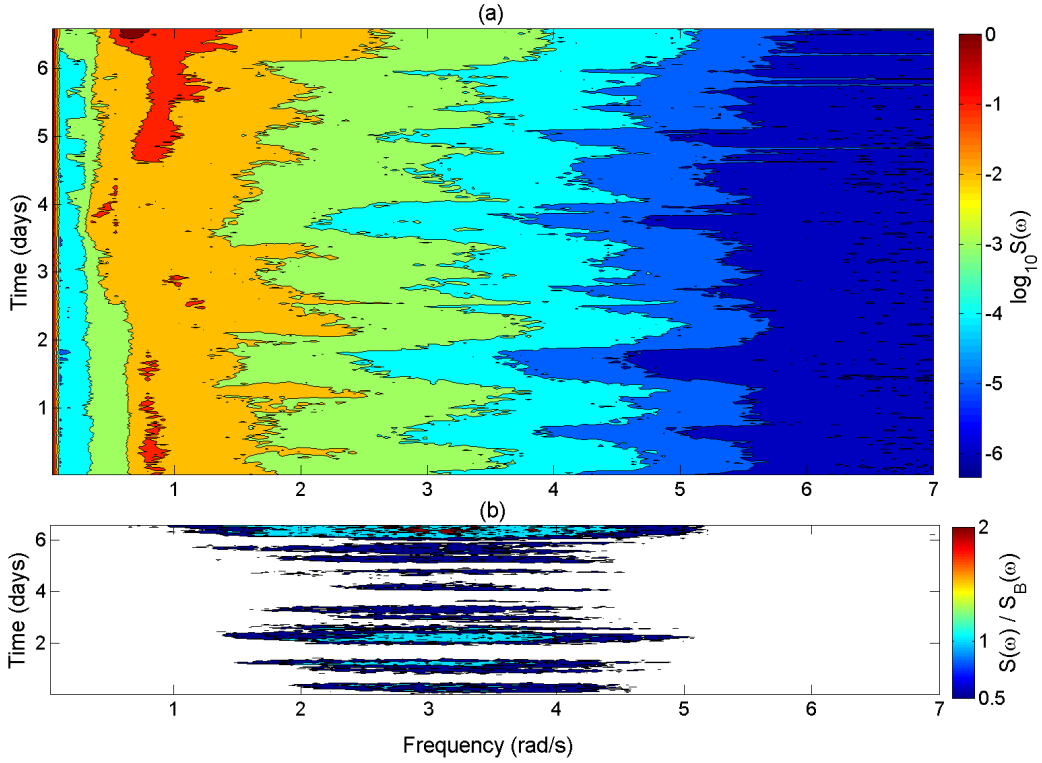


FIGURE 7.9: Gold Coast January (a) The measured wave spectrum every 30 mins for one week (b) The ratio of the measured wave spectrum to the Burling spectrum.

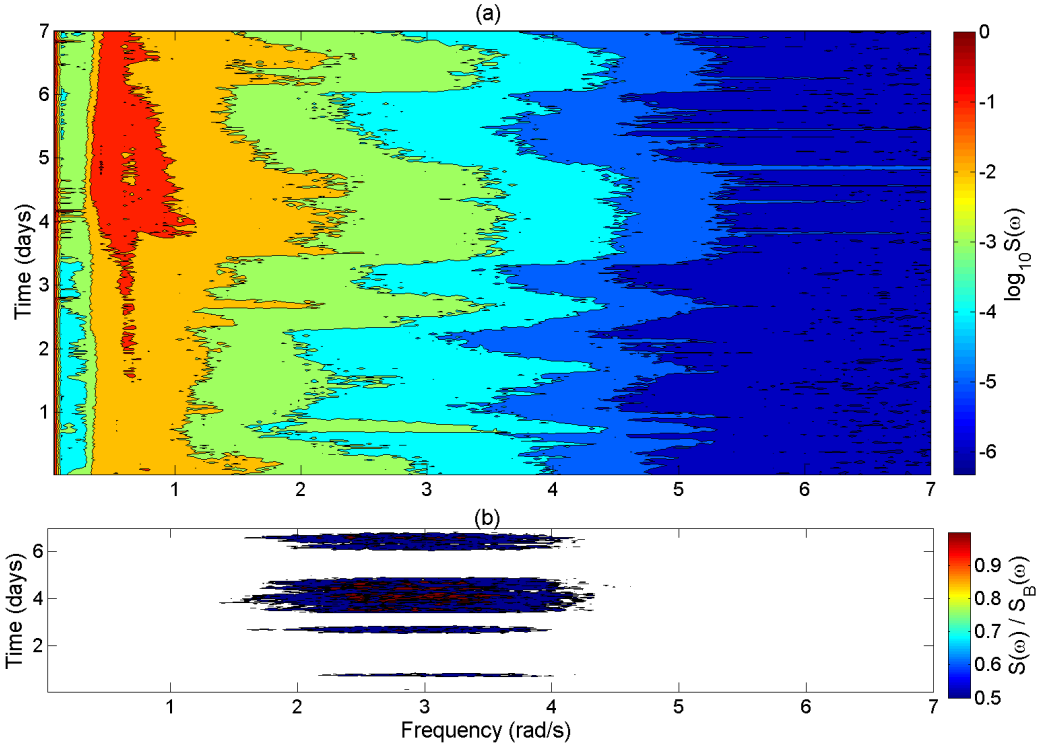


FIGURE 7.10: Gold Coast July (a) The measured wave spectrum every 30 mins for one week (b) The ratio of the measured wave spectrum to the Burling spectrum.

### 7.2.2 Estimating the temporal persistence of the high frequecy tail of ocean wave spectra from measured wind data

The high frequency tail is generated by the local winds. This section seeks to evaluate the hypothesis that Burling spectrum with a low frequency cutoff of 3.14 rad/s is omnipresent in the measured wave data, by analysing the wind conditions necessary to create such a spectrum and then assessing the occurrence of such winds.

Figure 7.11, was obtained from [179], and graphs the wave height and period as a function of wind speed, duration and fetch. From Figure 7.11 it can be seen that a wave spectrum with a 2 second peak period, requires a wind of 5m/s, with a 10km fetch and blowing for a 2 hour duration (red dot). As the wind speed increases the fetch and durations required decreases, for example a wind speed of 10m/s only requires a fetch of 4km and duration of less than an hour (blue dot).

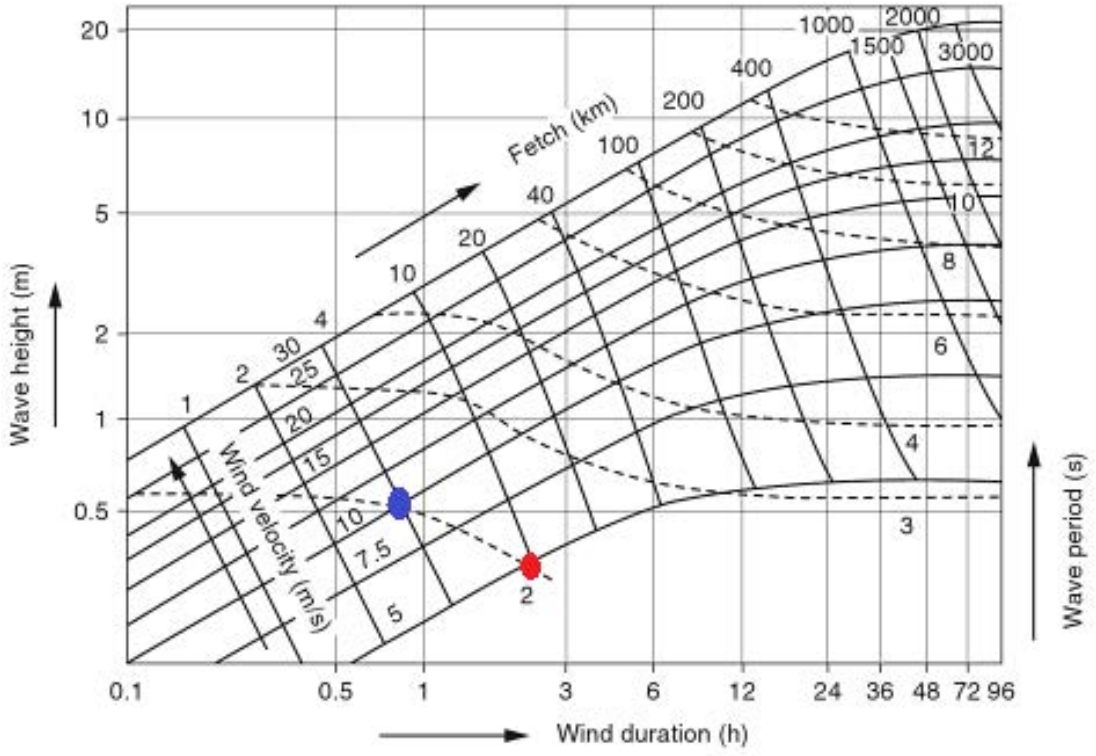


FIGURE 7.11: Wave height and pariod as a function of wind speed, duration and fetch [179].

Figure 7.12, was then created to further assess the creation of a 2 second peak period for wind speeds less than 5m/s, which is not available on Figure 7.11. Figure 7.12 compares the JONSWAP spectrum against the Burling spectrum for 2, 3 and 4m/s wind speeds, using Equation 4.15, whereby the fetch was manually adjusted until a 2s peak was obtained for the corresponding wind speed. Figure 7.12 shows that wind speeds of 3 and

4m/s will create a spectrum with greater amplitude than the Burling spectrum with 2s (3.14 rad/s) low frequency cut-off, and that even wind speeds as low as 2m/s will create a comparable spectrum to the Burling spectrum above 3.14 rad/s.

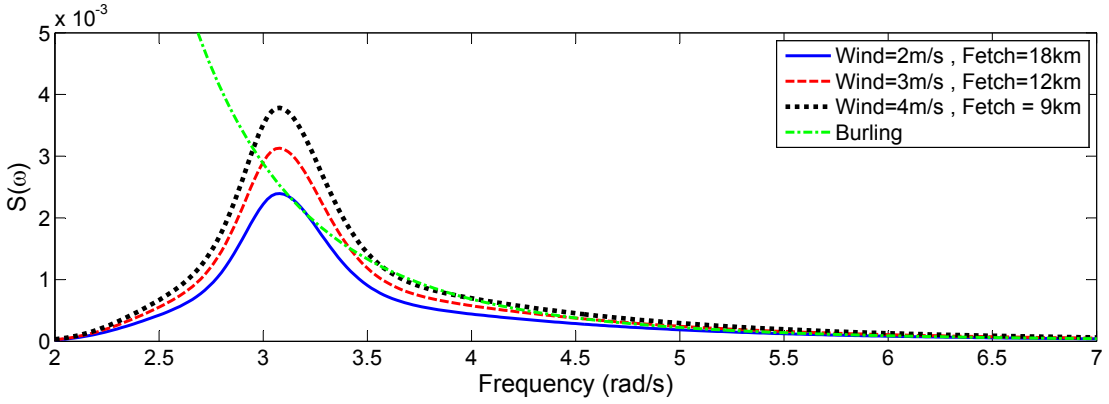


FIGURE 7.12: JONSWAP spectrums with a peak period of 2s for various wind speed and fetch combinations compared to the Burling spectrum.

The hypothesised Burling spectrum can therefore be created by winds with speeds of 2-3m/s and fetches of 10-20km. Faster wind speeds will create larger amplitude spectra, and longer fetches will create spectra with peaks at lower frequencies, but whose high frequency tails converge to the Burling spectrum. To assess the typical availability of such meteorological wind conditions, data was obtained from the Australian Institute of Marine Science (AIMS) weather obersvation [180], which maintain over ten stations along the QLD coast, mostly focussing on the Great Barrier Reef region. Four sites were selected along the QLD coast; the most northerly, the most southerly and two in between, and are marked in Figure 7.13. One year's of wind data was obtained, in the form of 10 minute average wind speed samples, resulting in over 52500 samples. The data was then binned into 1m/s bins and used to produce the histograms in Figure 7.14.

Figure 7.14 shows that the wind speed required to create the hypothesised Burling spectrum appears to be very commonly exceeded at the array of sites investigated. Wind speeds equal to or above 3m/s are available in excess of 90% of the time, and that wind speeds of 2m/s and above are available over 97% of the time. Therefore, so long as the deployment site is not located with a leeward shore within 10-20km, the hypothesised Burling spectrum should be present in excess of 90% of the time. If the deployment site is sheltered by a nearby shore, then the occurrence of the hypothesised Burling spectrum may be reduced by the percentage of time the wind blows from that particular direction.

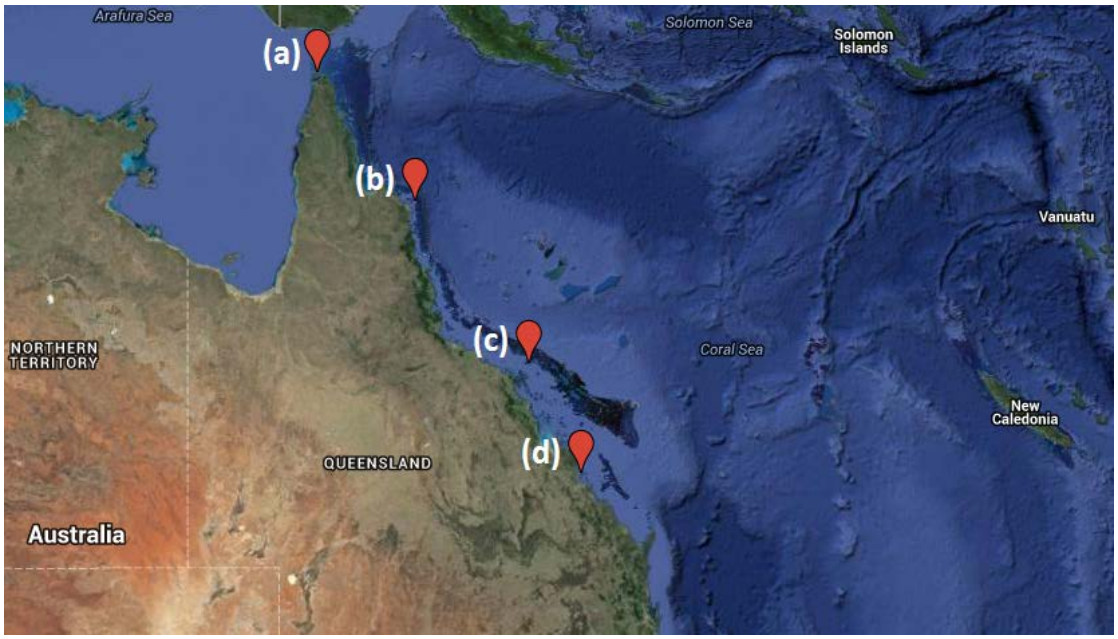


FIGURE 7.13: The locations of the wind speed measurements (a) Thursday Island, (b) Lizard Island, (c) Hardy Reef and (d) Square Rocks.

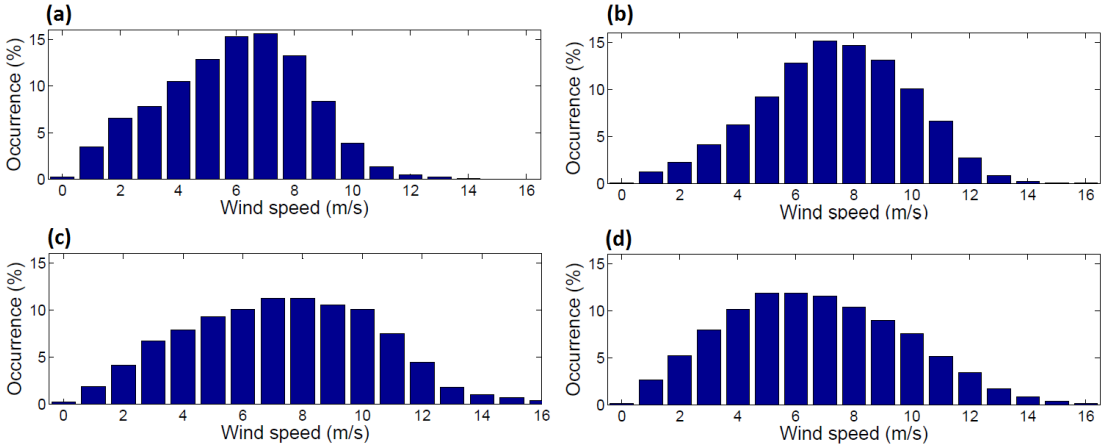


FIGURE 7.14: The percentage occurrence of wind speeds at (a) Thursday Island, (b) Lizard Island, (c) Hardy Reef and (d) Square Rocks.

### 7.2.3 The high frequency cut-off for input spectrum

The low frequency cut-off for the Burling spectrum has been selected at 3.14 rad/s, this section assesses the selection of the high frequency cut-off. The Burling spectrum decays with the negative fifth power of the frequency and very rapidly becomes negligibly small. Therefore, there will be no discernible difference to the WEC performance between any two Burling spectra which both have sufficiently large cut-off frequencies, so selecting any arbitrarily large high frequency cut-off will ensure accurate results. However, while it is trivial to calculate the spectrum value in the frequency domain for arbitrarily

high frequencies, and is also not too demanding to include a large number of sinusoidal components in the time domain to accommodate a broad frequency range, choosing a parsimoniously small high frequency cut-off value saves a great deal of computation from the system side. Calculating the hydrodynamic co-efficients is done on a frequency by freqeucny basis. Additionally, it is performed on a a panel by panel basis over the body geometry, and the higher the frequency values the smaller the panel sizes need to be. Therefore, both the number of frequencies to be calculated and the number of panels to be solved for at each frequency increases when the high frequency cut-off increases, significantly increasing the computation time to obtain the hydrodynamic coefficients for each WEC geometry.

Figure 7.15 shows the significant wave height and power per metre of wave front as a function of the high frequency cut-off. The significant wave height asymptotes to a value of 0.17m and the power to asymptotes to 23 W/m. From this graph, the high frequency cut-off is selected at 8 rad/s, where the power is 99% of its asymptotic value.

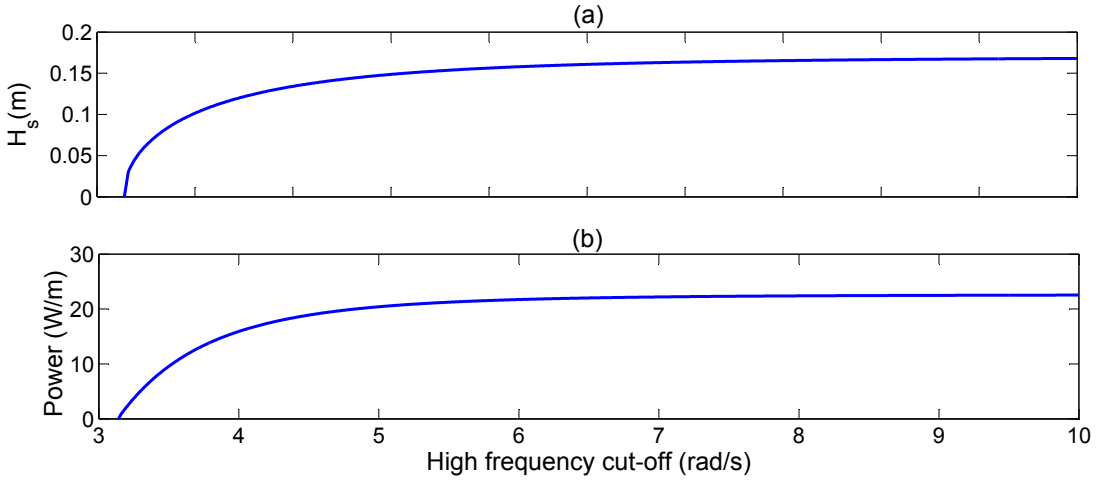


FIGURE 7.15: The significant wave height, (a), and power per metre of wave front, (b), as a function of the high frequency cut-off for the Burling spectrum.

## 7.3 The input wave spectra for pitch motion analysis

The truncated Burling spectrum is selected to assess the power output of the CIPMLG WEC because it is omnipresent, irrespective of the site location and time, representing the minimum wave spectrum expected anywhere. Energy content from other parts of the spectrum will, at worst, only add extra power to the output. However, for the analysis of the WEC's pitch motion, the pitching angle must be minimised in response to all input waves. Therefore, while the pitch motion must be kept small during for the truncated Burling spectrum, it must also be kept small for the low frequency part of

the spectrum as well. In fact, the low frequency part of the spectrum contains much more energy, so it is especially important that the PDTF be very small in this frequency range. To analyse the pitch motion, PM spectra with increasing wind speeds will be used as input, to assess its performance across a wide range of possible sea states.

## 7.4 Summary of the input wave spectrum

The input wave spectrum drives the output for a given WEC system. The variability of the input wave spectrum, both temporally at a specific site and spatially between different sites, means the performance of the WEC will also be variable, whereby a design that works well at one particular site or time, may not perform well at the next. However, the analysis identified that the high frequency tail of ocean wave spectra is omnipresent spatially and temporally and is well suited to the inherently high natural frequencies of the small sized buoy and linear generator of the proposed CIPMLG WEC.

The high frequency tail characterised by the Burling spectrum, Equation 7.1, between 3.14 and 8 rad/s shall be used as input for the subsequent assessment of the WEC performance, presented in Chapters 7 and 8. Figure 7.16-(a) plots the truncated Burling spectrum to be used as input for assessment of the WECs performance and Figure 7.16-(b) plots a realisation of the FSE derived from the this input spectrum. The hypothesis is that the output power calculated by this input will always be matched or surpassed at any given site and time, because any given ocean wave spectra will always contain, at minimum, this part of the spectrum.

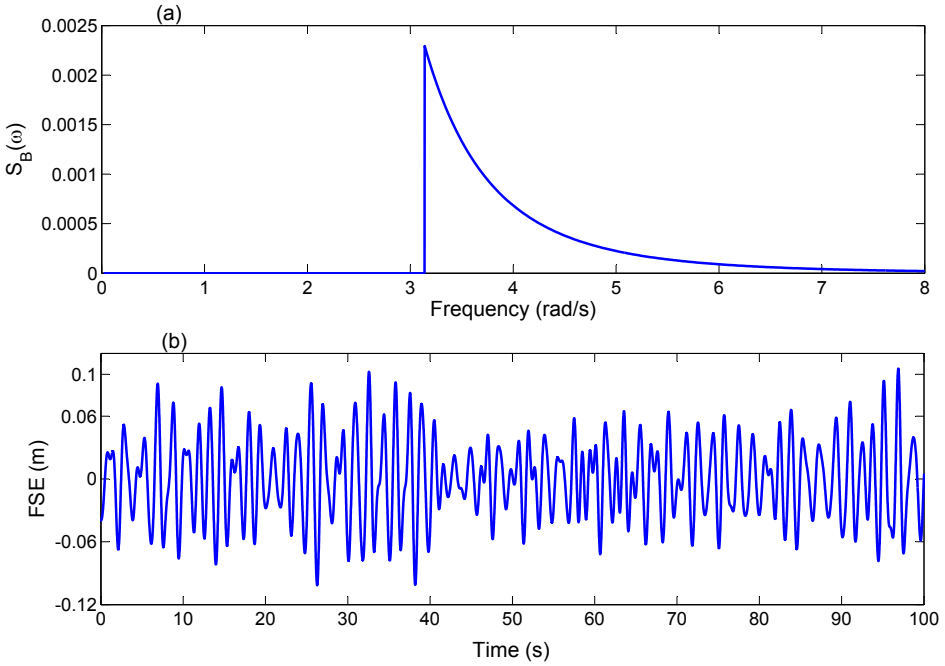


FIGURE 7.16: (a) The truncated Burling spectrum to be used as input for assessment of the WECs performance, (b) Time domain realisation of the Burling spectrum in (a).

# Chapter 8

# Results of the CIPMLG Wave Energy Converter analysis

## 8.1 Introduction

In this chapter, the numerical model developed in Chapter 5, is used to calculate the output power, stroke displacement and pitch displacement of the CIPMLG WEC, in response the input wave conditions described in Chapter 7. The results of these calculations are analysed and presented, with the aim of selecting values for the design parameters which best allow the CIPMLG WEC to fulfil the performance requirements outlined in the design problem (Section 4.3.3.1).

The performance requirements entail; harvesting 1W of average power, minimising the size and weight of the device, designing a 'one size fits all' device able to perform well in any deployment site, and minimising the pitch motion of the device. A 'one size fits all' device is ensured in this analysis, by using the wave conditions identified from Chapter 7 as input for the design process, because these waves are present at all locations and times. Minimising the size and weight of the device will be achieved by constraining the total system mass to small values. Once the total mass is constrained, the design parameters will be optimised for that particular mass value, with the objective of maximising the output power and minimising the pitch motion. By examining a number such constrained total system mass cases, this chapter will estimate the smallest possible size and weight for the CIPMLG WEC which can fulfil the output power and pitch resilience requirements.

Section 8.2 will examine a 20kg device, Section 8.3 a 40kg device and Section 8.4 an 80kg device. Section 8.5 then outlines a number practical aspects that should be considered

when analysing the results from the numerical model, such as; the effect of mechanical damping and generator efficiencies, the realistically achievable levels of electromagnetic damping by the IPMLG within the geometrical constraints of the WEC, the physically realisable spring constant values, and the effect of the translator mass on the pitch motion. Section 8.5 then concludes by considering the results presented in Sections 8.2-8.4 in conjunction with the outlined practical issues, to answer whether the CIPMLG WEC can fulfil the performance requirements. Section 8.6 then proposes an improvement to the cylindrical WEC geometry and shows some results. Finally, the chapter is summarised and conclusions given in Section 8.7.

## 8.2 Results for a twenty kilogram system

Here the total system mass is constrained to 20kg. This section first investigates the maximum output power that the 20kg system can produce. Next the stroke is analysed, to ensure that the stroke lengths required to produce the maximum power are feasible within the geometrical constraints of the buoy's hull. Finally, the pitch motion for the 20kg system is assessed.

### 8.2.1 Power

The output power is dependent on the buoy's radius and draught, the generator's damping, spring constant and translator mass. The goal of this section is to find the best combination of these parameters to maximise the output power for the 20kg device. Section 8.2.1.1 outlines the analysis approach used to search the parameter space for the maximum output power, and then Section 8.2.1.2 presents the results.

#### 8.2.1.1 Analysis approach

Once the total mass of the CIPMLG WEC is set, the radius and draught values become related, via Equation 6.1, and follow the contour lines of constant mass plotted in Figure 6.1. The analysis approach therefore first sets the radius value, which in turn immediately sets the draught value. Additionally, once the draught value is set, the maximum allowable stroke length becomes constrained, because it is assumed herein that the stroke length can't exceed half the draught value ($X_{sL} < 0.5D$) to ensure that the generator can fit inside the buoy. Constraining the maximum allowable stroke length, constrains the generator natural frequency above a minimum value, $\omega_{ng(MIN)}$, given by

the relationship in Equation 6.11:

$$\omega_{ng(MIN)} = \sqrt{\frac{g}{0.5D}}. \tag{8.1}$$

which for the 20kg buoy can be expressed in terms of the radius as:

$$\omega_{ng(MIN)} = \sqrt{\frac{\rho_w g \pi R^2}{10}}. \tag{8.2}$$

The next step in the analysis approach is to set the generator natural frequency value, $\omega_{ng}$. For most radius values, the maximum power output occurs when $\omega_{ng} = \omega_{ng(MIN)}$, because $\omega_{ng(MIN)}$ is generally already much higher than the peak frequency of the input wave spectrum. Therefore, the pragmatic approach taken by the present analysis is to set $\omega_{ng}$ to $\omega_{ng(MIN)}$, and then incrementally increase $\omega_{ng}$ until the output power reduces (which generally occurs immediately).

Once $\omega_{ng}$ is set, the spring constant and translator mass values become related via Equation 6.6. At this point, only two parameters remain free, the generator damping value and either the spring constant or translator mass value. The two free parameters can then be varied and analysed on a contour plot, from which the maximum power can be determined for the given radius and $\omega_{ng}$ combination.

The advantage of using this analysis approach, rather than a numerical optimisation scheme to search for the optimal parameter combination, is that the contour plots allow the effect of the free parameters to be visually analysed. Indeed, a numerical optimisation scheme, such as a genetic algorithm, could be used from the outset to search through all the parameter combinations and return the parameter values which yield the maximum output power. However, the visual analysis of the contour plots gives an insight into the dependence of the output power on the different parameters. Such visual insights can be useful, for example, when investigating trade-offs between generator damping, translator mass/ and output power values. An additional set back to using a numerical optimisation scheme for the present analysis is that the hydrodynamic co-efficients for the WEC geometry would need to be calculated inside of the optimisation loop, putting a high computational demand on each loop iteration.

### Comparison of three different buoy radii

The analysis approach is applied here to three 20kg CIPMLG WECs with varying radius values. Figures 8.1 -(a), (b) and (c) show the output power for a 20kg CIPMLG WEC with a radius of 0.05, 0.1 and 0.2m, respectively. The $\omega_{ng}$ value for each WEC is set to

$\omega_{ng(MIN)}$ for the given radius value. The generator damping and translator mass values are then varied along the $x$ and $y$ axis, respectively.

The 0.05m radius WEC is shown in Figure 8.1 -(a), where the maximum output power is less than 1mW and occurs for a very lightly damped generator combined with a translator mass 20% of the total WEC mass. For the 0.10m radius WEC in Figure 8.1-(b), the output power is over 1W for generator damping values of 3 - 30Ns/m combined with translator mass values over 50% of the total WEC mass. The 0.20m radius WEC in Figure 8.1-(c), shows output power values of over 0.4W for generator damping values of 200 - 500Ns/m combined with translator mass values over 90% of the total WEC mass.

Of the three different WECs compared in Figure 8.1, the one with the radius of 0.10m is seen to offer the best performance, which can be attributed to its buoy's natural frequency, $\omega_{nb}$, coinciding with a high amplitude region of the input truncated Burling spectrum (Figure 7.16). The natural frequencies of the 0.05, 0.10 and 0.20m radius buoys are 2.0, 3.7 and 6.2 rad/s, respectively, whereas the input truncated Burling spectrum is zero for frequencies below its peak at 3.14 rad/s, and then decreases rapidly with increasing frequency away from its peak (to less than 10% of the peak value by 5 rad/s). The 0.10m radius buoy's natural frequency of 3.7 rad/s is therefore well aligned with the input truncated Burling spectrum. The natural frequency of the 0.05m radius buoy occurs where the input truncated Burling spectrum has zero amplitude and thus results in very low power outputs, however it would likely achieve higher power outputs than this in real wave spectra which do not abruptly decrease to zero amplitude at frequencies below 3.14 rad/s.

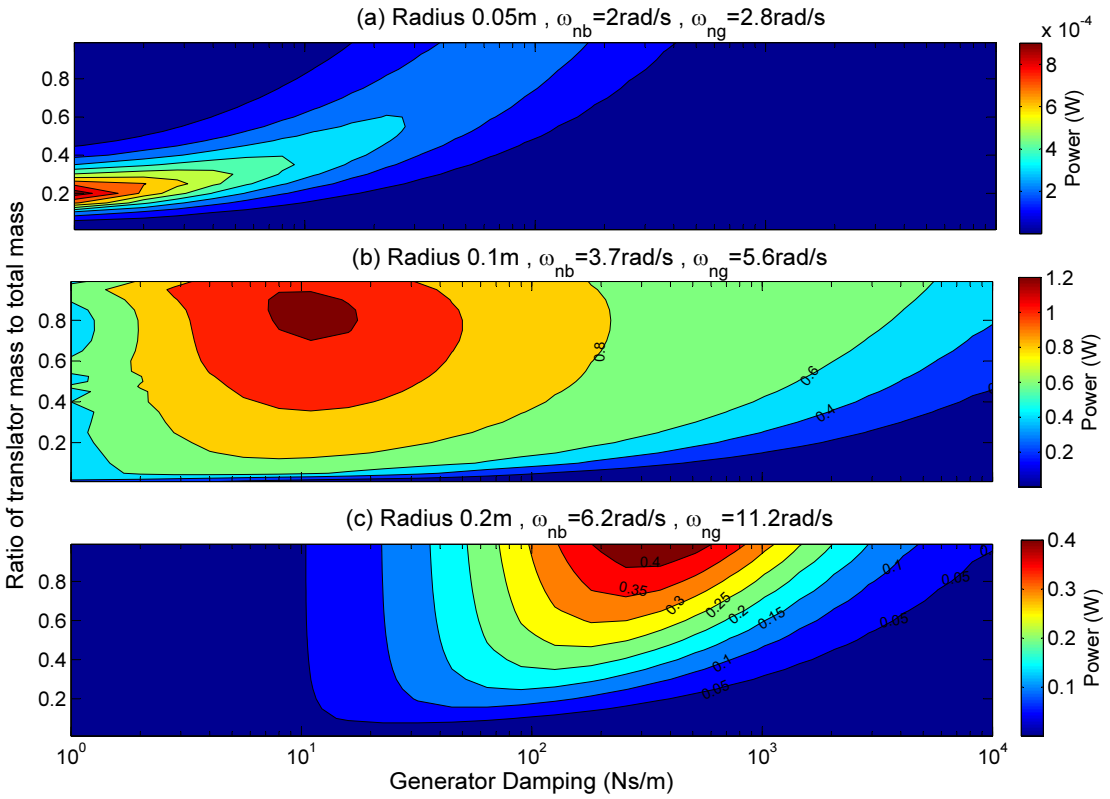


FIGURE 8.1: Output power as a function of generator damping and translator mass for three 20kg CIPMLG WECs with differing radius values.

### Changing the generator's natural frequency

The results presented in Figure 8.1 assumed the $\omega_{ng}$ value equalled $\omega_{ng(MIN)}$, for the given radius value. For the 0.10 and 0.20m radius WECs, $\omega_{ng(MIN)}$ equals 5.6 and 11.2 rad/s respectively, therefore increasing the value of $\omega_{ng}$ greater than $\omega_{ng(MIN)}$, only serves to move $\omega_{ng}$ further from the high amplitude region of the input truncated Burling spectrum (3.14 - 5 rad/s). However, for the 0.05m radius buoy, $\omega_{ng(MIN)} = 2.8$ rad/s, therefore $\omega_{ng}$ is set below the peak of the truncated Burling spectrum. The effect of using a higher generator natural frequency for the 0.05m radius buoy, by reducing the stroke limit below the maximum allowable length, is investigated in Figure 8.2.

Figure 8.2-(a) shows the results for the 0.05m radius WEC when $\omega_{ng}$ is increased to the peak of the input truncated Burling spectrum, at 3.14 rad/s. A four fold increase in the maximum power can be seen in Figure 8.2-(a) compared to the case in Figure 8.1-(a). Additionally, the region in the contour plot (in the generator damping - translator mass parameter plane) of high output power values is seen to broaden, with 50% of the maximum power value available for a wider range of generator damping and translator mass values. The $\omega_{ng}$ value was then incrementally increased from 3.14 rad/s, and the maximum power output value was found to correspondingly decrease, while the region in the contour plot of maximum power output was seen to broaden. At an

$\omega_{ng}$ value of 3.3 rad/s, plotted in Figure 8.1-(b), the maximum output power value occurs everywhere along a parabolic curve in the generator damping - translator mass plane, from $d$=1Ns/m combined with $m = 0.1M_{Total}$ up to $d$=100Ns/m combined with $m = 0.99M_{Total}$. Further increasing the $\omega_{ng}$ value reduces the maximum output power, while the region of maximum power in the contour plot shrinks and moves towards larger damping and translator mass values, as shown in Figure 8.2-(c) for the case of $\omega_{ng} = 3.6$ rad/s.

For the 0.1 and 0.2m radius buoys, from Figures 8.1-(b) and -(c), the maximum power was found to occur for $\omega_{ng} = \omega_{ng(MIN)}$. Increasing $\omega_{ng}$ resulted in the maximum output power decreasing in value while occurring for larger generator damping and translator mass values.

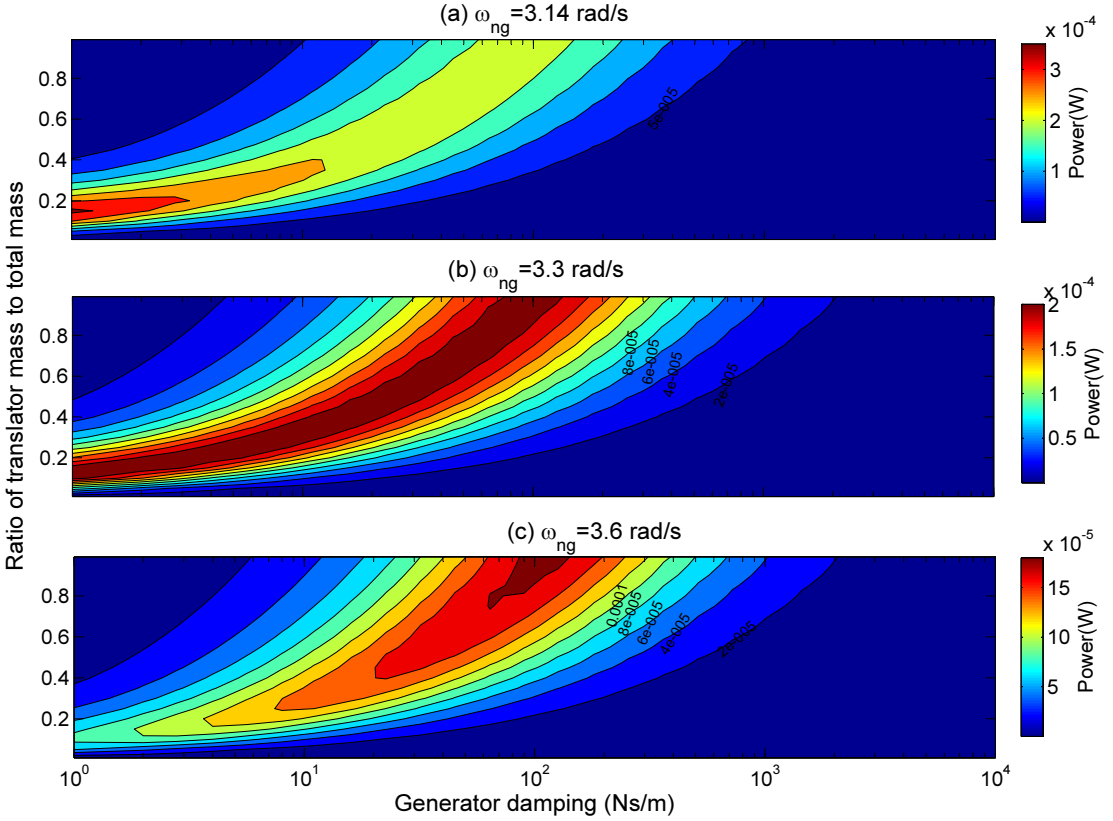


FIGURE 8.2: Output power as a function of generator damping and translator mass for a 20kg buoy with 0.05m radius and varying $\omega_{ng}$.

#### 8.2.1.2 Results

Here the analysis approach is used to determine the maximum power output for the 20kg CIPMLG WEC. The examples shown in Figure 8.1 revealed the importance of selecting the radius of the buoy, such that the buoy's hydrodynamic natural frequency,

$\omega_{nb}$, matches well with the input truncated Burling spectrum. Figure 8.3, plots the contour lines for a 20kg buoy (also 40 and 80kg buoys) as a function of radius and draught, superposed with the contour lines of $\omega_{nb}$. The input truncated Burling spectrum, Figure 7.16, is seen to have a large amplitude between 3.14 and about 5 rad/s, which from Figure 8.3, is seen to equate to a 20kg buoy with a radius of about 0.09 to 0.14m.

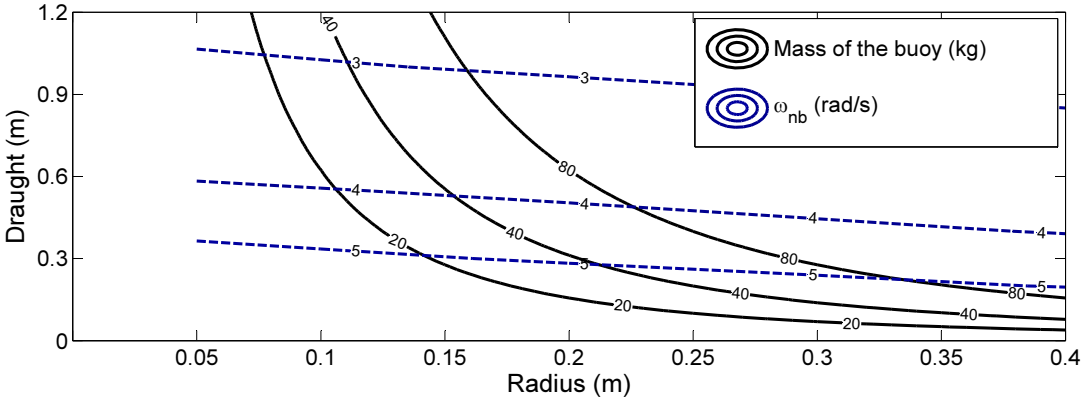


FIGURE 8.3: Mass and hydrodynamic natural frequency of the buoy as a function of radius and draught.

Figure 8.4 plots the maximum output power value obtained for different radius values, where the same range of generator damping and translator mass values as in the contour plots of Figures 8.1 were considered, but only the maximum output power value is presented. Figure 8.4 shows that a WEC with a 0.11m radius produces the greatest amount of power, which has a $\omega_{nb}$ of 4.1 rad/s and a $\omega_{ng}$ of 6.2 rad/s.

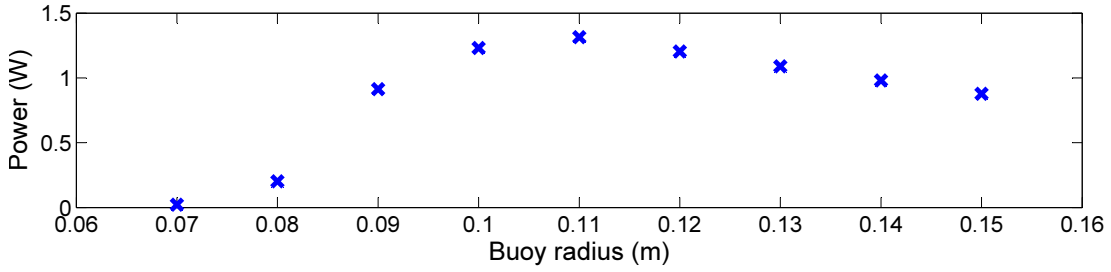


FIGURE 8.4: Maximum putput power for 20kg bouy for varying radius values.

Figure 8.5 displays the output power contour plot for the 0.11m radius 20kg WEC, showing that the maximum power is above 1.2W and occurs for a generator damping value of 10 - 80 Ns/m combined with very large translator mass values. The region on the generator damping - translator mass plane in which half the maximum output power is available is very large, covering close to half of the displayed contour plot, ranging from $d$=2Ns/m combined with $0.1M < m < 0.99M$, to $d$=100Ns/m combined with $0.2M < m < 0.99M$, up to $d$=3000Ns/m combined with $m = 0.99M$.

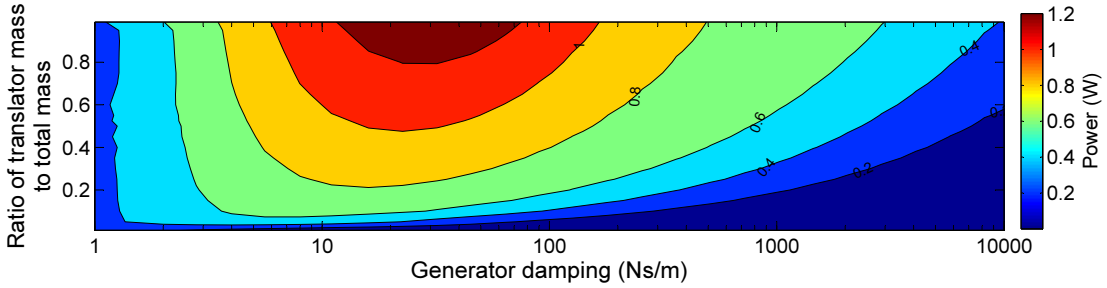


FIGURE 8.5: Power as a function of generator damping and translator mass for a 20kg buoy with 0.11m radius ($\omega_{nb}$ 4.1 rad/s, $\omega_{ng}$ 6.2rad/s).

### Constraining the translator mass value

The results showed that the maximum output power occurs for translator mass values approaching 100% of the total mass. Clearly this is infeasible, as the buoy itself will have significant mass due to the weight of the hull, ballast mass, the generator coils, batteries, MBS components such as sensors, antenna for data transmission, etc. Therefore, in the analysis to follow, the translator mass will be assumed to be constrained to a maximum value of 50% of the total mass, and the maximum output power will be searched for within translator mass values below this.

Figure 8.6 is the equivalent of Figure 8.4, except that the translator mass is constrained to a maximum value of 50% the total mass. Here, the maximum output power value of 1.1W is seen to occur for a buoy with a radius of 0.10m. The output power contour plot for the 0.10m radius buoy is displayed in Figure 8.7, where output power values in excess of 1W can be seen for generator damping values around 10Ns/m combined with translator mass values above 35% of the total mass.

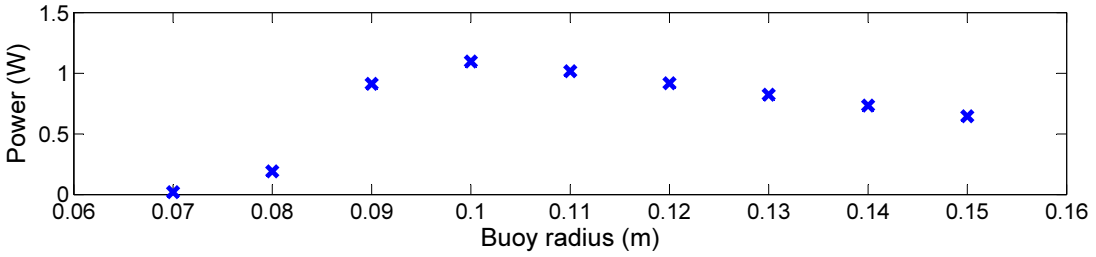


FIGURE 8.6: Maximum output power for 20kg bouy, with the translator mass value constrained less than 50% of the total mass, for varying radius values.

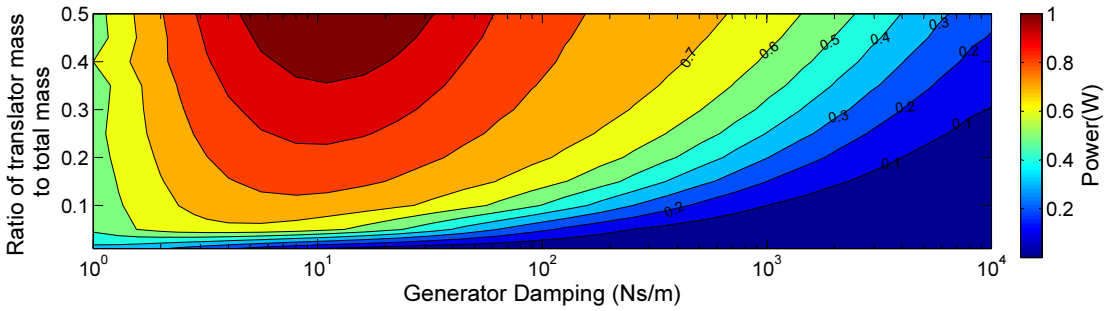


FIGURE 8.7: Output power as a function of generator damping and translator mass for a 20kg buoy with 0.10m radius ($\omega_{nb}$ 3.8 rad/s, $\omega_{ng}$ 5.6 rad/s).

### 8.2.2 Stroke

Figure 8.8 displays a contour plot of the RMS stroke displacement for the 0.10m radius 20kg CIPMLG WEC, where a maximum value of around 0.23m occurs when the generator is very lightly damped. The RMS stroke displacement is seen to decrease with increasing generator damping, with a value of about 0.1m at 10 Ns/m, where the maximum output power occurs in Figure 8.7. The RMS stroke displacements in Figure 8.8 do not exceed the maximum allowable stroke length of 0.31m for the 0.10m radius CIPMLG WEC (which has a draught of 0.62m).

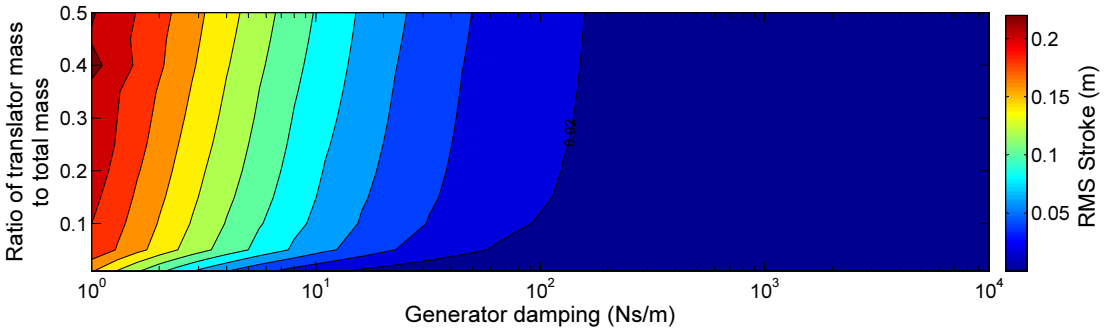


FIGURE 8.8: RMS stroke displacement as a function of generator damping and mass for a an 20kg buoy with 0.10m radius.

To examine whether the maximum stroke displacements are also less than the maximum allowable stroke length, time domain analysis is used. Figure 8.9 is a plot of the stroke displacement in the time domain for a 20kg buoy with a 0.10m radius, $\omega_{ng}$ of 5.6 rad/s, generator damping of 10Ns/m and translator mass 40% of the total mass. The system in Figure 8.9 has an RMS stroke displacement of 0.09m and the stroke displacement is seen to exceed the RMS value 31% of the time with a maximum value of 0.27m, about 3 times the RMS value. Examining 100 time series, revealed that in general the stroke displacement exceeded the RMS value an average of 32% of the time, the maximum

value was on average 2.9 times the RMS value and the overall maximum displacement from the 100 times series was 3.7 times the RMS value.

Taking the average across all the systems in Figure 8.8, the stroke displacement was found to exceed the RMS value 33% of the time and the maximum stroke displacement was 2.8 times the RMS value. Therefore, only systems with RMS stroke displacement values less than about 0.11m will have maximum stroke displacements less than the maximum allowable stroke length of 0.31m. Figure 8.8 shows that systems with generator damping values greater than about 10Ns/m have RMS stroke displacements less than the required 0.11m.

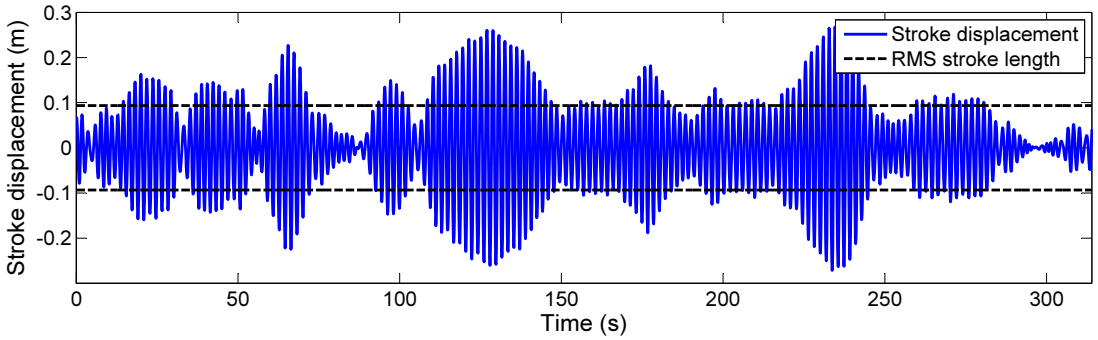


FIGURE 8.9: The time domain stroke displacement for a 20kg buoy with a 0.10m radius, $\omega_{ng}$ of 5.6 rad/s, generator damping of 10Ns/m and translator mass 40% of the total mass.

### 8.2.3 Pitch

The preliminary analysis in Section 6.5 showed that the pitch motion is dependent on the CIPMLG WEC's radius, draught, CoM and MoI. Section 7.3 then described that the CIMPLG WEC's pitch motion will be evaluated across a wide range of possible sea states, whereby PM spectra with increasing wind speeds are used as input. Therefore once the radius and draught are set, the pitch motion is dependent on three variable parameters; the CoM, the MoI and the input wind speed.

The effect that these three parameters have on the pitch resilience of the CIPMLG WEC, will be analysed in this chapter using contour plots of the RMS pitch displacement. Two of the parameters will be varied on the $x$ and $y$ axes of the contour plot, and the third parameter will be varied across a number of these plots. Figure 8.10 is such a contour plot of the RMS pitch displacement for the 0.1m radius 20kg CIPMLG WEC. The wind speed used to create the input PM spectrum is varied along the $y$-axis, ranging from 3m/s up to 15m/s, and the vertical position of the buoy's CoM is varied along the $x$-axis, ranging from 50% to 100% of the draught depth, so that it remains at or below the

buoy's CoB and within the buoy's geometry. The MoI is then varied between Figures 8.10-(a), (b) and (c).

The MoI considers three cases, which are determined from; the smallest possible MoI value (the case shown in Figure 6.2 - (b)), the largest possible MoI value (the case shown in Figure 6.2 - (d)), and a value which is chosen geometrically half way between the smallest and largest values. The smallest possible MoI value for the 0.10m radius 20kg CIPMLG WEC, is calculated from a solid sphere, $I = \frac{2}{5}MR^2$, which for a 20kg ball of steel with density 7600kg/m$^3$ equals 0.059kgm$^2$. The largest possible MoI value occurs when the mass is distributed as far from the CoM as possible, which can't exceed the extreme case of a point mass of 20kg located a the length of the draught, 0.62m, away, $I = MR^2 = 20 \times 0.62^2 = 7.7$kgm$^2$. From these two extreme values, MoI values of 0.05, 0.5 and 5kgm$^2$ are selected for analysis of the 20kg WEC, shown in Figures 8.10-(a), (b) and (c) respectively.

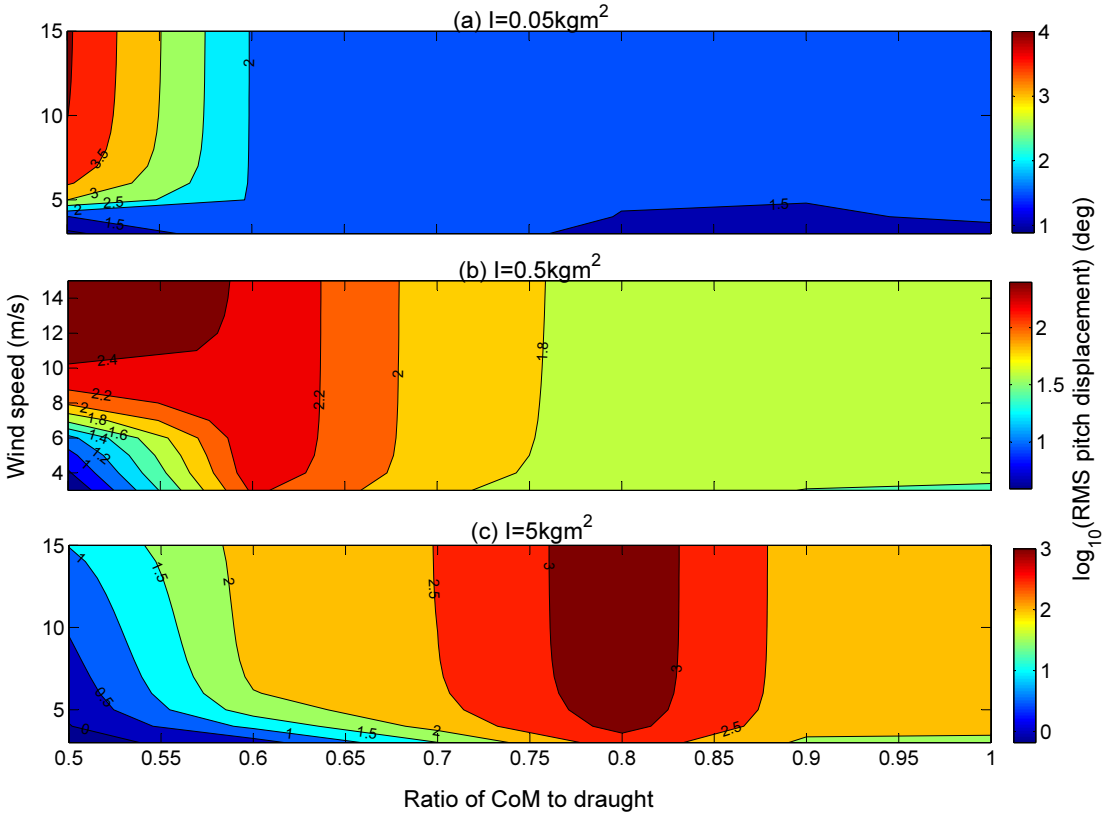


FIGURE 8.10: RMS pitch displacement (plotted on a logscale), for a 20kg buoy with 0.10m radius, as a function of the CoM's depth and the input PM spectrum sea state parameterised by the wind speed.

The pitch displacements in Figure 8.10 are plotted in a log base 10 scale and are seen to reach values as large as 10,000 degrees ($10^4$). This is a clear limitation of the linear modelling approach taken, which is only valid for small displacements. Once the pitch

displacement exceeds a certain angle the buoy will capsize and no longer be adequately described by the linear model. Simulations which result in pitch displacement values exceeding 90 degrees can be considered non physical and relate to WEC configurations that are vertically unstable.

The results displayed in Figure 8.10 show that the systems with smaller MoI values, Figures 8.10 -(a) and (b), have smaller pitch displacements than the system with the large MoI value, Figure 8.10-(c). This can be explained by comparing Figures 6.23 and 7.1, where it can be seen that increasing the MoI values in Figure 6.23 decreases the PDTF's resonant peak towards the low frequencies where the PM wave spectra in Figure 7.1 have large amplitudes. Increasing the depth of the CIMPLG WEC's CoM is shown in Figures 8.10 -(a) and (b) to reduce the pitch motion, and also decrease the dependence of the pitch displacement on the input wave spectrum (illustrated by the nearly vertical contour lines). Whereas for the system with the large MoI value, in Figure 8.10 -(c), the maximum pitch motion occurs when the CoM is 80% of the draught depth. The reasons for the different results obtained for the different MoI and CoM values is further examined in Section 8.2.3.2, by investigating the PDTFs.

The pitch constraint, outlined in Section 4.3.3.2, required that the pitch displacement remain less than 40 degrees, which equates to 1.6 on the log base 10 scale plotted in Figure 8.10. The results in Figure 8.10 show that, only systems with small MoI values and with CoMs near 100% of the draught depth, have RMS pitch displacements less than the required $10^{1.6}$ degrees constraint. However the pitch displacement will often be greater than the RMS value, as displayed in Figure 8.11, which is a time domain plot for the case of a 10m/s input wind speed, MoI value of 0.5kgm$^2$ and CoM value of 80% of the draught depth. The system in Figure 8.11 has a RMS pitch displacement of 53 degrees ($10^{1.7}$ degrees) and the pitch displacement exceeds the RMS value over 30% of the time, with a maximum value of 162 degrees, over 3 times the RMS value.

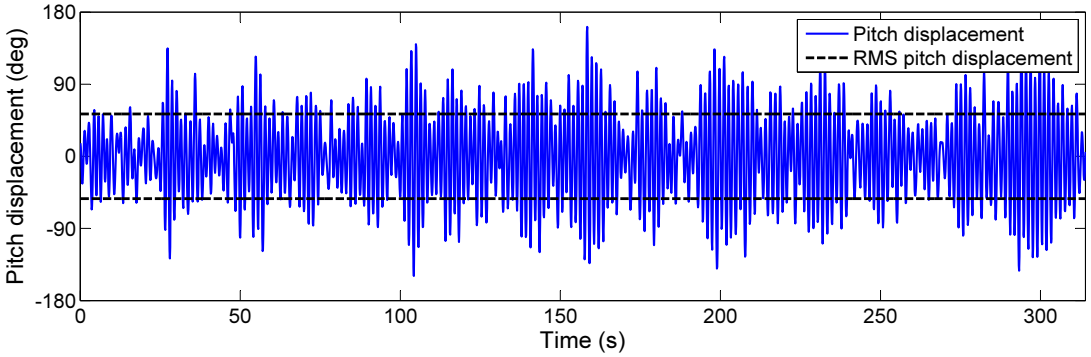


FIGURE 8.11: Time domain pitch displacement for a 20kg buoy with 0.10m radius, I=0.5kgm$^2$, CoM 80% of the draught depth in a 10m/s wind speed PM spectrum.

Figure 8.12 shows that the maximum pitch displacement is in general 1.5 to 3.5 times larger than RMS depending on the windspeed, CoM and MoI parameters, whereby the maximum values reported in this figure are obtained by taking the average maximum value from 50 time domain simulations. Considering that the maximum displacement can be up to 3.5 times the RMS displacement, the RMS pitch displacement should therefore aim to remain below 12 degrees ($10^{1.08}$ degrees) to ensure the CIPMLG WEC obeys the 40 degrees pitch constraint.

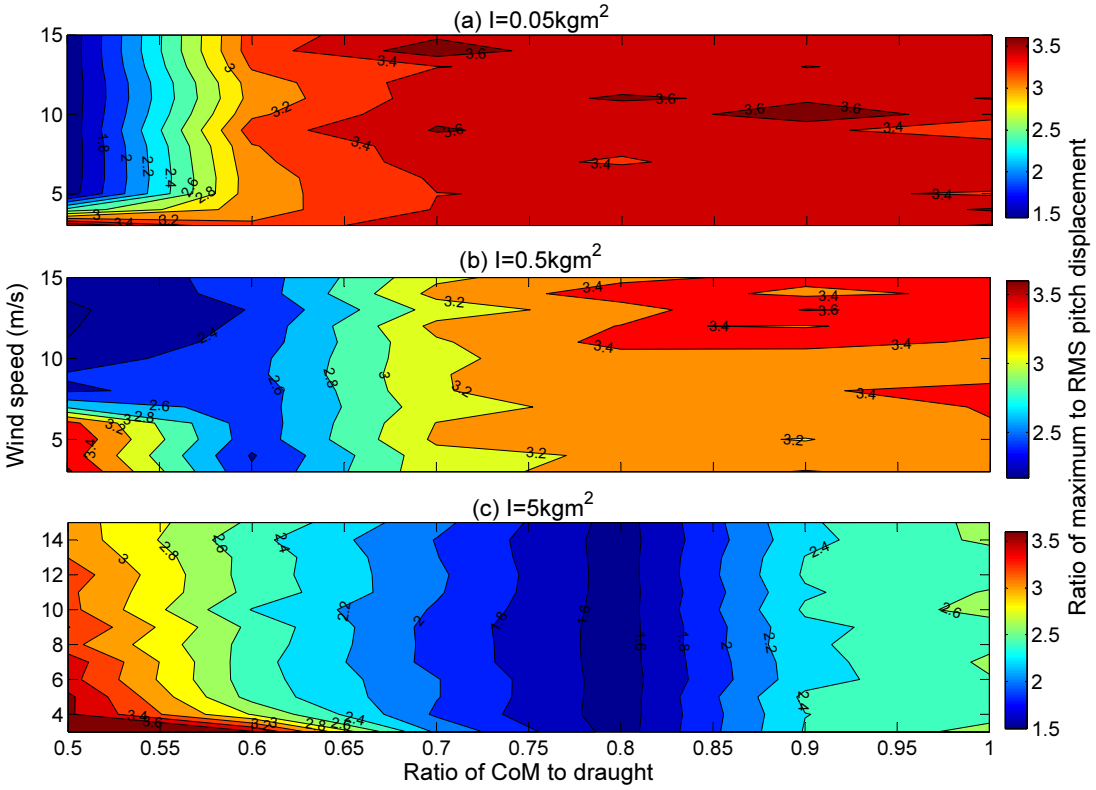


FIGURE 8.12: Ratio of the maximum pitch displacement to RMS pitch displacement, for a 20kg buoy with 0.1m radius, as a function of CoM and PM spectrum sea state parameterised by the wind speed.

#### 8.2.3.1 Increasing the buoy radius

The pitch displacement results in Section 8.2.3, indicated that the 20kg CIPMLG WEC with a 0.10m raidus is not well suited to satisfying the pitch constraints. The preliminary analysis in Section 6.5, revealed that buoys with larger radii were more pitch resilient than their thinner counterparts. Therefore in this subsection, the radius of the buoy is increased to examine its effect on the calculated pitch motion.

The buoy radius is increased to 0.15m in Figure 8.13, and then 0.20m in Figure 8.14. The results displayed in these figures show that an RMS pitch displacement does indeed decrease with increasing buoy radius. The ratio of the maximum pitch displacement

to the RMS pitch displacement, was found to slightly increase with the radius, with the maximum pitch displacement for the systems in Figures 8.13 and 8.14 being up to 3.7 times larger than the RMS value. Therefore, the RMS pitch constraint should be below 11 degrees ($10^{1.04}$ degrees), which the 0.2m radius buoy with very small MoI values would be able to satisfy, as shown in Figure 8.14-(a). However, the increased pitch stability of the larger radii values comes at the cost of decreased power output, whereby the maximum power output calculated for the 0.15m radius buoy was 0.65W and for the 0.20m radius buoy 0.30W.

Interestingly, the pitch displacement for the buoys with small MoI values, in Figures 8.13-(a) and 8.14-(a), have little dependence on the CoM values, resulting in horizontal contour lines. Whereas, the pitch displacement for the buoys with medium MoI values, in Figures 8.13-(b) and 8.14-(b), have little dependence on the input wind speed values, resulting in vertical contour lines. To understand why some of these contour plots are horizontally banded and some are vertically banded, with the effect being more pronounced for buoys with larger radii, the next subsection investigates the PDTFs from these systems to give an insight into this behaviour.

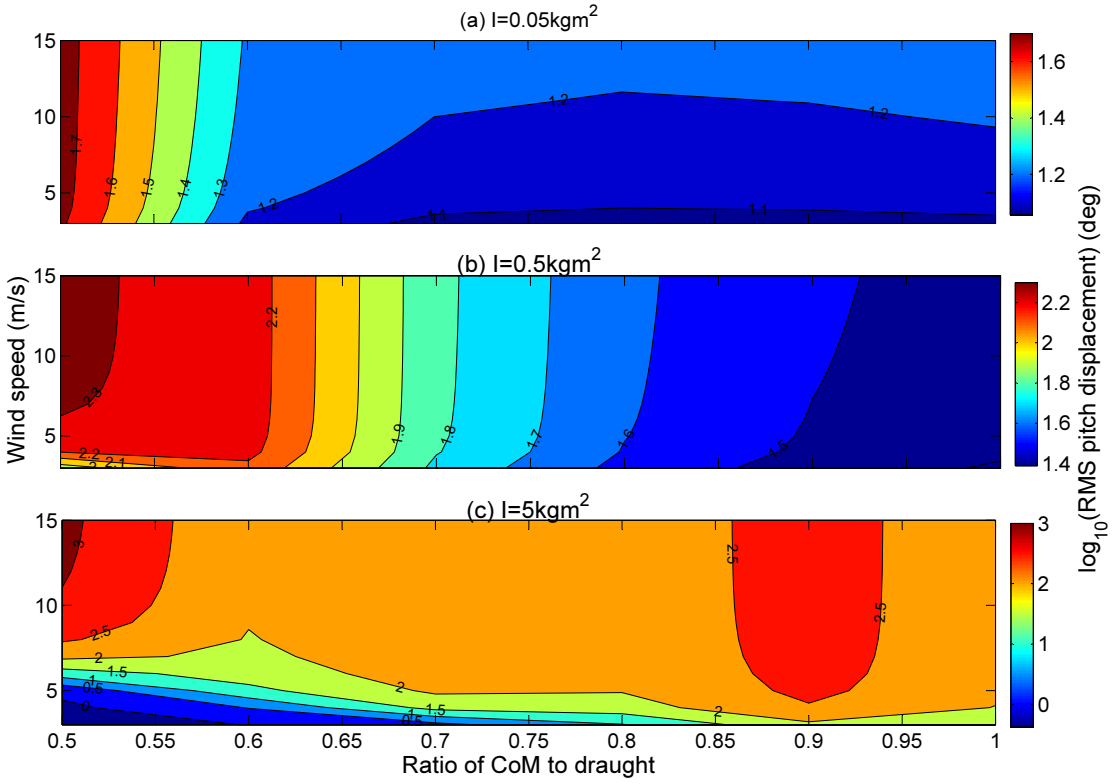


FIGURE 8.13: RMS pitch displacement, for a 20kg buoy with 0.15m radius, as a function of CoM and PM spectrum sea state parameterised by the wind speed.

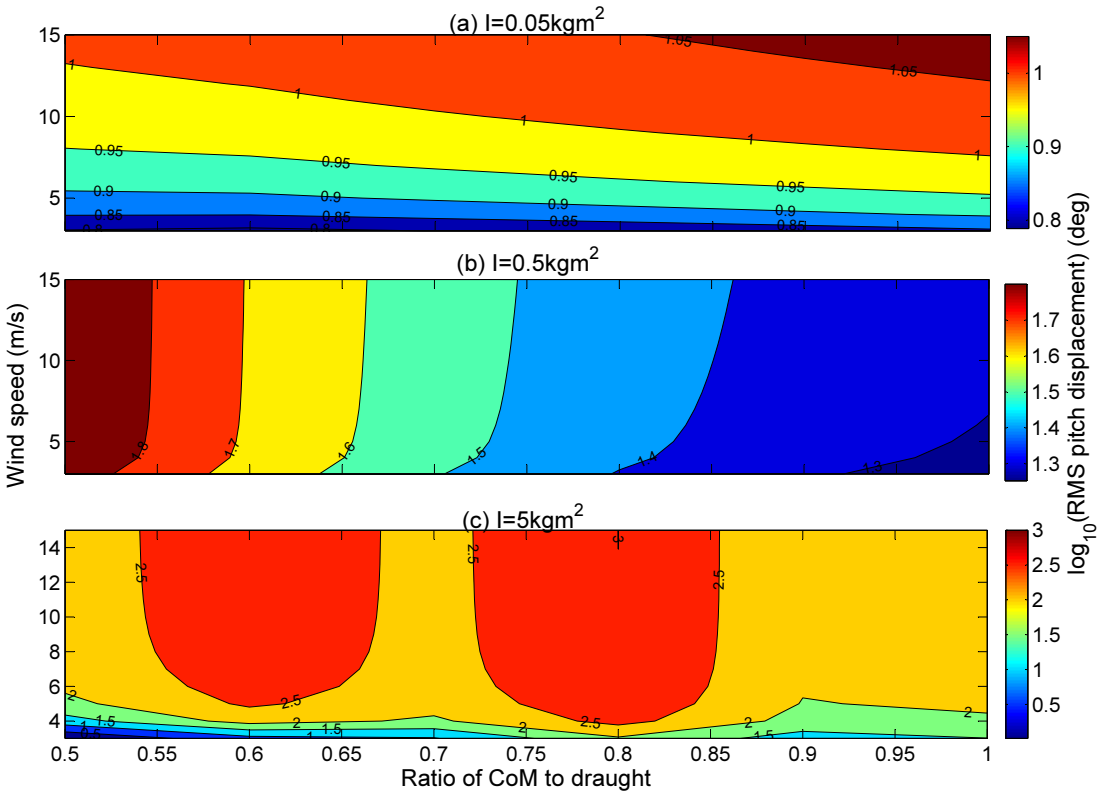


FIGURE 8.14: RMS pitch displacement, for a 20kg buoy with 0.20m radius, as a function of CoM and PM spectrum sea state parameterised by the wind speed.

#### 8.2.3.2 The pitch displacement transfer functions

To explain the different results obtained for the systems with different radius, MoI and CoM values in Sections 8.2.3 and 8.2.3.1, the PDTFs for these systems are examined here. The general effect of the design parameters on the PDTFs was discussed in Section 6.5. Here, the PDTFs for the systems considered in Figures 8.10 and 8.14, are plotted in Figure 8.15 to explain the resulting pitch displacements.

Comparing Figure 8.15 with Figures 8.10 and 8.14 shows that when the peak frequency of the PDTF is higher than the peak frequency of the input PM spectrum, then the output pitch displacement contour lines are vertical. The reason being, that once the peak frequency of the PDTF is in the tail of the PM spectrum, further increases in the wind speed only increases the amplitude of the input PM spectrum at lower frequencies and does not effect the amplitude of tail of the spectrum where the PDTF's peak is. Changing the depth of the CoM moves the peak frequency of the PDTF within the tail of the PM spectrum, and therefore changes the output pitch displacement, resulting in the vertically banded contour lines in Figures 8.10 - 8.14.

For the system whose output pitch displacement contour lines are horizontal, Figure 8.14-(a) and the deep CoM values in Figures 8.13-(a), the peak frequency of the PDTF occurs at very high frequencies where the input PM spectrum amplitudes are essentially zero. The amplitude of the PDTFs for the different CoM values are then equal in the lower frequency regions where the input PM spectrum is significant, therefore the output pitch displacements for these systems do not depend on the CoM, resulting in the horizontally banded contour lines.

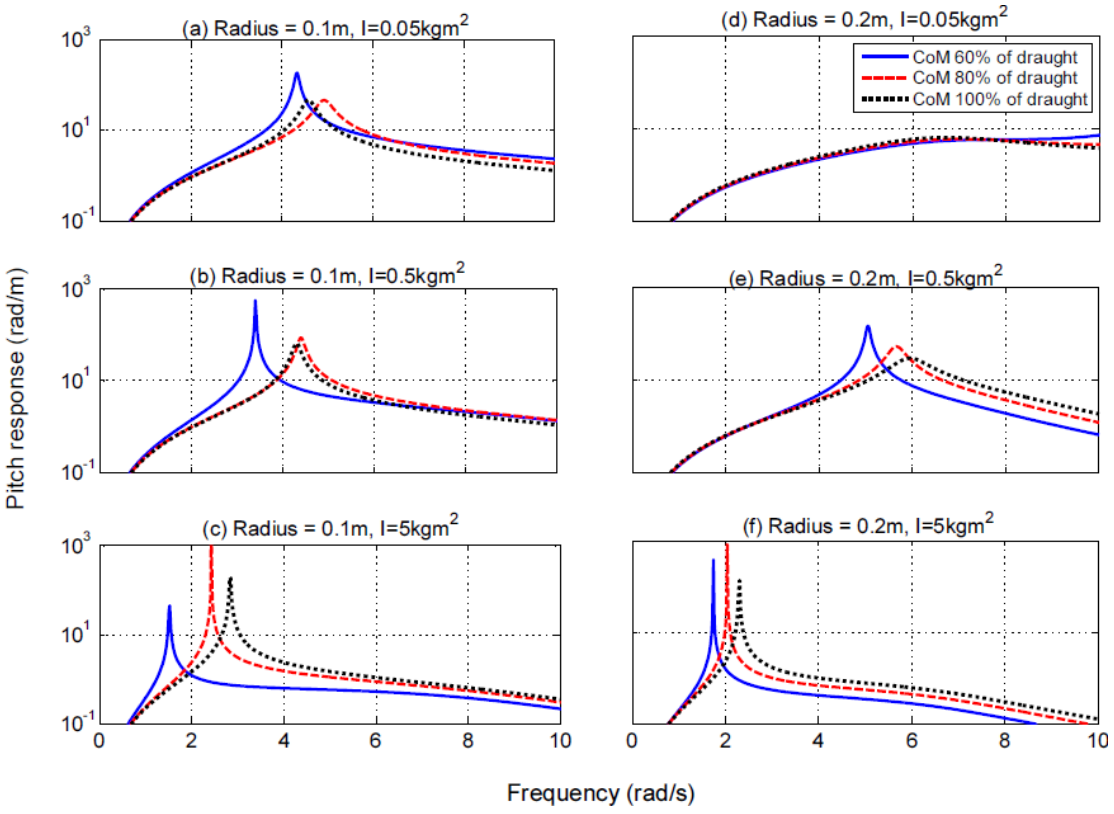


FIGURE 8.15: PDTF for a 20kg buoy with 0.10m and 0.20m radius, for various CoM and MoI values.

## 8.3 Results for a forty kilogram system

Here the CIPMLG WEC mass is increased to 40kg and a similar analysis approach is applied as for the case of the 20kg WEC in Section 8.2.

### 8.3.1 Power

Figure 8.16 plots the maximum output power of the 40kg CIPMLG WEC for various radius values, analogous to Figure 8.4, for the two cases of the translator mass being either unconstrained or constrained to 50% of the total mass. For small radius values,

the maximum output power for the two cases is equivalent. At a radius value of 0.14m, where $\omega_{nb=}$ 3.9 rad/s and $\omega_{ng}$ = 5.9 rad/s, the constrained translator mass case reaches its largest maximum power output of about 2W and the two cases begin diverging.

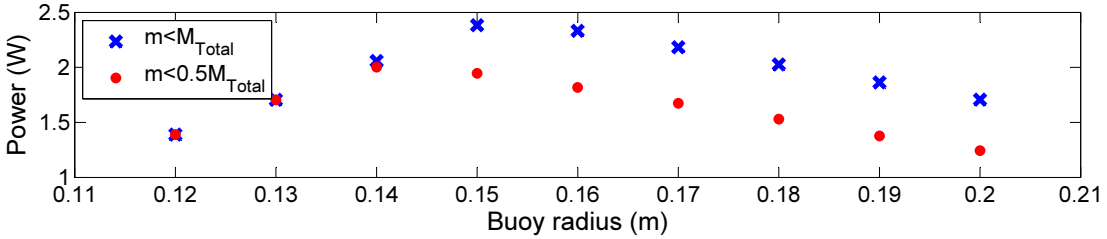


FIGURE 8.16: Maximum output power for 40kg bouy for varying radius values.

The output power contour plot for the 0.14m radius 40kg WEC, as a function of generator damping and translator mass (constrained to less that 50% of the the total mass), is shown in Figure 8.17. Here it can be seen that the maximum output power of 2W occurs for generator damping values of 20 - 60 Ns/m combined with translator masses 35 - 50% of the total WEC mass. Figure 8.17 also shows that the output power exceeds 1W for a very large range of generator damping and translator mass values, spanning from generator damping values of 3Ns/m combined with translator mass values over 5% of the total WEC mass up to generator damping values of 3,000Ns/m combined with translator mass values 50% of the total WEC mass.

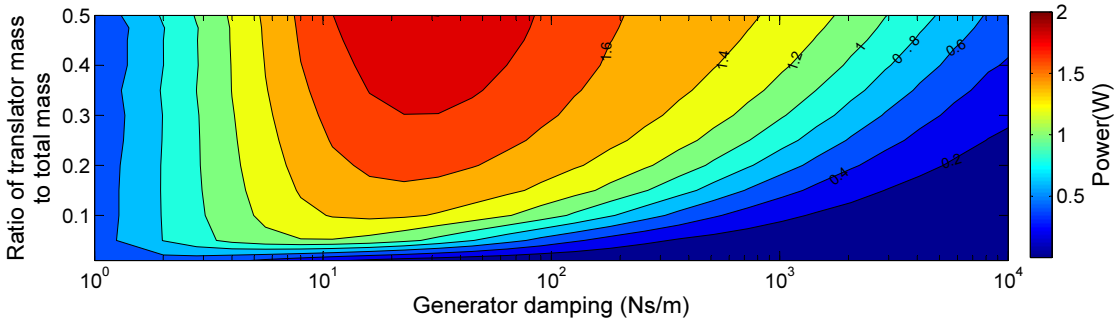


FIGURE 8.17: Output power as a function of generator damping and mass for a 40kg buoy with 0.14m radius ($\omega_{nb}$ 3.9 rad/s, $\omega_{ng}$ 5.9 rad/s).

### 8.3.2 Stroke

Figure 8.18 displays a contour plot of the RMS stroke displacement for the 0.14m radius 40kg CIPMLG WEC. Like the 0.10m radius 20kg CIPMLG WEC in Figure 8.8, the maximum RMS stroke displacement occurs when the generator is very lightly damped, but for the present 40kg WEC the maximum stroke displacement is slightly less with a value of 0.20m. Once again, the RMS stroke displacement is seen to decrease with

increasing generator damping, with a value of about 0.05m at 30 Ns/m, where the maximum output power occurs in Figure 8.17.

The maximum allowable stroke length for the 0.14m radius 40kg buoy with a draught of 0.64m, equals 0.32m. Therefore the RMS stroke displacements in Figure 8.18 do not exceed the maximum allowable stroke length. Similar to the time domain analysis results for the 0.10m radius 20kg CIPMLG WEC, the stroke displacement in the time domain for the 0.14m radius 40kg WEC exceeds the RMS value on average 33% of the time and the maximum stroke lengths are on average 2.9 times larger than the RMS values. Therefore, the stroke displacements for all the systems in Figure 8.18 with generator damping values larger than 7Ns/m will remain less than the maximum allowable stroke length.

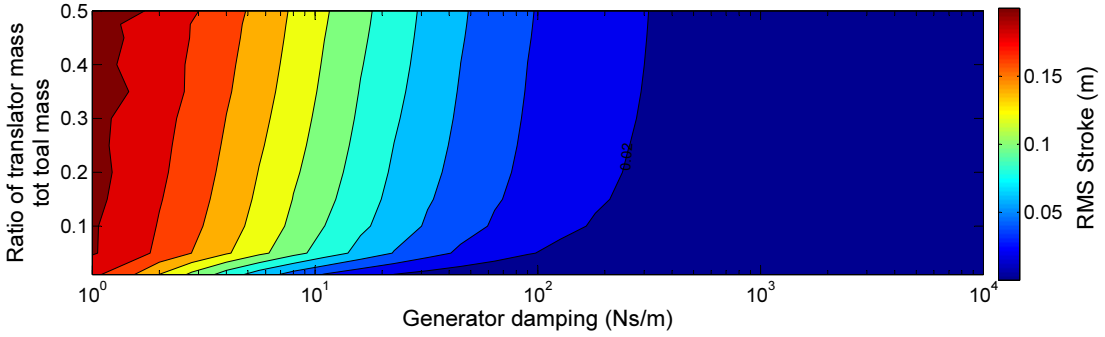


FIGURE 8.18: RMS stroke displacement as a function of generator damping and translator mass for a an 40kg buoy with 0.14m radius.

### 8.3.3 Pitch

A similar method is used to analyse the pitch for the 0.14m radius 40kg CIPMLG WEC, as used for the 0.10m radius 20kg CIPMLG WEC in Section 8.2.3. Here, the range of MoI values are chosen considering a 40kg ball of steel, $I = 0.16kgm^2$ and for a point mass of 40kg located the draught length of 0.64m away from the CoM, $I = 16kgm^2$. From these two extreme cases, the analysis selects MoI values of 0.16, 1.6 and 16 kgm$^2$ for the 0.14m radius 40kg CIPMLG WEC, displayed in Figures 8.19 -(a), (b) and (c), respectively.

Using time domain analysis, the maximum pitch displacement for the 0.14m radius 40kg WEC was found to be on average up to 3.6 times larger than the RMS pitch displacement, similar to the results shown in Figure 8.12 for the 0.10m radius 20kg CIPMLG WEC. Therefore, once again the RMS pitch displacement should remain below 11 degrees to satisfy the pitch constraint. Except for the systems with very large MoI values and CoM near the centre of the buoy, shown in Figure 8.19-(c), the majority of the systems in Figure 8.19 would not be able to satisfy the pitch constraint.

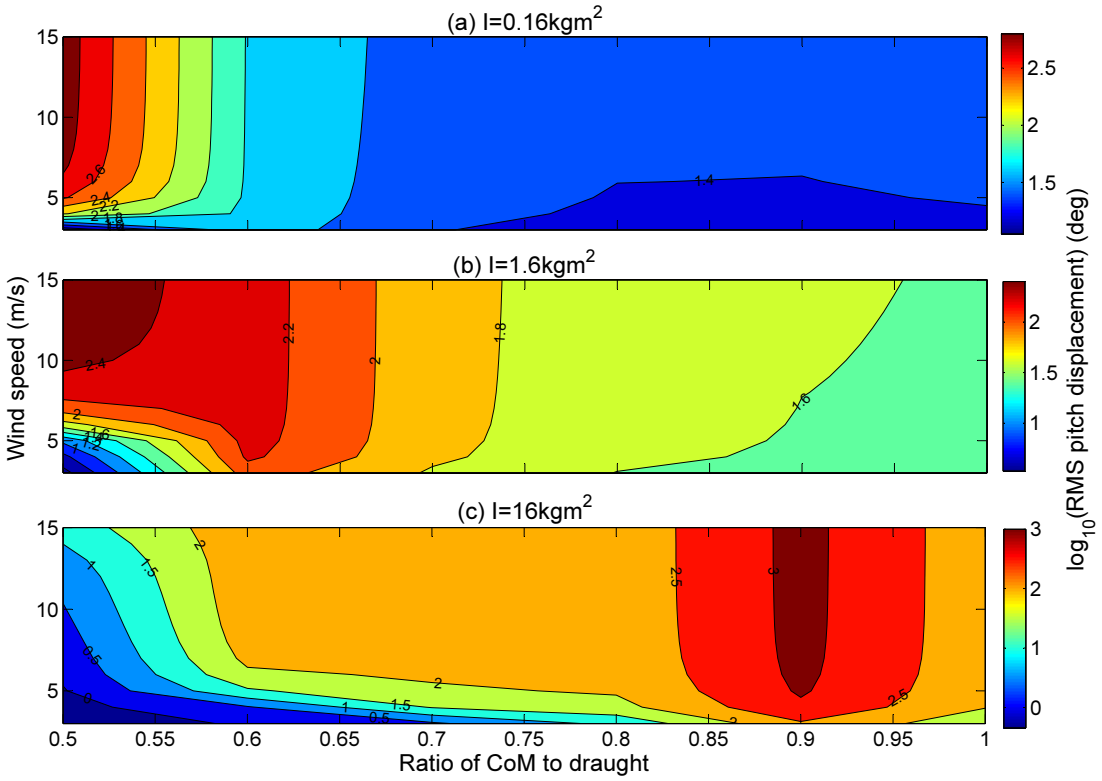


FIGURE 8.19: RMS pitch displacement, for a 40kg CIPMLG WEC with 0.14m radius, as a function of CoM depth and input PM spectrum sea state parameterised by the wind speed.

#### 8.3.3.1 Increasing the radius

Here the radius of the 40kg CIPMLG WEC is increased to 0.20m in Figure 8.20 and to 0.25m in Figure 8.21. Similar to the situation in Section 8.2.3.1, increasing the radius is seen to decrease the pitch displacement of the CIPMLG WEC. However, increasing the radius also decreases the output power, with a maximum power outputs for the 0.20m and 0.25m radius CIPMLG WECs of 1.24W and 0.66W respectively.

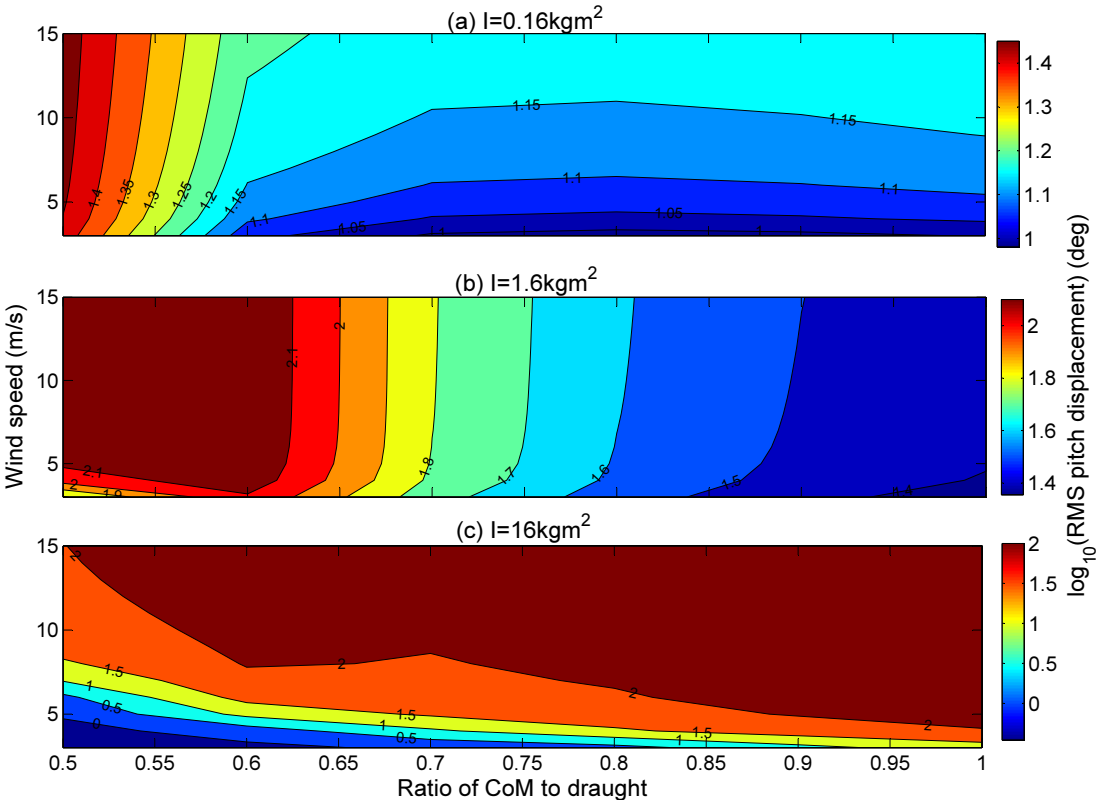


FIGURE 8.20: RMS pitch displacement, for a 40kg buoy with 0.20m radius, as a function of CoM and PM spectrum sea state parameterised by the wind speed.

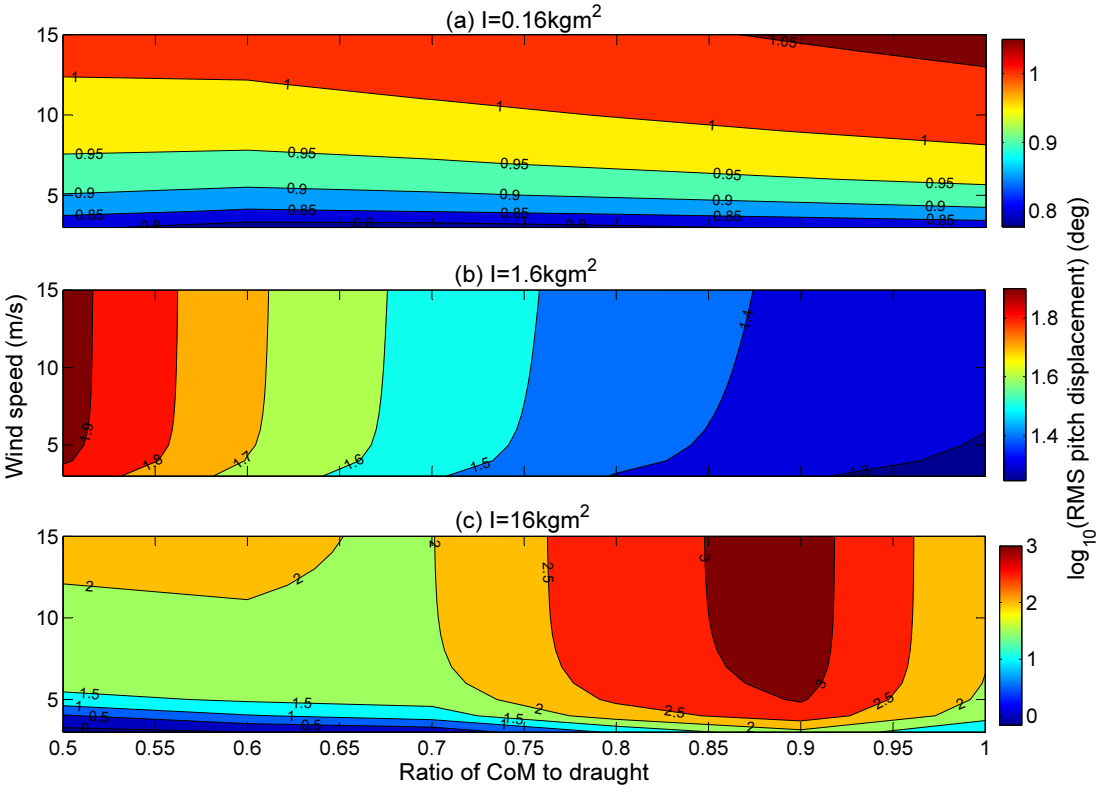


FIGURE 8.21: RMS pitch displacement, for a 40kg buoy with 0.25m radius, as a function of CoM and PM spectrum sea state parameterised by the wind speed.

## 8.4 Results for an eighty kilogram system

Here an 80kg CIPMLG WEC is analysed in the same way as the 20 and 40kg CIPMLG WECs in Sections 8.2 and 8.3.

### 8.4.1 Power

For the 80kg CIPMLG WEC, a radius value of 0.21m was found to produce the maximum output power (of nearly 3.5W), where the buoy natural frequency is 3.8 rad/s and the generator natural frequency is 5.9 rad/s. The output power contour plot for the 0.21m radius 80kg CIPMLG WEC is presented in Figure 8.22, where it can be seen that power outputs exceeding 3W occur for a generator damping of 50 - 300 Ns/m combined with a translator masses 35-50% of the total WEC mass.

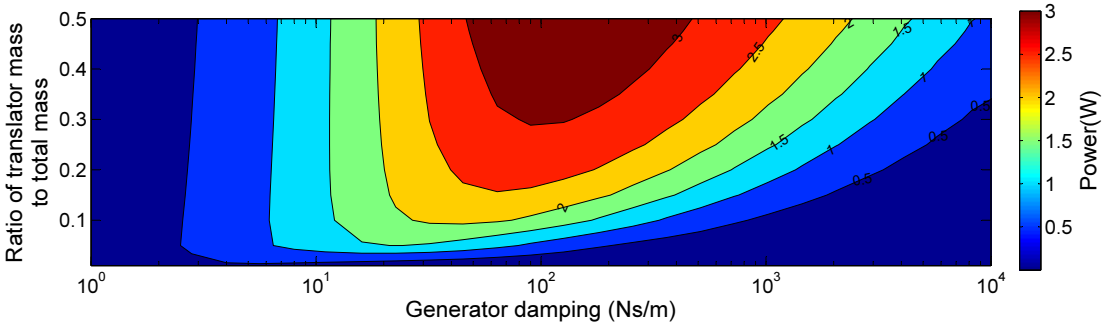


FIGURE 8.22: Output power as a function of generator damping and translator mass for a 80kg buoy with 0.21m radius ($\omega_{nb}$ 3.8 rad/s, $\omega_{ng}$ 5.9 rad/s).

### 8.4.2 Stroke

Figure 8.23 displays a contour plot of the RMS stroke length for the 0.21m radius 80kg CIPMLG WEC. The maximum RMS stroke displacement occurs when the generator is very lightly damped, and is seen to once again decrease in value with the increase in WEC mass, down to a maximum value of 0.12m compared to 0.20m for the 40kg WEC and 0.23m for the 20kg WEC. The RMS stroke displacement for the 0.21m radius 80kg CIPMLG WEC has a value of about 0.04m for generator damping values around 200 Ns/m, where the maximum output power occurs in Figure 8.22. Using time domain analysis, the maximum stroke displacements for the systems in Figure 8.23 ranged from 2.6 - 3.3 the RMS values. The draught of the 80kg WEC is 0.57m, therefore the maximum allowable stroke length is 0.28m. Figure 8.23 shows that the stroke displacements for all the systems with generator damping values greater than 30Ns/m will remain less than the maximum allowable stroke length.

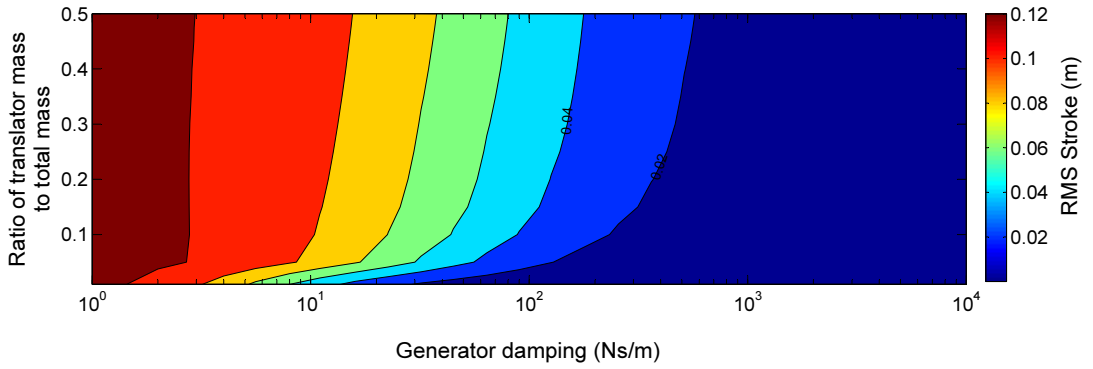


FIGURE 8.23: RMS stroke displacement as a function of generator damping and translator mass for a an 80kg buoy with 0.21m radius.

### 8.4.3 Pitch

The RMS pitch displacement for the 0.21m radius 80kg is displayed in Figure 8.24. Here the MoI values of 0.6, 4 and 26kgm$^2$ were selected considering an extreme minimum value of an 80kg ball of steel, $I = 0.6kgm^2$, an extreme maximum value for an 80kg point mass located the draught length of 0.57m away from the CoM, $I = 26kgm^2$, and the value of $I = 4kgm^2$ geometrically halfway between the minimum and maximum values. The results in Figure 8.24 shows that none of the systems are able to satisfy the pitch constraints across the range of input wind conditions.

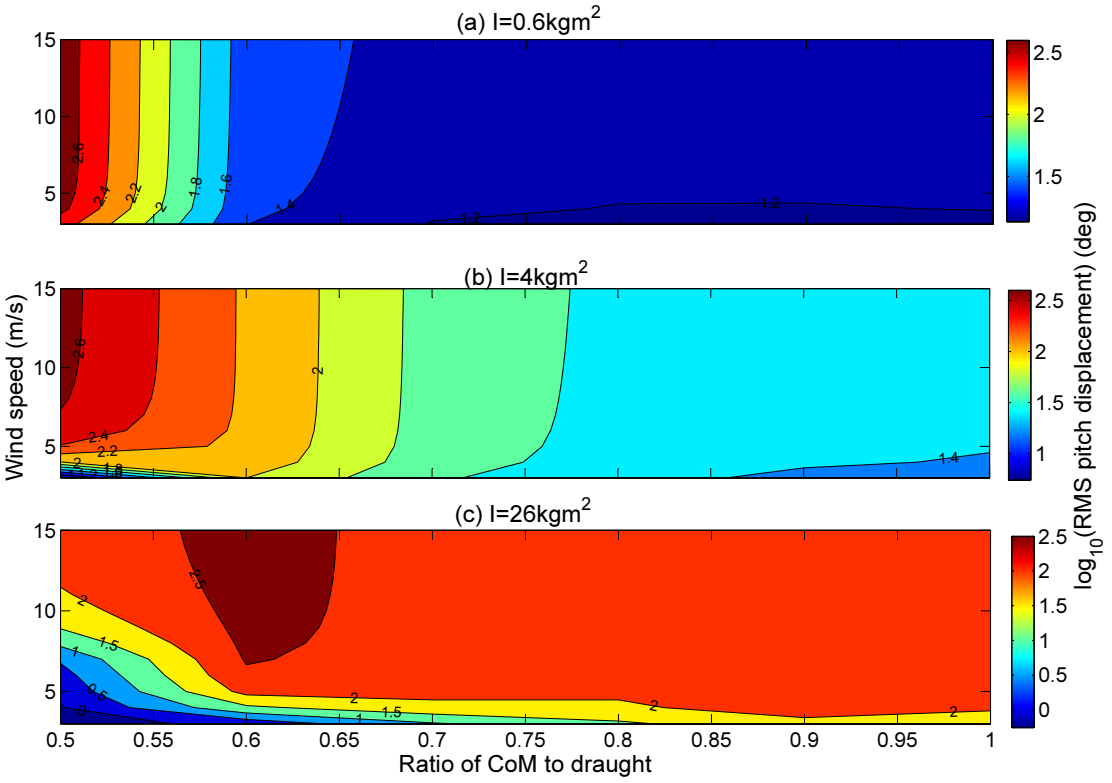


FIGURE 8.24: RMS pitch displacement, for a 80kg buoy with 0.21m radius, as a function of CoM and PM spectrum sea state parameterised by the wind speed.

### 8.4.3.1 Increasing the radius

Here the radius of the 80kg WEC is increased to 0.25m in Figure 8.25, 0.30m in Figure 8.26 and to 0.35m in Figure 8.27. Once again, increasing the WEC radius is seen to decrease the pitch displacement, where the larger radii WECs with small MoI values, Figures 8.26-(a) and 8.27-(a), are able to satisfy the pitch constraints across the full range of wind conditions. Although increasing the radius also decreases the output power, the maximum power outputs for the 0.25, 0.30 and 0.35m radius WECs still remain above or close to the 1W threshold, with maximum power output values of 2.68W, 1.67W and 0.97W respectively.

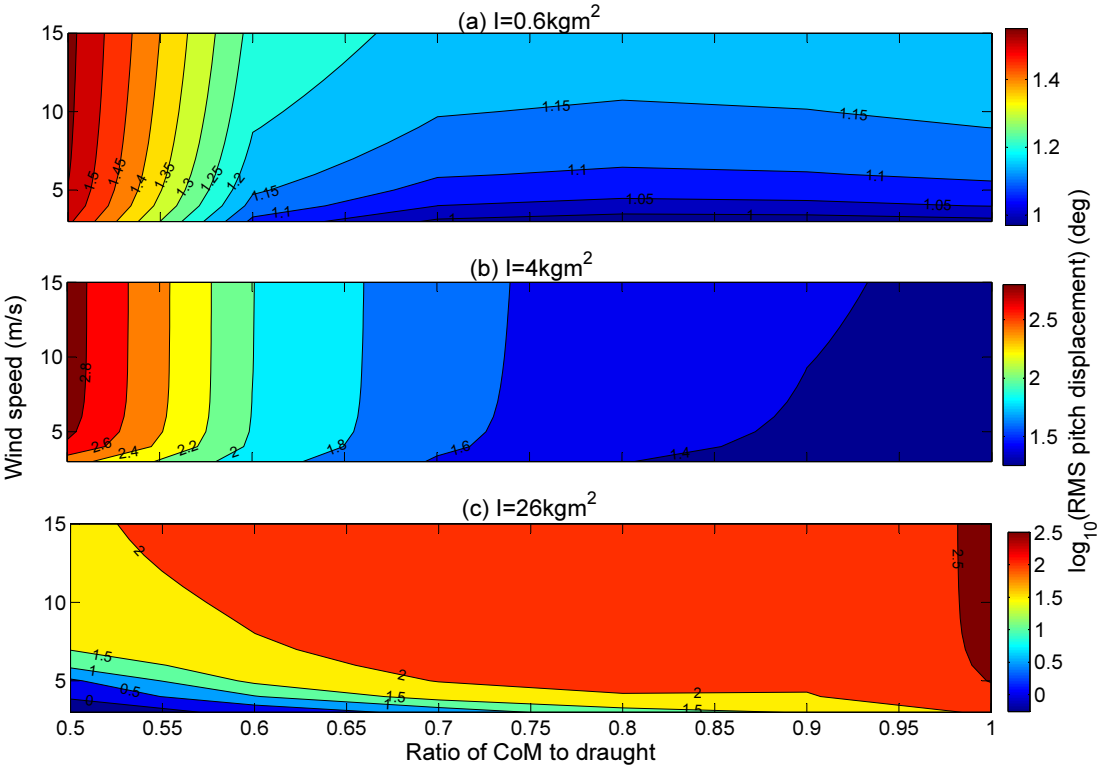


FIGURE 8.25: RMS pitch displacement, for a 80kg buoy with 0.25m radius, as a function of CoM and PM spectrum sea state parameterised by the wind speed.

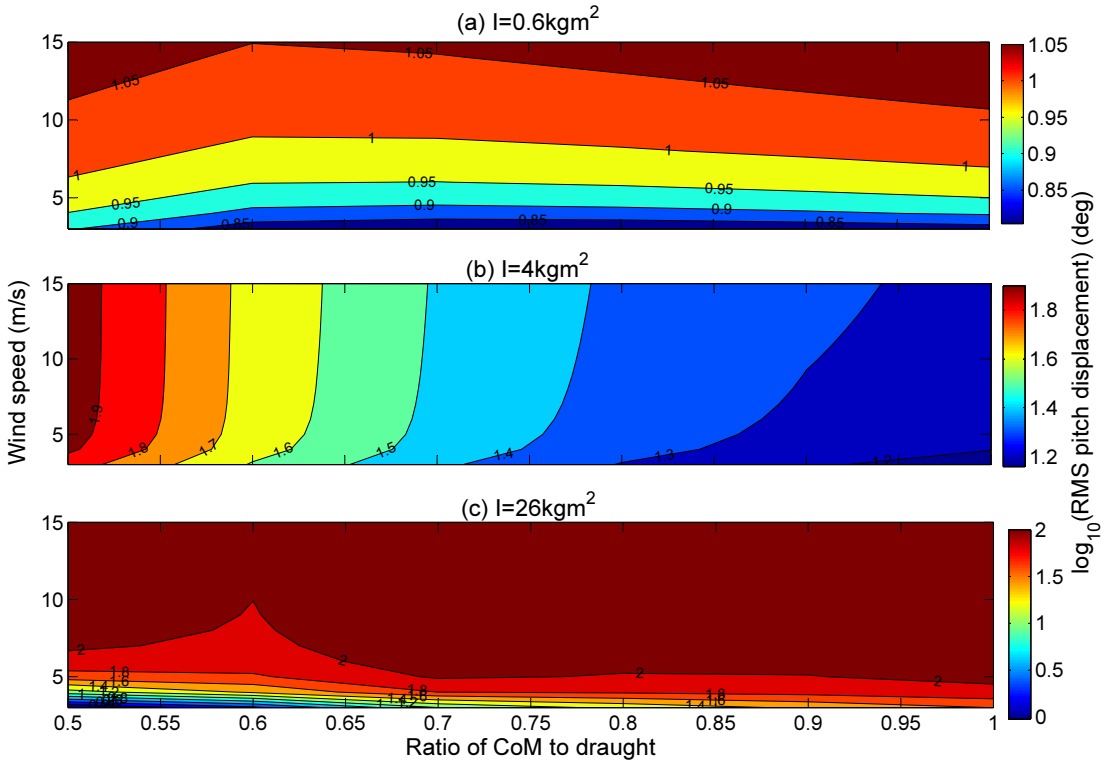


FIGURE 8.26: RMS pitch displacement, for a 80kg buoy with 0.30m radius, as a function of CoM and PM spectrum sea state parameterised by the wind speed.

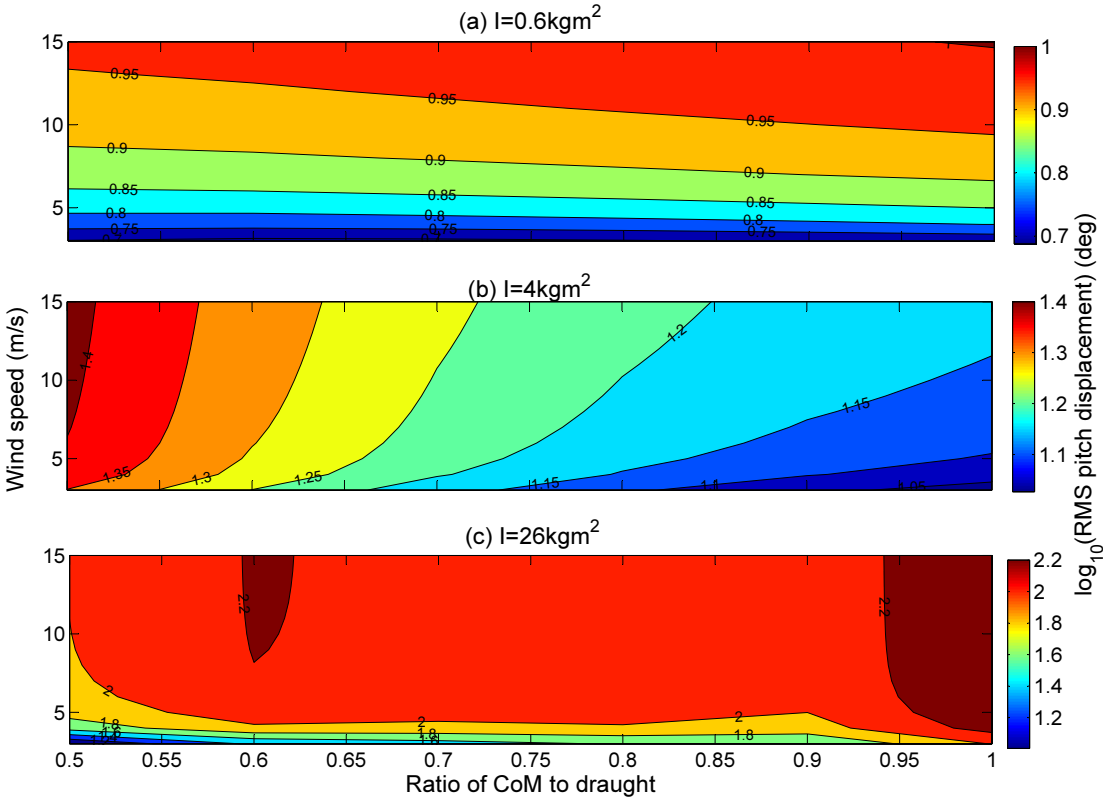


FIGURE 8.27: RMS pitch displacement, for a 80kg buoy with 0.35m radius, as a function of CoM and PM spectrum sea state parameterised by the wind speed.

## 8.5 Practical considerations

This section discusses a number of practical considerations that were neglected in the numerical analysis used to obtain the results in this chapter. Aspects such as the effect of mechanical damping, the generator inefficiencies, whether the required levels of electromagnetic damping can be realistically achieved by a permanent magnet linear generator within the volume constraints of the buoy, whether appropriate springs with the required spring constant values can be physically achieved, and the effect of the translator mass on the pitch displacement, are discussed in this section. With consideration of these practical aspects, the section concludes with an assessment of the realistically achievable performance ability of the CIPMLG WEC and an evaluation of whether the CIPMLG WEC can practically satisfy the performance requirements outlined in Section 4.3.3.1.

### 8.5.1 Generator efficiency

The output power results presented in this chapter assumed a perfectly efficient generator, neglecting any losses which will inherently occur in the conversion from the mechanical energy in the translator mass to the electrical energy stored in the battery. To give an idea of the likely inefficiencies expected for the present IPMLG system, a number of reported efficiencies for similar cases are presented here. Bastien et al [142], who used anchored linear generators driven by heaving surface buoys, claim that the efficiency for small linear electric generator designs and driven at the low speeds of ocean waves is experimentally found to be high ($\geq$90%), however another 30% power conversion loss occurs for the required DC to DC conversion and battery charging etc, resulting in total efficiencies $\geq$63%. Grilli et al [146] reported an 83% efficiency of mechanical to electric power in their linear electrical generator, due to various magnetic losses and imperfect winding of the generator. Along with these electrical type inefficiencies in the generator, the overall efficiency will also be effected by mechanical damping in the generator, as discussed in the next subsection.

### 8.5.2 Mechanical damping

As previously mentioned in Section 6.2.7, a value for the mechanical damping can not be determined numerically, only measured experimentally after the system is constructed. Ideally the mechanical damping should be zero, and the system should be carefully designed to minimise the amount of friction, air resistance and other effects which contribute to mechanical damping. However, it is impossible to completely eliminate these parasitic damping effects, therefore this subsection evaluates and discusses the effect of non-zero mechanical damping values on the output power.

Figures 8.28 -(a), (b) and (c) show the output power contour plots for the 0.14m radius 40kg buoy, when 1, 10 and 100Ns/m of mechanical damping, $d_m$, is applied to the system respectively. The generator damping is the sum of the mechanical and electromagnetic damping (Equation 5.29), therefore the generator damping values that are less than the mechanical damping value in Figures 8.28 -(a), (b) and (c) are not possible and the corresponding output power values are left blank. Figures 8.29 then compares the output power in Figure 8.28 to the case for the 0.14m radius 40kg buoy with no mechanical damping, Figure 8.17, by plotting the relative output power percentage.

These figures show that a significant reduction in output power occurs when the level of mechanical damping is comparable to the electromagnetic damping. Therefore, the results in Sections 8.2 - 8.4 obtained with very low levels of electromagnetic damping

values may not be practically achievable in the presence of mechanical damping. For this reason, when examining the contour plots to select the best value for the generator damping parameter, it might be wise to choose the highest generator damping value possible for a given output power contour line, to reduce the effect of mechanical damping. Another reason to choose high generator damping values over low ones, is that the stroke length decreases with increasing generator damping value. However, larger electromagnetic damping values require larger generators, therefore the next subsection, investigates the levels of electromagnetic damping practically achievable by a generator small enough to fit inside the CIPMLG WEC's geometrical and mass constraints.

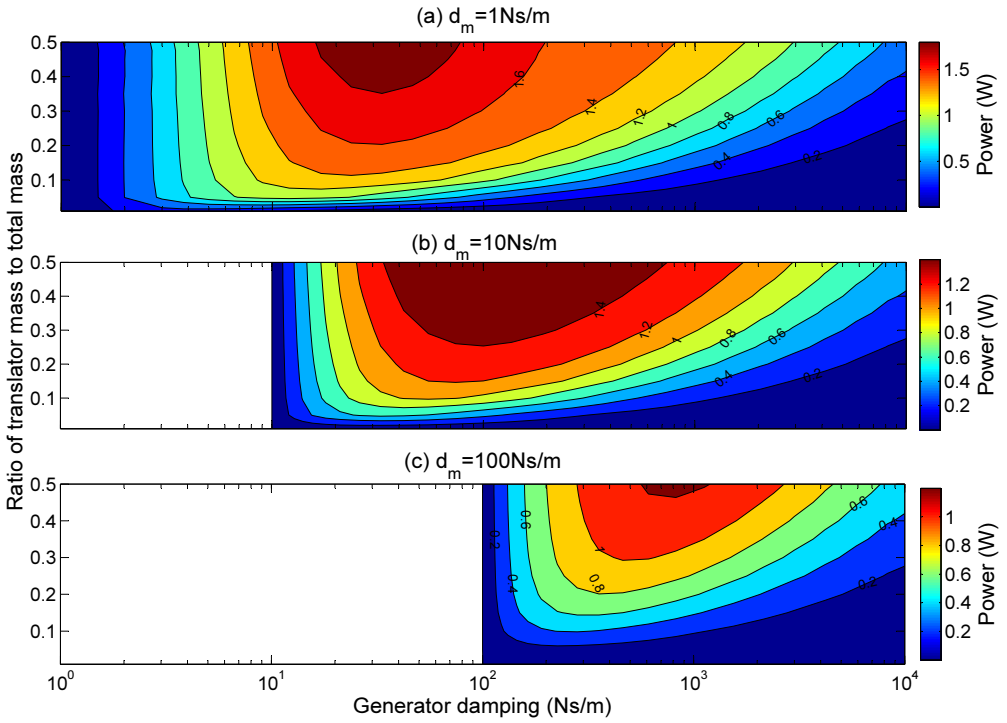


FIGURE 8.28: Power as a function of generator damping and translator mass for a 40kg buoy with 0.14m radius and varying amounts of mechanical damping.

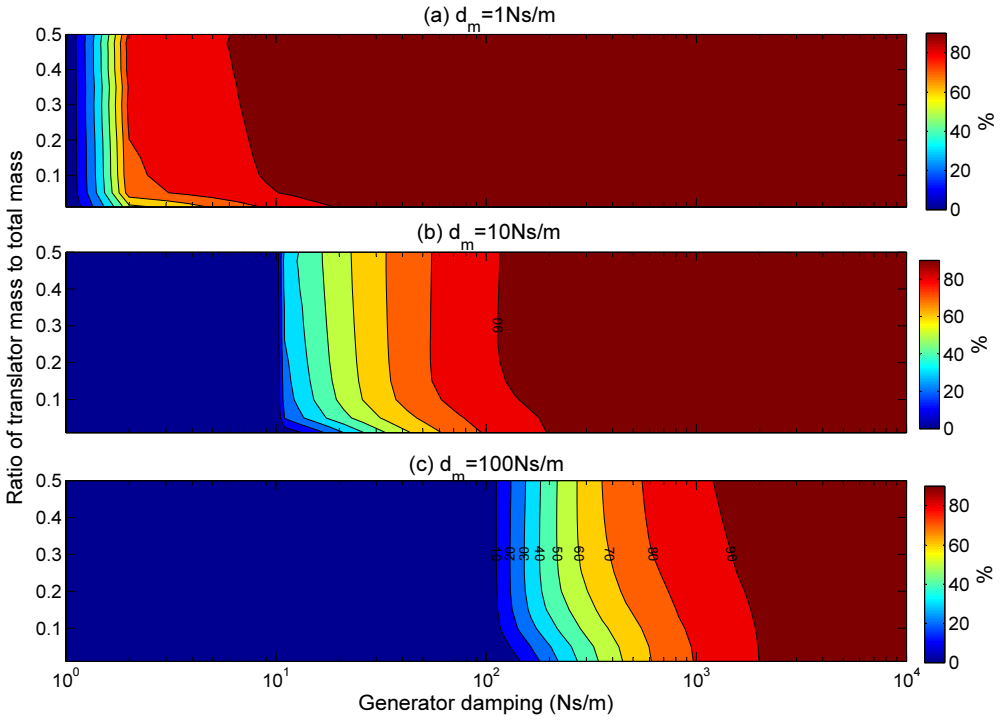


FIGURE 8.29: The generator efficiency as a function of generator damping and translator mass for a 40kg buoy with 0.14m radius and varying amounts of mechanical damping values.

### 8.5.3 Electromagnetic damping

The results in this chapter showed that the IPMLG may be required to provide electromagnetic damping co-efficients over 1000Ns/m. It is not immediately clear what physically sized generator would be required to provide these levels of electromagnetic damping and whether such a generator could fit into the geometrical constraints of the WEC's volume. No information could be found in the literature relating to this question, therefore Appendix A derives an electromagnetic model of the generator, including a finite element analysis of the magnetic field provided by different sized magnets. From this analysis, it seems likely that engineers can construct a generator of sufficiently small size and weight to satisfy the electromagnetic damping requirements of the CIPMLG WEC, whereby it is estimated that a generator with a diameter less than 15cm and a length less than a few tens of cms can provide the required electromagnetic damping values.

### 8.5.4 Spring

Cheung and Childress [150] discussed the practical issues related to physically realising springs with the required specifications for their IMPLG WEC's. They state that springs

with periods below 2s are difficult, "For low frequency operation ($\geq$2 sec period), the spring performance becomes more demanding. The required load, longer extension, and lower stiffness represent a set of specifications that metal springs have difficulty meeting." Therefore, Cheung and Childress investigated special types of springs (magnetic and elastomer), able to perform well in low frequency operation, in order to couple them to the peak of the wave spectrum. However for high frequency devices ($\leq$ 2s period) as is the case for the present work, Cheung and Childress state that metal springs are adequate because they require high stiffness and short extension. Therefore, the philosophy of the present work to aim for the high frequency tail of the input wave spectrum due to its omnipresence, is also advantageous with respect to the required performance of the IPMLG's springs.

### 8.5.5 Effect of generator on pitch

The results showed that the translator mass will need to be relatively large compared to the total WEC mass, in which case the effect of the translator mass on the pitch motion may be significant. To ensure that the translator mass does not detrimentally effect the buoy's pitch motion, the stroke of the generator should therefore be constrained below the CoB. The CoB is located at half the draught depth, which means that the maximum allowable stroke length would be restricted to 25% of the draught depth. Reducing the maximum allowable stroke length results in an increased $\omega_{ng}$ value and therefore a reduced power output for most of the results presented in this chapter. The reduced maximum allowable stroke length also means that large generator damping values should be used where possible to minimise the stroke displacement.

### 8.5.6 Mooring forces

In most cases, the MBS will have a mooring system designed to keep it on station, unless it is a drifting MBS such as proposed by [15]. Unlike a freely floating body, a moored body experiences enhanced coupling between various modes of motion [185]. As the device heaves, the moorings induce pitch and surge forces, which may be in or out of phase with the wave excitation and can therefore be constructive or destructive to the device motion in these modes of motion [186]. So although the axisymmetric geometry, of the proposed MBS energy harvesting WECs analysed in this thesis, eliminated any hydrodynamic coupling between modes of motion, the inclusion of mooring lines will necessitate consideration of coupling between the modes of motion when assessing the WEC's performance. The degree to which the moorings induce coupling between modes

of motion, depends on the location of the mooring's attachment point(s) on the body's hull, which should become another design parameter for optimisation.

In addition to enhanced coupling between modes of motion, a mooring system can also add resistance and reactance to the WEC system. The mooring line's inertia and elasticity can have a reactive effect on the motion of the WEC, which can change the WEC's resonant frequency. Mooring line damping will result from the line friction on the sea bed, internal friction damping within the line and from the drag force along the line as it moves through the fluid, and will therefore add resistance to the WEC system and dissipate energy. These resistive and reactive effects depend on the mooring's geometry and materials .

The mooring system, and its effect on the overall WEC performance, should be analysed in future development of the MBS energy harvesting WEC. Similar analysis has been performed for large scale WECs, which provides a number of methods and models that can be followed for the present work [185–187] . For example, although mooring forces are inherently nonlinear, Fitzgerald and Bergdahl [186] have shown a method to include the mooring forces in the frequency domain, which could be a useful method to apply to the frequency domain analyses performed in this thesis. There is a wide diversity in mooring approaches and systems, from which future analysis should select one well suited to the design objectives of the overall WEC system.

### 8.5.7 Practical performance of the CIPMLG WEC

With consideration of the results and practical considerations presented in this chapter, it seems unlikely that the CIPMLG WEC would be able to satisfy the design requirements outlined in Section 4.3.3.1. The design problem required a small, light easily deployable device, therefore the total mass of the system will ideally be below 50kg, so that a single person can easily deploy it from any vessel. The results showed that the 20 and 40kg WECs would be unable to satisfy both the 1W output power requirement and the pitch constraint. The 80kg WEC showed promise to satisfy both the power requirement and the pitch constraint, although only marginally. When the generator efficiency and mechanical damping are taken into consideration, and the constraint that generator stroke length remain below the CoB is imposed, then it becomes unlikely that a CIPMLG WEC system under 100kg would be able to fulfil the output power and pitch resilience design requirements.

## 8.6 New proposed geometry - The Wedgetop WEC

The geometry of the CIPMLG WEC, was chosen as a vertical cylinder due to its axisymmetric shape eliminating any dependency on the directionality of the incoming waves, because its long vertical geometry is more accommodating for an internal linear generator, and for cost purposes, with cheap premade materials like PVC piping envisioned to be ideal for the buoy's hull. The results presented in this chapter suggest that the performance of the cylindrical geometry is inadequate for the present application, therefore this section investigates the effect of changing the geometry of the buoy.

While an infinite number of possible axisymmetric geometries exist, the example targeted in this section focusses on a particular shape that is envisaged to perform well, based on knowledge gained during the course of the thesis. The perceived reason for the cylindrical geometry's poor performance is that it is not a particularly good wave maker, and as discussed in Section 4.2.1 "for an object to be a good wave absorber it must be a good wave maker" [110]. To improve the wave absorbing ability of the WEC, an axisymmetric wedge (cone) geometry will be added to the top of the buoy, to increase its coupling to the waves. The new WEC geometry investigated in this section shall be termed the "Wedgetop WEC", and is illustrated in Figure 8.30.

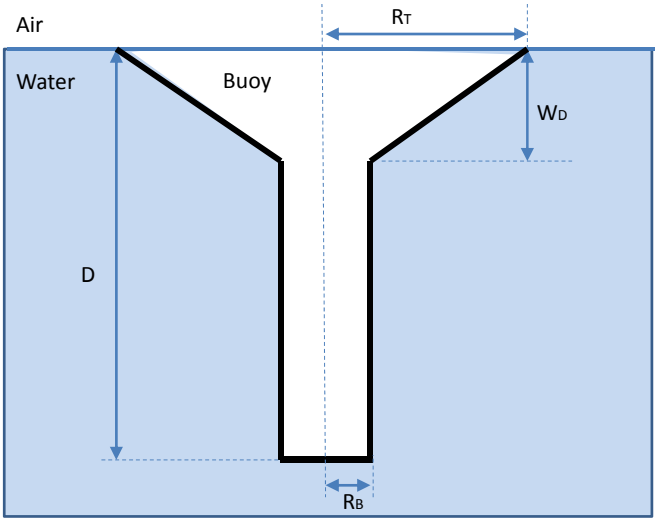


FIGURE 8.30: The dimensions of the new buoy geometry, the Wedgetop WEC, with top radius, $R_T$, bottom radius, $R_B$, draught, $D$, and wedge depth, $W_D$.

Plunger type wavemakers, with a wedge shaped cross section, are often used in laboratories instead of piston or flap type paddles, because the wave making ability of an immersed wedge making small vertical motions is the same as for a piston wavemakers making large strokes [181]. The addition of the wedge to the buoy is also inspired by the 'Free Floating Clam' WEC by Francis Farley [182], which consists of a rigid front and

rear plate, flexibly connected at the bottom and held apart by the air pressure between them, to form a flexible wedge. The Free Floating Clam device heaves in resonance with the incoming waves and the changing pressure in the water surrounding the WEC makes the wedge open and shut, pumping air through a Wells turbine. Farley states that, 'the Clam acts like a vertically driven wedge which is strongly coupled to the waves'.

Another advantage of the Wedgetop WEC over the CIPMLG WEC design, for the present application, is the increase in maximum allowable stroke length for a given total WEC mass and top radius. The buoy's hydrodynamic natural frequency is determined by the radius of the WEC at the surface, and the radius value in turn determines the draught depth of the cylindrical geometry for a given mass. The depth of the draught then constrains the maximum allowable stroke length for the generator. However, because the Wedgetop WEC does not have a constant cross-section, whereby its radius decreases below the surface, the draught depth can be deeper for a given WEC mass and hydrodynamic natural frequency. Additionally, the large volume of the wedge shape at the top compared to the thinner cylindrical shape on the bottom, means that the CoB will be closer to the surface than 50% of the draught depth. Therefore not only is the draught deeper for the Wedgetop WEC, but its maximum allowable stroke length can also use a greater portion of that draught depth, if it is constrained below the CoB location as suggested in Section 8.5.5.

### 8.6.1 Example Wedgetop WEC results

The Wedgetop WEC has two additional parameters, $R_B$ and $W_D$ (see Figure 8.30), compared to the CIPMLG WEC. Therefore, the analysis of the new geometry is complicated by the increased dimensionality of the parameter space, and the same analysis approach used to find the best combination of parameters for the CIPMLG WEC can not be used for the Wedgetop WEC. Therefore, the aim of this section is not to determine the optimal parameters for the Wedgetop WEC, but rather to demonstrate the improved performance of the Wedgetop WEC over the CIPMLG WEC and verify its potential to fulfil the design requirements of Section 4.3.3.1. The results presented in this section indicate that a complete optimisation of the Wedgetop WEC's parameters is warranted in future work and is discussed in Chapter 10.

The example shown in this section is for a 40kg Wedgetop WEC. The bottom radius is assumed to have a value of 0.075m, which could accommodate a generator (see Appendix A) with a 0.04m radius magnet, 0.02m coil width, 0.005m airgap and 0.01m for the thickness of the buoy's hull. The values for the top radius and wedge depth were then varied using trial and error until a system was found which had a total mass of 40kg and

satisfied both the output power requirement and pitch constraint, as shown in Figures 8.31 and 8.32 respectively. The system in Figures 8.31 and 8.32 has a top radius of 0.40m, a wedge depth of 0.10m and a draught of 1.18m. The draught was varied for each top radius and wedge depth combination so that the volume of the buoy displaced 40kg of sea water. The CoB was calculated for this geometry, having a depth of 0.32m, and the maximum allowable stroke length set to half the distance between the CoB and the draught, resulting in a $\omega_{ng}$ value of 4.8 rad/s. The maximum power output for the Wedgetop WEC system in Figure 8.31 is greater than 2W and the RMS pitch displacement is shown for this system to be less than 15 degrees ($10^{1.18}$ degrees) across the full range of sea states for both the low and medium MoI values, Figures 8.31-(a) and (b).

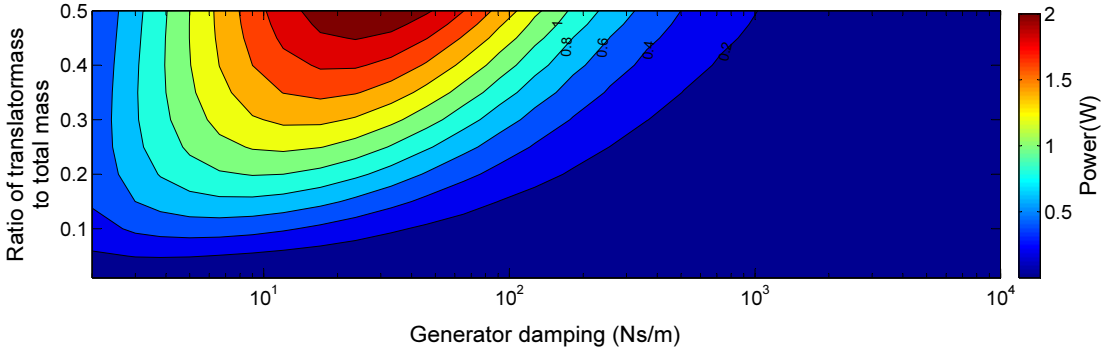


FIGURE 8.31: Power output for a 40kg Wedgetop WEC with a 0.40m top radius, 0.075m bottom radius, 0.10m wedge depth and 1.18m draught.

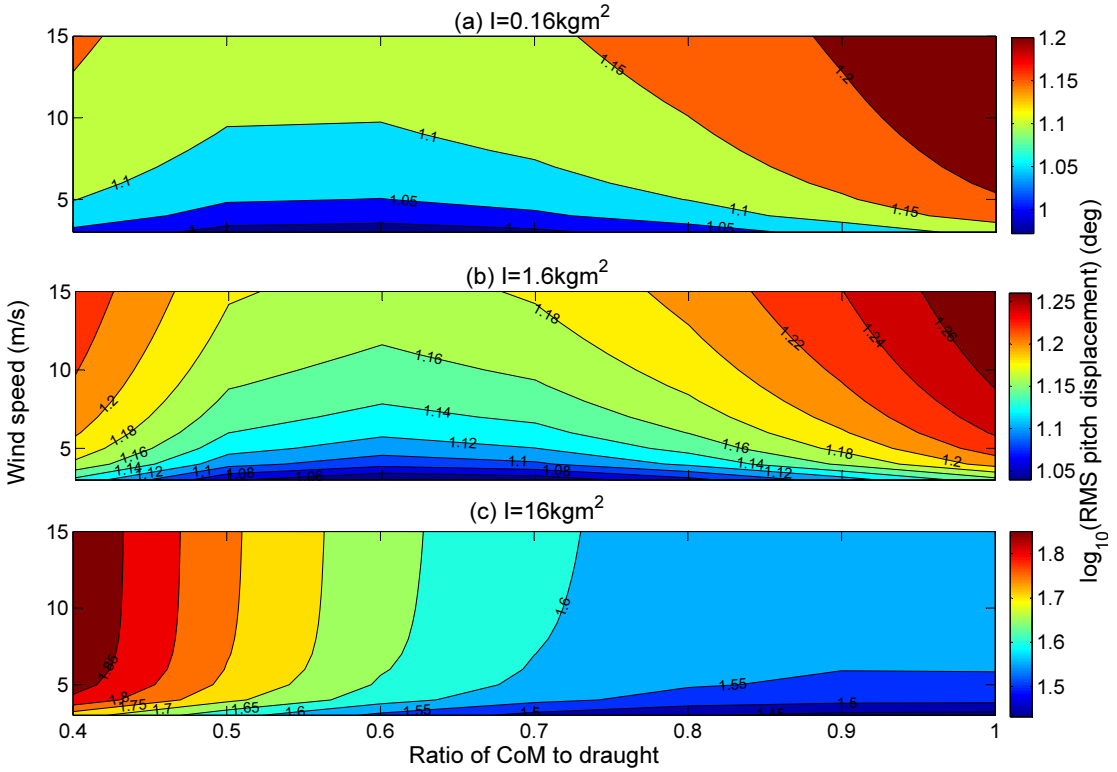


FIGURE 8.32: RMS pitch displacement for a 40kg Wedgetop WEC with a 0.40m top radius, 0.075m bottom radius and 0.10m wedge depth.

### 8.6.2 Potential performance of the Wedgetop WEC

The performance of the 40kg Wedgetop WEC in Figures 8.31 and 8.32 shows promising potential for Wedgetop WEC compared to the CIPMLG WEC. The maximum output power for the system in Figure 8.31 was more than double the 1W design requirement, and would therefore be practically able supply the required output power with realistic generators efficiency values as low as 50%. The RMS pitch displacements in Figure 8.32 were within a few degrees of the required pitch constraint across the full set of sea states and for a wide range of MoI values. These results give confidence that, with further design optimisation effort by searching through the geometry parameter space, the Wedgetop WEC can satisfy the output power requirement and pitch constraint, with a total mass of under 50kg, thus fulfilling the complete design requirements specified in Section 4.3.3.1.

## 8.7 Conclusion

To ensure that the CIPMLG WEC can provide 1W of power at any location and at any time, so that a "one size fits all" design can be built, the output power from the

numerical model was calculated in response to the omnipresent truncated Burling spectrum from Chapter 7. Based on the modelling, input wave spectrum and other analysis assumptions, plus assuming a generator efficiency of 50%, the results showed that a device with a mass greater than 40kg could be designed to reliably provide 1W of average power to the MBS.

The pitch motion of the body depends strongly on the distribution of mass throughout the WEC. The mass distribution is unknown until later stages of the design process when all the MBS components, such as sensors, antennas, batteries, generator etc, are positioned in the WEC. However, the results in this chapter can give a guide as to the best CoM and MoI values that the design should aim to achieve when positioning the mass throughout the WEC. The results have shown that systems with small MoI values and with CoMs located towards the bottom of the WEC are most stable. The maximum pitch displacement was found to be up to 3.6 times larger than the RMS value. Therefore, to obey the pitch constraint of 40 degrees, the RMS pitch displacement should remain less than about 11 degrees. Only systems with large radii were able to satisfy this constraint.

Although the WECs with large radii can satisfy the pitch constraints, they also have relatively high hydrodynamic natural frequencies that are not well aligned with the peak frequency of the input truncated Burling spectrum, resulting in poor output power performance. The results indicate that none of the 20, 40 nor 80kg CIPMLG WECs evaluated in this chapter would be able to satisfy both the power requirement and pitch constraint. Extrapolating the results suggests that the required size of the device would likely exceed 100kg, which far exceeds the target size for the device. Therefore it is concluded that the CIPMLG WEC can not fulfil all of the design requirements specified in Section 4.3.3.1.

A new geometry, The Wedgetop WEC, was proposed to improve the device's performance, by including a wedge shape to the top of the WEC to improve its wave absorbing abilities. Initial analysis of The Wedgetop WEC shows significant improvement compared to the original CIPMLG WEC, both in terms of power output and in pitch resilience. The results indicate that the Wedgetop WEC performance has a strong potential to fully satisfy the design requirements specified in Section 4.3.3.1. Further optimisation, via a thorough analysis of all configurations is necessary. Additionally, parabolic wedge shapes may further improve the results, again greatly increasing the solution space to search for optimal results.

# Chapter 9

# Thermal energy harvesting across the air-water interface

## 9.1 Introduction

The temperature gradient existing between the water and ambient air offers a potential renewable power source. The ocean will be either a few degrees warmer or colder than the air directly above it; dependant on factors such as the time of day, time of year and global latitude. A thermal energy harvester is a device that promotes the flow of heat energy across this thermal gradient, a portion of which is converted into electrical energy for powering the MBS. This concept was inspired by similar energy harvesting research, reviewed in Section 2.2.2, utilising the thermal gradient between the soil and ambient air to power terrestrial based sensor nodes [57, 58, 104, 105].

This chapter offers a first investigation into harvesting thermal energy from the temperature difference across the air/water interface for the purpose of distributed power generation in the marine environment. Section 9.2 begins by assessing the resource, using temperature datasets as input to a mathematical model of a prototype thermal energy harvesting device, to estimate the potential level of power available for powering a MBS. Section 9.3 then documents a number of experiments performed on a physical thermal energy harvester prototype that was built following the findings from Section 9.2. Section 9.4 then summarises the initial analysis of the thermal energy harvesting concept detailed in this chapter and evaluates the potential of the thermal energy harvester concept for powering a MBS.

## 9.2 Estimating the resource

This section looks to estimate the resource potentially available for powering a MBS utilising the thermal gradient between the air and water in the ocean, and is based off the the following publication by the author [106]. To accomplish this, environmental parameters such as the air and water temperatures are needed. Two different datasets, which are vastly different in temporal and spatial scales, are used here to develop a feel for the resource available. Example subsets of the two datasets are plotted in Figures 9.1 and 9.2.

Figure 9.1 graphs the air and water temperature measured every 30 minutes for a 48 hour period at the Australian Institute of Marine Science (AIMS) weather station located at Orpheus Island (Lat: 18.612808 S, Lon: 146.483094 E) in late January 2009. It also plots the difference in temperature between the two, which is seen to follow a diurnal cycle. The maximum temperature difference between the air and water is seen to occur in the early hours of the morning when the air is at its coldest, whereas the minimum temperature difference occurs when the air is at its warmest in the late afternoon. The magnitude of the temperature difference ranges from about 0 - 5 Kelvin. The water's temperature is seen to fluctuate less across the day than the air's, as a result of its larger thermal mass. In this particular data subset, the water was warmer than the air, but this is not always the case depending on the time of day/year. The location also has a significant impact as illustrated in Figure 9.2 which displays the yearly mean air/water temperature difference for large spatial areas spanning the entire globe.

The map displayed in Figure 9.2 was created using data from the National Centers for Environmental Prediction (NCEP) Reanalysis project which uses an analysis/forecast system to perform data assimilation using past data from 1948 to the present. It has global coverage using a T62 Gaussian Grid of 192 x 94 points, with each set of results reported every 6 hours. The generated map displays the average of the absolute air/water temperature difference across the Earth's oceans. Each pixel corresponds to one of the grid points from the NCEP data, with the displayed value representing the average absolute value of the air/water temperature difference calculated from each time sample for the year of 2008.

The results indicate that there is an average air/water temperature difference on the order of a few degrees Kelvin throughout all of the Earth's oceans. Some regions display a higher average than others, due to local conditions such as latitude, shoreline proximity, incoming currents etc. An example of this is the visible effect of the Gulf Stream Current shown by the light coloured areas directly east of the USA and Canada. The high values here, presumably occur due to the dominating effect of the Gulf Stream

Current transporting warm water from the Equator northward into in the cold northern hemisphere winter.

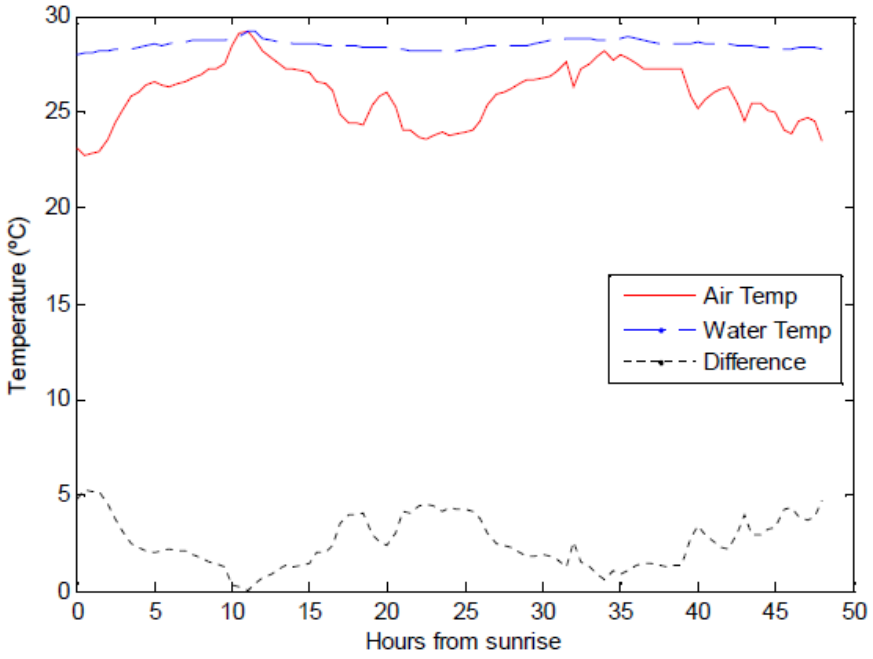


FIGURE 9.1: Air and water temperatures measured at Orpheus Island for the 48 hours following 5.30am 26/01/2009.

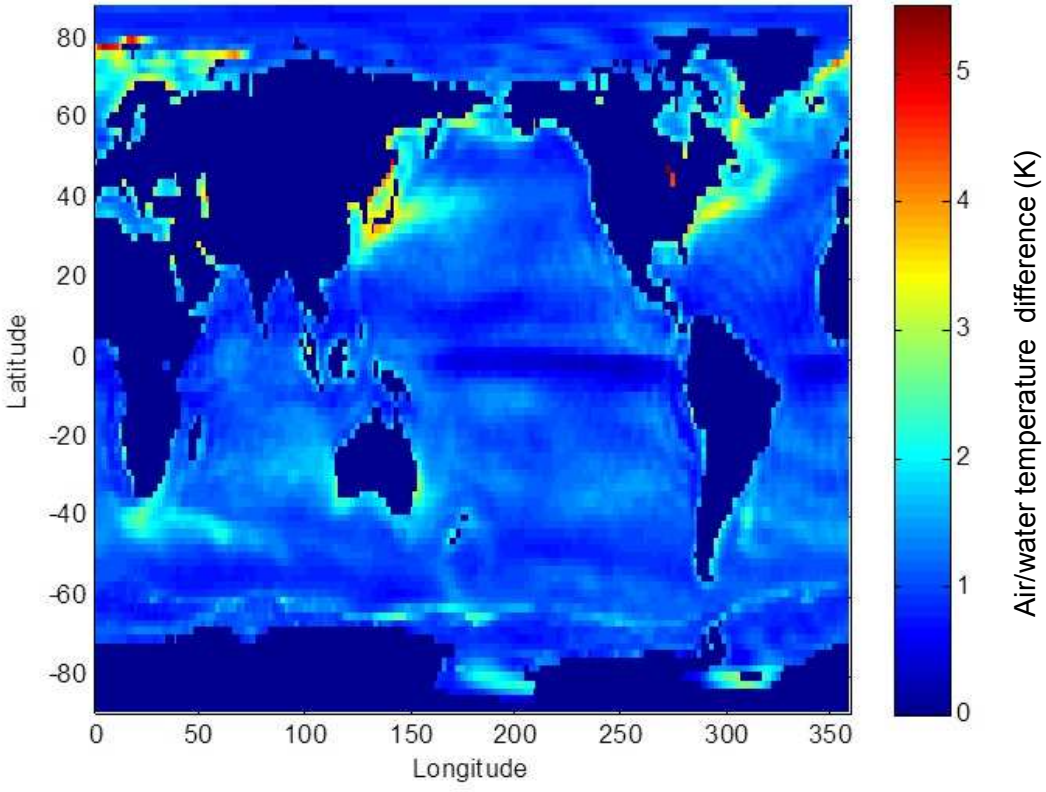


FIGURE 9.2: Average of absolute air/water temperature differences for 2008.

### 9.2.1 Mathematical model of the thermal energy harvesting device

The physical set up of the thermal energy harvesting device is depicted in Figure 9.3. A good thermal conductor is introduced across the air/water interface to promote a generous heat flow. The airside heat exchanger is assumed to thermalise with the ambient air at a temperature $T_a$. Likewise, the waterside heat exchanger is assumed to thermalise with the sea water at a temperature $T_w$. A heat pipe, consisting of a thermal conductor insulated around its outside, then acts as an efficient medium for heat transfer between the exchangers. Sandwiched in the middle of the heat pipe is a thermoelectric (TE) device, which converts the flow of heat into electrical power (as detailed in Section 2.2.2.1). This is the water based equivalent of the land based thermal energy harvesting device reviewed in Section 2.2.2.2 [57, 58, 104, 105] (see Figure 2.12).

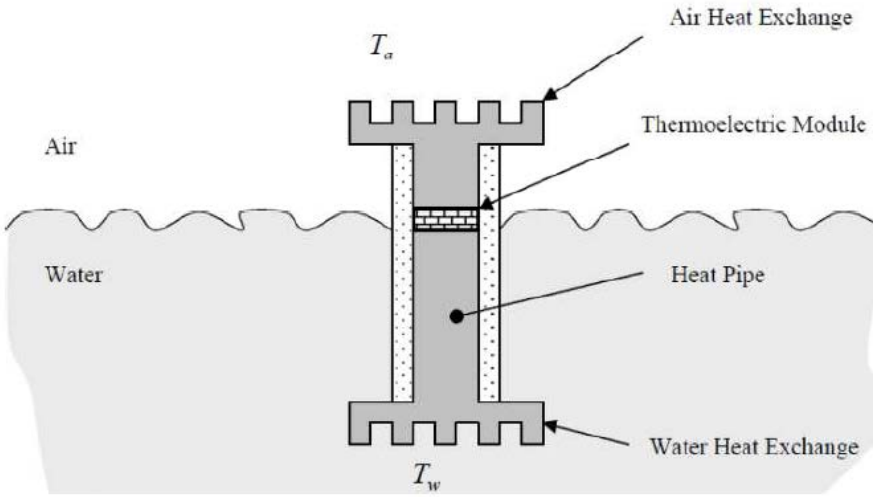


FIGURE 9.3: Thermal energy harvesting device.

To gain an upper limit estimate on the amount of output power that the thermal energy harvesting device could possibly produce, Roundy *et al's* [30] method is applied, Equation 2.3, to estimate the amount of heat conducted through the TE device. This amount of heat is then multiplied by the corresponding Carnot efficiency, Equation 2.2, to give the upper estimate on the maximum amount of output power harvestable from this heat flow. It is assumed that no temperature drop occurs in the heat pipe, therefore the temperature difference across the TE device is:

$$\Delta T = T_a - T_w. \tag{9.1}$$

From Equation 2.3, the rate of heat transfer through the TE device due to conduction is therefore:

$$\dot{Q} = \frac{kA(T_a - T_w)}{\Delta x}. \tag{9.2}$$

Multiplying the flow of heat through the TE device by the Carnot efficiency, gives the upper limit estimate for the output power:

$$P = \eta\dot{Q} = (\frac{T_a - T_w}{max\{T_a, T_w\}})(\frac{kA(T_a - T_w)}{\Delta x}) = \frac{kA(T_a - T_w)^2}{max\{T_a, T_w\}\Delta x}, \tag{9.3}$$

where the $max\{\}$ function returns the largest input argument. Applying the temperature data from Figures 9.1 and 9.2, as input to Equation 9.3, results in the predicted power outputs displayed in Figures 9.4 and 9.5 respectively.

Figure 9.4 is a plot of the calculated output power, for the two days of data from the AIMS Orpheus Island site in Figure 9.1. The output power is seen to follow the temperature difference's diurnal cycle, with a maximum power output of about 11 W/m$^2$ occurring early in the morning and then dropping down to around zero in the late afternoons. The average power output for the two days is 3.3W/m$^2$. For the global scale data, Figure 9.5 shows a yearly average power output on the order of 100mW/m$^2$.

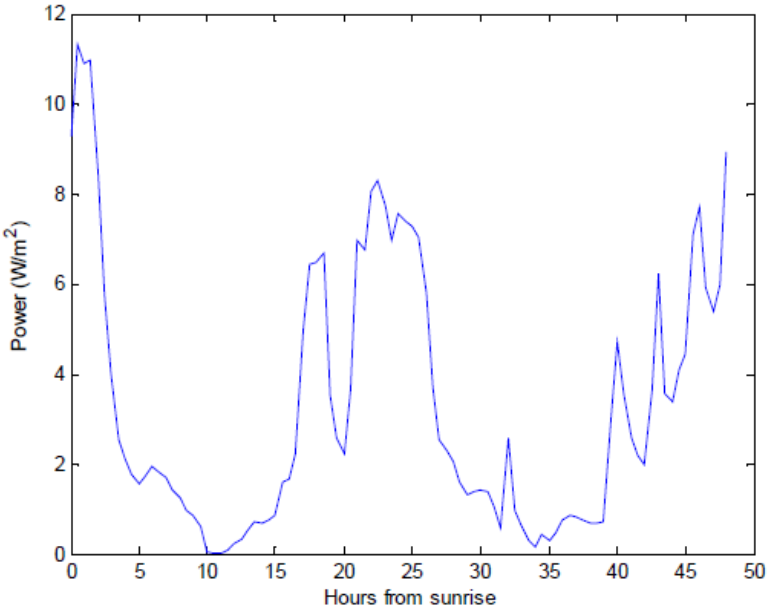


FIGURE 9.4: Power output from the thermal energy harvester model for the temperature input from Figure 9.1.

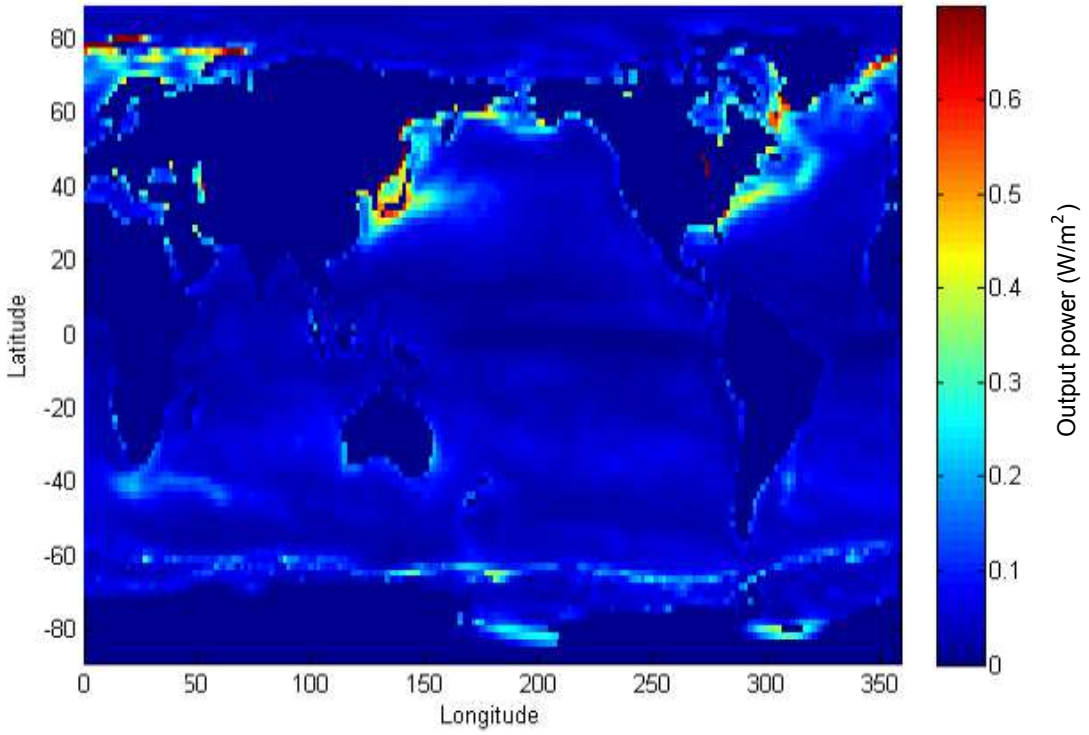


FIGURE 9.5: Average power output from the thermal energy harvester model for 2008.

### 9.2.2 Including a solar thermal collector

The results calculated in the previous section imply that the thermal energy harvesting device must occupy many square meters of area on the ocean surface to harvest the required 1W of output power for the MBS. To help improve this situation, the harnessing of solar thermal energy to increase the airside temperature of the TE device is investigated in this section.

The concept that, a black object subjected to sunlight will heat up due to the object absorbing the incoming solar energy, inspired the new thermal energy harvester device configuration, depicted in Figure 9.6. The new thermal energy harvester device is similar to the original design in Figure 9.3, but with the addition of the top collector plate on the airside of the TE device. The purpose of top collector plate is to absorb the incoming solar radiation, heating up to temperatures greater than the temperature of the surrounding air.

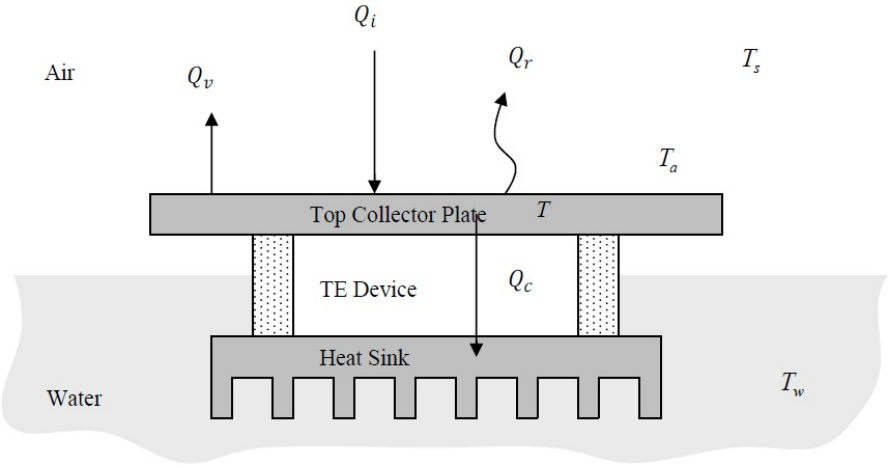


FIGURE 9.6: Physical setup of the solar thermal concept.

#### 9.2.2.1 Model

The top collector plate's temperature, $T$, changes in response to the four heat transfer processes illustrated in this figure; the incoming solar radiation, $Q_i$ , the outgoing radiation, $Q_r$, conduction down through the TE device, $Q_c$, and convection from its top surface, $Q_v$. The time rates of these four heat transfer processes, can be expressed in terms of the air temperature, $T_a$, water temperature, $T_w$, and sky temperature, $T_s$, [183]:

$$\dot{Q}_i = \alpha A_c I, \tag{9.4}$$

$$\dot{Q}_c = -kA_{TE}\frac{T - T_w}{\Delta x},, \tag{9.5}$$

$$\dot{Q}_v = -hA_c(T - T_a), \tag{9.6}$$

$$\dot{Q}_r = \epsilon\sigma A_c(T^4 - T_s^4), \tag{9.7}$$

where the overdot denotes time derivative, $A_c$ and $A_{TE}$ are the areas of the collector plate and TE device respectively, $\alpha$ is the absorptivity of the collector plate, $I$ is the incoming solar insolation, $h$ is the convection coefficient, $\epsilon$ the emissivity of the collector plate and $\sigma$ is Stefan-Boltzmann's constant.

The total rate of heat transfer to/from the top collector plate, $\dot{Q}_t$, is the sum of these four heat transfer processes:

$$\dot{Q}_t = \dot{Q}_i + \dot{Q}_c + \dot{Q}_v + \dot{Q}_r. \tag{9.8}$$

The net amount of heat energy absorbed/emitted by the top collector plate in a given time, $\Delta t$, is:

$$Q = \dot{Q}_t \Delta t. \tag{9.9}$$

The change in heat energy from the top collector plate results in corresponding a temperature change:

$$\Delta T = \frac{Q}{mc}, \tag{9.10}$$

where $m$ is the mass of the collector plate and $c$ is its specific heat capacity. The present work assumes a 1cm thick aluminium plate relating to a $mc$ value of 24,300 J/K/m$^2$.

The model runs iteratively, updating the temperature of the top section at each step;

$$T_{n+1} = T_n + \Delta T, \tag{9.11}$$

until $\Delta T = 0$ i.e. the temperature value converges to its steady state value for the given inputs at that time step. The output power is then calculated as the rate of heat flowing through the TE device, multiplied by the corresponding Carnot efficiency:

$$P = \eta \dot{Q}_c \tag{9.12}$$

#### 9.2.2.2 Convection coefficient

The convection co-efficient, $h$, is dependent on the local windspeed. For a horizontal flat plate, the convection co-efficient is related to the Reynold's number, $Re$, and Prandtl's number, $Pr$, via [183]:

$$h = 0.003 Re^{4/5} Pr^{1/3}. \tag{9.13}$$

#### 9.2.2.3 Absorptivity and emissivity

Initially the absorptivity and emissivity values for the collector plate were both set to 0.9. The resulting output power was only marginally greater than the results previously obtained without the solar thermal collection. To improve this, the collector plate must utilize selective absorbing materials that are designed to have high absorptivity in the visible light range of the spectrum, whilst exhibiting low emissivity in the infra-red range where the collector plate will be emitting most of its energy from [183]. Common selective absorbing materials can have absorptivities of 0.9 with emissivities of 0.1, these values are therefore employed in the current model.

#### 9.2.2.4 Collector plate and TE device area

To allow the calculated power outputs to be represented in W/m$^2$, the collector plate area is set to 1m$^2$. The relative area of the TE device then has a significant effect on

the output power. For example decreasing the TE device's area restricts the amount of heat escaping the top collector plate, which increases the temperature difference across the device. The increased temperature difference results in higher Carnot efficiencies, however at the cost of reduced amounts of heat energy flowing through the TE device available for conversion. Conversely, increasing the TE device's area allows a large amount of heat to flow through the TE device, but decreases the temperature difference across the device and therefore the Carnot efficiency.

An optimum TE device area would allow a generous heat flow while maintaining an appropriate temperature difference for efficient conversion. Here, the optimal area of the TE device is estimated by comparing the calculated average power outputs for varying TE device areas using the Orpheus Island data as input. From these results, a TE device area 5% of the collector plate's area ($0.05\text{m}^2$) was found to produce the largest power output and is therefore used in calculating the following results.

#### 9.2.2.5 PAR to solar insolation conversion

Solar insolation wasn't recorded at the Orpheus Island site, but Photosynthetically Active Radiation (PAR) was. PAR is a measure of the incoming sunlight used by plants for photosynthesis, the 400 - 700nm wavelength spectral band. Values for the solar insolation are estimated from the PAR readings via the procedure in Appendix B, where a conversion factor from PAR to solar insolation is derived by the present author.

#### 9.2.2.6 Results

The calculated output power for the Orpheus Island dataset are displayed in Figure 9.7, and for the global dataset in Figure 9.8. The Orpheus site has a mean value of $5\text{W/m}^2$, and a maximum value exceeding $50\text{W/m}^2$ which relates to a period of strong solar insolation coinciding with very low wind speeds. The output power is significantly larger during the daylight hours and is spiky in nature, due to factors such as; passing cloud coverage reducing the incoming solar radiation and fluctuating wind speeds convectively removing heat from the plate, causing this irregular power flux.

For the global data, the average output power increased by a factor of about 30 compared to the values previously calculated in Figure 9.5. The geographical regions with the largest potential are now in the tropical zones, which experience high solar insolation values. To illustrate the seasonal variability of the resource, Figure 9.9 shows the results for the month of January alone and Figure 9.10 for the month of June, where much larger output power values are seen in the local summers than winters.

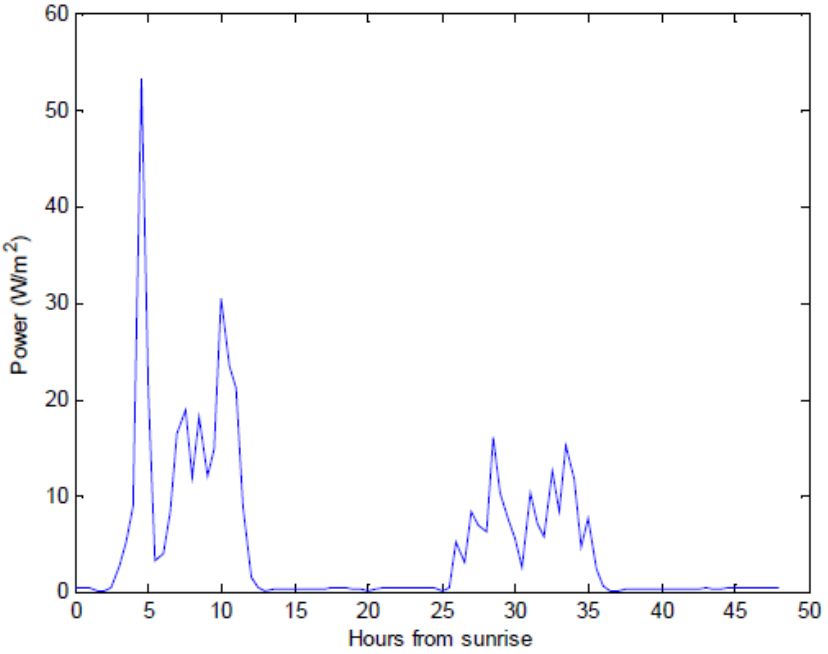


FIGURE 9.7: Power output from Orpheus Island Site utilising the solar thermal harvesting model.

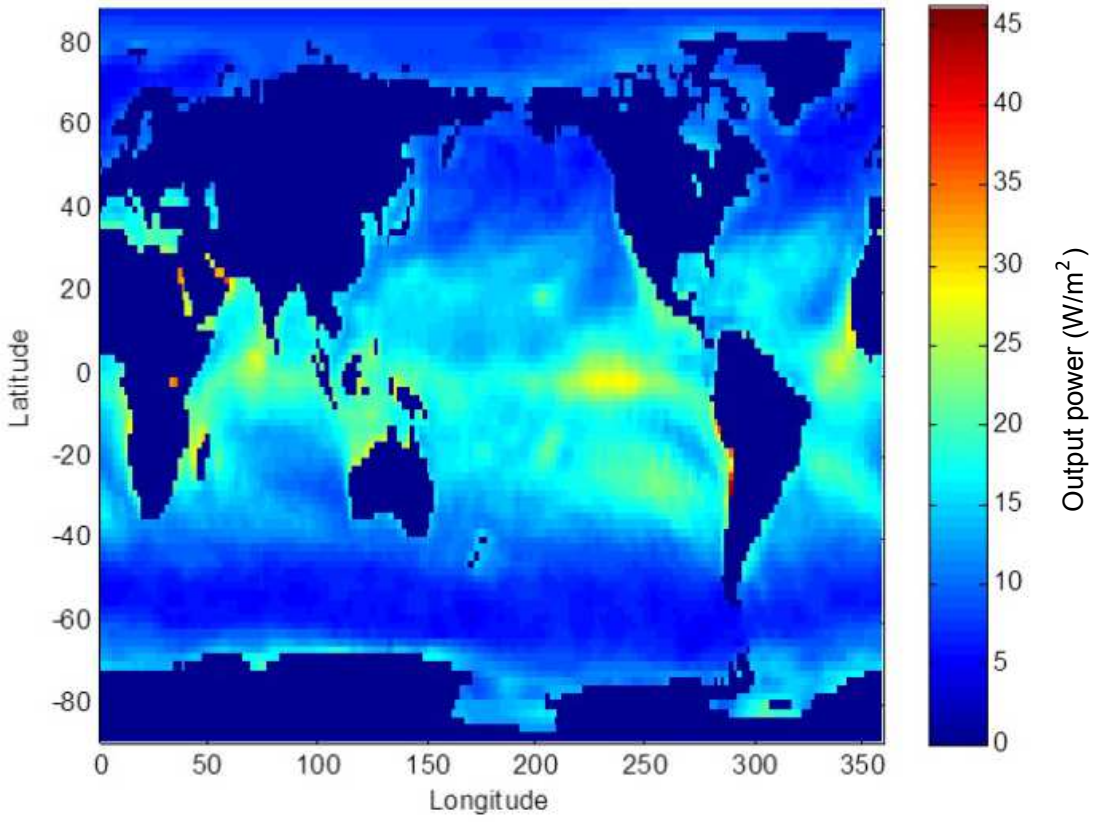


FIGURE 9.8: Average output power for 2008 utilising the Solar thermal harvesting model.

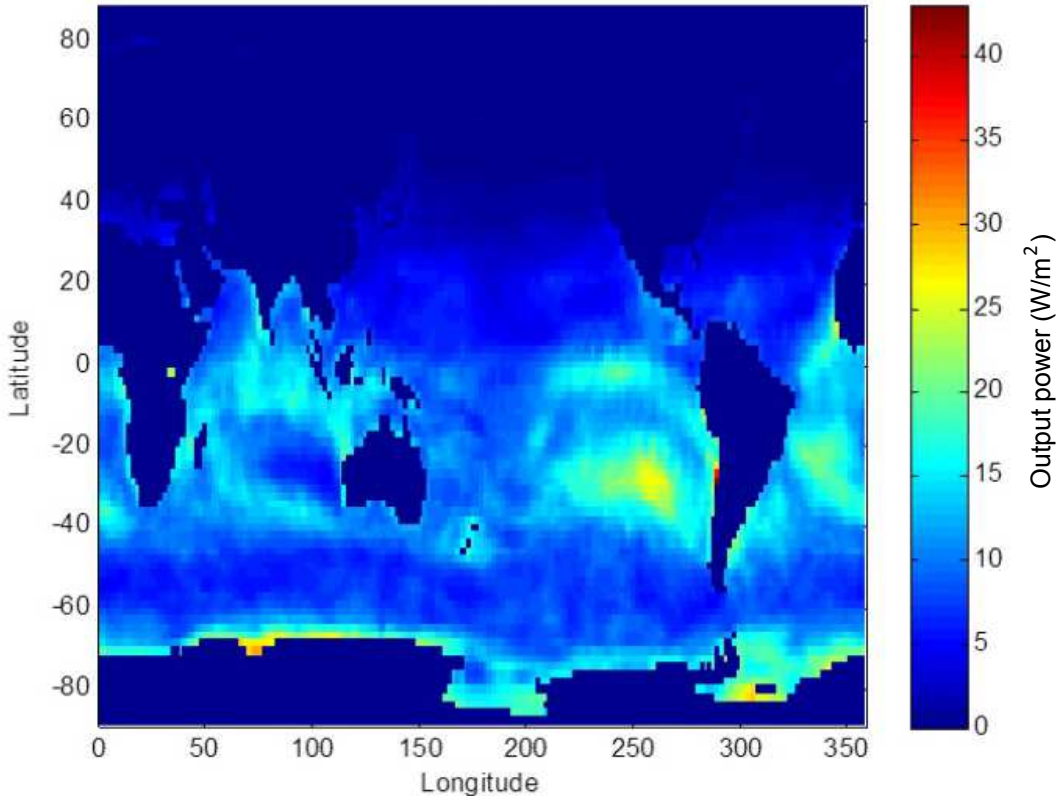


FIGURE 9.9: Average output power for January 2008.

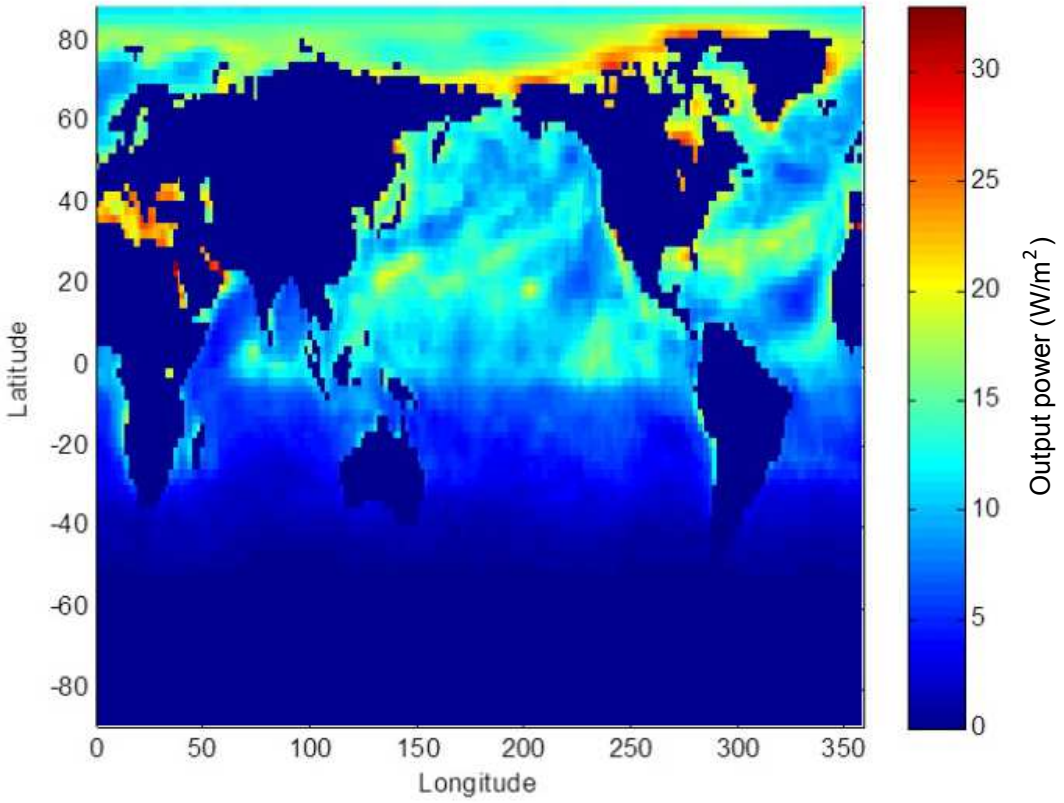


FIGURE 9.10: Average output power for June 2008.

### 9.2.3 Discussion

The aim of this section was to gauge the thermal energy harvesting potential across the air/water interface. The results estimated an average power output on the order of 100mW/m$^2$ by utilizing the natural temperature gradient existing between the water and ambient air. Including a solar thermal collector increased the predicted potential to around 10W/m$^2$. These preliminary results favour towards an upper limit to the available power from this resource, stemming from the optimistic assumptions made during the calculations, such as the TE device operating at the Carnot efficiency and no heat losses occurring throughout the system.

The results showed large fluctuations in the expected power outputs over many time scales. The power output oscillated daily in response to the transitions of the Sun, had sudden drops due to cloud coverage and strong winds, and varied across the year in response to the changing seasons. For use with MBSs, this necessitates secondary energy storage to ensure a constant robust power supply.

The power outputs could be increased through the use of glass or Perspex covers which are transparent to the incoming sunlight but opaque to the outgoing radiation, which is common practice in solar thermal engineering [183]. It has the effect of increasing the temperature of the collector plate by reducing the amount of outgoing radiation, $Q_r$, and reducing the amount of heat lost through convection, $Q_v$, by shielding the plate from the wind.

The optimal area of the TE device should be the focus of further investigation. The one dimensional modelling performed in this chapter assumes the temperature does not vary across the collector plate. In reality the area of the collector plate directly above the TE device will be different to other parts of the plate due to the extra heat transfer there. This will result in thermal gradients developing across the plate's surface with conduction flowing between these regions. To model this better, a three dimensional treatment of the problem should be implemented (or two dimensional if axisymmetric operation is assumed). If time and resources permitted, modelling the heat transfer processes throughout the system using CFD would allow a better understanding of the effect of the TE device area on the output power. CFD simulations would also allow the effect of the glass/Perspex cover mentioned in the previous paragraph to be implemented in the model and also permit a more realistic treatment of the heat pipes and exchangers.

As shown by Equations 9.2 and 9.5, not only is the rate of conduction from the collector plate through the TE device, $\dot{Q}_c$, dependent on the area of the TE device, $A$, but it is also inversely proportional to the thickness of the TE device, $\delta x$. The TE device thickness, $\delta x$, was assumed to be 1cm, as a reasonable estimate of the thickness of commercially

available devices. However the value chosen for this parameter does not greatly affect the output power results from this analysis, because the TE device area, $A$, was optimised in Section 9.2.2.4, using $\delta x = 0.01m$. Since the output power is linearly proportional to $\frac{A}{\delta x}$, if a different value for the device thickness been chosen then the selected TE device area from the trial simulations would have varied accordingly. Thus the choice of TE device thickness mainly affects the choice of TE device area and not the output power.

The data sets used were the polar opposite of each other. The Orpheus island data gave actual readings taken at one precise location every 30 minutes for 48 hours yielding a good indication of the power output available for one site at one time of the year for one set of environmental conditions. Had the data been taken from a different location, a different time of the year or if it had have been a rainy day for example, the results may have been substantially different. Whereas the global data gave interpolated predicted readings averaged over a spatial area of 10,000km$^2$ every 6 hours for one year. While the results from this data gave a good indication of the average outputs expected they have extremely poor time and spatial resolution telling you nothing about specific sites and actual outputs. Together these two datasets give a ballpark insight into the potential thermal resource in the marine environment, but to gain a better understanding of the resource more datasets should be considered.

## 9.3 Experiments

A number of physical experiments were conducted in collaboration with colleagues from CSIRO's Energy Technology Division, Newcastle, Australia, to further investigate and prove thermal energy harvesting concept as a viable power source for MBSs. The work presented in this section is based off the paper Thermoelectric Energy Harvesting as a Wireless Sensor Node Power Source [108] and the book chapter 'Thermal energy harvesting for wireless sensor nodes with case studies' [107] published by the author and Chris Knight from CSIRO.

### 9.3.1 Thermal energy harvester prototype

The design of the thermal energy harvester prototype used in the experiments is illustrated in Figure 9.11 and photographed in Figure 9.12 and Figure 9.13. Following the design proposed in the previous section, it consists of a TE module sandwiched between a top plate and aluminium block heat sink. A transparent plastic dome encloses the air

side of the TE module to reduce wind induced convective heat losses, which were identified as a major source of heat loss in the model simulations. The whole device floats on a foam collar which also provides thermal insulation between the air and water.

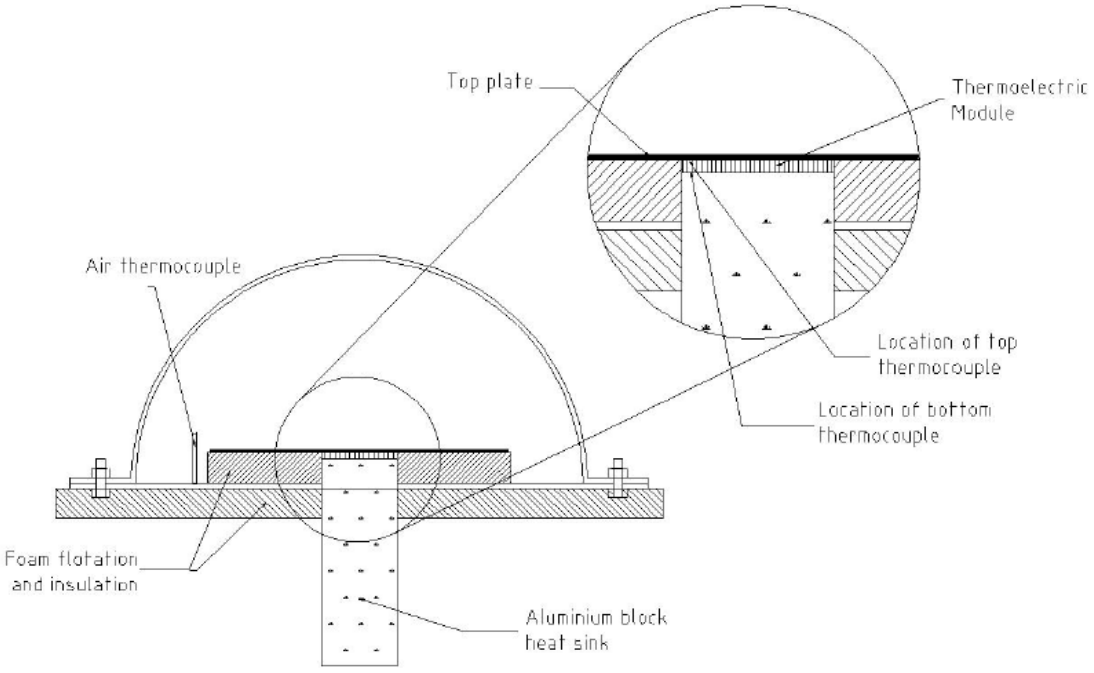


FIGURE 9.11: Thermal energy harvester design.

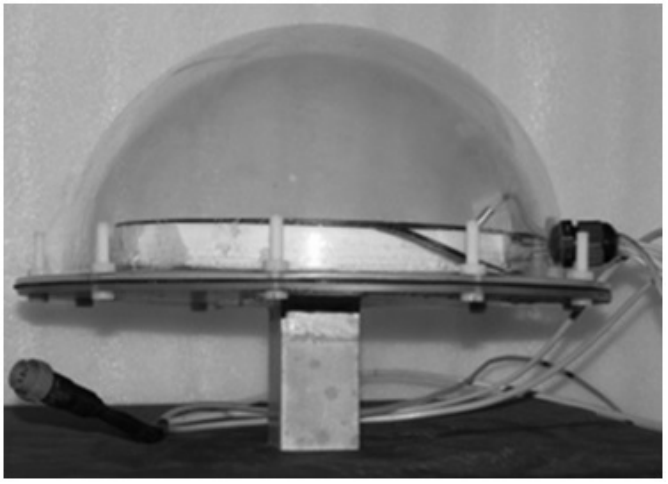

FIGURE 9.12: Photograph of thermal energy harvester prototype used in experiments.

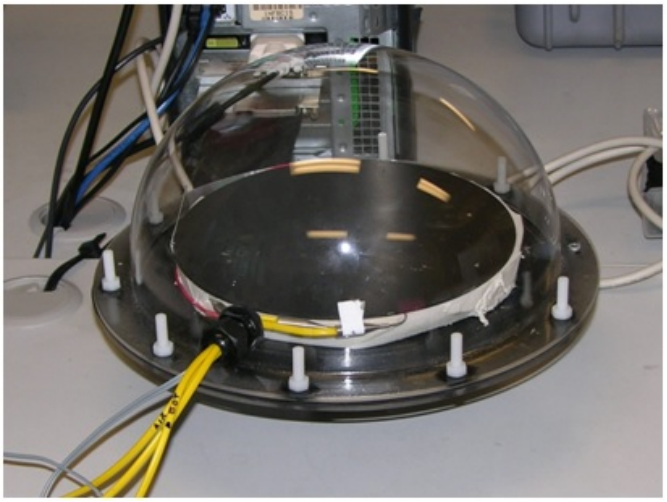

FIGURE 9.13: Photograph of thermal energy harvester sitting on a desk during assembly before waterside aluminium block heat sink is attached.

### 9.3.2 Aim of the experiments

There were four main aims to the experiments:

- Monitor the temperature parameters throughout the system. This will give an indication of the actual temperature differences across the TE device, the effect of the collector plate in increasing the airside temperature of the TE device and how well the heat sink performs in removing heat etc.
- Vary the TE device area ($A_{TE}$) and investigate its influence on the output power.
- Vary the size of the collector plate ($A_c$) and investigate its influence on the output power.
- Proof of concept. Actually use the thermal energy harvester to power wireless sensor node and transmit the results of the experiment to a receiving node.

### 9.3.3 Experimental details

The body of water used in these experiments is a plastic tub filled with approximately 250 litres of fresh water. The tub was chosen for convenience of access and for the security of the experiment, which was conducted on the grounds of the CSIRO Energy Technology Division, Newcastle, Australia. Approximating the real ocean environment with a tub of water introduced two main issues. The first being, the lack of mixing and turbulence in the water, which may lead to stratification of the temperatures with the heat sink sitting in a layer of warm water. The second issue, is that the tub of water's

low thermal mass may result in its temperature fluctuating more, in response to the surrounding air temperature and exhaust heat from the energy harvester, than a large body of water whose temperature is less variant. The effect of using the tub of water on the results obtained is discussed later.

Thermocouples are used to measure temperature values for the air, collector plate, bottom heat sink and water. As shown in Figure 9.11, a thermocouple is located on the underside of the collector plate and another on the top side of the heat sink, thus directly measuring the temperature difference across the TE device. A third thermocouple measures the air temperature inside the dome and a fourth measures the water temperature. These thermocouples are connected directly to a datalogger. The output from the thermal energy harvester is also connected directly to the datalogger, except for the proof of concept experiment where the data is transmitted via CSIROs Fleck3B wireless nodes.

To investigate the effect of varying the TE module's cross sectional area, $A_{TE}$, the number of TE devices side-by-side inside the module was varied. Each TE device is square in shape with an area of $1.6 \times 10^{-3} m^2$. Three different thermal energy harvesters were concurrently tested, each with a $0.031\text{m}^2$ collector plate but with either one, two or four TE devices operating thermally in parallel and electrically in series inside the TE module.

To investigate the effect of varying the collector plate area, $A_C$, a small, medium and large collector plate were attached to three different energy harvesters for testing. The collector plates are black aluminium disks, the small collector has a diameter of 160mm (area $0.020\text{m}^2$), the medium a diameter of 200mm (area $0.031\text{m}^2$) and the large a diameter of 240mm (area $0.045\text{m}^2$).

### 9.3.4 Results and discussion

#### 9.3.4.1 Temperature values

The measured air and collector plate temperature values for a 24 hour period are plotted in Figure 9.14-(a). This graph illustrates the success of the thermal energy harvester in increasing the top side temperature of the TE device above the ambient air value. At midday, the top side of the TE device is heated more than 20K above the air temperature. However, overnight when the air temperature drops, to around 10K below the water temperature as shown in Figure 9.14-(b), the collector plate is seen to hold its heat from the daytime and remain warmer than the air, roughly halving the potential

temperature difference with the water. The use a thinner collector perhaps may alleviate this problem by reducing its thermal mass and therefore resistance to temperature change. The thickness of the collector plate is another parameter which should be investigated further, finding an optimal value for this parameter could be another task for the CFD simulations suggested in the Section 9.2.3.

Figure 9.14-(b) shows the actual temperature of the bottom heat sink compared with that of the water. During the night hours the heat sink is seen to remain about 1K colder than the water, however during the day, when large amounts of heat is being transferred from the hot collector plate, the heat sink rises up to 5K warmer than the water temperature. The model in the previous chapter assumed that these two temperatures were always equal. The poor performance of the heat sink may in part be due to the experimental set up, whereby the water sat stationary in a tub, which is unlike the real ocean environment, where the currents, waves and other fluid motions would greatly increase the removal of heat from the sink via convection. The graph shows that the water temperature changes by over 20K across the day, this is also an artefact of using a tub of water as opposed to an actual large body of water such as a lake, river or ocean, whose temperatures tends to remain relatively constant across the day due to their large thermal masses (see Figure 9.1 for example).

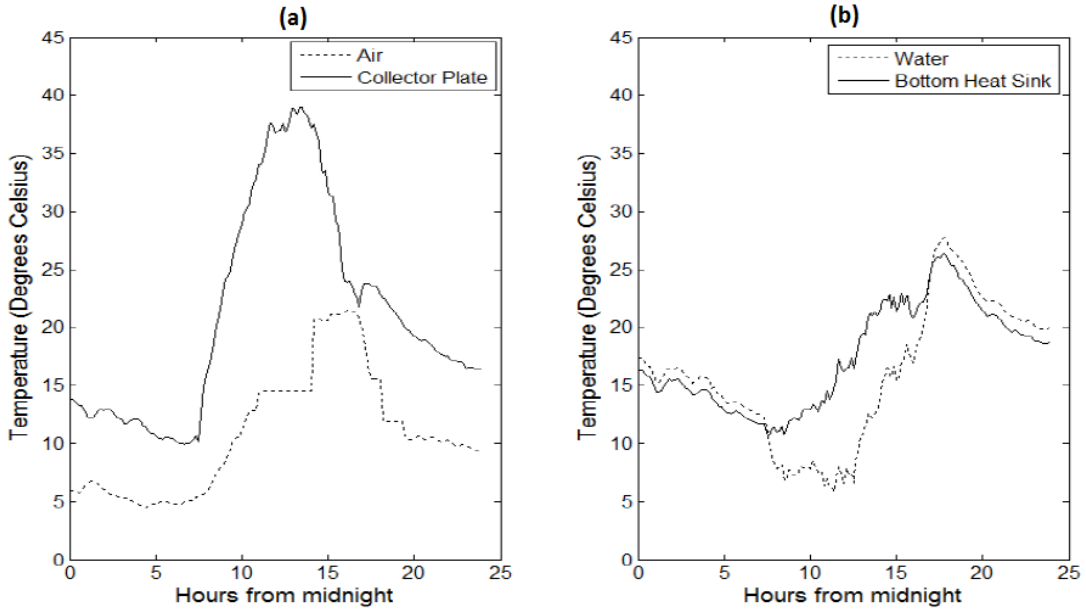


FIGURE 9.14: (a) Temperature of the ambient air and collector plate. (b) Temperature of the water and bottom heat sink.

#### 9.3.4.2 Varying the number of TE devices trial

The results of the experiments involving the variation of the number of TE devices are presented in Figure 9.15 and Figure 9.16. Figure 9.15 shows the total power output from the three different thermal energy harvesters. It shows a full 24 hour period starting from midnight, with the power outputs rising during the daylight hours in response to the incoming solar radiation, with a peak around midday. The power output is seen to correlate very strongly with the solar insolation, which was measured concurrently at a station less than 100m away and is plotted in Figure 9.17. The dip in output power observed in the 14th hour in Figure 9.15 but not in the solar insolation in Figure 9.17, was due to a nearby wind turbine pole shadowing the experimental set up but not the pyranometer collecting solar data.

In Figure 9.15, it is observed that the energy harvesters with the greater number of TE devices achieved the higher power outputs, with 18, 25 and 36mW of peak power produced by the harvesters with one, two and four TE devices respectively. However, the output power does not increase linearly with the number of TE devices. Increasing the number of TE devices increases the surface area for conduction, which promotes a larger heat flow for conversion. However, the increased amount of heat energy conducted through the TE device, decreases the temperature difference between the top plate and bottom sink, which decreases the Carnot efficiency of the conversion process. This is evidenced in Figure 9.16 which is a plot of the temperature difference across the TE devices. It shows that the thermal energy harvester with one TE device experienced the largest working temperature difference throughout the day, with a peak of 21K occurring at noon, while the thermal energy harvester with four TE devices recorded the lowest working temperature difference, with a peak of around 5K.

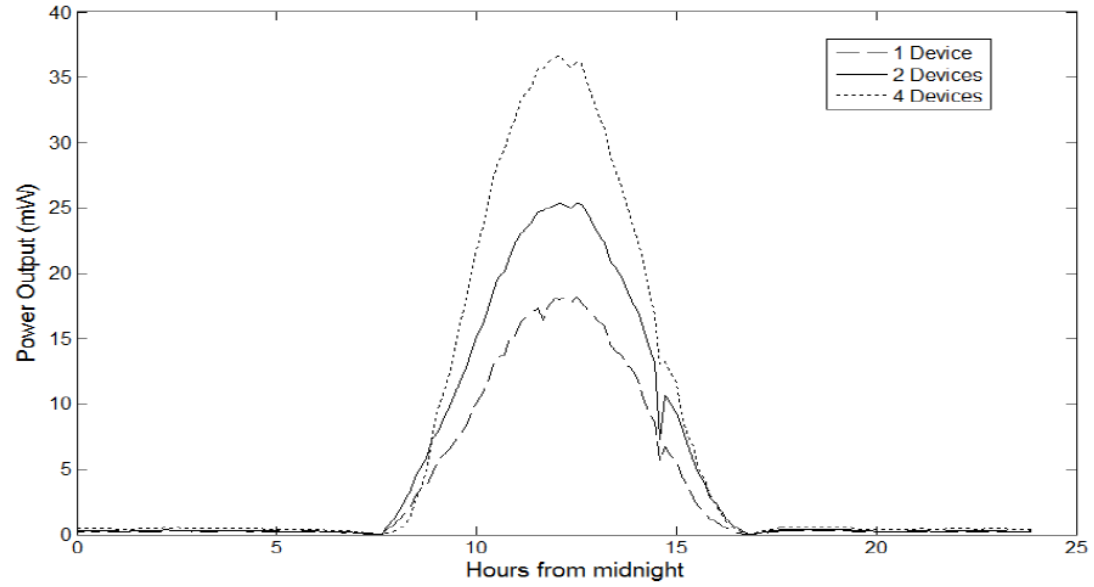


FIGURE 9.15: Power output from the varied number of TE devices experiment.

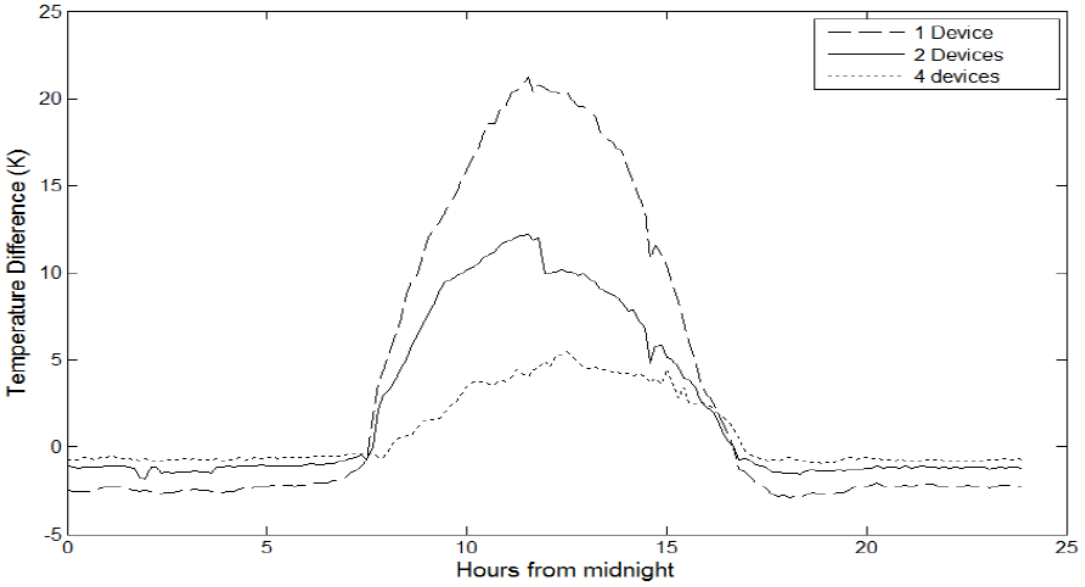


FIGURE 9.16: Temperature difference across TE devices in the varied number of TE devices experiment.

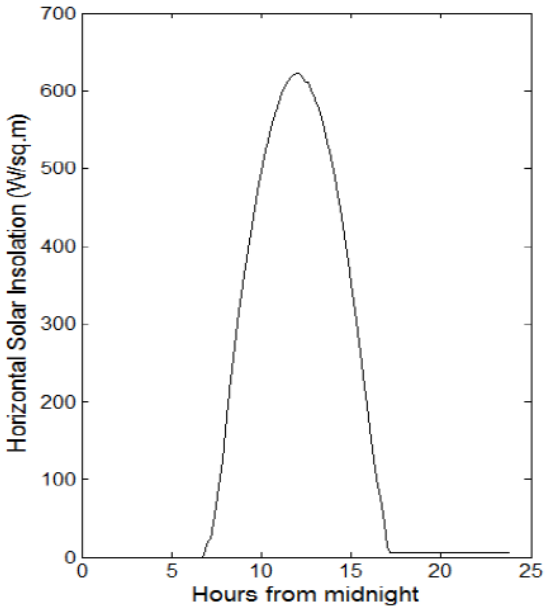


FIGURE 9.17: Solar insolation for the varied number of TE devices experiment.

#### 9.3.4.3 Varying the collector plate area experiment

The power outputs from the experiment investigating the variation of the collector plate area are plotted in Figure 9.18. As the size of the collector plate increases, so too does the output power, with the large collector recording a peak power output of 48mW compared to 31mW for the medium collector and 22mW for the small collector. However, when the power outputs are normalised against the size of the collector plates, to give the output power per unit area, it can be seen that the power flux is similar for all three devices as shown in Figure 9.19.

The solar insolation measured during this trial is plotted in Figure 9.20 where the afternoon values are spikey due to passing cloud cover. The influence of this cloud cover is also seen on the harvesting devices' outputs in Figure 9.19, where the output power drops and spikes at the corresponding times. Comparing Figure 9.19 and Figure 9.20 reveals that the thermal energy harvesters output approximately $1W/m^2$ during an input solar insolation of $640W/m^2$, which relates to a solar energy conversion efficiency of less than 0.2%.

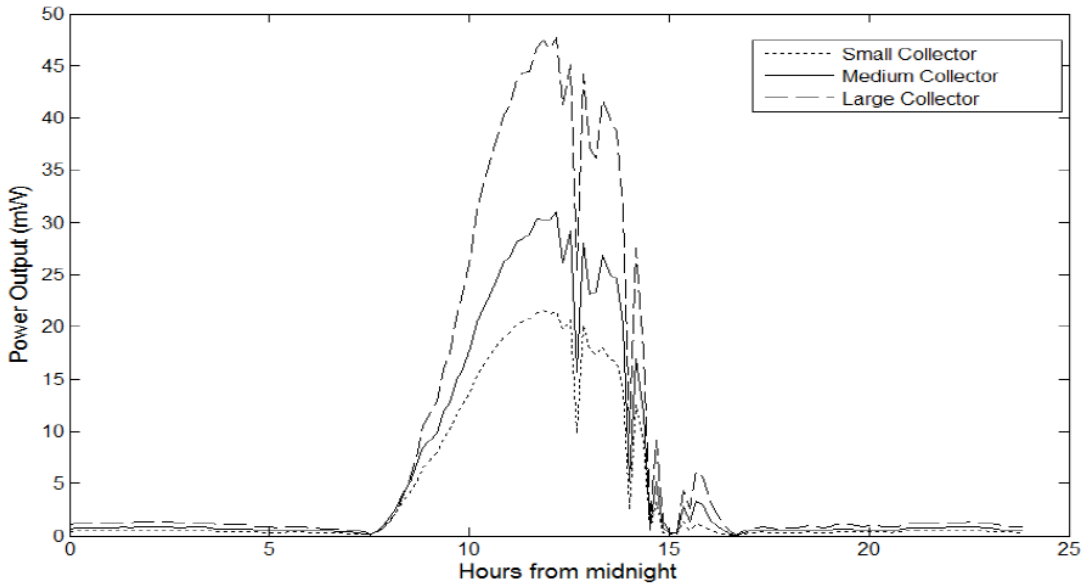


FIGURE 9.18: Power output from varied collector plate sizes experiment.

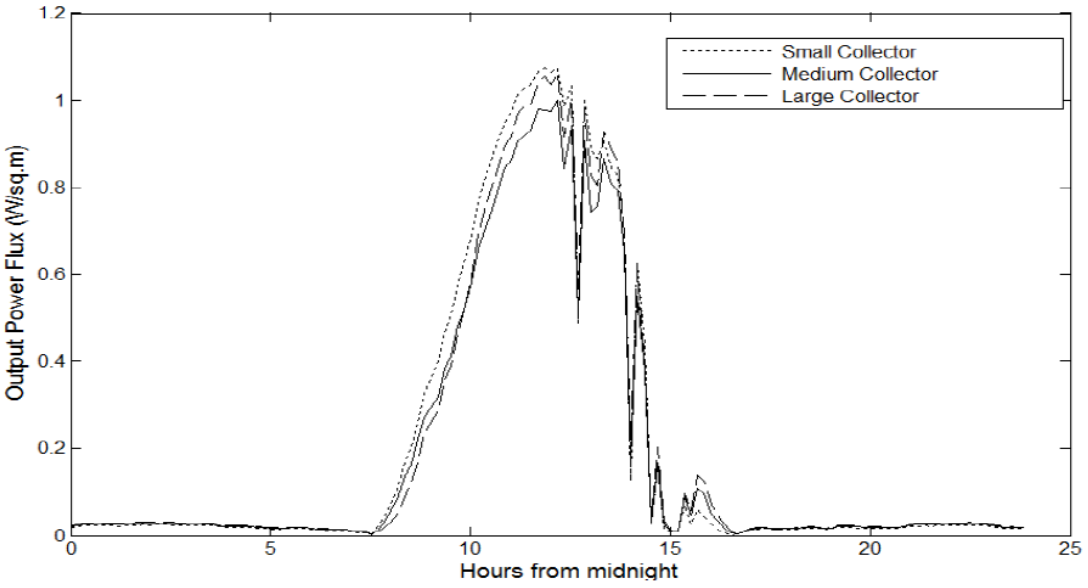


FIGURE 9.19: Normailised power output from varied collector plate sizes experiment.

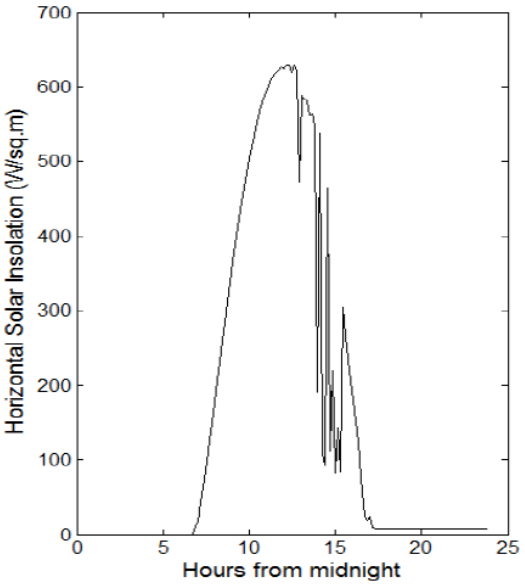


FIGURE 9.20: Solar insolation for varied collector size experiment.

#### 9.3.4.4 Powering a wireless sensor node

The final experiment aimed to directly power a wireless sensor node from the output of the thermal energy harvester. The Fleck 3B node was programmed to record the air temperature every two minutes and transmit the sample wirelessly to a nearby datalogger. It was left to run for almost two days, with the logger receiving over 280 samples in this time. Thermocouples connected directly to a datalogger measured the temperature difference across the TE module for the duration of the experiment, the results are plotted in Figure 9.21. The secondary axis on this graph is a binary indication of whether samples were received by the logger at a given time, revealing that the energy harvester could only power the node when the temperature difference exceeded 10K. The cause of the disrupted sampling on the second day when there appeared to be ample working temperature difference is unknown.

The results in Figure 9.21 reveal large portions of time when the direct output from the harvester was insufficient to power the sensor node. This problem can be rectified by incorporating a secondary battery into the design allowing continuous data transmission by storing excess energy harvested during the day to power the node during the night and at other times when there is insufficient direct output power from the energy harvester.

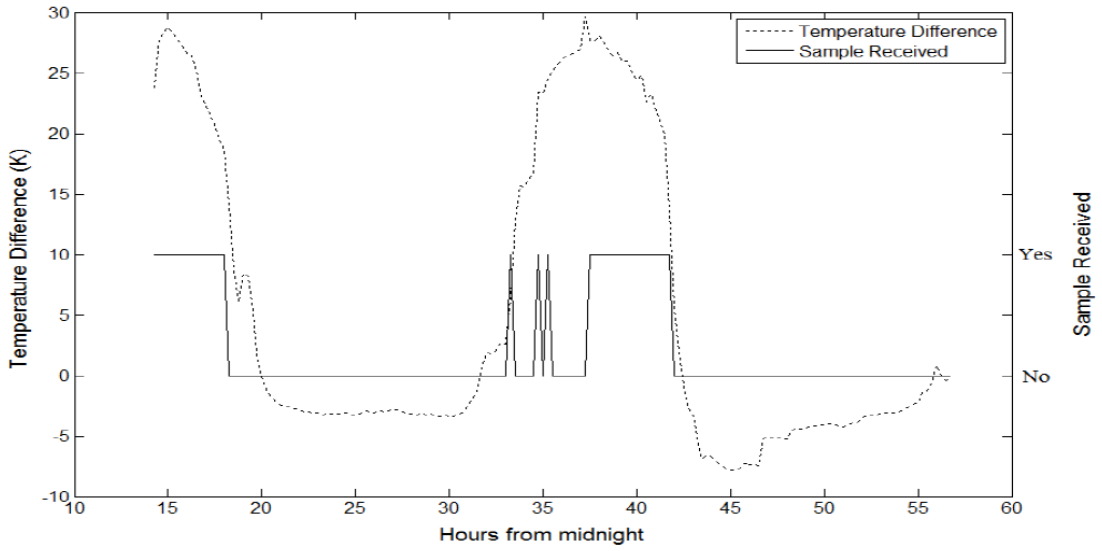


FIGURE 9.21: Results from the experiment directly powering of a wireless sensor node by the thermal energy harvester.

## 9.4 Evaluation of the thermal energy harvester concept

This Section aims to use the information from numerical and experimental studies in Sections 9.2 and 9.3, to evaluate the potential of the thermal energy harvester concept for powering a MBS. The analyses in Sections 9.2 and 9.3 are summarised and then the ability of a thermal energy harvester to provide 1W of average power for a MBS is estimated.

A thermal energy harvester prototype, which promotes the flow of heat across the thermal gradient at the air/water interface and converts a portion of this heat flow into electrical energy via a TE device, was proposed and modelled in Section 9.2. The numerical model was used to simulate the performance of the thermal energy harvester prototype, employing real environmental datasets as input, to gauge the potential power production of the thermal energy harvester for the given input environmental conditions. The input data ranged in spatial and temporal scales, to give a picture of the thermal energy harvester's performance across the course of a day at a single location and its average monthly or yearly performance across the whole globe. By assuming the TE devices were operating at the Carnot efficiency, the simulations predicted power outputs on the order of $100\text{mW/m}^2$. These results indicated the natural thermal gradient existing between the water and air to be an unpromising energy resource. To improve this potential, the use of a solar thermal collector plate to increase the airside temperature of the TE device was investigated. Model predictions showed this concept increasing the power outputs to around $10\text{W/m}^2$.

To estimate the size of a thermal energy harvesting device capable of producing 1W of power, the inherent system inefficiencies need to be accounted for, because the analysis in Section 9.2 represents the maximum achievable power outputs ignoring any losses or inefficiencies. The first inefficiency to consider is the realistic performance of a TE device. Although the state-of-the-art TE materials have a dimensionless figure of merit of around 2.4 at room temperature, corresponding to an efficiency about 20% of the ideal Carnot efficiency, in practice commercial products use TE materials with figure of merit below 1, with an efficiency of around 5% to 10% of the ideal Carnot efficiency [184]. Therefore, the estimated power outputs from the models, which assumed the device to be operating at the Carnot efficiency, immediately decrease by an order of magnitude from $10W/m^2$ to around $1W/m^2$.

The experiments in Section 9.3 showed a peak power output of $1W/m^2$, with an average value of $0.2W/m^2$. A second significant system inefficiency, not accounted for by the models, was revealed by the experiments, namely; the non-ideal performance of the heat sink. The model assumed that the temperature on the bottom of the TE device was the same as the water, with no temperature drop occurring across the heat sink. However, the results from the experiments showed the bottom heat sink to be up to 10K hotter than the water during times of strong incident sunshine (Figure 9.14), which reduces the potential output power. The non-ideal performance of the heat sink was also reported in Lawrence and Snyder [58] for their experiments on terrestrial based thermal energy harvesters across the soil/air interface (see Section 2.2.2.2), whereby temperature drops of up to 4.5 K out of the 10 K total across the air and soil were reported to occur in their 30cm long heat pipes. However, it is likely for the present application that the removal of heat from the bottom heat sink would be improved in the real ocean, as opposed to the tub of water used in the experiments in Section 9.3 or in the soil used in Lawrence and Snyder [58], whereby the mixing of water from the ocean waves and currents should increase the convective heat transfer from the bottom heat sink.

The expected size of a thermal energy harvesting device capable of producing on average 1W of power, would therefore be around $1m^2$ if the heat sink was 100% efficient, but in reality will need to be larger than this due to the expected thermal losses in the heat sink. For a small, light, easily deployable MBS, a $1m^2$ collector plate would be towards the upper limit of what would be acceptable, and for devices larger than this the appeal of the thermal energy harvester concept would start to quickly diminish. For example, a $1m^2$ aluminium collector plate with a thickness of 1cm would weigh 40kg. Additionally, the model results in Section 9.2.2.6 show a large reduction in the output power produced in winter compared to summer, therefore the device would need to be even larger to operate sufficiently during winter months.

From the evaluation in this section, based on the analysis in this chapter, it seems the potential of the thermal energy harvester concept would most likely not be sufficient for the present MBS application. Conclusions and future work for the thermal energy harvester are given in Chapter 10.

# Chapter 10

# Conclusions and future work

An energy harvesting solution is sought to enable the autonomous operation of environmental monitoring in the ocean using MBSs. The average power demands of a MBS's various electronic components, such as the processing microcontroller, transceiver and one or more sensors, was estimated in Chapter 3 to be on the order of 1W. This thesis then identified and investigated two potential renewable energy sources to supply this power; wave energy and the thermal gradient across the air/water interface. Conclusions and future work for these two potential energy sources are given in Sections 10.1 and 10.2, and then general conclusions for energy harvesting for MBSs given in Section 10.3.

## 10.1 Wave energy

Wave energy was the core focus of this thesis. Ocean waves transport a large consistent power flux compared to other renewable energy resources. The thesis hypothesised, that properly designing the MBS buoy with respect to the ocean waves, could provide a two-fold solution to the power supply problem; harvesting renewable energy from the waves to recharge the batteries, and decreasing the power demand of the MBS's wireless communication, by minimising the wave induced pitch motion and tilting of the antenna.

In addition to providing 1W of average power and remaining pitch resilient, the thesis also detailed that for a WEC to be a viable energy harvesting solution for a MBS, it must be cost effective. To ensure the cost effectiveness of a possible MBS energy harvesting WEC, the following properties were identified as being desirable:

- Small and lightweight with low cost materials. A total system weight of less than 50kg was identified as an appropriate target.

- Easily deployable/retrievable.
- A 'one size fits all' design able to operate at any deployment location.

A prototype device, the CIPMLG WEC, was proposed in Chapter 4 to satisfy these requirements, and in Chapter 5 a mathematical model was derived to analyse the WEC's performance in Chapters 6 - 8. A number of conclusions from the analysis of the CIPMLG WEC system are outlined in this section.

### 10.1.1 High frequency operation

The main conclusion from the analysis in this thesis is that a MBS energy harvesting WEC should be optimised to operate towards the high frequency tail of ocean wave spectra, diverging from the traditional philosophy of large scale WECs, which target the peak energy in the lower frequencies of the spectrum. This conclusion is drawn for a number of reasons:

- **Wave resource :** The assessment of the wave resource, detailed in Chapter 7, identified that the high frequency tail of ocean wave spectra is relatively spatially and temporally omnipresent. Therefore, designing the CIPMLG WEC to operate effectively in response to these high frequency waves, ensures its ability to function consistently at any site, which is crucial because its deployment location is dictated by the monitoring objectives of the MBS and not for favourable local wave conditions.
- **Size of the WEC :** Small devices have fast dynamics, therefore the high frequency tail of ocean wave spectra is determined to be well matched with the resonant hydrodynamic frequency of a small sized WEC. Additionally, it was shown in Section 6.4.3 that the natural frequency of the generator is dependent on the maximum allowable stroke length, whereby generators requiring low resonant frequencies need very long stroke lengths and would therefore be prohibitively large for the present application.
- **Spring capabilties :** Operating a higher frequencies is identified to place less demand on the required performance of the generator's mechanical spring. The spring couples the translator mass to the hull of the buoy, and the required load, longer extension, and lower stiffness at lower frequency operation represent a set of specifications that metal springs have difficulty meeting [150].

By analysing standard wave formula derived in the literature, and by using real measured wave data from a number of different case study locations along the coast of Queensland,

a suitable single input wave spectrum was identified for use in assessing the CIPMLG WEC's performance in response to the high frequency tail of ocean wave spectra. This spectrum is depicted in Figure 7.16, and represents the high frequency tail proposed by the Burling spectrum [178], Equation 7.1, truncated at a frequency 3.14 rad/s. The input truncated Burling spectrum represents the high frequency wind sea ripple and has a peak period therefore of 2 seconds, a significant wave height of 0.17m and transports 23W of power per metre of wave front. The wind conditions required to create the input truncated Burling spectrum were observed to be present more than 90% of the time at any of the case study sites, presented in Section 7.2.2.

### 10.1.2 CIPMLG WEC performance

The results of the CIPMLG WEC performance, presented in Chapter 8, showed that trade-offs exist between power capture and pitch stability. Larger radii buoys were more pitch resilient, but produced less output power. It can be concluded that the CIPMLG WEC would not be able to simultaneously satisfy the output power and pitch stability requirements, whilst remaining below the target mass of 50kg.

This conclusion holds for the hypothesis that optimising the WEC to the high frequency tail of ocean wave spectra, represented by the input truncated Burling spectrum identified in Chapter 7, would guarantee satisfactory performance at any deployment site allowing a 'one size fits all' design. Whether it is possible to optimise the CIPMLG WEC parameters to the larger power resource in the lower frequencies could be investigated. Due to the variability of the wave resource at these lower frequencies, the optimisation would have to be performed on a site-by-site basis given prior knowledge of the wave climate. Such a strategy would likely involve harvesting surplus amounts of power, during predominant wave conditions, to charge batteries with large enough capacities to withstand periods of less favourable wave conditions and lower power outputs. This strategy also depends if production can be manufactured in such a way that bespoke designs are financially feasible.

#### 10.1.2.1 Geometry

Although the performance of the CIPMLG WEC was inadequate, the results in Section 8.6 showed that modifying the geometry of the WEC's hull, from a cylinder to other shapes that are better coupled to the input waves, can lead to significant improvements. The Wedgetop WEC design, is shown to have the potential of fully satisfying the design requirements. It can be concluded that, with optimisation of the WEC's geometry, a WEC device using an IPMLG PTO can be designed to provide the required 1W average

power output from the high frequency tail of ocean wave spectra, whilst obeying pitch displacement constraints of 40 degrees across a wide range of sea states and having a total system mass of less that 50kg.

#### 10.1.2.2 Mass distribution

The performance of the WEC is heavily influenced by the mass distribution. The output power is influenced by what fraction of the total mass is allocated for the translator mass, and the pitch motion is influenced by how the mass distribution affects the MoI and CoM values. However, the pitch motion of the Wedgetop WEC geometry was seen to be less dependent on the MoI and CoM values, which is another advantage of this geometry, allowing more flexibility in the mass distribution.

Further WEC refinement and design, should be done in conjunction with the overall MBS design, taking into consideration the location and mass density of the various MBS components. In terms of a 'one size fits all' approach, designated compartments with allocated mass budgets can be placed within the buoy for the various MBS equipment. Extra ballast mass can be added into the compartments if the mass of MBS equipment is below the allocated amount. The analysis approach given in this thesis can aide in appropriately selecting the target CoM and MoI values that the mass distribution should aim to fulfil.

### 10.1.3 Pitching motion

Although care is taken to minimise the pitching motion of the buoy, the performance of the data transmission may still be affected by the pitch induced tilt of the antenna during certain sea conditions. Therefore, it may be prudent to only transmit data during times when the sea state is known to produce minimal torques on the buoy. General wave conditions, i.e. sea states, can be predicted many hours in advance. This prior knowledge may be fed from the base station to the sink node, which can then co-ordinate the next several hours of communication, based on the known weather windows. Nodes may choose to send data during certain sea conditions, and sinks and stations will know the correct time to send instructions to and receive data from the nodes.

While this thesis considered only the wave induced motions, both the currents of air (wind) and water (tidal flows), will also produce torques on the buoy, inducing an angle of pitch. Additionally, depending on where the mooring lines are attached to the buoy, there can also be torques applied to the buoy due to the mooring forces, as discussed in the next subsection. Further development of the MBS energy harvesting WEC should

take into account these additional pitch inducing effects, to ensure pitch stability for the MBS buoy and correct alignment of its antenna for data transmission.

### 10.1.4 Comparison against other systems

The predominant energy harvesting method currently used for powering MBSs is solar PV. Chapter 3 reviewed the different energy resources in the marine environment, detailing that the commercial readiness of the well-established solar PV technology, with off the shelf solutions available, is a key reason for their adoption in initial energy harvesting systems for MBSs. However, solar PV can suffer from reliability issues, with the amount of incident solar power diminishing during cloudy days, high latitude winters and/or when the PV panel surface becomes covered with dust, bird droppings, water and marine salt. Short-term deficiencies in solar PV outputs due to cloud coverage can probably be solved by over-sizing the system, using solar PV panels with maximum power ratings in the 10's - 100's of Watts range, which can easily be achieved using solar PV panels with surface areas on the order of $1m^2$ or less. As discussed in Section 3.3, the energy storage required for one day's operation (24Wh) can be fulfilled by lithium-ion batteries with a mass of 0.1kg, therefore a battery bank of 1kg could keep the system running for over a week if persistent bad weather hindered the solar panel's outputs. The required structure on the MBS buoy above the water surface, on which to mount the PV panels, could pose a potential drawback for solar PV, with increased risk of vandalism or theft, and possible detrimental affect the pitching motion of the buoy. A wave energy harvester on the other hand, is shown in this thesis to provide a reliable power output, due to the relative consistency of the wave resource compared to the intermittent solar resource. Additionally, the wave energy harvesting solution offers the potential to minimise the pitching motion of the buoy, to ensure robust data transmission.

While this thesis investigated one proposed type of WEC design, there exist many other possibilities which may also have potential. A number of such solutions were reviewed in Section 4.3.4, which also sought to harvest wave energy for distributed power generation, albeit with power outputs one to two orders of magnitude greater than that solicited in the present thesis. The chief difference between these other WECs and the CIPMLG WEC, is the frame of reference which the floating buoys react against to derive useful power. The CIPMLG WEC reacts against an internal inertial mass whereas the other WECs react against the sea floor or a resistance plate.

The use of an internal reaction mass for the present application was envisioned to allow a smaller, more reliable and easily deployable device, as the system is compact, completely

sealed and requires no specialised moorings. Additionally, due to the highly corrosive marine environment, a completely sealed internal generator was seen as favourable. The concept of the IPMLG was inspired following similar designs used in vibration energy harvesting (reviewed in Section 2.2.3.3), whereby the ocean waves can be viewed as vibrations on the water's surface. Although vibration energy harvesters are typically reported for used in the $\mu$W - mW power range, the analysis in this thesis indicates that an electromagnetic vibration energy harvester could also applicable for the 1W power output range required for MBSs.

For larger amounts of power, exceeding the 1W target of the present work, it may be advantageous to use a resistance plate to increase the available inertia, allowing the system to react against the mass of the surrounding fluid, without requiring the WEC to provide the extra mass and become prohibitively heavy. Indeed this was the case for the small scaled WECs reviewed in Section 4.3.4, which were targeting power outputs of 10's-100's of Watts.

Other PTO mechanisms such as oscillating water columns or gyroscopic PTOs could also warrant investigation. The proposed WEC design offered in this thesis is one possibility, which seems to have merit and whose results are now available for future comparison against other WEC configurations.

### 10.1.5 Limitations

The assessment of the CIPMLG WEC performed in this thesis has been limited to numerical analysis via mathematical models. In particular, the analysis has been based on linear modelling techniques. The linear models have allowed a preliminary analysis of the system and a general understanding of the different effects the different design parameters have on the system's performance. From this initial analysis, the vast solution space is narrowed, through the elimination of design parameter combinations with predicted poor performance, and by allowing candidate designs with good potential to be identified. To further assess these candidate designs, any nonlinearities neglected by the linear models should then be included in the analysis where possible, to give further insight into the system behaviour and allow increased confidence in the results. The development of nonlinear models is discussed in the "Future work" section (10.1.6).

The numerical analysis needs to be validated by physical experiments. Parameters such as mechanical damping can only be measured by physical experiments, therefore the development of more refined models should go hand-in-hand with tests of physical prototypes. The work in this thesis has laid the groundwork for informing the general

prototype design on which the experiments should focus on, and offers a guide to aide the experimenter in selecting appropriate design parameter values.

### 10.1.6 Future work

The ultimate goal for future work on the wave energy harvester is a full prototype deployment in the ocean. Due to the costs involved in physical prototype development and deployment, particularly in the marine environment, it is important to have a well refined device by the time it reaches the sea. The majority of the learning process and optimisation iterations should be performed more cost effectively beforehand using numerical tools, computer simulations and laboratory scale physical experiments. The numerical modelling and analysis in this thesis has already allowed the development and evaluation of the original CIPMLG WEC prototype and lead to an evolution in its design, the Wedgetop WEC.

The immediate first steps in future work is therefore further device evaluation, refinement and optimisation using numerical tools. The level to which this can be achieved is directly related to the accuracy and detail of these tools, requiring an extension from the linear models used in this thesis and supplementary physical experiments. This section describes the work, planned and in progress, towards further numerical analysis and optimisation of the wave energy harvester.

#### 10.1.6.1 Hydrodynamic modelling

A background on the field of hydrodynamic modelling and the choice of linear analysis for the present application, was given in Section 5.2.1. While linear hydrodynamic models have been well verified and validated for many circumstances, there are certain conditions there the linearising assumptions breakdown. Two of these conditions are present for the case of the Wedgetop WEC. Firstly, while viscous effects can often be neglected for large scale marine structures, when the size of the structure decreases the importance of viscosity increases. Therefore viscous effects may be important when analysing the performance of the small scale devices investigated in this thesis. Secondly, while the assumptions of linear restoring and excitation forces holds well for the cylindrical geometry of the CIPMLG WEC, which has a constant cross-sectional area, the Wedgetop WEC's strongly varying cross-section around the water's free surface intrinsically leads to nonlinear restoring and excitation forces [159, 163].

One option to analyse the nonlinear hydrodynamic behaviour of the Wedgetop WEC is through physical wave tank testing. However, access to specialist wave tank facilities,

where testing is charged on a per day basis, and evaluating geometrical parameter variation, which requires constructing multiple prototypes, is expensive. As an intermediate step to further refine the device geometry and better understand the device performance, before moving advanced designs into the expensive wave tanks, high fidelity numerical wave tanks (NWTs) based on CFD may be used.

CFD allows fully nonlinear hydrodynamic calculations, including effects neglected by traditional linear velocity potential methods such as viscosity, large wave amplitudes and body motions, green water and vortex shedding, however at great computational expense. Typical computation times can be up to 1000 times the simulation time i.e. 1 s of simulation time takes 1000 s to compute, which is a major drawback of using CFD for WEC optimisation, through multiple design iterations, where long-time simulations in real sea states are required. Therefore, a new modelling methodology, aimed at combining the accuracy of CFD simulations with the computational efficiency of parametric models, has been investigated by the author, whereby system identification techniques are used to identify nonlinear parametric hydrodynamic models from CFD generated data.

This section outlines research performed by the author, with the Centre for Ocean Energy Research at Maynooth University, Ireland, to develop nonlinear hydrodynamic models identified from CFD based NWT experiments [158–166].

- In [162] the author details the implementation of a CFD based NWT configured for wave energy experiments, using the open source CFD software OpenFOAM.
- In [158] and [160] the author demonstrates identifying the parameters of a linear state space state model such as the one outlined in Section 5.2.2.2, by using system identification techniques on the outputs of wave energy experiments performed in a CFD NWT. The resulting linear models are shown to be dependent on the operating conditions, and the paper shows that different linear models can be used to be representative of different operating conditions. As the amplitude of the oscillations in the experiments decrease, the paper shows that the parameters of the identified linear models converge towards the parameters obtained using the hydrodynamic coefficients from BEM software, such as those outlined in Section 6.2.4, which are based on the linearising assumptions of small amplitude motion.
- In [159] the author demonstrates identifying nonlinear discrete time hydrodynamic models from NWT experiments. A nonlinear static block is included to the hydrodynamic model to account for the effect of nonlinear restoring forces, and the parameters of the nonlinear block are identified from WEC experiments. In particular, the paper uses a cone shaped geometry as a case study to demonstrate

the nonlinear restoring force, which is particularly useful for the analysis of the Wedgetop WEC. The paper also demonstrates the use of discrete time models (such as the well known ARX model), rather than the conventional continuous time models, because they are better suited to the identification problem due to the intrinsic discretisation of the sampled data from the NWT experiments.

- In [161] the range of tests available in a NWT from which linear and nonlinear hydrodynamic models can be derived is examined from a system identification perspective. Recommendations are given as to the optimal configuration of such system identification tests. The paper demonstrates using neural networks trained on CFD data to produce nonlinear hydrodynamic models.

- In [163] nonlinear excitation force kernals are identified from NWT experiments. In the paper, a range of linear and nonlinear modelling methodologies, based on system identification from NWT tests, are developed for a range of device geometries including a wedge shape. The results demonstrate a significant benefit in adopting a nonlinear parameterisation and show that models are heavily dependent on incident wave amplitude.

- In [164] and [165] the identification of mathematical models describing the behaviour of WECs in the ocean through the use of NWT experiments is investigated. [164] deals with the identification tests used to produce the data for the model identification. NWTs, implemented using CFD, are shown as an effective platform to perform the identification tests. The design of the NWT experiments to ensure the production of information-rich data for the model identification is discussed, and a case study is presented to illustrate the design and implementation of NWT experiments for the identification of WEC models. [165] proposes, for WEC modelling, the use of discrete-time nonlinear autoregressive with exogenous input (NARX) models, as an alternative to continuous-time models. Techniques of model identification are also explained and applied to the case study from [164].

- A complete overview and summary of these modelling techniques can then be found in the chapter titled, *'Identifying models using recorded data'* [166], in the book *'Numerical Modeling of Wave Energy Converters: State-of-the-art techniques for single WEC and converter arrays'*.

Now that these nonlinear hydrodynamic modelling techniques have been developed, future work involves using them to simulate and optimise the performance of the Wedgetop WEC or other potential WEC devices for powering MBSs.

#### 10.1.6.2 Generator modelling

The generator modelling in this thesis relied on a linear damping term to represent the electromagnetic force acting between the translator and stator. Although this has been shown to be a fairly accurate model for electromagnetic systems [173], a more refined model can aide in the physical design of the generator and allow more accurate simulation and optimisation of the total WEC system by accounting for losses and inefficiencies in the generator. Preliminary steps have been taken towards increasing the detail of the generator model, as outlined in Appendix A, where a finite element magnetic model of the translator has been developed. Future work involves using the finite element magnetic model of the translator to develop a high fidelity model of the generator system.

The generator model will be a subsystem of the overall WEC model, calculating the induced voltage and current in the generator coils, to determine the electromagnetic force on the translator and also the electrical energy generated by the system. Delving to this level of detail in the model requires the physical architecture and topology of the generator to be known, therefore the modelling should go hand-in-hand with the physical design of the generator. Compared to the hydrodynamics, the generator system can cheaply and easily be tested in a laboratory, so the modelling and design should be performed in parallel with bench-top testing of the generator system and its subcomponents. In addition to the electromagnetic force, a mechanical damping force will also be introduced to the model, being empirically derived from experimental results. Other generator inefficiencies such as energy dissipation due to the internal resistance of the generator coils will also be accounted for.

The model of the generator subsystem will also include a number of nonlinear effects, neglected in the initial model, such as end-stop collisions and power conditioning. When the stroke displacement reaches the stroke limit, the translator will collide with an end-stop, which can be modelled as a stiff spring with some level of mechanical damping. Through modelling and experimentation, strategies such as heavily damping the generator towards the ends of its stroke to reduce end stop collisions, or including additional springs at the end stops to more gently reverse the translator motion, can be investigated. Power conditioning, such as voltage rectification and battery charging circuitry will be included into the model. The induced voltage in the generator coils will be alternating and therefore need rectification before charging the battery. Using a full bridge rectifier incurs a voltage drop across two diodes, totalling between 0.6 - 1.5V depending on the type of diode used, and should be included in the model to aide in the optimisation of the generator design.

## 10.2 Thermal energy harvesting

The second potential renewable energy resource explored was the thermal gradient existing across the air/water interface on the ocean surface. A body of water and the adjacent parcel of air will generally have different temperatures, providing a temperature gradient from which to draw energy. A thermal energy harvester design was proposed, which utilised a thermoelectric device as the conversion mechanism. A model of the proposed energy harvester was derived and used in simulations, inputting real environmental datasets to gauge the potential of its power outputs. By assuming the thermoelectric devices were operating at the Carnot efficiency, power outputs on the order of 100mW/m$^2$ were predicted. These results indicated the natural thermal gradient existing between the water and air to be an unpromising energy resource.

This led to a modification to the proposed thermal energy harvester, through the inclusion of a black solar thermal collector plate to the airside of the thermoelectric device, with the goal of increasing the airside temperature to values higher than that of the ambient air. The new design was modelled and simulated with the calculated power outputs closely following the magnitude of the incident solar irradiation, signifying that the new design is essentially a solar thermal energy converter which uses the water as a cool sink. The predicted average power outputs were much more promising, being around 10W/m$^2$.

A number of experiments were conducted to monitor temperature values, investigate the effect of varying certain parameters and as a proof-of-concept for the thermal energy harvesting concept. Temperature readings illustrated the success of the collector plate in increasing the airside temperature of the TE device, but also revealed the poor performance of the heat sink. The analysis of the temperature readings also suggested that the thickness of the collector plate is an important parameter influencing the output power and should be investigated in future work. The first parameter variation investigated the effect of changing the TE module area. These experiments found that increasing the number of TE devices operating in the TE module increased the heat flow and thus dropped the temperature difference across the module. While the output power increased with the number of devices it did not increase linearly. With one device the peak output was approximately 17mW, two devices increased the output by about 40%, and four devices approximately doubled the output of over one device. The second parameter variation investigated the effect of changing the size of the collector plate. The output power was seen to increase with the collector plate area, however, when the output is normalised against collector plate's area the results for the different collectors were similar with peak power outputs of approximately 1W/m$^2$. The final experiment aimed to use output of the thermal energy harvester to directly power a WSN without

any energy storage and succeeded in doing so when the temperature difference across the TE device exceeded 10K.

Although reported last in this thesis (Chapter 9), the thermal energy harvester was investigated first, and occurred as a detour from the intended main focus of the thesis, wave energy harvesting. The concept was envisioned following similar work into thermal energy harvesting across the air/soil interface to power terrestrial based WSNs, reviewed in Section 2.2.2.2. The work presented in this thesis, on thermal energy harvesting across the air/water interface for powering MBSs, was aimed as a first investigation into this previously unexplored concept, to gauge its potential and then report on the concept and findings in a number of publications [106–108].

### 10.2.1 Estimated power output

An estimation of the potential power output from the thermal energy harvester concept was given in Section 9.4, which took into consideration the numerical results from Section 9.2 and the experimental findings from Section 9.3, and gauged that the power output would likely be somewhat below $1W/m^2$ of collector plate area. From this estimation it can be concluded that, in general the thermal energy harvester concept would not be an attractive option for the present application of powering MBSs. However, as shown in Figures 9.8 - 9.10, there are Equatorial regions which display higher levels of output power than average and which can produce these power levels all year round, and could therefore possibly be suitable for using the thermal energy harvester concept for powering MBSs.

### 10.2.2 Comparison against other systems

Compared to the wave energy harvester, the robustness of the thermal energy harvester's power outputs may be more dependent on factors such as the deployment location and time of year. While the wave energy harvester is designed to harvest an energy resource that is constant at any deployment location, the environmental inputs for the thermal energy harvester are highly variable between different locations. Temporally, the average power outputs of the thermal energy harvester for the winter months were seen to be an order of magnitude or more lower than for the summer months in some places, and were also seen to vary significantly across the course of the day.

With the addition of the collector plate, the thermal energy harvester device essentially became a solar thermal energy converter, and should therefore be compared against solar PV. The efficiency of this device was seen to be very low in the experiments

(Section 9.3.4.3), with a solar energy conversion efficiency of less than 0.2%, which is 100 times lower than conventional solar PV cells. Although there is some room for improvement in the experimental prototype, e.g. optimised heat sink, the thermal energy harvester will never reach the same efficiency as the solar PV (about 20%). To understand this, consider that for the Carnot efficiency to reach 20% there needs to be a temperature difference of about 50K (more than double the maximum amount achieved in the experiments), but even if this occurred and also assuming that all of the incoming solar is converter to thermal energy and that all of it flows through the TE device with no heat losses occuring elsewhere, then the state-of-the-art TED devices only operate at about 20% of the Carnot efficiency, so the overall efficiency would be 4%. The perceived advantage of the thermal energy harvester over solar PV, was that it could produce power from the thermal gradient across the air/water interface at night or during cloudy days, however the analysis in this thesis suggests the power outputs are quite low and simply using solar PV with ample energy storage would likely be more beneficial.

Only in a few niche applications would the thermal energy harvester concept be more attractive than wave energy or solar PV. For example, Jones et al [109] used this method (without the solar collector) for powering sea ice instrumentation, during the polar winter when other energy sources are either unavailable or unreliable. Or perhaps the thermal energy harvester concept could be used for applications in small bodies of water, such as ponds or creeks, where no waves are present and which require very low levels of power.

### 10.2.3 Limitations

Being a first investigation into this concept, and with the main focus of the thesis aimed towards wave energy conversion, the depth of the investigation performed in this thesis for this concept was very preliminary. As such, there are many limitations to the analysis, which are outlined in this section.

#### 10.2.3.1 Numerical modelling

The numerical model developed for the thermal energy harvesting device is very preliminary and follows the method of Roundy *et al* [30] to estimate the power available from a heat flow for WSNs, which gives a reasonable first approximation of the underlying processes. However, a more rigorous treatment of TE modelling can be found in specialised texts on this topic, which take into consideration effects such as the Peltier heat transfer of the TE device and thermal resistance circuits of the system. This level of detail would be warranted if the thermal energy harvester concept seemed promising for

the present MBS application and a more in depth analysis was required. However due to the expected poor performances of the thermal energy harvester concept and the large expected potential of the wave energy resource, it was decided to halt investigation on the thermal energy harvester at the preliminary analysis performed and shift the focus towards the wave energy harvester.

#### 10.2.3.2 Experiments

The experiments largely served as a demonstration of the concept, and were performed over a number of days during a trip to CSIRO in Newcastle, with the data later analysed and reported on in a number of publications [107, 108]. After the experiments were completed and reported upon, the focus of the research in this thesis returned towards wave energy harvesting. Thus there remains large scope for improvements in the experiments.

One of the major limitations of the experiments, is that it is not well matched with the numerical modelling in the previous section and was not intended as a validation exercise. For example, the Perspex dome included in the experiments is not considered in the modelling. The concept of the Perspex dome was inspired from the modelling, to limit the convective heat transfer from the top collector plate due to wind, which was identified as a large source of heat loss in the models. The idea of the Perspex dome was an evolution in the thermal energy harvester's design, and was decided to be included in the experiments which were intended to show-case the thermal energy harvester concept. The perspex domes are transparent to visible light but opaque to infrared light, allowing the dome to act as mini-greenhouse, however this effect is not captured by the preliminary modelling methods used.

Perhaps the biggest limitation of the experiments was the use of a plastic tub of water instead of a large body of water with natural dynamic mixing, like the ocean. This had the effect of reducing convective heat transfer from the bottom heat sink, and also resulted in the relatively large water temperature fluctuations across the day compared to a larger body of water with a greater thermal mass.

### 10.2.4 Future work

Although there is no plans to pursue further work on the thermal energy harvester concept, the work presented in Chapter 9 did raise a number of questions which could lead to a better understanding and optimisation of the thermal energy harvester prototype:

- **Ratio of TE device to collector plate area:** The cross-sectional area of the TE device, through which the heat is conducted and transferred into electrical energy, was shown to be an important design parameter. Increasing the area of the TE device increases the flow of heat energy available for conversion, but also decreases the temperature difference between the hot and cold sides, which reduces the conversion efficiency according the Carnot principle. It is believed that there is an optimum ratio between collector area and TE device area which would allow good heat flow while maintaining large temperature difference to enable maximum conversion efficiency.

- **Thickness of the collector plate :** The greater the thickness of the collector plate, the larger its thermal mass and the slower its temperature will change in response to the changing solar irradiance. This can have both positive and negative effects on the output power, therefore the thickness of the collector plate is an important design parameter for consideration.

- **Design of optimal heat exchangers :** The experiments showed that a significant temperature drop can occur across the heat sink between the bottom of the TE device and the water, which leads to a reduction in the potential power output. Although the experiments only considered an aluminium block for the heat sink, more advanced geometries designed to increase the available surface area for heat conduction could be employed. Another factor to consider in the ocean environment is the effect that marine growth may have on the heat sink.

## 10.3 General conclusions

Here a number of general conclusions for energy harvesting for MBSs is given. Renewable energy harvesting is very case specific, and the analysis in this thesis was for the problem of providing 1W of power to a MBS surface buoy with a data transmitting antenna. Had the power requirements been larger or smaller, or had the problem considered MBSs on the sea floor for example, then the analysis and solution would have been different. The conclusion from this thesis is that wave energy harvesting is a promising solution for powering MBSs due to the consistent flux of wave power and because it can solve problems related to the vertical alignment of the data transmitting antenna.

### 10.3.1 Combination of energy harvesting devices

To increase the robustness of the power supply component, it may be advantageous to use a combination of renewable energy sources, such as solar PV and wave energy

harvesting. Using a combination of energy harvesting devices offers a level of redundancy for the power supply, should one of the energy resources temporarily diminish or should one of the energy harvesting devices fail and require maintenance. This approach might be particularly relevant for applications requiring larger amounts of power, allowing the MBS's power supply component to harvest this power from a number of sources. The drawback of this approach is of course increased cost.

### 10.3.2 Storage capacity and duty cycles

Appropriately sizing the energy storage to be used in combination with the energy harvesting device for MBSs is important. As discussed in Chapter 3, partially charging and discharging the battery every day can cause a severe reduction in the battery's nominal energy capacity. To overcome this, it was proposed to follow Alippi et al's [84] idea of employing two identical battery packs and switching between them so that while one battery pack powers the system the other is under charge, thereby separately performing full discharge and charge cycles on each battery. Where possible, the duty cycle of the MBS's tasks with high power requirements should be scheduled to wait until the battery under charge is full, and then proceed to perform these high power tasks to drain the remaining power from the partially charged battery which is currently powering the system. This reduces the amount of time when the energy harvester might be producing energy but charging no battery, while eliminating the risk of draining the current battery and requiring a switch before the battery under charge is completely full.

### 10.3.3 Multi-disciplinary

A general conclusion is that energy harvesting for MBSs requires a multi-disciplinary solution which can best be served through collaboration and open sharing between researchers in different relevant fields. The work in this thesis required theoretical and numerical analysis from fields such as oceanography, hydrodynamics, electromagnetics and thermodynamics, and required collaboration with the experimental expertise from colleagues at CSIRO. The same multi-disciplinary requirements is true for the general field of offshore renewable energy, which energy harvesting for MBSs can be considered a sub-field.

To address this need for collaboration and open sharing within the offshore renewable energy field, the International Network on Offshore Renewable Energy (INORE) was founded in 2007. INORE is a network of PhD students, early stage researchers and those at a similar stage in industry or government. The members work in all aspects

of research or development for offshore renewable energy, from social policy to technical engineering, and on many different technology concepts. INORE serves as a hub for international and multidisciplinary collaboration between researchers at early stages of their careers and provides a forum for knowledge exchange between these various people, and between these people and those who are more established in this sector. INORE facilitates collaboration through a variety of activities, events, and programs as well as via its online presence.

During the course of this thesis, the present author joined INORE, served on the INORE committee, was the committee Chairman and published one paper at the *Asian Wave and Tidal Energy Conference* promoting INORE [188] and another at the *International Conference on Ocean Energy* detailing the role of international collaboration and INORE for innovation in offshore renewable energy [189].

# Appendix A

# Electromagnetic force capability of the IPMLG

The results in Chapter 8 revealed that the IPMLG may be required to provide electromagnetic damping co-efficients exceeding 1000Ns/m. However, it was unknown if such levels of damping are physically achievable within the size constraints of the CIPMLG WEC's geometry, with no reported literature relating to permanent magnet linear generator sizes and corresponding damping values able to be found. Therefore, the electromagnetic force capability of the IPMLG is analysed here, to determine the physical generator size required for a given electromagnetic damping value. It should be mentioned that the full design of the IPMLG is outside the scope of the present thesis. Instead this chapter is intended to provide an estimation if a suitable generator is theoretically possible. From this analysis, it seems likely that engineers can construct a generator of sufficiently small size and weight to satisfy the electromagnetic damping requirements of the CIPMLG WEC.

The electromagnetic force capability of a generator is the maximum amount of damping the generator can provide to the internally oscillating translator mass. This occurs when the generator is operating with its stator coils short-circuited. For a translator mass with a given stroke velocity, the electromagnetic damping from the generator will be reduced if a resistive load is connected to the generator coils compared to the short-circuited case. When a resistive load is added to the generator coils, a lower current will flow though the coils leading to a weaker magnetic field being produced by induction, resulting in a lower electromagnetic force for the same stroke velocity.

Buren and Troster [175] explain that the separate optimization of the force capability is justified because if two generators A and B have force to velocity ratios $d_A$ and $d_B$ where $d_A > d_B$, then generator A will have a higher power output under comparable operating

conditions. This occurs because if generators A and B are connected to load resistances in such a way as to achieve matching effective force to velocity ratios then the same amount of mechanical energy is converted to electrical energy by the two generators when driven by the same motion. However, in order to achieve the same effective force to velocity ratios, generator B will have lower ratio of load resistance to coil resistance than generator A, therefore more energy is lost in the coil resistance and less energy is available in the load for generator B.

## A.1 Electromagnetic force

An expression for the electromagnetic force, $F_g(t)$, acting between the generator's translator mass and stator coils is derived from the conservation of energy. The kinetic energy lost by the translator due to the electromagnetic force is converted to electrical energy in the generator:

$$F_g(t)\dot{x}_s(t) = V(t)I(t), \tag{A.1}$$

where $V(t)$ is the induced voltage in the generator coils and $I(t)$ is the electrical current.

The electromagnetic force can therefore be expressed as:

$$F_g(t) = \frac{V(t)I(t)}{\dot{x}_s(t)}. \tag{A.2}$$

### A.1.1 The generator voltage

The voltage can be calculated from Faraday's law of induction:

$$V(t) = N\frac{d\phi}{dt} = N\dot{x}_s(t)\frac{d\phi}{dx_s}, \tag{A.3}$$

where $N$ is the number of turns of wire in the generator coil and $\phi$ is the magnetic flux intercepted by the coil.

#### A.1.1.1 The inductance of the generator

Inductance leads to a voltage drop of $V(t) = L\frac{di}{dt}$, where $L$ is the inductance of the coil. For the present analysis, the inductance of the generator is assumed negligible and not included in the electromagnetic model. The range of values for both terms, $L$ and $\frac{di}{dt}$, is expected to be small for the present system, warranting the assumption of negligible inductance for the first analysis. Inductance is also ignored in the electromagnetic force capability calculations of Buren and Troster [175].

The air-cored topology of the IPMLG leads to a very low inductance in the generator coil, compared to conventional iron-cored designs, due to the high reluctance values of air. An air-cored topology was chosen because it avoids unwanted magnetic forces attracting the translator to the stator, which would increase the mechanical damping [130, 175]. Additionally, the air-cored topology has less weight, which is advantageous. However, the disadvantage of an air-cored machine is a poorer electromechanical performance than a conventional iron-cored design [134]. Additionally, due to the relatively slow speeds of the CIPMLG WEC's translator stroke, the term $\frac{di}{dt}$ will not be large.

### A.1.2 The generator current

The current can be calculated from Ohm's law;

$$I(t) = \frac{V(t)}{R_c + R_L}, \tag{A.4}$$

where $R_C$ is the internal resistance of the coil and $R_L$ is the load resistance.

### A.1.3 Generated Power

The generated power is the useful electrical power delivered to the load. Not all of the total power absorbed by the generator will be delivered to the load, due to the internal resistance of the coil which dissipates some of the power as heat. The fraction of power dissipated by the coil, is equivalent to the fraction of the coil resistance to total resistance $\left(\frac{R_c}{R_c+R_L}\right)$. The remaining power will be delivered to the load and can be calculated via;

$$P(t) = V(t)I(t)\left(\frac{R_L}{R_c + R_L}\right), \tag{A.5}$$

### A.1.4 Electromagnetic force capability

Combining Equations A.2, A.3 and A.4, gives the following expression for the electromagnetic force:

$$F_g(t) = \frac{N^2(\frac{d\phi}{dx_s})^2}{R_c + R_L}\dot{x}_s(t). \tag{A.6}$$

The electromagnetic force capability of the generator is the damping the generator can provide when the coils are short-circuited, i.e. $R_L = 0$. The electromagnetic force in this case equals:

$$F_g(t) = \frac{N^2(\frac{d\phi}{dx_s})^2}{R_c}\dot{x}_s(t), \tag{A.7}$$

which shows that the short-circuit electromagnetic damping coefficient / force capability, can be represented as:

$$d_{fc} = \frac{N^2(\frac{d\phi}{dx_s})^2}{R_c}. \tag{A.8}$$

## A.2 Genetator Parameters

Equation A.8 showed that the electromagnetic force capability is dependent on three generator parameters, which are examined in this section:

- The electrical resistance of the coil, $R_c$,
- The number of turns of wire in the coil, $N$, and
- The magnetic flux gradient, $\frac{d\phi}{dx_s}$.

### A.2.1 The electrical resistance of the coil

The electrical resistance of the coil, $R_c$, depends on the length of the copper wire in the coil and its resistance per unit length, $r_c$:

$$R_c = \pi D_c N r_c \tag{A.9}$$

where $D_c$ is the average diameter of the generator coil (see Figure A.1). Although the turns of wire on the inner part of the coil have a smaller circumference than those on the outer part of the coil, the circumference is linearly related to the diameter and therefore the average diameter of the coil can be used.

The resistance per unit length of wire is given by the resistivity of the material, $\rho_c$, (in this case copper $= 17 \times 10^{-9}\Omega m$) divided by the wire's cross-sectional area, $A_w$;

$$r_c = \frac{\rho_c}{A_w}. \tag{A.10}$$

The wire's cross-sectional area determines how many turns of wire, $N$, can fit into the coil's cross-sectional area:

$$N A_w = c_w c_l f_f, \tag{A.11}$$

where $c_w$ is the coil width and $c_l$ the coil length and a fill factor, $f_f$, which accounts for the gaps of area in between the wire. The fill factor is a dimensionless number between zero and one, where a fill factor of zero would correspond to an empty coil and a fill

factor of one would represent a solid piece of copper filling the entire coil volume. In copper wire wound transformers fill factors in the range of 0.5 to 0.6 can be achieved [190]. In the analysis in this chapter a constant fill factor of 0.5 will be assumed.

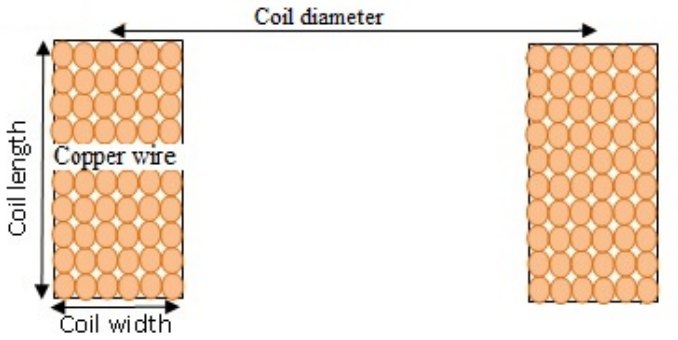


FIGURE A.1: Cross-sectional view of the generator coil

Substituting Equations A.10 and A.11 into Equation A.9 gives the following expression for the coil resistance:

$$R_c = \frac{\pi D_c \rho_c N^2}{c_w c_l f_f}. \tag{A.12}$$

Combining this with Equation A.8, shows that the force capability can be expressed as:

$$d_{fc} = \frac{c_w c_l f_f (\frac{d\phi}{dx_s})^2}{\pi D_c \rho_c}. \tag{A.13}$$

### A.2.2 Number of turns of wire

Equation A.11 showed that the number of turns of wire, $N$, is limited by the cross-sectional area of the coil (Equation A.11):

$$N = \frac{c_w c_l f_f}{A_w}. \tag{A.14}$$

The cross-sectional area of the thinnest commercially available Copper wire, which can have diameters below 0.1mm, is on the order of $10^{-6} - 10^{-6} mm^2$. Therefore, $A_w$ can have any value larger than that.

As shown by Equation A.13, the electromagnetic force capability does not depend on the number of turns of wire directly, but only on the length and width of the coil ($c_l$ and $c_w$) and the fill factor with which the wire fills that coil ($f_f$). This means that coil containing say, 5 turns of a thick wire, will produce the same electromagnetic force capability as a coil containing 10 turns of a thinner wire, providing they have the same

fill factor. Therefore, for the present analysis of the electromagnetic force capability, the number of turns of wire is not important. However, the number of turns of wire is still an important design parameter for other aspects of the system, such as the induced voltage which is linearly proportional to this parameter, Equation A.3.

### A.2.3 The magnetic flux gradient

The term, $\frac{d\phi}{dx_s}$, is the magnetic flux gradient, which represents how rapidly the magnetic flux cutting the coil of wire changes with distance along the axis of the coil. The magnetic flux depends on the magnetic fields produced by the different types, geometries and distributions of magnetic materials present in the generator and how the coil of wire intersects these fields.

#### A.2.3.1 Calculating the magnetic flux gradient

To calculate a value for the magnetic flux gradient parameter, a finite element magnetic model of the generator is implemented, using the software Finite Element Method Magnetics (FEMM) version 4.2 [194]. Figure A.2-(a) shows a screenshot from the FEMM preprocessor depicting the computational domain set-up to calculate the magnetic field for the magnet array translator (see Figure A.4-(b)). The finite element magnetic model is declared to be axisymmetric in the FEMM solver, so that only the cross-sectional area on one side of the axis of revolution needs to be modelled. Figure A.2-(b) then shows a screenshot of the postprocessor depicting the calculated magnetic field. Figure A.3 shows a zoom in of the mesh used discretise the spatial computational domain into finite elements. The mesh resolution inside of the translator, where the magnetic materials are, is very fine. In the inner air domain, close to the translator, the mesh increases in size but still remains relatively fine to capture the magnetic fields in this region. The mesh in the outer air domain, where the magnetic fields are negligible, is quite coarse to reduce the total number of nodes required in the calculation. In total 493,000 nodes are used to discretise the computational domain around the translator.

Surfaces can be defined in the postprocessor and the magnetic flux through the surface calculated. In this way the magnetic flux through a generator coil of given radius can be calculated, by defining a circular surface with the same radius as the coil centred on the translator axis. By calculating the magnetic flux through numerous circular surfaces along the axis of the translator (0.5mm apart) the magnetic flux gradient along the length of the translator can be calculated using numerical differentiation (a central difference scheme was used). FEMM has a scripting language, which was used to generate models and calculate the magentic flux gradient for many different generator topologies with

varying coil heights, coil lengths, magnet heights and magnet widths, as reported in Sections A.2.3.3 - A.2.3.6.

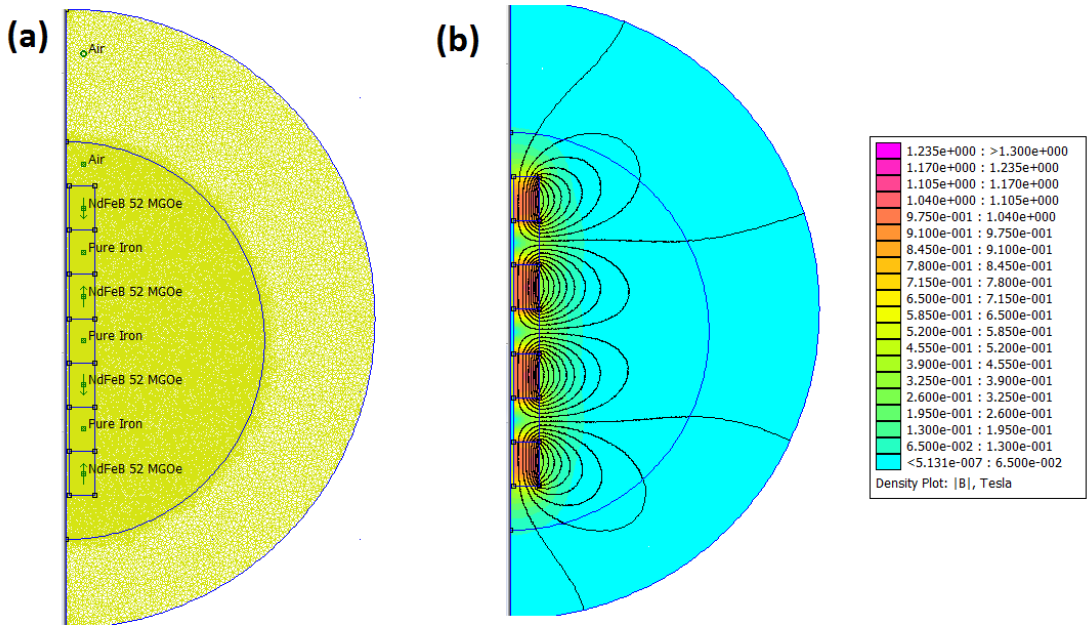


FIGURE A.2: Screenshot of the FEMM software used to calculate the magnetic field produced by the translator (a) The preprocessor view of the finite element mesh used to discretise the problem domain, and (b) Post process view of the calculated magnetic field.

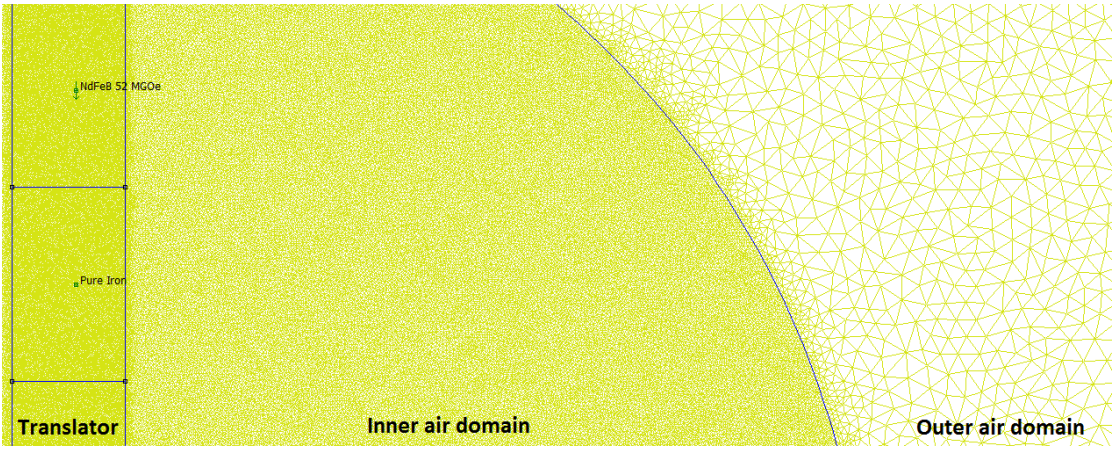


FIGURE A.3: Zoomed in screenshot view of the mesh used in the FEMM software calculation of the magnetic field.

### A.2.3.2 Translator topology

The magnetic flux gradient depends on the geometrical distribution of magnetic materials in the translator. Two different translator topologies were considered and are depicted in Figure A.4. Both topologies consist of axially magnetised ring shaped neodymium-iron-boron (Nd2Fe14B) magnets that sit on a nonmagnetic shaft. Cheung

and Childress [150] concluded that axial generators should be used for all systems that allow a linear design, because axial generators are more easily produced and provide comparable power when compared to transversal generators. The neodymium-iron-boron alloy was chosen for the magnets because it is the strongest type of permanent magnet made. These magnets are commercially available in various grades with Maximum Energy Product (MEP) ratings ranging from 28 MGOe to 52 MGOe. The present work shall therefore assume that the strongest available magnets, with an MEP rating of 52 MGOe, are used.

The translator in Figure A.4-(a) has a single magnet whereas the one in Figure A.4-(b) comprises of an array of magnets separated by steel spacers. The magnetisation directions of neighbouring magnets in the array oppose each other. The steel spacers act as flux concentrators and also to reduce the repellent forces between neighbouring magnets. This type of translator topography has been proposed in large scale wave energy conversion and vibration energy harvesting [131, 150, 175, 191, 192], as it increases the achievable magnetic flux gradient. The steel spacer's geometry is chosen to be identical to the magnet's following Wang et al's [193] investigation into the optimal magnet to steel spacer height ratio. The top of the nonmagnetic shaft is connected to the spring and extra weight can be added to the bottom of the shaft to increase the translator mass, $m$, to any desired value.

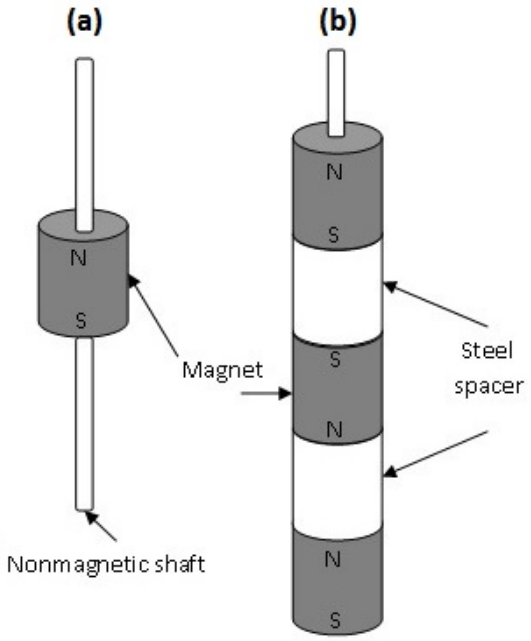


FIGURE A.4: The two translator designs considered, (a) the single magnet translator, and (b) the magnet array translator.

Figures A.5 and A.6 shows a comparison of the calculated magnetic flux gradient of both translator topologies for a given magnet and coil size. These results show the maximum flux gradient of the magnet array translator is approximately double that of the single magnet translator. Another advantage of the magnet array translator over the single magnet translator is its spatial distribution. The single magnet only acts over a small distance, whereas the useful magnetic field from the magnet array can be made as long as is needed by adding more magnets and steel spacers. For these two reasons the array topology shall be used in all further work.

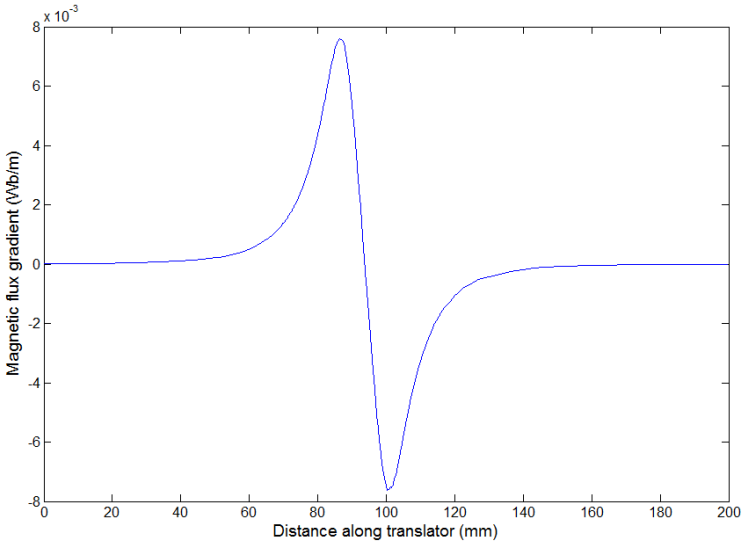


FIGURE A.5: The magnetic flux gradient along the length of the single magnet translator

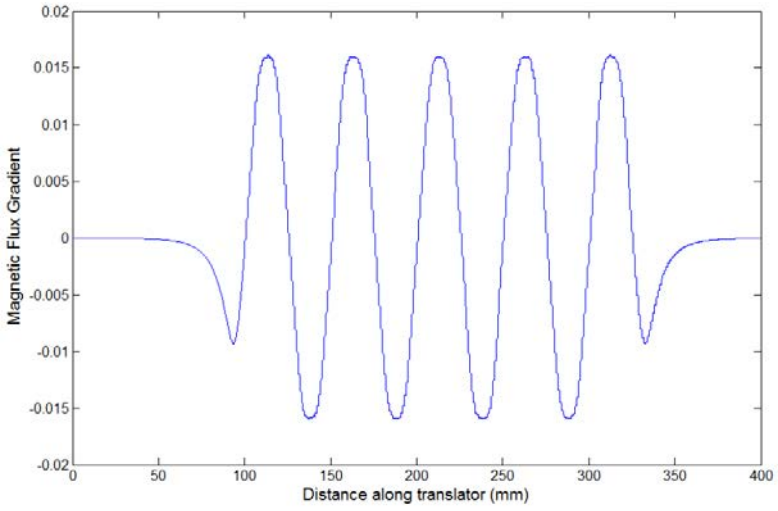


FIGURE A.6: The flux gradient along the length of the magnet array translator

#### A.2.3.3 Effect of the coil length

The magnetic flux gradient for the magnet array translator, Figure A.6, is positive in some regions and negative in others. Therefore, if the translator moves inside a long coil it will induce voltages of opposite polarity along the length of the coil, resulting in the voltages induced in different regions cancelling either other. To stop this effect from occurring, the coil length should not be made longer than the length/height of the magnet. However, the generator stator may consist of an array of individual short coils, connected in such a way that their outputs add constructively together.

#### A.2.3.4 Effect of coil width

The effect of increasing the coil radius is shown in Figures A.7 and A.8. Figure A.7 plots the magnetic flux gradient along the length of a particular translator for three cases; when the coil radius is 5, 10 and 15mm larger than the translator radius. The magnitude of the magnetic flux gradient can be seen to decrease with the radius of the coil in this figure. The observed reduction in magnetic flux gradient with increasing coil radius occurs because the magnetic field lines cutting the middle of the coil in one direction are able to return back in the opposite direction whilst remaining inside the larger radius coil (see A.2-(b)), thus contributing a zero net flux through the coil. Figure A.8 plots the peak value of magnetic flux gradient for several different coil radii, showing that the magnetic flux gradient decreases approximately linearly with increasing coil radius for small radius values, and then sub-linearly for larger radius values.

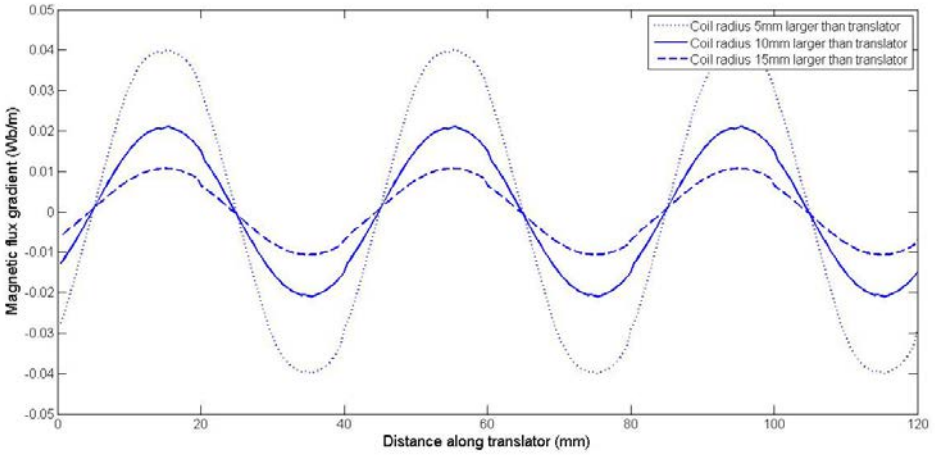


FIGURE A.7: The flux gradient along the length of the magnet array translator for varying coil radius

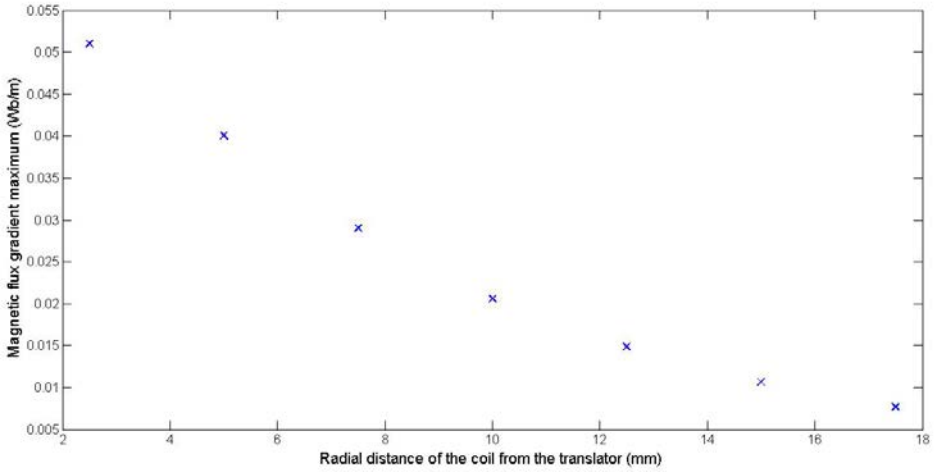


FIGURE A.8: The peak magnetic flux gradient value for increasing coil radius

#### A.2.3.5 Effect of the magnet height

The effect of changing the height of the individual magnets and steel spacers within the translator array is investigated here. Figure A.9 presents a contour plot of the magnetic flux gradient along the length of the generator which intersects coils of various radii. The results are shown for three different magnets with varying heights of 10, 20 and 40mm. The $x$-axis in this figure, represents the coil radius measured from the outside edge of the translator, and the $y$-axis represents the axial distance along the generator. The distance on the $y$-axis is measured from the centre of one magnet in the array to the centre of the next one, including the steel spacer in between, and therefore has a range of twice the magnet height. The contour plots show that the magnets with three different heights all have the same maximum magnetic flux gradient value, however, the magnetic flux gradient is seen to decrease more rapidly with radial distance from the translators with the shorter magnets.

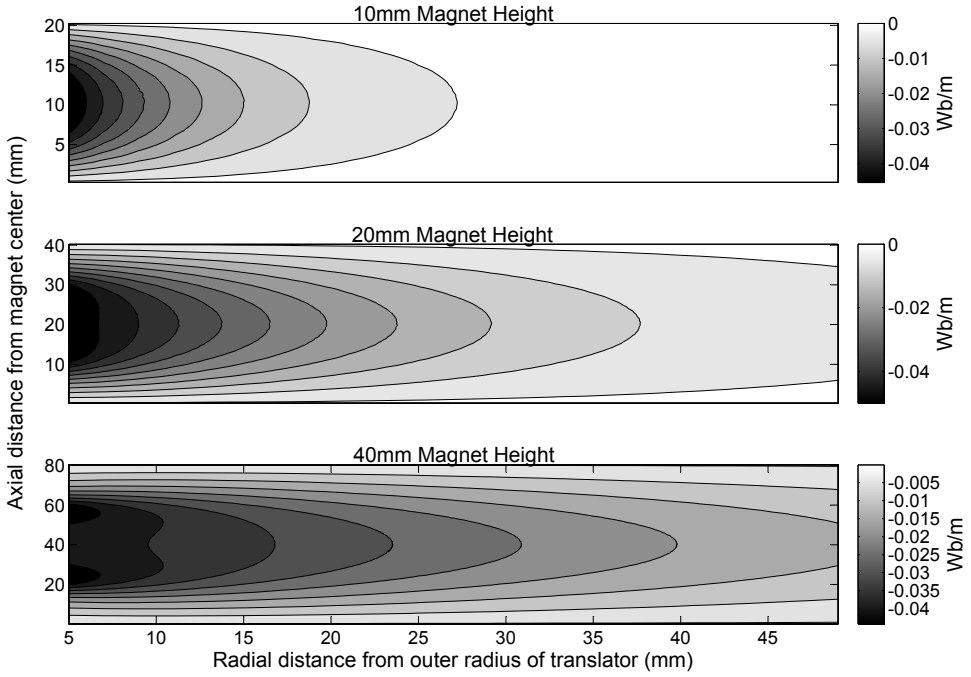


FIGURE A.9: The magnetic flux gradient for a magnet with 20mm radius for 3 different magnet heights.

#### A.2.3.6 Effect of the magnet width

The effect of changing the magnet width is shown in Figure A.10. Here it can be seen that increasing the magnet width increases the magnetic flux gradient. Doubling the magnet radius from 20mm to 40mm in Figure A.10, is seen to result in a threefold increase in magnetic flux gradient value.

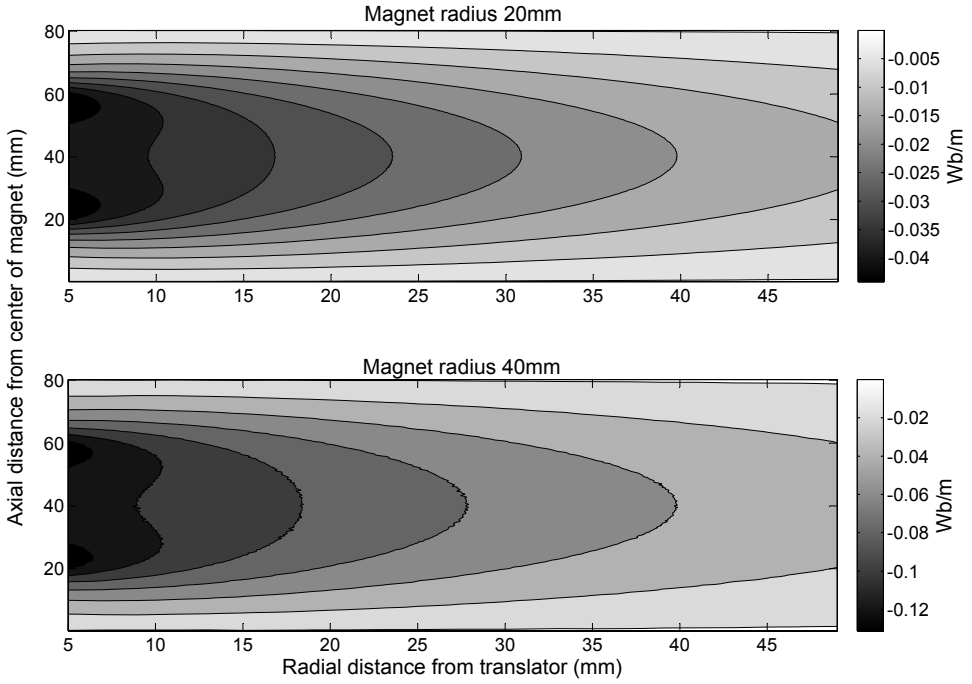


FIGURE A.10: The magnetic flux gradient for a magnet with 20mm radius for 2 different magnet radii

## A.3 Evaluating the electromagnetic force capability

An expression for the electromagnetic force capability was given in Equation A.13:

$$d_{fc} = \frac{c_w c_l f_f (\frac{d\phi}{dx_s})^2}{\pi D_c \rho_c}.$$

The value of the magnet flux gradient varies across the cross-sectional area of the coil. Therefore to evaluate the electromagnetic force capability, the area of the coil is discretised into small areas, $\Delta_w \Delta_l$, in which the value of magnetic flux gradient can be considered constant, as depicted in Figure A.11. The electromagnetic force capability is calculated for each of the small areas and then summed to give the total electromagnetic force capability:

$$d_{fc} = \sum_{i=1}^{N} \sum_{j=1}^{M} \frac{\Delta_w \Delta_l f_f (\frac{d\phi}{dx_s})^2_{i,j}}{\pi D_{c,i} \rho_c}, \tag{A.15}$$

where $N = \frac{c_w}{\Delta_w}$ and $M = \frac{c_l}{\Delta_l}$.

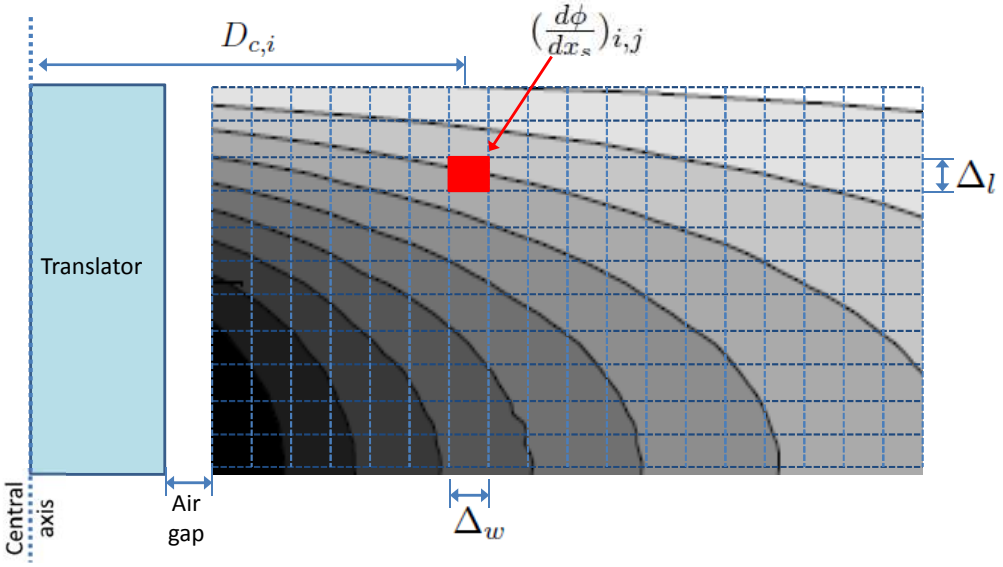


FIGURE A.11: Discretisation of the magnetic flux gradient across the cross-sectional area of the coil.

The electromagnetic force capability will depend on the magnet height, magnet radius, coil length, the coil width, the number of active coils and the air-gap between the translator and the coil. The air-gap in this analysis is assumed to be 5mm. The coil length will be set equal to the magnet height, due to the reasons discussed in Section A.2.3.3. Therefore there remains four free parameters to vary: the magnet height, magnet radius, the coil width and the number of coils. Figure A.12 shows the calculated electromagnetic force capability for a single active coil with various magnet heights, magnet radii and coil widths.

The results in Figure A.12 show that the electromagnetic force capability increases with magnet height and magnet radius. Increasing the coil width also increases the electromagnetic force capability up to a maximum point (different for each magnet height and radius), and then further increasing in the coil width unnecessarily increases the coil resistance with relatively little increase the intercepted magnetic flux gradient through the coil. A translator with a magnet radius and height of 40mm, can produce an electromagnetic force capability of over 700Ns/m for a coil with a width of 20mm.

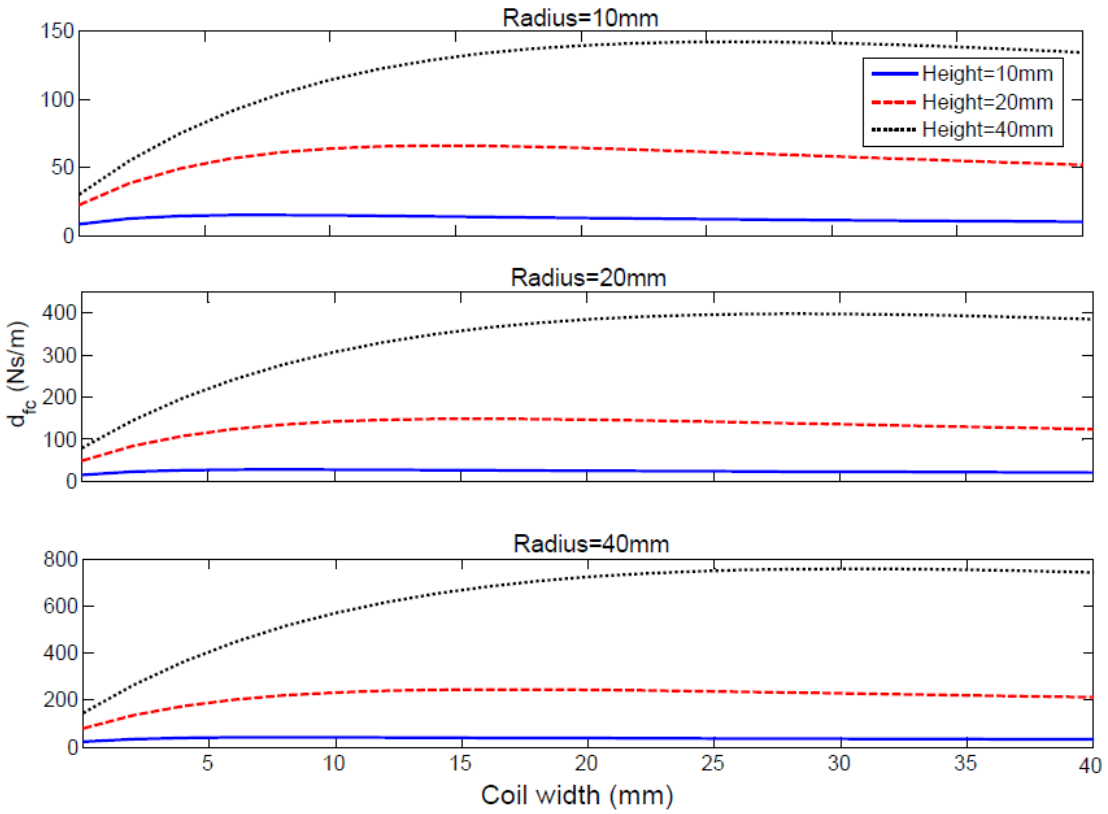


FIGURE A.12: The electromagnetic force capability for a single coil with various magnet heights, magnet radii and coil widths.

## A.4 Conclusion

The results in Section A.3 indicated that an electromagnetic force capability of several hundred Ns/m can be produced by a single active generator coil with a length less than 40mm and width of 20mm, in the presence of a magnet array translator with a magnet length and radius less than 40mm. When the generator is connected to a load, the electromagnetic damping co-efficient of the generator will decrease compared to the electromagnetic force capability value by an amount proportional to, $\frac{R_C}{R_C+R_L}$. However as shown in Section A.1.3, the amount of energy dissipated in the coils is also proportional to $\frac{R_C}{R_C+R_L}$. Therefore to increase the efficiency of the generator $\frac{R_C}{R_C+R_L}$ should be as small as practical, which will significantly reduce the electromagnetic damping co-efficient compared to the electromagnetic force capability value. However, multiple active coils may be used to increase the electromagnetic damping co-efficient. It therefore seems likely that the electromagnetic damping values required by the CIPMLG WEC could be satisfied using a generator with a coil width of about 20mm and a translator with a radius of less than 40mm, resulting in a total generator diameter of less than about 140mm, and the length of the generator would be less than half a meter.

This analysis was performed as an aside to the core focus of the thesis and therefore appears in the Appendix, rather than being afforded proper chapter status. The goal of the analysis was to provide a sanity check on the feasibility of a reasonable sized generator being able to produce the required levels of electromagnetic damping highlighted in Chapter 8. Had the analysis indicated that an excessively large sized generator would be required, then further investigation and focus should have been applied to the electromagnetic performance of the generator to investigate if it is a potential 'show stopper' for the IPMLG concept. However, the results in this Appendix indicate that engineers should be able to easily design a suitably sized generator capable of doing the required job. A full design of the generator is outside the scope of the present thesis and is a task for future work, see Section 10.1.6.2.

# Appendix B

# PAR to solar insolation value conversion

Photosynthetically Active Radiation (PAR) is a measure of the incoming sunlight in the 400  700 nanometer wavelength range. This part of the solar spectrum is used by plants for photosynthesis, thus is a frequently used parameter by biologists, marine and terrestrial alike, therefore many environmental monitoring stations measure and record PAR readings. In this appendix a method for converting measured PAR values to solar insolation values is described, revealing that dividing a given PAR reading by two yields the corresponding solar insolation value.

The units of PAR readings are microeinsteins per second per square meter, where one Einstein is one mole of photons. This photon count needs to be converted into a corresponding solar insolation energy flux value. This can be achieved using the fact that each photon has an energy equal to;

$$E = hf, \tag{B.1}$$

where $h$ is Plancks constant (6.626x10-34 Js) and $f$ is the frequency of the photon.

The PAR reading is for all photons with frequencies in the 430  750 THz range, therefore the photons have a corresponding range of individual energy values. The standard frequency distribution of incident terrestrial solar irradiation is shown in Figure B.1, which plots the power in each spectral band centred on a resolution of 0.5nm [195]. Dividing each point on this graph by its corresponding frequency and plancks constant, $hf$, gives the number of photons in that 0.5nm spectral band per second per square meter. This photon frequency distribution can be used to appropriately separate the photons in the PAR reading into frequency bins from which corresponding energy values

can be calculated and then summed to calculate the incident power per square meter in the PAR spectral band. This yields the result that the power in the PAR band equals the PAR reading multiplied by 0.21.

Comparing the incident terrestrial solar irradiation in the PAR band to the total incident solar irradiation in Figure B.1, reveals that the total incident power is 2.36 times the power in the PAR band. Therefore, to convert the PAR reading to a solar insolation value multiply it by; $0.21 \times 2.36 = 0.5$.

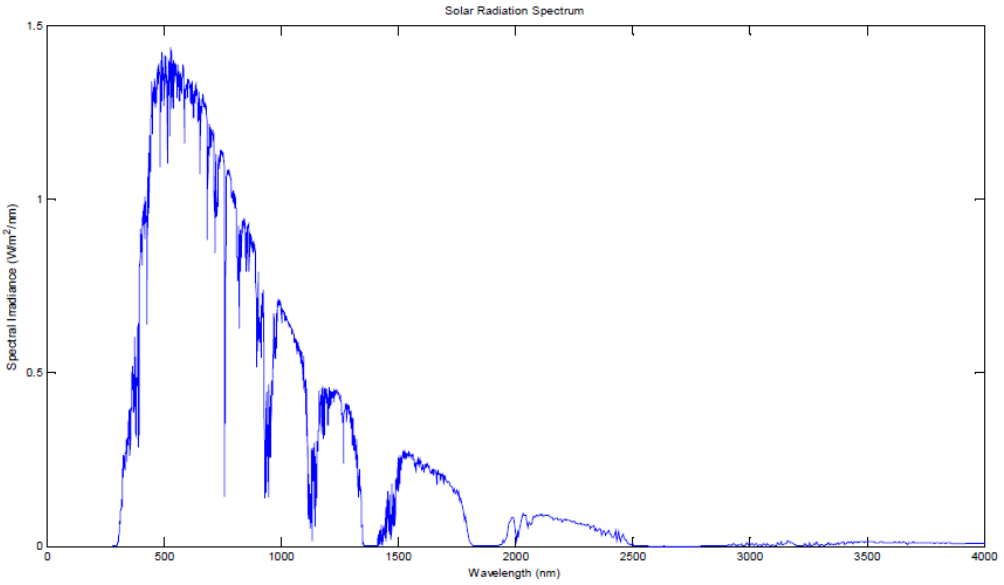


FIGURE B.1: Standard terrestrial solar spectral irradiance distribution [195].

# Bibliography


[1] 21 ideas for the 21st century. *Business Week*, pages 78–167, Aug 30, 1999.

[2] C.Y. Chong and S.P. Kumar. Sensor networks: evolution, opportunities, and challenges. *Proceedings of the IEEE*, 91:1247–1256, 2003.

[3] R. Min, M. Bhardwaj, S.H. Cho, N. Ickes, E. Shih, A. Sinha, A. Wang, and A Chandrakasan. Energy-centric enabling technologies for wireless sensor networks. *IEEE Wireless Communication Magazine*, 9:28–39, 2002.

[4] Thomas B Curtin, James G Bellingham, Josko Catipovic, and Doug Webb. Autonomous oceanographic sampling networks. *Oceanography*, 6(3):86–94, 1993.

[5] Sutharshan Rajasegarar, Jayavardhana Gubbi, Olga Bondarenko, Stuart Kininmonth, Slaven Marusic, Scott Bainbridge, Ian Atkinson, and Marimuthu Palaniswami. Sensor network implementation challenges in the great barrier reef marine environment. In *Proceedings of the ICT-MobileSummit 2008 Conference*, 2008.

[6] Umberto M. Cella, Nicholas Shuley, and Ron Johnstone. Wireless sensor networks in coastal marine environments: a study case outcome. In *Proceedings of the Fourth ACM International Workshop on UnderWater Networks*, 2009.

[7] Trina Myers, Ian Atkinson, and Ron Johnstone. Semantically enabling the semat project: extending marine sensor networks for decision support and hypothesis testing. In *Complex, Intelligent and Software Intensive Systems (CISIS), 2010 International Conference on*, pages 974–979. IEEE, 2010.

[8] Jarrod Trevathan, Ron Johnstone, Tony Chiffings, Ian Atkinson, Neil Bergmann, Wayne Read, Susan Theiss, Trina Myers, and Tom Stevens. Semat the next generation of inexpensive marine environmental monitoring and measurement systems. *Sensors*, 12(7):9711–9748, 2012. ISSN 1424-8220. doi: 10.3390/s120709711. URL http://www.mdpi.com/1424-8220/12/7/9711.

[9] Kebin Liu, Zheng Yang, Mo Li, Zhongwen Guo, Ying Guo, Feng Hong, Xiaohui Yang, Yuan He, Yuan Feng, and Yunhao Liu. Oceansense: Monitoring the sea with wireless sensor networks. *ACM SIGMOBILE Mobile Computing and Communications Review*, 14(2):7–9, 2010.

[10] Zheng Yang, Mo Li, and Yunhao Liu. Sea depth measurement with restricted floating sensors. In *Real-Time Systems Symposium, 2007. RTSS 2007. 28th IEEE International*, pages 469–478. IEEE, 2007.

[11] Olga Bondarenko, Stuart Kininmonth, and Michael Kingsford. Underwater sensor networks, oceanography and plankton assemblages. In *Intelligent Sensors, Sensor Networks and Information, 2007. ISSNIP 2007. 3rd International Conference on*, pages 657–662. IEEE, 2007.

[12] Thiemo Voigt, Fredrik Österlind, Niclas Finne, Nicolas Tsiftes, Zhitao He, Joakim Eriksson, Adam Dunkels, Ulf Båmstedt, Jochen Schiller, and Klas Hjort. Sensor networking in aquatic environments-experiences and new challenges. In *Local Computer Networks, 2007. LCN 2007. 32nd IEEE Conference on*, pages 793–798. IEEE, 2007.

[13] Cristina Albaladejo, Pedro Snchez, Andrs Iborra, Fulgencio Soto, Juan A. Lpez, and Roque Torres. Wireless sensor networks for oceanographic monitoring: A systematic review. *Sensors*, 10(7):6948–6968, 2010. ISSN 1424-8220. doi: 10.3390/s100706948. URL http://www.mdpi.com/1424-8220/10/7/6948.

[14] Guobao Xu, Weiming Shen, and Xianbin Wang. Applications of wireless sensor networks in marine environment monitoring: A survey. *Sensors*, 14(9):16932–16954, 2014.

[15] P. Barbosa, N.M. White, and N.R. Harris. Wireless sensor network for localized maritime monitoring. In *Advanced Information Networking and Applications - Workshops, 2008. AINAW 2008. 22nd International Conference on*, 2008.

[16] Jaime Lloret, Sandra Sendra, Miguel Garcia, and Ginés Lloret. Group-based underwater wireless sensor network for marine fish farms. In *GLOBECOM Workshops (GC Wkshps), 2011 IEEE*, pages 115–119. IEEE, 2011.

[17] John G Proakis, Ethem M Sozer, Joseph Rice, Milica Stojanovic, et al. Shallow water acoustic networks. *Communications Magazine, IEEE*, 39(11):114–119, 2001.

[18] Keat G Ong, Xiping Yang, Niloy Mukherjee, Haidong Wang, Shrawan Surender, and Craig A Grimes. A wireless sensor network for long-term monitoring of aquatic environments: Design and implementation. *Sensor Letters*, 2(1):48–57, 2004.

[19] J. Heidemann, W. Ye, J. Wills, A. Syed, and Y. Li. Research challenges and applications for underwater sensor networking. In *Wireless Communications and Networking Conference, 2006. WCNC 2006. IEEE*, 2006.

[20] Jun-Hong Cui, Jiejun Kong, Mario Gerla, and Shengli Zhou. The challenges of building mobile underwater wireless networks for aquatic applications. *Network, IEEE*, 20:12–18, 2006.

[21] M. Chitre. A holistic approach to underwater sensor network design. In *Proceedings of Naval Technology Seminar (NTS) 2011.*, 2011.

[22] Pranaw Kumar, Pooja Priyadarshini, et al. Underwater acoustic sensor network for early warning generation. In *Oceans, 2012*, pages 1–6. IEEE, 2012.

[23] So-Nam Yun, Eun-A Jeong, Hwang-Hun Jeong, and Ky-Yun Lee. Wireless power generation strategy using eap actuated energy harvester for marine information acquisition. *Wireless Sensor Network*, 3(09):313, 2011.

[24] Matt Bromage, Katia Obraczka, and Donald Potts. Sea-labs: A wireless sensor network for sustained monitoring of coral reefs. In *NETWORKING 2007. Ad Hoc and Sensor Networks, Wireless Networks, Next Generation Internet*, pages 1132–1135. Springer, 2007.

[25] Eric D Thosteson and Maila Sepri. The florida indian river lagoons potential for supporting a sustainably powered environmental observation system. In *An International Forum on Sustainability*, page 190.

[26] Cristina Albaladejo, Fulgencio Soto, Roque Torres, Pedro Snchez, and Juan A. Lpez. A low-cost sensor buoy system for monitoring shallow marine environments. *Sensors*, 12(7):9613–9634, 2012. ISSN 1424-8220. doi: 10.3390/s120709613. URL http://www.mdpi.com/1424-8220/12/7/9613.

[27] URL http://www.navysbir.com/.

[28] J. Davidson, C. Knight, and S. Behrens. Csiro scoping study: Energy harvesting for wireless sensor networks. Technical report, CSIRO, 2008.

[29] C. Knight, J. Davidson, and S. Behrens. Energy options for wireless sensor nodes. *Sensors*, 8:8037–8066, 2008.

[30] S. Roundy, P.K. Wright, and J.M. Rabaey. *Energy scavenging for wireless sensor networks: with special focus on vibrations*. Springer, 2004.

[31] Joseph Paradiso, Thad Starner, et al. Energy scavenging for mobile and wireless electronics. *Pervasive Computing, IEEE*, 4(1):18–27, 2005.

[32] Eugenio Cantatore and Martin Ouwerkerk. Energy scavenging and power management in networks of autonomous microsensors. *Microelectronics Journal*, 37 (12):1584–1590, 2006.

[33] J.P. Thomas, M.A. Qidwai, and J.C. Kellogg. Energy scavenging for small-scale unmanned systems. *Journal of Power sources*, 159:1494–1509, 2006.

[34] E.O. Torres and G.A. Rincon-Mora. Long-lasting, self-sustaining, and energy-harvesting system-in-package (sip) wireless micro-sensor solution. In *International Conference on Energy, Environment, and Disasters (INCEED), Charlotte, NC, USA*, 2005.

[35] R.W. Hart, H.S. White, B. Dunn, and D.R. Rolison. 3-d microbatteries. *Electrochemistry Communications*, 5:120–123, 2003.

[36] H. Nishide. Toward flexible batteries. *Surfaces*, 4, 2008.

[37] AG Pandolfo and AF Hollenkamp. Carbon properties and their role in supercapacitors. *Journal of Power Sources*, 157:11–27, 2006.

[38] CSIRO. Supercapacitors - powerful mobile energy storage devices. Technical report, http://www.csiro.au/science/Supercapacitors.html, 2005.

[39] Toshiba. Toshiba announces world's first small form factor direct methanol fuel cell for portable pc's. Technical report, 2003.

[40] Panasonic. Press release: Matsushita battery develops new micro fuel cell technology for portable electronics device. Technical report, 4 January, 2006.

[41] Angstrom Power Inc. Press release: Angstrom power demonstrates fully integrated fuel cell powered mobile device. Technical report, 8 January, 2008.

[42] W.R. Corliss and D.G. Harvey. *Radioisotopic power generation.* Prentice-Hall, 1964.

[43] A. Lal, R. Duggirala, and H. Li. Pervasive power: a radioisotope-powered piezoelectric generator. *Pervasive Computing, IEEE*, 4:53–61, 2005.

[44] Australian Bureau of Meteorology. climate map for solar exposure annual. Technical report, http://www.bom.gov.au/cgi-bin/climate/cgi bin scripts/solar-radiation.cgi., 2005.

[45] Robert Bogue. Solar-powered sensors: a review of products and applications. *Sensor Review*, 32:95–100, 2012.

[46] Tim Wark, Wen Hu, Peter Corke, Jonathan Hodge, Aila Keto, Ben Mackey, Glenn Foley, Pavan Sikka, and Michael Brünig. Springbrook: Challenges in developing a long-term, rainforest wireless sensor network. In *Intelligent Sensors, Sensor Networks and Information Processing, 2008. ISSNIP 2008. International Conference on*, pages 599–604. IEEE, 2008.

[47] V. Raghunathan, A. Kansal, J. Hsu, J. Friedman, and M. Srivastava. Design considerations for solar energy harvesting wireless embedded systems. In *Proceedings of the 4th international symposium on Information processing in sensor networks*, 2005.

[48] V. Kyriatzis, NS Samaras, P. Stavroulakis, H. Takruri-Rizk, and S. Tzortzios. Enviromote: A new solar-harvesting platform prototype for wireless sensor networks/work-in-progress report. In *Personal, Indoor and Mobile Radio Communications, 2007. PIMRC 2007. IEEE 18th International Symposium on*, 2007.

[49] J. Walker, D. Halliday, and R. Resnick. *Fundamentals of physics*. Wiley New York, 2008.

[50] SB Riffat and X. Ma. Thermoelectrics: a review of present and potential applications. *Applied Thermal Engineering*, 23:913–935, 2003.

[51] L. Weiling and TU Shantung. Recent developments of thermoelectric power generation. *Chinese Science Bulletin*, 49, 2004.

[52] R. Venkatasubramanian, E. Siivola, T. Colpitts, and B. O'quinn. Thin-film thermoelectric devices with high room-temperature figures of merit. *Nature*, pages 597–602, 2001.

[53] M. Ferrari, V. Ferrari, M. Guizzetti, D. Marioli, and A. Taroni. Characterization of thermoelectric modules for powering autonomous sensors. In *Instrumentation and Measurement Technology Conference Proceedings, 2007. IMTC 2007. IEEE*, 2007.

[54] Y. Hishinuma, TH Geballe, BY Moyzhes, and TW Kenny. Refrigeration by combined tunneling and thermionic emission in vacuum: Use of nanometer scale design. *Applied Physics Letters*, 78:2572–2574, 2001.

[55] Hongyun Yu, Yanqiu Li, Yonghong Shang, and Bo Su. Design and investigation of photovoltaic and thermoelectric hybrid power source for wireless sensor networks. In *Nano/Micro Engineered and Molecular Systems, 2008. NEMS 2008. 3rd IEEE International Conference on*, pages 196–201. IEEE, 2008.

[56] WANG Jian-jun. The temperature influence on solar pv generation [j]. *Journal of Qinghai Normal University (Natural Science Edition)*, 1:28–30, 2005.

[57] J.W. Stevens. Optimal placement depth for air–ground heat transfer systems. *Applied thermal engineering*, 24:149–157, 2004.

[58] EE Lawrence and GJ Snyder. A study of heat sink performance in air and soil for use in a thermoelectric energy harvesting device. In *Thermoelectrics, 2002. Proceedings ICT'02. Twenty-First International Conference on*, 2002.

[59] Y. Meydbray, R. Singh, and A. Shakouri. Thermoelectric module construction for low temperature gradient power generation. In *Proceedings of the 24th International Conference on Thermoelectrics (ICT05*, 2005.

[60] A. Bodensohn, R. Falsett, M. Haueis, and M. Pulvermüller. Autonomous sensor systems for car applications. *Advanced Microsystems for Automotive Applications*, pages 225–232, 2004.

[61] J.A. Paradiso and T. Starner. Energy scavenging for mobile and wireless electronics. *Pervasive Computing, IEEE*, 4:18–27, 2005.

[62] T. Starner and J.A Paradiso. Human generated power for mobile electronics. *Low-power electronics design*, pages 1–35, 2004.

[63] M. Kishi, H. Nemoto, T. Hamao, M. Yamamoto, S. Sudou, M. Mandai, and S. Yamamoto. Micro thermoelectric modules and their application to wristwatches as an energy source. In *Thermoelectrics, 1999. Eighteenth International Conference on*, 1999.

[64] G.W. Taylor, J.R. Burns, SA Kammann, W.B. Powers, and T.R. Welsh. The energy harvesting eel: a small subsurface ocean/river power generator. *Oceanic Engineering, IEEE Journal of*, 26:539–547, 2001.

[65] Michael A Weimer, Regan Zane, et al. Remote area wind energy harvesting for low-power autonomous sensors. In *Power Electronics Specialists Conference, 2006. PESC'06. 37th IEEE*, pages 1–5. IEEE, 2006.

[66] A. Singh and T. Aung. Effect of barometric pressure on sea level variations in the pacific region. *The South Pacific Journal of Natural and Applied Sciences*, 23: 9–15, 2005.

[67] S. Roundy, P.K. Wright, and J. Rabaey. A study of low level vibrations as a power source for wireless sensor nodes. *Computer Communications*, 26:1131–1144, 2003.

[68] P.D. Mitcheson, T.C. Green, E.M. Yeatman, and A.S. Holmes. Architectures for vibration-driven micropower generators. *Microelectromechanical Systems, Journal of*, 13:429–440, 2004.

[69] Sravanthi Chalasani and James M Conrad. A survey of energy harvesting sources for embedded systems. In *Southeastcon, 2008. IEEE*, pages 442–447. IEEE, 2008.

[70] James M Gilbert and Farooq Balouchi. Comparison of energy harvesting systems for wireless sensor networks. *international journal of automation and computing*, 5(4):334–347, 2008.

[71] Cian Ó Mathúna, Terence ODonnell, Rafael V Martinez-Catala, James Rohan, and Brendan OFlynn. Energy scavenging for long-term deployable wireless sensor networks. *Talanta*, 75(3):613–623, 2008.

[72] Mile K Stojčev, Mirko R Kosanović, and Ljubi AR Golubović. Power management and energy harvesting techniques for wireless sensor nodes. In *Telecommunication in Modern Satellite, Cable, and Broadcasting Services, 2009. TELSIKS'09. 9th International Conference on*, pages 65–72. IEEE, 2009.

[73] Yen Kheng Tan and Sanjib Kumar Panda. Review of energy harvesting technologies for sustainable wireless sensor network. *Sustainable wireless sensor networks*, pages 1–30, 2010.

[74] Sujesha Sudevalayam and Purushottam Kulkarni. Energy harvesting sensor nodes: Survey and implications. *Communications Surveys & Tutorials, IEEE*, 13(3):443–461, 2011.

[75] D Lee, G Dulai, and Vassili Karanassios. Survey of energy harvesting and energy scavenging approaches for on-site powering of wireless sensor-and microinstrument-networks. In *SPIE Defense, Security, and Sensing*, pages 87280S–87280S. International Society for Optics and Photonics, 2013.

[76] ASM Zahid Kausar, Ahmed Wasif Reza, Mashad Uddin Saleh, and Harikrishnan Ramiah. Energizing wireless sensor networks by energy harvesting systems: Scopes, challenges and approaches. *Renewable and Sustainable Energy Reviews*, 38:973–989, 2014.

[77] Gongbo Zhou, Linghua Huang, Wei Li, and Zhencai Zhu. Harvesting ambient environmental energy for wireless sensor networks: A survey. *Journal of Sensors*, 2014, 2014.

[78] Alim Dewan, Suat U Ay, M Nazmul Karim, and Haluk Beyenal. Alternative power sources for remote sensors: A review. *Journal of Power Sources*, 245:129–143, 2014.

[79] AA Bhaskar, R Champawat, and SA Bhaskar. Current developments of energy scavenging, converting and storing in wsns. *International Journal of Computer Applications*, 125(7), 2015.

[80] Aquadopp. Spec. sheet. URL www.nortekusa.com/en/products/.../aquadopp-3dcurrent-meter.

[81] LB Hormann, Philipp M Glatz, Christian Steger, and Reinhold Weiss. A wireless sensor node for river monitoring using msp430® and energy harvesting. In *Education and Research Conference (EDERC), 2010 4th European*, 2010.

[82] Ohmex instrumentation, spec. sheet, available from www.ohmex.com.

[83] Track800d, spec. sheet, available from www.marinetrack.com.

[84] C. Alippi, R. Camplani, C. Galperti, and M. Roveri. A robust, adaptive, solar-powered wsn framework for aquatic environmental monitoring. *Sensors Journal, IEEE*, 11:45 – 55, 2011.

[85] Thomas DC Little, Janusz Konrad, and Prakash Ishwar. A wireless video sensor network for autonomous coastal sensing. In *Proc. Conference on Coastal Environmental Sensing Networks,(CESN 2007)*. Citeseer, 2007.

[86] Sea-Hee Hwangbo, Jun-Ho Jeon, and Sung-Joon Park. Wireless underwater monitoring systems based on energy harvestings. *Sensors & Transducers*, 18(1):113, 2013.

[87] C Albaladejo Pérez, M Jimenez, F Soto, R Torres, J López, A Iborra, et al. A system for monitoring marine environments based on wireless sensor networks. In *OCEANS, 2011 IEEE-Spain*, pages 1–6. IEEE, 2011.

[88] Roque Torres, Fulgencio Soto, Cristina Albaladejo, Honorio Navarro, Juan Antonio Lopez, and Carlos Fernandez. Auto-positioning solar panel for harvesting power system in wsn marine buoys. *Instrumentation Viewpoint*, (18):74–74, 2015.

[89] César Ortega-Corral, Luis E Palafox, J Antonio García-Macías, Jaime Sánchez-García, and Leocundo Aguilar. End-to-end message exchange in a deployable marine environment hierarchical wireless sensor network. *International Journal of Distributed Sensor Networks*, 2014, 2014.

[90] URL http://www.nasa.gov/images/content/257995main_quikscat-wind-browse.jpg.

[91] Andrew R Henderson, Colin Morgan, Bernie Smith, Hans C Sørensen, Rebecca J Barthelmie, and Bart Boesmans. Offshore wind energy in europea review of the state-of-the-art. *Wind energy*, 6(1):35–52, 2003.

[92] James F Manwell, Jon G McGowan, and Anthony L Rogers. *Wind energy explained: theory, design and application*. John Wiley & Sons, 2010.

[93] AS Bahaj and LE Myers. Fundamentals applicable to the utilisation of marine current turbines for energy production. *Renewable energy*, 28(14):2205–2211, 2003.

[94] J. Dai, X. Li, B. Li, and L. Wang. Design and modeling of an underwater energy harvesting system. In *Proceedings of the international congress on analytical sciences (ICAS 2011)*., 2011.

[95] Clare E Reimers, Leonard M Tender, Stephanie Fertig, and Wei Wang. Harvesting energy from the marine sediment-water interface. *Environmental science & technology*, 35(1):192–195, 2001.

[96] K Scott, I Cotlarciuc, I Head, KP Katuri, D Hall, JB Lakeman, and D Browning. Fuel cell power generation from marine sediments: Investigation of cathode materials. *Journal of Chemical Technology and Biotechnology*, 83(9):1244–1254, 2008.

[97] C. Donovan, A. Dewan, H. Peng, D. Heo, and H. Beyenal. Power management system for a 2.5 w remote sensor powered by a sediment microbial fuel cell. *Journal of Power Sources*, 196:1171–1177, 2011.

[98] Farzaneh Rezaei, Tom L Richard, Rachel A Brennan, and Bruce E Logan. Substrate-enhanced microbial fuel cells for improved remote power generation from sediment-based systems. *Environmental science & technology*, 41(11):4053–4058, 2007.

[99] Conrad Donovan, Alim Dewan, Deukhyoun Heo, and Haluk Beyenal. Batteryless, wireless sensor powered by a sediment microbial fuel cell. *Environmental science & technology*, 42(22):8591–8596, 2008.

[100] J. Falnes. A review of wave-energy extraction. *Marine Structures*, 20(4):185–201, 2007.

[101] D. Mollison. *Hydrodynamics of ocean wave energy utilization*, chapter Wave climate and the wave power resource. Springer, 1986.

[102] Australian energy resource assessment. Technical report, Australian Bureau of Agricultural and Resource Economics, 2010.

[103] Robin Pelc and Rod M Fujita. Renewable energy from the ocean. *Marine Policy*, 26(6):471–479, 2002.

[104] J. Stevens. Heat transfer and thermoelectric design considerations for a ground-source thermo generator. In *Thermoelectrics, 1999. Eighteenth International Conference on*, 1999.

[105] J.W. Stevens. Optimal design of small delta t thermoelectric generation systems. *Energy Conversion and Management*, 42:709–720, 2001.

[106] J Davidson, M Collins, and S Behrens. Thermal energy harvesting between the air/water interface for powering wireless sensor nodes. In *SPIE Smart Structures and Materials+ Nondestructive Evaluation and Health Monitoring*, pages 728814–728814. International Society for Optics and Photonics, 2009.

[107] C Knight and J Davidson. *Advances in Wireless Sensors and Sensor Networks*, chapter Thermal energy harvesting for wireless sensor nodes with case studies, pages 221–242. Springer, 2010.

[108] C. Knight and J. Davidson. Thermoelectric energy harvesting as a wireless sensor node power source. In *Proc. of SPIE Vol 7643*, 2010.

[109] Bryn L Jones, Keith Jackson, Alistair James, David Meldrum, and Michael C Rose. Powering sea-ice instrumentation via the seebeck effect. *Cold Regions Science and Technology*, 68:60–67, 2011.

[110] J. Falnes. *Ocean Waves and Oscillating Systems : linear interactions including wave-energy extraction*. Cambridge Universtity Press, 2002.

[111] Queensland governmet wave monitoring, . URL http://www.qld.gov.au/environment/coasts-waterways/beach/monitoring/.

[112] Malcolm John Tucker and Edward G Pitt. *Waves in ocean engineering*. Number Volume 5. Elsevier, 2001.

[113] Willard J Pierson Jr and Lionel Moskowitz. A proposed spectral form for fully developed wind seas based on the similarity theory of sa kitaigorodskii. Technical report, DTIC Document, 1963.

[114] Klaus Hasselmann, TP Barnett, E Bouws, H Carlson, DE Cartwright, K Enke, JA Ewing, H Gienapp, DE Hasselmann, P Kruseman, et al. Measurements of wind-wave growth and swell decay during the joint north sea wave project (jonswap). Technical report, Deutches Hydrographisches Institut, 1973.

[115] Robert Henry Stewart. *Introduction to physical oceanography*. Texas A & M University, 2004.

[116] Alain Clément, Pat McCullen, António Falcão, Antonio Fiorentino, Fred Gardner, Karin Hammarlund, George Lemonis, Tony Lewis, Kim Nielsen, Simona Petroncini, et al. Wave energy in europe: current status and perspectives. *Renewable and Sustainable Energy Reviews*, 6:405–431, 2002.

[117] R. Bracewell. *Frog and PS Frog: A study of two reactionless ocean wave energy converters,*. PhD thesis, Lancaster University, 1990.

[118] F de O Antonio. Wave energy utilization: A review of the technologies. *Renewable and sustainable energy reviews*, 14(3):899–918, 2010.

[119] Benjamin Drew, AR Plummer, and M Necip Sahinkaya. A review of wave energy converter technology. *Proceedings of the Institution of Mechanical Engineers, Part A: Journal of Power and Energy*, 223(8):887–902, 2009.

[120] Michael E McCormick. *Ocean wave energy conversion*. Courier Corporation, 2013.

[121] João Cruz. *Ocean wave energy: current status and future prespectives*. Springer Science & Business Media, 2007.

[122] DV Evans. A theory for wave-power absorption by oscillating bodies. *Journal of Fluid Mechanics*, 77:1–25, 1976.

[123] Stephen H Salter. Wave power. *Nature*, 249:720–724, 1974.

[124] MJ French. On the difficulty of inventing an economical sea wave energy converter: a personal view. *Proceedings of the Institution of Mechanical Engineers, Part M: Journal of Engineering for the Maritime Environment*, 220:149–155, 2006.

[125] Iraide López, Jon Andreu, Salvador Ceballos, Iñigo Martínez de Alegría, and Iñigo Kortabarria. Review of wave energy technologies and the necessary power-equipment. *Renewable and Sustainable Energy Reviews*, 27:413–434, 2013.

[126] European marine energy centre. URL http://www.emec.org.uk/marine-energy/wave-developers/.

[127] Morten M. Kramer & Enrique Vidal Rico H. Hansen. Discrete displacement hydraulic power take-off system for the wavestar wave energy converter. *Energies*, 6: 4001–4044, 2013.

[128] Henk Polinder, Michiel EC Damen, and Fred Gardner. Linear pm generator system for wave energy conversion in the aws. *Energy Conversion, IEEE Transactions on*, 19:583–589, 2004.

[129] Mats Leijon, Hans Bernhoff, Olov Agren, Jan Isberg, Jan Sundberg, Marcus Berg, Karl Erik Karlsson, and Arne Wolfbrandt. Multiphysics simulation of wave energy to electric energy conversion by permanent magnet linear generator. *Energy Conversion, IEEE Transactions on*, 20:219–224, 2005.

[130] MA Mueller and NJ Baker. Direct drive electrical power take-off for offshore marine energy converters. *Proceedings of the Institution of Mechanical Engineers, Part A: Journal of Power and Energy*, 219:223–234, 2005.

[131] Ken Rhinefrank, EB Agamloh, Annette von Jouanne, AK Wallace, Joe Prudell, Kelly Kimble, Jess Aills, E Schmidt, P Chan, B Sweeny, et al. Novel ocean energy permanent magnet linear generator buoy. *Renewable Energy*, 31:1279–1298, 2006.

[132] MA Mueller, Henk Polinder, and Nick Baker. Current and novel electrical generator technology for wave energy converters. In *Electric Machines & Drives Conference, 2007. IEMDC'07. IEEE International*, 2007.

[133] Dara L OSullivan and Tony Lewis. Electrical machine options in offshore floating wave energy converter turbogenerators. In *Proceedings of the Tenth World Renewable Energy Congres (WREC X)*, pages 1102–1107, 2008.

[134] H Polinder, MA Mueller, M Scuotto, and M Goden de Sousa Prado. Linear generator systems for wave energy conversion. In *Proceedings of the 7th European Wave and Tidal Energy Conference, Porto, Portugal*, 2007.

[135] S Astariz and G Iglesias. The economics of wave energy: A review. *Renewable and Sustainable Energy Reviews*, 45:397–408, 2015.

[136] J Fievez and T Sawyer. Lessons learned from building and operating a grid connected wave energy plant. In *Procedings of 11th European Wave and Tidal Energy Conf.(EWTEC), Nantes*, 2015.

[137] Border lengths - states and territories, . URL http://www.ga.gov.au/scientific-topics/national-location-information/dimensions/border-lengths.

[138] URL www.google.com/maps.

[139] David P Arnold. Review of microscale magnetic power generation. *Magnetics, IEEE Transactions on*, 43(11):3940–3951, 2007.

[140] David Morgan. *A handbook for EMC testing and measurement*, volume 8. Iet, 1994.

[141] G Bracco, E Giorcelli, G Mattiazzo, M Pastorelli, and J Taylor. Iswec: design of a prototype model with gyroscope. In *Clean Electrical Power, 2009 International Conference on*, pages 57–63. IEEE, 2009.

[142] S.P. Bastien, RB Sepe, A.R. Grilli, S.T. Grilli, and M.L. Spaulding. Ocean wave energy harvesting buoy for sensors. In *Energy Conversion Congress and Exposition, 2009. ECCE 2009. IEEE*, 2009.

[143] Douglas Gemme, Steven P Bastien, Raymond B Sepe, John Montgomery, Stephan T Grilli, Annette Grilli, et al. Experimental testing and model validation for ocean wave energy harvesting buoys. In *Energy Conversion Congress and Exposition (ECCE), 2013 IEEE*, pages 337–343. IEEE, 2013.

[144] Douglas Gemme, H Ronald Greene, Travis Tucker, Raymond B Sepe, Steven P Bastien, et al. Hybrid resonant wave energy harvesting buoy for sensor applications. In *Oceans-San Diego, 2013*, pages 1–6. IEEE, 2013.

[145] A.R. Grilli, J. Merrill, S.T. Grilli, M.L. Spaulding, and J. Cheung. Experimental and numerical study of spar buoy-magnet/spring oscillators used as wave energy absorbers. In *Proceedings of the Seventeenth (2007) International Offshore and Polar Engineering Conference*, 2007.

[146] S.T. Grilli, A.R. Grilli, S.P. Bastien, R.B. Sepe Jr, and M.L. Spaulding. Small buoys for energy harvesting: Experimental and numerical modeling studies. In *Proceedings of the Twenty-first (2011) International Offshore and Polar Engineering Conference*, 2011.

[147] Deanelle Symonds, Edward Davis, and R Cengiz Ertekin. Low-power autonomous wave energy capture device for remote sensing and communications applications. In *Energy Conversion Congress and Exposition (ECCE), 2010 IEEE*, pages 2392–2396. IEEE, 2010.

[148] M Engelmann, E Davis, and D Symonds. Non-resonant, rotary-drive wave energy conversion device for distributed remote sensing and communications applications. In *OCEANS 2011*, pages 1–4. IEEE, 2011.

[149] S.N. Avadhany, C. Tucker, H.J. Fought, and R. Granger. Optimized wave energy harvester for distributed application. In *Oceans, 2012*, Oceans, 2012.

[150] Jeffrey T Cheung and Earl F Childress III. Ocean wave energy harvesting devices. Technical report, DTIC Document, 2007.

[151] Jochem Weber. Wec technology readiness and performance matrix–finding the best research technology development trajectory. In *Int. Conf. Ocean Energy Dublin Irel*, 2012.

[152] Alexander H-D Cheng and Daisy T Cheng. Heritage and early history of the boundary element method. *Engineering Analysis with Boundary Elements*, 29(3): 268–302, 2005.

[153] Y. Li and Y. Yu. A synthesis of numerical methods for modeling wave energy converter - point absorbers. *Renewable and Sustainable Energy Reviews*, 16:4352–4364, 2012.

[154] Reza Taghipour, Tristan Perez, and Torgeir Moan. Hybrid frequency–time domain models for dynamic response analysis of marine structures. *Ocean Engineering*, 35:685–705, 2008.

[155] WE Cummins. The impulse response function and ship motions. Technical report, DTIC Document, 1962.

[156] Hugh A Wolgamot and Colm J Fitzgerald. Nonlinear hydrodynamic and real fluid effects on wave energy converters. *Proceedings of the Institution of Mechanical Engineers, Part A: Journal of Power and Energy*, page 0957650915570351, 2015.

[157] Markel Penalba Retes, Giuseppe Giorgi, and John Ringwood. A review of non-linear approaches for wave energy converter modelling. In *Proceedings of the 11th European Wave and Tidal Energy Conference*. European Wave and Tidal Energy Conference 2015, 2015.

[158] Josh Davidson, Simone Giorgi, and J Ringwood. Linear parametric hydrodynamic models based on numerical wave tank experiments. In *9th European Wave and Tidal Energy Conference (EWTEC), Aalborg*, 2013.

[159] Josh Davidson, Simone Giorgi, and John V Ringwood. Numerical wave tank identification of nonlinear discrete time hydrodynamic models. *Renewable Energies Offshore*, page 279, 2015.

[160] Josh Davidson, Simone Giorgi, and John V Ringwood. Linear parametric hydrodynamic models for ocean wave energy converters identified from numerical wave tank experiments. *Ocean Engineering*, 103:31–39, 2015.

[161] John V Ringwood, Josh Davidson, and Simone Giorgi. Optimising numerical wave tank tests for the parametric identification of wave energy device models. In *ASME 2015 34th International Conference on Ocean, Offshore and Arctic Engineering*, pages V009T09A020–V009T09A020. American Society of Mechanical Engineers, 2015.

[162] Josh Davidson, Marie Cathelain, Louise Guillemet, Thilbault Le Huec, and John Ringwood. Implementation of an openfoam numerical wave tank for wave energy experiments. In *Proceedings of the 11th European Wave and Tidal Energy Conference*. European Wave and Tidal Energy Conference 2015, 2015.

[163] Simone Giorgi, Josh Davidson, and John V Ringwood. Identification of nonlinear excitation force kernels using numerical wave tank experiments. In *Procedings of 11th European Wave and Tidal Energy Conf.(EWTEC), Nantes*, 2015.

[164] Josh Davidson, Simone Giorgi, and John V Ringwood. Identification of wave energy device models from numerical wave tank data - part 1: Numerical wave tank identification tests. *IEEE Transactions on Sustainable Energy*, 2016.

[165] Simone Giorgi, Josh Davidson, and John V Ringwood. Identification of wave energy device models from numerical wave tank data - part 2: Data-based model determination. *IEEE Transaction on Sustainable Energy*, 2016.

[166] J. V. Ringwood, J Davidson, and S. Giorgi. *Numerical Modeling of Wave Energy Converter: State-of-the-art techniques for single WEC and converter arrays*, chapter Identifying models using recorded data. Elsevier, 2016.

[167] *WAMIT User Manual, Version 6.4 (available at www.wamit.com).*

[168] Aurélien Babarit and Gérard Delhommeau. Theoretical and numerical aspects of the open source bem solver nemoh. In *11th European Wave and Tidal Energy Conference (EWTEC2015)*, 2015.

[169] A Roessling and JV Ringwood. Finite order approximations to radiation forces for wave energy applications. *Renewable Energies Offshore*, page 279, 2015.

[170] Z. Yu and J. Falnes. State-space modelling of a vertical cylinder in heave. *Applied Ocean Research*, 17:265–275, 1995.

[171] CB Williams and Rob B Yates. Analysis of a micro-electric generator for microsystems. *sensors and actuators A: Physical*, 52(1):8–11, 1996.

[172] Rajeevan Amirtharajah and Anantha P Chandrakasan. Self-powered signal processing using vibration-based power generation. *Solid-State Circuits, IEEE Journal of*, 33(5):687–695, 1998.

[173] Shad Roundy, Paul K Wright, and Jan Rabaey. A study of low level vibrations as a power source for wireless sensor nodes. *Computer communications*, 26(11): 1131–1144, 2003.

[174] Steve P Beeby, RN Torah, MJ Tudor, P Glynne-Jones, T O'Donnell, CR Saha, and S Roy. A micro electromagnetic generator for vibration energy harvesting. *Journal of Micromechanics and microengineering*, 17(7):1257, 2007.

[175] Thomas von Büren and Gerhard Tröster. Design and optimization of a linear vibration-driven electromagnetic micro-power generator. *Sensors and Actuators A: Physical*, 135:765–775, 2007.

[176] Abigail Wacher and Kim Nielsen. Mathematical and numerical modeling of the aquabuoy wave energy converter. *Mathematics-in-Industry Case Studies*, 2, 2010.

[177] Oliver M Phillips. The equilibrium range in the spectrum of wind-generated waves. *Journal of Fluid Mechanics*, 4:426–434, 1958.

[178] Ronald William Burling. *Wind generation of waves on water*. PhD thesis, Imperial College, University of London, 1955.

[179] DHI. Deutches hydrographisches institut: Handbach des atlantischen ozeans, no. 2057. Technical report, 1981.

[180] URL www.weather.aims.gov.au.

[181] Robert A Dalrymple and Robert George Dean. *Water wave mechanics for engineers and scientists*. Prentice-Hall, 1991.

[182] Francis JM Farley. The free floating clam-a new wave energy converter. In *Proceedings of the 9th European Wave and Tidal Energy Conference, Southampton*, 2011.

[183] John A Duffie and William A Beckman. *Solar engineering of thermal processes*. Wiley New York, 2006.

[184] Liping Liu. Feasibility of large-scale power plants based on thermoelectric effects. *New Journal of Physics*, 16(12):123019, 2014.

[185] Majid A Bhinder, Madjid Karimirad, Sam Weller, Yannick Debruyne, Matthieu Guérinel, and Wanan Sheng. Modelling mooring line non-linearities (material and geometric effects) for a wave energy converter using aqwa, sima and orcaflex. In *Proceedings of the 11th European Wave and Tidal Energy Conference*. European Wave and Tidal Energy Conference 2015, 2015.

[186] John Fitzgerald and Lars Bergdahl. Including moorings in the assessment of a generic offshore wave energy converter: A frequency domain approach. *Marine Structures*, 21(1):23–46, 2008.

[187] Robert E Harris, Lars Johanning, and Julian Wolfram. Mooring systems for wave energy converters: A review of design issues and choices. *Proceedings of the 2004 MAREC, Blyth*, pages 1–10, 2004.

[188] Kate Freeman and Josh Davidson. An internation network on offshore renewbale energy. In *1st Asian Wave and Tidal Conference Series*, 2012.

[189] Cameron McNatt, Matthew Hall, Josh Davidson, Adrian de Andres, and Soraya Hamawi. Innovation in offshore renewable energy: International collaboration and inore. In *5th International Conference on Ocean Energy*, 2014.

[190] Colonel Wm T McLyman. *Transformer and inductor design handbook*. CRC press, 2011.

[191] Nick J Baker, MA Mueller, and E Spooner. Permanent magnet air-cored tubular linear generator for marine energy converters. In *Power Electronics, Machines and Drives, 2004.(PEMD 2004). Second International Conference on (Conf. Publ. No. 498)*, volume 2, pages 862–867. IET, 2004.

[192] Varun Lobo, Arindam Banerjee, Nyuykighan Mainsah, and Jonathan Kimball. Hydrokinetic energy harvesting system from vortex induced vibrations of submerged bodies. In *ASME 2011 5th International Conference on Energy Sustainability*, pages 1229–1236. American Society of Mechanical Engineers, 2011.

[193] J Wang, GW Jewell, and D Howe. Design optimisation and comparison of tubular permanent magnet machine topologies. In *Electric Power Applications, IEE Proceedings-*, volume 148, pages 456–464. IET, 2001.

[194] David Meeker. Finite element method magnetics. *FEMM*, 4:32, 2010.

[195] American society for testing and materials (astm) terrestrial reference spectra for photovoltaic performance evaluation. http://rredc.nrel.gov/solar/spectra/am1.5.